Title
Hybrid Simulations for the Seismic Evaluation of Resilient Highway Bridge Systems

Author
Wu, Yingjie

Publication Date
2020

Peer reviewed|Thesis/dissertation

Hybrid Simulations for the Seismic Evaluation of Resilient Highway Bridge Systems

By

Yingjie Wu

A dissertation submitted in partial satisfaction of the

requirements for the degree of

Doctor of Philosophy

in

Engineering – Civil and Environmental Engineering

in the

Graduate Division

of the

University of California, Berkeley

Committee in charge:

Professor Khalid M. Mosalam, Chair
Professor Filip C. Filippou
Professor Panayiotis Papadopoulos

Spring 2020

COPYRIGHT

Hybrid Simulations for the Seismic Evaluation of Resilient Highway Bridge Systems

ABSTRACT

Hybrid Simulations for the Seismic Evaluation of Resilient
Highway Bridge Systems

By

Yingjie Wu

Doctor of Philosophy in Engineering – Civil and Environmental Engineering

University of California, Berkeley

Professor Khalid M. Mosalam, Chair

Bridges often serve as key links in the local and national transportation networks. Any bridge closures can have severe costs not only in the form of repair or replacement, but also in the form of economic losses related to medium- and long-term interruption of businesses and disruption to the communities. In addition, continuous functionality of bridges is very important after any seismic event for emergency response and recovery purposes. Considering the importance of these structures, the associated structural design philosophy is shifting from collapse prevention to maintaining functionality in the aftermath of moderate to strong earthquakes (Resiliency). Moreover, the associated construction philosophy is being modernized with the utilization of accelerated bridge construction (ABC) techniques to reduce impacts of construction work on traffic, society, economy and on-site safety during construction. This dissertation presents two bridge systems targeting the aforementioned issues. A combined numerical and experimental research was undertaken to characterize the seismic performance of these bridge systems.

The first part of the study focuses on the structural system level response of highway bridges that incorporate a class of innovative connecting devices called the "V-connector", which can be used to connect two components in a structural system, e.g., the column and the bridge deck, or the column and its foundation. This device, designed by ACII, Inc., results in an isolation surface at the connection plane via a connector rod placed in a V-shaped tube embedded into the concrete. Energy dissipation is provided by friction between a special washer located around the V-shaped tube and a top plate. Because of the period elongation due to the isolation layer and the limited amount of force transferred by the relatively flexible connector rod, bridge columns are protected from experiencing damage, leading to an improved seismic behavior. The V-connector system also facilitates the ABC by allowing on-site assembly of prefabricated structural parts including those of the V-connector.

A single-column, two-span highway bridge located in Northern California was used for the proof-of-concept of the proposed V-connector protective system. The V-connector was designed to result in an elastic bridge response based on nonlinear dynamic analyses of the bridge model

with the V-connector. Accordingly, a 1/3-scale V-connector was fabricated based on a set of selected design parameters. A quasi-static cyclic test was first conducted to characterize the force-displacement relationship of the V-connector, followed by a hybrid simulation (HS) test in the longitudinal direction of the bridge to verify the intended linear elastic response of the bridge system. In the HS test, all bridge components were analytically modeled except for the V-connector, which was simulated as the experimental substructure in a specially designed and constructed test setup. Linear elastic bridge response was confirmed according to the HS results. The response of the bridge with the V-connector was compared against that of the as-built bridge without the V-connector, which experienced significant column damage. These results justified the effectiveness of this innovative device.

The second part of the study presents the HS test conducted on a 1/3-scale two-column bridge bent with self-centering columns (or broadly defined as "resilient columns" in this study) to reduce (or ultimately eliminate) any residual drifts. The comparison of the HS test with a previously conducted shaking table test on an identical bridge bent is one of the highlights of this study. The concept of resiliency was incorporated in the design of the bridge bent columns characterized by a well-balanced combination of self-centering, rocking and energy dissipating mechanisms. This combination is expected to lead to minimum damage and low levels of residual drifts. The ABC is achieved by utilizing precast columns and end members (cap beam and foundation) through an innovative socket connection. In order to conduct the HS test, a new hybrid simulation system (HSS) was developed, utilizing commonly available software and hardware components in most structural laboratories, namely, a computational platform using Matlab/Simulink (MathWorks, 2015), an interface hardware/software platform dSPACE (2017), and MTS controllers and data acquisition (DAQ) system for the utilized actuators and sensors. The operation of the HSS was verified using a trial run without the test specimen.

In the conducted HS test, the two-column bridge bent was simulated as the experimental substructure while modeling the horizontal and vertical inertia masses and the corresponding mass proportional damping in the computer. The same ground motions from the shaking table test, consisting of one horizontal component and the vertical component, were applied as input excitations to the equations of motion in the HS. Good matching was obtained between the shaking table and the HS test results, demonstrating the appropriateness of the defined governing equations of motion and the employed damping model, in addition to the reliability of the developed HSS with minimum simulation errors. The small residual drifts and the minimum level of structural damage at large peak drift levels demonstrated the superior seismic response of the innovative design of the bridge bent with self-centering columns. The reliability of the developed HS approach was the motivation of a follow-up HS study focusing on the transverse direction of the bridge where the entire two-span bridge deck and its abutments represented the computational substructure while the two-column bridge bent was the physical substructure. This investigation was effectively utilized to shed more light on the system level performance of the entire bridge system with innovative bridge bent design beyond what can be achieved via shaking table tests, which are usually limited by large-scale bridge system testing capacities.

Those times when you get up early and you work hard;
those times when you stay up late and you work hard;
those times when you don't feel like working, you are too tired, you don't want to push yourself,
but you do it anyway,
that is actually the DREAM.

In memory of Kobe Bryant (*1978-2020*)

ACKNOWLEDGEMENTS

It is time to say goodbye to my last journey and say hello to the next stage of my life. At this special moment, I have so many feelings and words in mind.

To begin with, I would like to express my deepest gratitude to my research advisor and my dissertation committee chair, Prof. Khalid M. Mosalam for his support, encouragement and guidance throughout the years. We first met during his visit in Tongji University, China in 2013 At that time, I was applying for graduate school in the United States. I was so lucky to be admitted by my dream school UC Berkeley, one of the best universities in the world. Even more fortunate was that after one year of master's study, I finally became his PhD student. He provided me not only with solid knowledge, inspiring ideas and cautious attitudes that will benefit me for the rest of my life, but also with generous and continuous financial support, without which my graduate studies would not have been possible. I felt more than blessed to have the opportunity to take on this incredible journey with him. No matter where I am or how far I go in the future, his mentorship and friendship will always be among the most valued things that accompanies me in every aspect of my life.

Besides, I greatly appreciate other professors at Berkeley. Special thanks to Prof. Filip C. Filippou for serving on my dissertation committee and chairing my qualifying exam committee; Prof. Panayiotis Papadopoulos for serving on my dissertation committee; Prof. Shaofan Li for being on my qualifying exam committee; Prof. Haiyan Huang for being my statistics minor advisor and Prof. Tarek I. Zohdi for being my computational mechanics minor advisor. Their impressive, fantastic lectures and informative technical advices truly expanded my visions and increased my knowledge.

My deepest gratitude and greatest appreciation extend to Dr. Selim Günay, who helped me like a big brother throughout my entire graduate studies at Berkeley over the past few years. His wealthy experience, brilliant thoughts, careful reviews and patient instructions made my endeavors much less painful. I will never forget the days and nights we spent together in the laboratory debugging codes, trying different parameters, playing with different types of equipment and analyzing the data over and over again.

I am grateful for the Pacific Earthquake Engineering Research (PEER) Center for sponsoring my study. I would like to recognize the technical and financial support of ACII, Inc., Irving, CA, founded by Dr. Su Hao, for the work related to the V-connector, which was made available via the support of the NCHRP-IDEA program by TRB. I would also like to recognize Prof. José I. Restrepo and Dr. Arpit Nema for their contribution in the early development of the resilient bridge bent. The administrative and practical support of Dr. Amarnath Kasalanati is greatly appreciated. The engineers and technicians from the Structural Laboratory on Berkeley campus and at Richmond Field Station were extremely helpful throughout my experimental studies. Special thanks to Dr. Shakhzod Takhirov for valuable inputs on the test configuration and the coordination on the testing equipment; Phillip Wong for checking and operating the testing facilities; Matt Cataleta, Llyr Griffith, Lobsang Garcia and Robert Cerney for the tough and challenging, yet perfect and precise labor work. I also want to thank some undergraduate/graduate/intern students from Berkeley, Wen Tang, Matthew Yeung, Efe Ozcanli,

Juan Meriles to name a few, and my Chinese friends Chenjie Gong, Yuzhou Zheng, Xiangxiang Ren and Baoshi Liu, who were involved in different phases of the experimental preparation.

My journey at Berkeley could not have been so lucky and enjoyable without being surrounded by a group of caring and wonderful friends: Jingyi Wang, Benshun Shao, Shanshan Wang, Cindy Qian, Daniel Miller, Barbara Simpson to name a few. We built strong relationships out of the challenges and pressure we faced together and the joy we had together. They have witnessed my growth during the years of my study, and I will always treasure the friendship with them.

I wish to express my warmest and deepest gratitude to my beloved parents. I thank my father Huiming Wu, a general and a pilot serving the Chinese People's Liberation Army Air Force, for inspiring me to fly higher and raising me up to more than I could be. I thank my mother Qiuya Zhu for her tremendous care and love in every aspect of my life ever since I was born. They offered me maximum amount of support, both mentally and financially, when I told them my desire to explore the new world overseas, despite the fact that they prefer to have me around because I am the only child in my family. Thank you for your education to make me become a better person and keep moving on. May the health and happiness always be with you!

Finally, I owe a big thank to my girlfriend and my significant other, Miss Yi Yang, who brought me joy, happiness and wonderful memories in the past 6 years. I firmly believe that meeting with her is a kind of predestination. Not only we share the same interests and positive attitudes towards life, but also the exact same birthday! May you always be a happy angel and wish us all the best in the bright future ahead.

Yingjie Wu

May. 1st, 2020

TABLE OF CONTENTS

LIST OF TABLES

LIST OF FIGURES

1 Introduction

1.1 GENERAL

As reported by the U.S. Geological Survey (2014), at least 40 percent of the United States can expect to experience earthquakes with the potential to damage highway bridges within their lifetime, refer to Figure 1.1. This problem is compounded by the fact that many bridges across the country are already considered structurally deficient as of 2018. These bridges often serve as key links in the local and national transportation networks, and any closures will have severe costs not only for repair or replacement, but also in the form of economic losses and other consequences related to medium- and long-term interruption of businesses, disruption of communities and difficulty in the emergency response operations.

Figure 1.1 Damaged bridges after 1994 Northridge earthquake (source: FEMA photo library).

In structural engineering practice, designing structures to respond elastically without damage under different levels of earthquakes has generally been considered infeasible for economic reasons; as a result, current bridge seismic design provisions like the California Department of Transportation (Caltrans) Seismic Design Criteria (SDC) or the American Association of State Highway and Transportation Officials (AASHTO) LRFD Bridge Design Specifications allow ductile behavior of the columns beyond the elastic limit and permit damage or even closure of ordinary bridges, provided that collapse is prevented. The damage at a design level ductility usually involves the forming of localized flexural plastic hinge regions at the top and/or bottom of the columns, featured by yielding of reinforcement and concrete spalling. In some cases, reinforcement is susceptible to buckling and fracture to accommodate deformations imposed by the ductile design provisions.

However, while the concept of structural damage is widely accepted in design practices, resilient communities are expecting strategic structures and bridges to survive moderately strong earthquakes with little or no disturbance to traffic and business. Considering that a significant number of bridges are located in earthquake-prone regions, the impact and cost of earthquake-induced damage on these structures have raised serious questions on whether the current seismic design philosophy can satisfy the needs of modern societies. In addition, because of their importance in the transportation networks, bridges are often found in densely populated urban areas, where the impacts of construction work on traffic, environment, society, and economy are considerable. The lengthy on-site bridge construction projects are also exposing construction workers to increased risk. Therefore, minimizing the construction time becomes an essential endeavor to reduce the aforementioned consequences on the public, workers, and the environment.

With the attempt to address the two issues mentioned above, namely reducing permanent damage and accelerating construction of bridges, the design philosophy is now shifting from collapse prevention to maintaining functionality in the aftermath of moderate to strong earthquakes. In addition to performance, the construction philosophy is also being modernized with the utilization of accelerated bridge construction (ABC) techniques to reduce impacts on traffic, society, economy and on-site safety during construction.

1.2 RESILIENCE CONCEPT

As part of the conceptualization of a framework to enhance the seismic resilience of communities (Bruneau et al., 2003), seismic resilience has been defined as the ability of a system to reduce the chances of a shock, to absorb such a shock if it occurs (abrupt reduction of performance) and to recover quickly after a shock (re-establish normal performance). More specifically, a resilient system is one that shows:

- Reduced failure probabilities;
- Reduced consequences from failures, in terms of lives lost, damage, and negative economic and social consequences; and
- Reduced time to recovery (restoration of a specific system or a set of systems to their "normal" level of functional performance).

A broad measurement of resilience that captures these key features can be expressed by the concepts illustrated in Figure 1.2. A measurement denoted with $Q(t)$, which varies with time, can be defined to represent the quality of the infrastructure of a community. Specifically, performance can range from 0% to 100%, where 100% means no degradation in quality and 0% means total quality loss. If an earthquake or another disaster occurs at time t_0, it could cause damage to the infrastructure such that the quality measurement $Q(t)$ is immediately reduced (from 100% to 50%, as an example, in Figure 1.2). Restoration of the infrastructure is expected to occur over time, as indicated in the figure, until time t_1 when it is completely repaired and back to normal operation (indicated by the quality metric going back to 100%). Hence, earthquake loss of the community resilience R with respect to that specific earthquake can be measured by the size of the expected degradation in quality over time. Mathematically, it is defined by:

$$R = \int_{t_0}^{t_1} [100 - Q(t)]dt \tag{1.1}$$

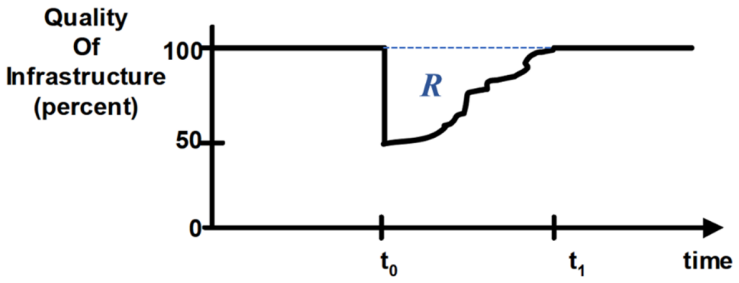

Figure 1.2 Schematic representation of the seismic resilience concept (Bruneau et al., 2003).

Resilience for both physical and social systems can be further defined as consisting of the following properties:

- **Robustness**: strength, or the ability of elements, systems, and other units of analysis to withstand a given level of stress or demand without suffering degradation or loss of function.
- **Redundancy**: the extent to which elements, systems, or other units of analysis exist that are substitutable, i.e., capable of satisfying functional requirements in the event of disruption, degradation, or loss of functionality;
- **Resourcefulness**: this can be conceptualized as the ability to apply materials (i.e., monetary, physical, technological, and informational) and human resources in the process of recovery to meet established priorities and achieve goals; and
- **Rapidity**: the capacity to meet priorities and achieve goals in a timely manner in order to contain losses, recover functionality and avoid future disruption.

Figure 1.2 addresses the first and last properties of resilience, namely robustness and rapidity. The main focus of this study deals with the robustness aspect of resilience. However, it should be noted that there exists a much bigger picture in terms of resilience and research in this domain will continue for the years to come.

1.3 PROBLEM STATEMENT AND OBJECTIVES

This study presents two bridge subsystems aiming at providing seismic resiliency and fast bridge construction. First of these systems is an innovative connection device that elongates the period of the structure by introducing an isolation layer between the bridge column and the footing or the bridge column and the bridge deck or the cap beam. The second system consists of enhanced response features including self-centering, rocking, and energy dissipation. The commonality of these two systems are reduced downtime and increased functionality after severe earthquakes either by keeping the bridge components in the elastic range of response and/or significantly reducing any residual displacements. Although these systems have significant potential for enhanced seismic response, they can only be fully utilized if they can be modeled and their

response can be properly predicted in the design phase of bridges. A blind prediction competition recently conducted by the Pacific Earthquake Engineering Research (PEER) Center from the shaking table test of the second system (Nema, 2018; Günay et al., 2020) demonstrated a large variation of the response predictions by researchers and practitioners. Therefore, there is an essential need to characterize the seismic response of these enhanced feature systems and improve their modeling and response predictions. For this purpose, a combined numerical and experimental research was undertaken.

1.3.1 V-connector

The first part of the research focuses on the structural system response of reinforced concrete (RC) highway bridges incorporating a class of innovative connecting devices called the "V-connector" (Hao, 2018), with the use of hybrid and analytical simulations to verify the design concept and goals. The research objectives include:

- Develop a set of design parameters to provide guidance on V-connector manufacturing;
- Characterize the hysteretic behavior of the V-connector by a quasi-static cyclic test;
- Develop and calibrate an analytical model for the V-connector based on the cyclic test results;
- Conduct a hybrid simulation (HS) test of a complete prototype bridge employing a V-connector; and
- Compare the responses of the prototype bridge with and without the V-connector and justify its effectiveness in improving the behavior of the bridge system under earthquake loading.

1.3.2 Resilient Column

The second part of the research is a study to investigate the system level response of bridges with enhanced response features including self-centering, rocking, confinement and energy-dissipation of columns. For this purpose, a 1/3-scale two-column bridge bent with enhanced response features was designed and subjected to a series of shaking table tests (Nema, 2018). As a result of the conducted shaking table tests, the bridge bent was observed to deliver good seismic performance with very small residual drifts. In this research, an identical bridge bent was constructed, with experimental and analytical work completed in two phases. The research objectives include:

- Develop a new hybrid simulation system (HSS), utilizing commonly available software and hardware components in most structural engineering laboratories;
- Validate the developed HSS and implemented algorithms;
- Conduct HS test on the identically constructed bridge bent and compare the test results against the shaking table test to verify the considered HS approach;

- Incorporate a full bridge system into the HS test and explore whether similar good performance could be achieved when the system level response is considered; and
- Investigate the effect of different parameters on the bridge response and interpret the test observations through parametric studies.

1.3.3 Connection to Hybrid Simulation

HS is a mixed computational/physical testing technique, with the idea to split a structure into analytical and experimental substructures. Analytical substructures are generally those that can be modeled with confidence, while experimental substructures are those that are difficult to model due to lack of prior knowledge, complicated geometry and boundary conditions, material inelastic behavior, etc. In the context of resilient bridge subsystems described above, there is generally limited data for the employed new technologies. Furthermore, it is practically not possible to test a complete bridge in any of the existing structural laboratories or shaking tables around the world. Therefore, HS comes forward as a very convenient approach to simulate the seismic response of resilient bridges. The experimental substructures can either be a new connection device as is the case in the V-connector study or a bridge bent with innovative and resilient features such as a well-balanced combination of self-centering, rocking and energy dissipation, while the analytical substructure is originated from the same prototype bridge for both studies. Refer to Figure 1.3 for the overall approach adopted in this dissertation for HS of the considered innovative designs.

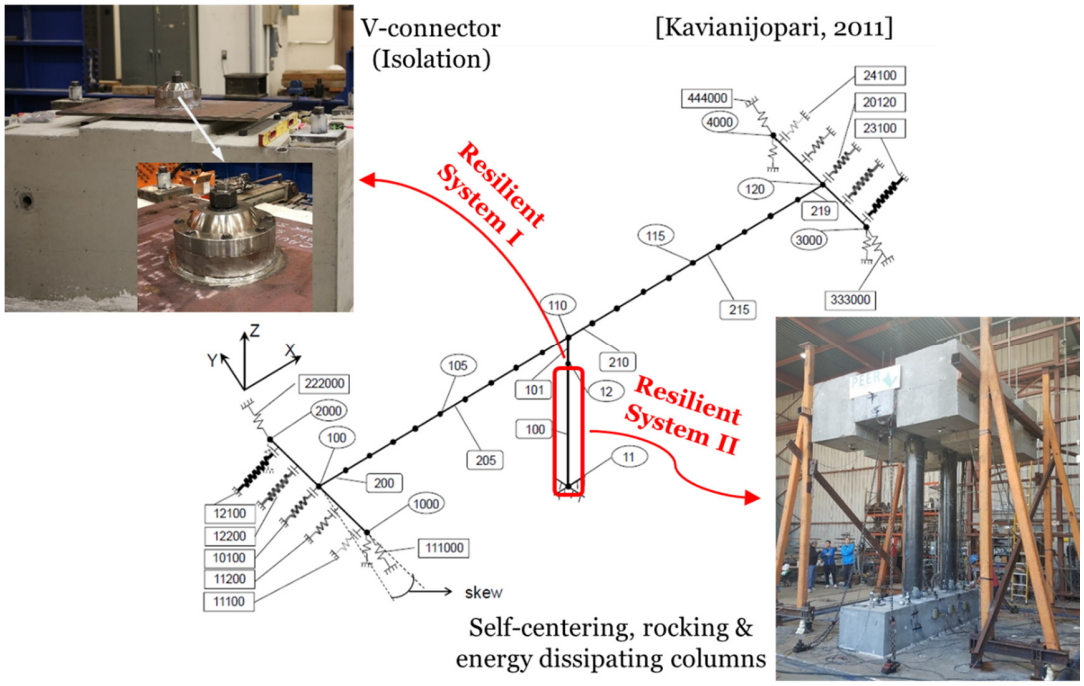

Figure 1.3 Hybrid simulation in the context of resilient bridge subsystems.

1.4 ORGANIZATION OF THE DISSERTATION

This dissertation consists of nine chapters and four appendices. Chapter 1 presents a general introduction of the problem statement, methodology, concept and main objectives of the undertaken study. Chapter 2 provides the necessary background. Some previous studies that focused on resilient structural systems (mainly in the form of re-centering behavior) and HS are reviewed and summarized in this chapter. The experimental study and discussions comprising the core of this dissertation are presented in Chapter 3 through Chapter 8 and can be divided into two parts, one for each subsystem.

The V-connector's study is documented in Chapters 3 to 5. In Chapter 3, the idea of the V-connector and its components are first introduced. Followed by the introduction are the test specimen's design and construction, test setup, loading protocol, material properties, and instrumentations used during the V-connector's experimental program. Chapter 4 starts by briefly summarizing the pre-test analyses carried out before embarking on the experimental program. It then discusses the experimental observations and results obtained from the quasi-static cyclic test of the V-connector, together with the analytical model calibration. The HS tests, including the HS trial test and the actual HS test conducted on the V-connector, and the test results are presented in Chapter 5.

The documentation of the study of the self-centering, rocking and energy dissipating columns (or resilient columns for short) spans Chapters 6 to 8. Similar to the discussions in Chapter 3, the development of the second experimental program is the essence of Chapter 6, with some innovative features of the resilient columns demonstrated at the beginning. Chapter 7 starts by briefly presenting the shaking table test conducted in (Nema, 2018), followed by a detailed description of the development and verification of the new HSS for phase I of the HS study of the resilient columns. The comparison of the HS results to the shaking table, which is the main goal of phase I, is also presented. Chapter 8 discusses the system level HS of the resilient bridge bent by incorporating a full bridge system. The modeling and implementation details, including some background on the formulation of the structural dynamic problems are discussed first. Some important findings from the system level testing, together with the parametric study, for interpretation of the test results are then presented. A brief summary, main conclusions and future directions based on the entire study are presented in Chapter 9. Several appendices are included at the end of the dissertation for completeness of the presented work. These appendices provide additional details of specimen design and construction, procedures of specimen assembly and test setup, and some Matlab functions utilized in the HSS development for future reference.

2 Background and Literature Review

Several early studies and approaches that focused on seismic-resistant and earthquake-protective systems were reviewed during the course of this study to understand the state-of-the-art technologies being employed. In addition, to successfully conduct the extensive experimental programs, some previously conducted theoretical and experimental works, especially those related to the HS tests of different bridge components, were reviewed. In this chapter, some of the relevant studies are briefly summarized for completeness and categorized into three subsections: seismic isolation, self-centering hybrid systems and HS fundamentals.

2.1 SEISMIC ISOLATION

Seismic isolation technology has gained increasing applications in many countries and practices to improve the performance of buildings and bridges and to avoid significant structural damage during ground shaking. By effectively delivering safe structures, it can also minimize economic losses due to downtime and repair costs. The idea of seismic isolation is to utilize specially-designed devices such as bearings to isolate the structural parts that are directly exposed to ground motions (e.g., bridge columns), so as to reduce the inertia forces transferred into the remaining parts of the structure (e.g., bridge superstructure), see Figure 2.1. Accordingly, the seismic deformations are concentrated in the isolators, which usually simultaneously provide supplemental energy dissipation.

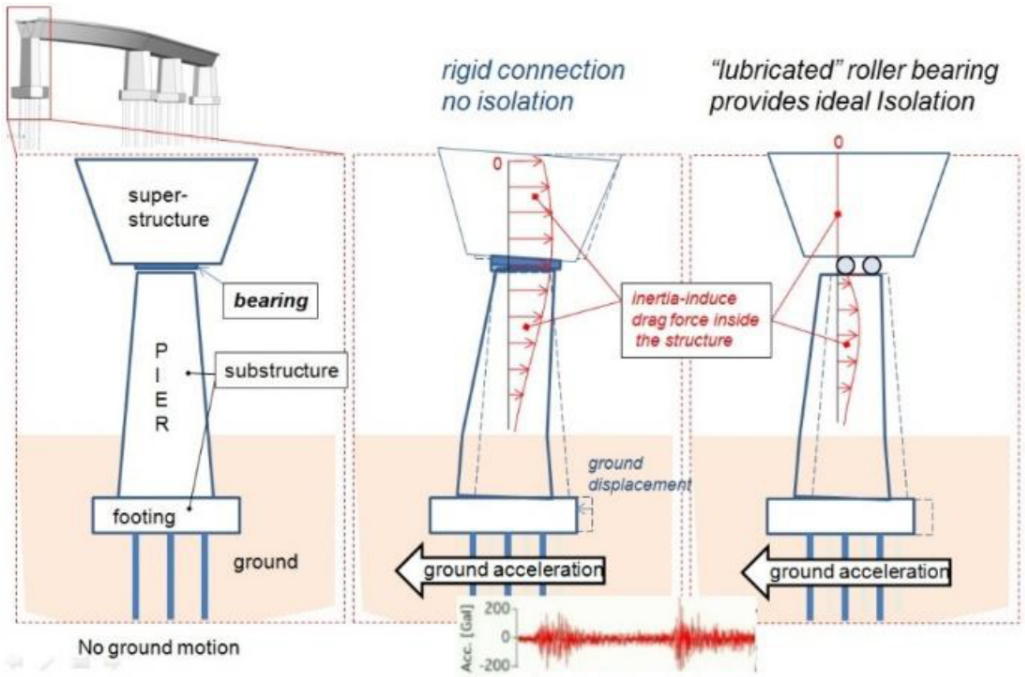

Figure 2.1 The concept of seismic isolation (Hao, 2018).

Currently, there are two major classes of isolation bearings in practical applications: elastomeric (rubber) bearings and friction sliding bearings. Rubber bearing isolation systems are well researched and prolific worldwide. Among rubber bearings, there are linear elastic bearings (often used with external energy dissipation devices), lead core rubber bearings (Figure 2.2), crystallizing rubber bearings and high damping rubber bearings. To maintain stability under large lateral displacements, bearing diameters become large. Increase in bearing diameter results in stiffer bearings, making isolation of light structures difficult. In addition, its capacity to resist strong earthquakes is hampered by the limited lateral resistance because it relies on the elastic modulus of the rubber and the friction between rubber layers and steel plates, which is also dependent on the axial loads.

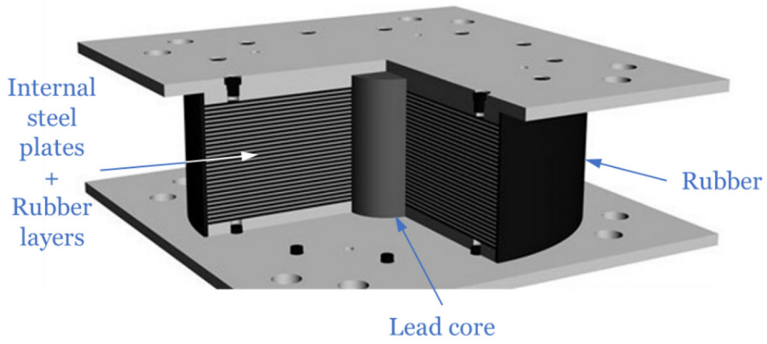

Figure 2.2 Lead core rubber bearing (source: Google Images).

On the contrary, the behavior of frictional sliding bearings is nominally independent of axial loads. There are two commonly used types of sliding bearings: flat sliding bearings, which are used in combination with elastomeric systems, and friction pendulum bearings. The single friction pendulum (SFP) bearing, shown in Figure 2.3(a), was first proposed by Zayas et al. (1987). The bearing consists of a frictional slider supported on a spherical concave surface. The term pendulum refers to the motion of the slider on the bearing under excitation. This bearing has a bilinear backbone curve that results from the linear stiffness associated with the pendulum motion and the constant frictional force. The hysteretic characteristics of the SFP bearing are similar to a lead plug rubber (LPR) bearing, or linear rubber bearing in combination with an external hysteretic devise, but the initial stiffness of the friction pendulum is often larger and the transition between initial and second stiffness is typically more sudden in the SFP bearing. To obtain enough lateral resistance, sufficient depth for the concave surface is necessary, which results in a large diameter bearing seat to assure the smoothness of the sliding motion and, subsequently, larger column diameters and extra cantilever abutments. This significantly increases the construction cost for a bridge. On the other hand, resonate vibration of superstructure on SFP bearings may occur under external excitation. To avoid this, the contact surface has to have high friction coefficient to dissipate vibration energy, sufficient strength to carry the weight of the superstructure, and to be sustainable with regard to the heat caused by friction.

In an effort to create a more adaptable bearing with smoother transitions, Earthquake Protection Systems (EPS) developed the triple friction pendulum (TFP) bearing, shown in Figure 2.3(b). The bearing has four stacked spherical sliding surfaces with two identical pairs, creating three distinct pendulum mechanisms. As motion occurs on all four sliding surfaces, the TFP bearing allows for the same displacement capacity with a bearing that is less than half as large in diameter as the SFP bearing. Additionally, as stated above, the sudden changes between sliding and non-sliding stages in the SFP bearing may trigger transient dynamic responses at the frequency of the supported structures. By creating more measured transitions in stiffness, the TFP bearing reduces these undesirable transient responses.

(a) (b)

Figure 2.3 **(a) Single friction pendulum bearing; and (b) triple friction pendulum bearing (source: Google Images).**

2.2 SELF-CENTERING HYBRID SYSTEMS

Structural systems that are able to rock and come back to their original configuration under lateral forces while dissipating energy through specific devices are referred to as the self-centering hybrid systems. Figure 2.4 compares the typical hysteretic response of these systems to conventional ductile systems and purely rocking systems. A conventional ductile system (Figure 2.4(a)) offers large energy dissipation, represented by “large” hysteretic loops, at the expense of structural integrity and significant residual displacement. A purely rocking system (Figure 2.4(b)) is

characterized by nonlinear elastic behavior with self-centering capability. However, the insufficient energy dissipation will result in excessive peak displacement demand (Makris and Roussos, 1998). A self-centering hybrid system (Figure 2.4(c)) provides a trade-off between the above two extremes. By proper tuning of the self-centering forces and the energy dissipation, it can produce a "flag-shaped" hysteretic response, with very small residual displacement but peak displacement capacity comparable to that of a conventional ductile system. Because of its excellent, low damage seismic performance and suitability for fast and high-quality construction using prefabricated components, this system has seen significant research in the past few decades.

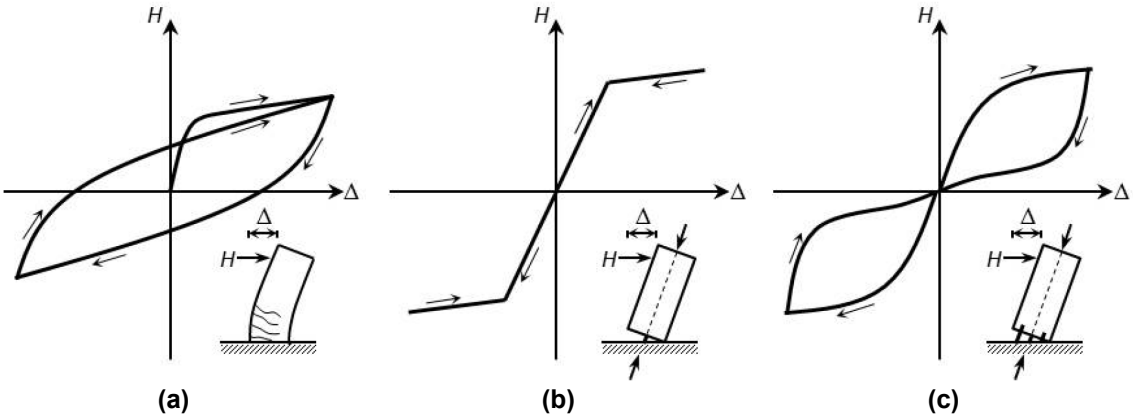

Figure 2.4 **Hysteretic response of (a) conventional ductile system; (b) pure rocking system; and (c) hybrid rocking system (Guerrini et al., 2015).**

The earliest reported implementation of re-centering systems was in an industrial chimney built in 1977 at the Christchurch, New Zealand airport (Sharpe and Skinner, 1983), Figure 2.5(a). The chimney employed a passive rocking mechanism coupled with hysteretic dampers to meet architectural and engineering requirements. A similar system was implemented in the "stepping" railway bridge over the South Rangitikei River, New Zealand, where rocking is combined with torsional hysteric energy dissipation devices (Cormack, 1988), Figure 2.5(b).

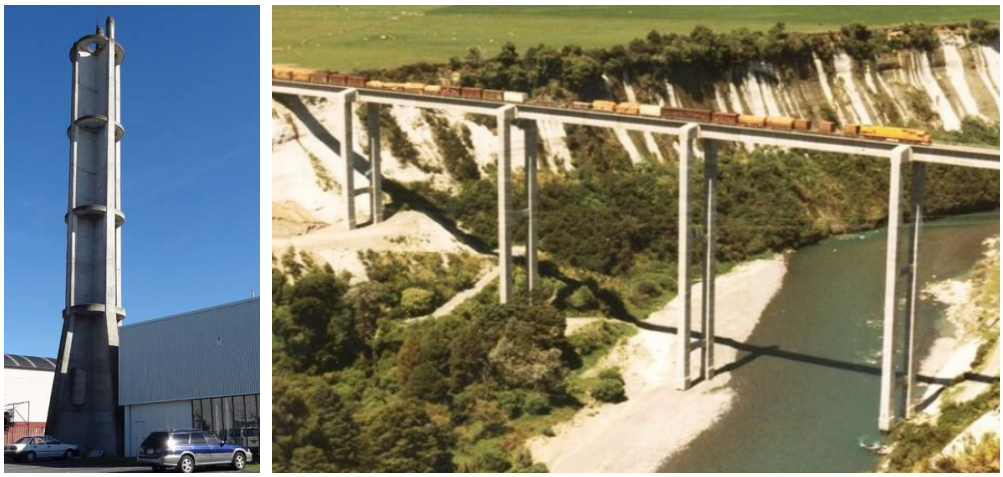

Figure 2.5 **(a) Industrial chimney at New Zealand Christchurch Airport; (b) South Rangitikei railway bridge (source: Google Images).**

Apart from the South Rangitikei River Bridge, the early development of self-centering hybrid systems focused mainly on applications in buildings. The analytical work of Priestley and Tao (1993) started with the aim of preserving prestressing forces under large ductilities, and studied the behavior of partially unbonded prestressing tendons in precast moment frame connections. Subsequently, MacRae and Priestley (1994) conducted experimental work on the beam-column subassemblies featuring unbonded post-tensioning details. The system was later on improved by incorporating mild steel reinforcement across the joints to provide hysteretic energy dissipation (Stone et al., 1995). The promising results from these studies led to the PREcast Seismic Structural System (PRESSS) program, in which a series of precast self-centering systems were investigated (El-Sheikh et al., 1999; Kurama et al., 1999). This program culminated with the simulated seismic test of a 60% scale, five-story structure (Nakaki et al., 1999; Priestley et al., 1999) incorporating a hybrid coupled wall designed to provide lateral resistance in one direction, and moment frames with/without unbonded tendons in the other direction.

The concept of hybrid re-centering systems has been extended to many other structural systems for buildings. Christopoulos et al. (2002) extended the concept of unbonded post-tensioning combined with energy dissipation to steel moment frames, Figure 2.6. Pérez et al. (2003) conducted experiments on vertically stacked wall segments prestressed with unbonded tendons, Figure 2.7. Holden et al. (2003) tested a precast hybrid wall incorporating mild steel energy dissipators, carbon fiber tendons, and steel fiber-reinforced concrete. In addition, various energy dissipation solutions like milled bars in grouted ducts (Restrepo and Rahman, 2007), viscous and mild steel external dissipators (Marriott et al., 2009), flexural external dissipators (Toranzo et al., 2009) and steel plate fuses (Eatherton and Hajjar, 2014), have been explored.

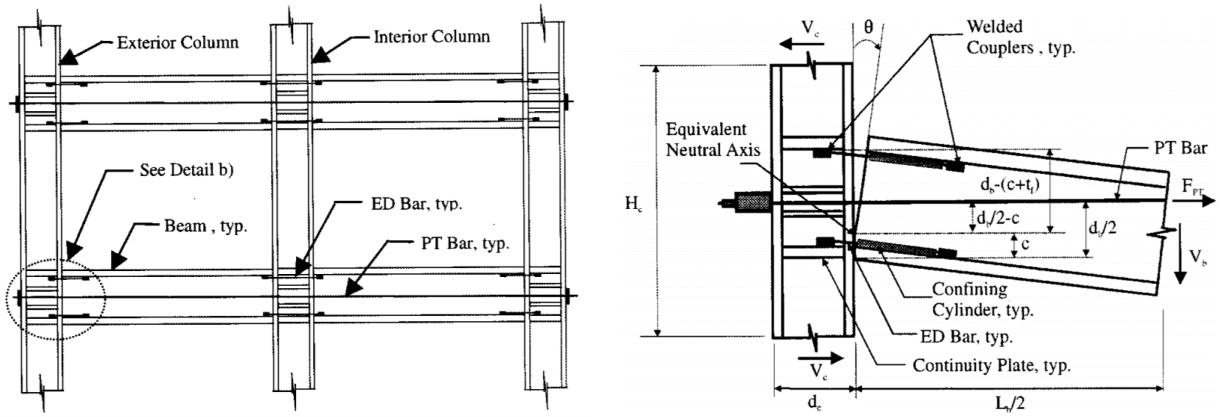

Figure 2.6 **(a) Steel frame with post-tensioning energy dissipating connections; (b) geometric configuration and free body diagram of exterior post-tensioning energy dissipating connection (Christopoulos et al., 2002).**

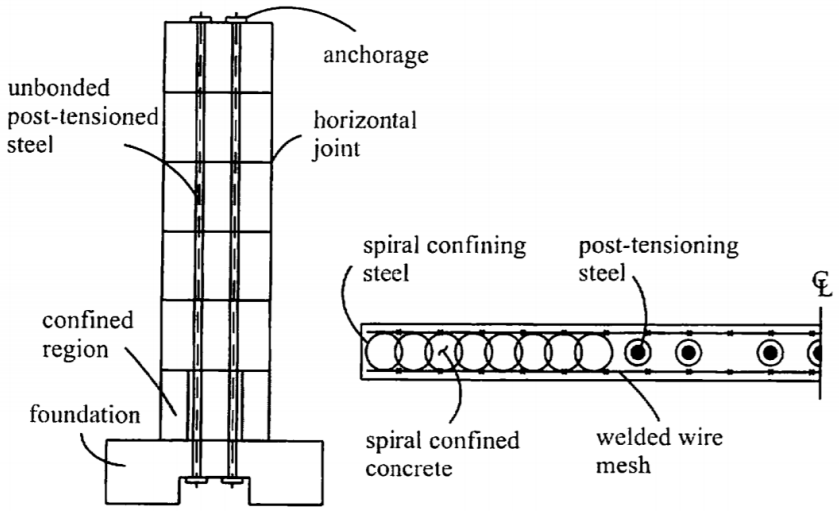

Figure 2.7 Unbonded post-tensioned wall with six precast segments (Pérez et al., 2003).

Interests in the application of self-centering hybrid systems to bridges has also been increasing over the past twenty years. A pioneering study on the application of rocking systems to bridges was carried out by Mander and Cheng (1997), including both theoretical development and experimental validation of hybrid bridge columns. This project was followed by a research program conducted by Hewes and Priestley (2002), who studied experimentally and analytically the performance of segmented rocking bridge columns with unbonded prestressing steel under different levels of initial prestress and varying thickness of steel jackets confining the plastic end regions of the columns. A number of analytical studies were subsequently carried out that considered potential applications of self-centering solutions to bridge columns (Kwan and Billington, 2003a, 2003b; Sakai and Mahin, 2004; Palermo et al., 2005; Heiber et al., 2005; Ou et al., 2006; Palermo and Pampanin, 2008). Marriott et al. (2009, 2011) developed analytical models utilizing multiple springs to model the rocking interface and conducted uni- and bi-directional quasi-static cyclic tests on monolithic and hybrid columns, exploring different energy dissipation solutions. Guerrini et al. (2015) tested dual shell hybrid bridge columns under cyclic loading and shaking table excitation. Their work explored options for external and internal energy dissipation and for improving deformability of the post-tensioning bar by the addition of polyurethane pads.

An extensive shaking table test program has been conducted by many researchers in the PEER Center under the support of the Transportation Systems Research Program (TSRP). Figure 2.8 shows different reinforcing details of the considered resilient specimen designs. The precast/pretensioned column was developed at the University of Washington with a precast plastic hinge shell made of Hybrid Fiber Reinforced Concrete (HyFRC) and a socket connection in the footing (Haraldsson et al., 2013). The dual steel shell column was designed by Guerrini and Restrepo (2013) at the University of California, San Diego. Previous examples of this system demonstrated its seismic resistance with alternative energy dissipating mechanisms (Guerrini et al., 2012). The HyFRC rocking column was developed by Trono et al. (2013) at the University of California, Berkeley. This design combined prior development and testing of the HyFRC material and its application in a rocking column (Kumar et al., 2011) with re-centering capabilities. The Carbon Fiber Reinforced Polymer (CFRP) column was designed by Mosalam et al. (2013) at the

University of California, Berkeley. It did not contain re-centering capabilities but was an example of CFRP to enhance concrete confinement in conventional design to reduce post-earthquake repair costs by eliminating or delaying concrete spalling in the plastic hinge region. All these columns were tested along with a conventionally designed reinforced concrete column at a 1/3-scale under tri-axial base excitation. The test results demonstrated that innovative column designs can resist seismic loading with re-centering capabilities at and beyond repeated design level demands. Furthermore, the tests showed that these designs eliminate or reduce concrete repair needs compared with those of a conventional design. Both of these features attest to the advanced seismic performance achieved though incorporation of damage resistant materials and improved designs.

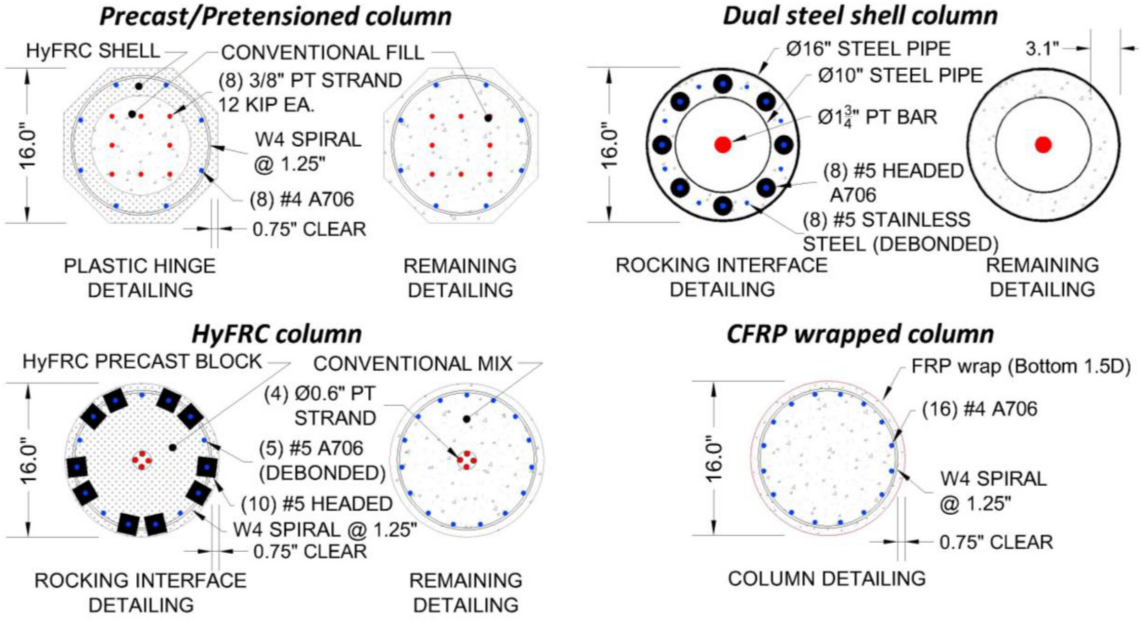

Figure 2.8 **Reinforcement details of the damage resistant, re-centering columns (Schoettler et al., 2013).**

2.3 HYBRID SIMULATION FUNDAMENTALS

Currently, there are several well-established methods to conduct laboratory testing for evaluating the seismic behavior of structural systems or structural components. The first and the most common technique is the quasi-static testing method, where the investigated structure is subjected to a pre-defined history of loading (forces or displacements) applied by actuators. By imposing the same loading history on a series of specimens, the effect of systematic changes in material properties, details, boundary conditions, loading rates, and other factors can be readily identified. While such tests are relatively easy and economical to execute, the applied loading patterns are generally inadequate for resembling the constantly changing loads that a structure undergoes during an actual seismic event, raising questions about whether the specimens were under- or over-tested for specific situations.

The second form of laboratory tests is by making use of shaking tables, Figure 2.9. Such tables are able to simulate conditions that closely resemble those that would exist during a particular earthquake. They provide important data on the dynamic response caused by specific

ground motions, considering the inertial and energy-dissipation characteristics of the tested structure and the consequences of geometric nonlinearities, localized yielding and damage, and component failure on the structural response. However, for a shaking table test, a complete structural system is generally required. The limited capacity and size of most available shaking tables place significant restrictions on the size, weight, and strength of a specimen that can be tested. As a result, reduced-scale or highly simplified specimens are commonly considered, and the specimens need to be carefully constructed following the laws of similitude (Harris and Sabnis, 1999) (see Figure 2.10). These factors call into question the realism of many shaking table tests. On the other hand, controlling real-time dynamic component tests, which require additional actuators besides the shaking tables, is particularly challenging and is still an open topic for research.

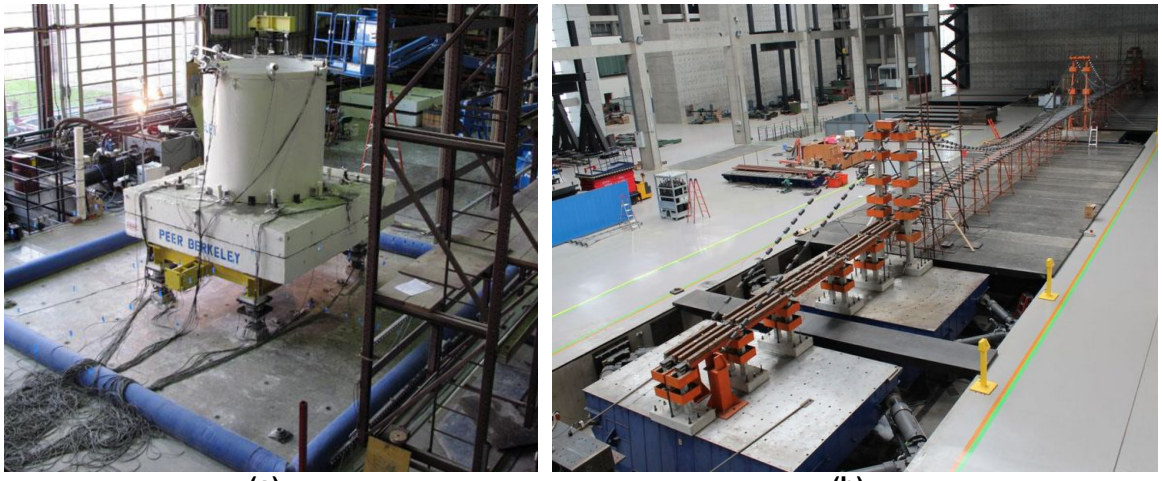

(a) (b)

Figure 2.9 **(a) PEER single shaking table with six-degree-of-freedom; (b) four shaking table system from Tongji University, China (source: Google Images).**

Figure 2.10 Reduced-scale buildings for shaking table tests in Tongji University, China (source: Google Images).

The third method is the HS test method, formerly known as the pseudo-dynamic test method or the online computer-controlled test method. It is an efficient and effective methodology which combines all the advantages of experimental testing and analytical simulations. A structure is divided into several substructures, which are either modeled analytically in the computer or experimentally tested (Figure 2.11), with the experimental and analytical substructures interacting during the simulation by enforcing the displacement compatibility and force equilibrium at shared nodes to advance the step-by-step numerical integration that is used to solve the governing differential equations of motion. The essence of HS is to use an online numerical portion of the structural system to update the input signal at each time step based on the force feedback from the physical portion. During the simulation, the physical portion of the overall hybrid model is tested in the laboratory using computer-controlled actuators, while the numerical portion is simultaneously analyzed on one or more computers. As such, HS can be viewed as an advanced form of actuator-based testing, where the loading histories for the physical components of the model are determined during the process of an experiment. Alternatively, HS can also be considered as a conventional finite element analysis, where physical models of some portions of the structure are embedded in the numerical model. Combining the realistic representation of dynamic excitation in shaking table tests, which are expensive and/or restrictive for full-scale testing, with the ability to test large-scale structures in the simpler quasi-static testing, which provide limited representation of the dynamic excitation, HS came forward in recent years as a cost-effective alternative for structural and mechanical testing.

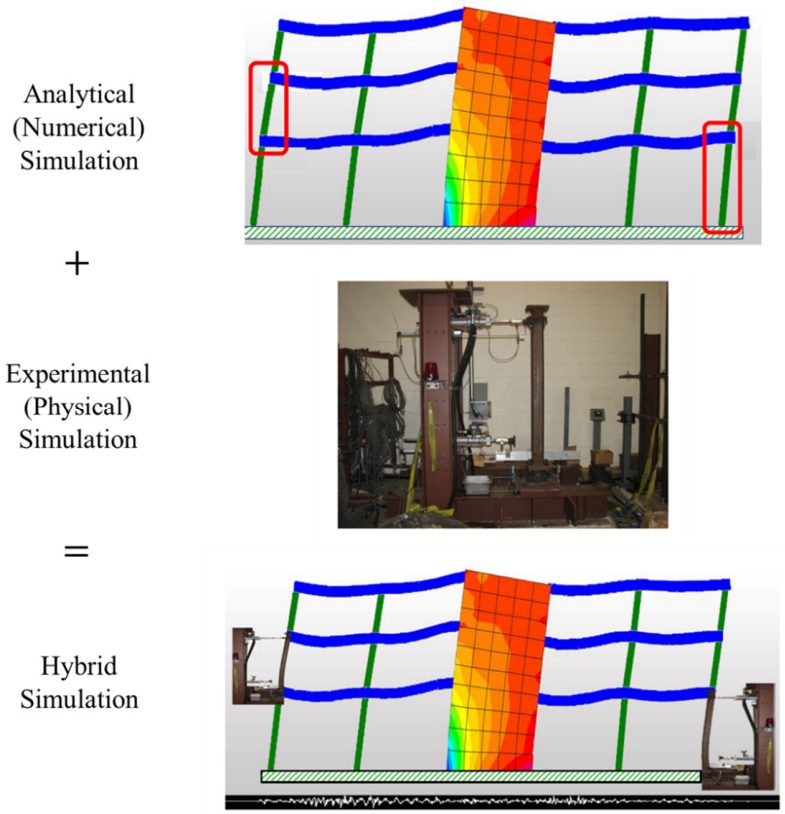

Figure 2.11 **Numerical and physical components of a structural system in hybrid simulation (Mosalam and Günay, 2013).**

2.3.1 Advantages

Because the HS testing technique combines analytical with experimental approaches to investigate a structural system and can be executed on expanded time scales of up to two orders of magnitude slower than the actual time scale, many advantages are gained. Some of the most important advantages are summarized below:

- In HS, the loading (the right-hand side of the equations of motion) is defined analytically, which provides the means to investigate the behavior of a structure excited by a wide range of loading conditions. These loading conditions can be simulated by incorporating them into the analytical portion of the hybrid model without changing the physical portion of the experiment.
- The HS method gives the researcher the ability to subdivide a large structure into subassemblies where the behavior is (1) well understood and can be modeled reliably using finite element models; and (2) highly nonlinear and/or numerically difficult to simulate and is thus obtained from a physical test in a laboratory. This reduces modeling uncertainties by replacing numerical models with actual physical components.

- Dynamic testing of full-scale specimens is made possible if the HS method is implemented for structural systems using a commonly available quasi-static, displacement-based test facility where the HS is executed on an extended time scale. The sizes and weights of the physical subassemblies are only limited by the available laboratory resources, such as the testing space, the strength of the strong floor/reaction systems (walls or frames), and the capacities of the transfer systems (e.g., actuators). Large-scale testing additionally eliminates the scaling difficulties encountered in shaking table tests.
- Because HS can be executed on extended time scales, quasi-static testing equipment including the actuators, the servo-valves, and the hydraulic power supply are generally sufficient. Oftentimes such equipment is readily available at existing testing facilities. This and the possibility of physically testing only the critical components of a structural system make HS a very economically convenient technique for performing laboratory tests (see Figure 2.12).
- Experimental and analytical subassemblies can be geographically distributed allowing researchers to take advantage of the different capabilities available in different laboratories.

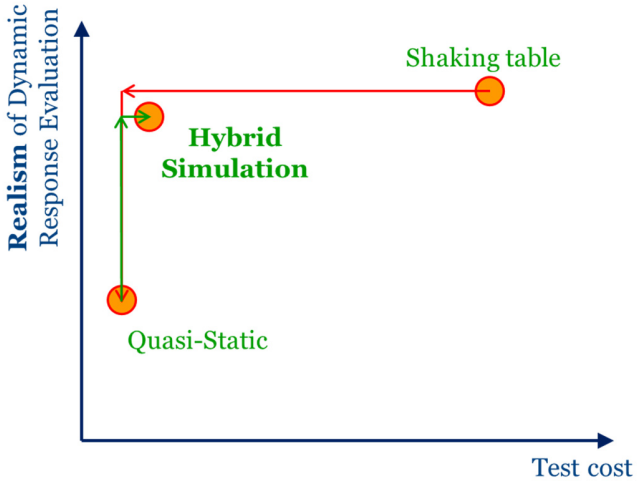

Figure 2.12 Economic convenience of hybrid simulation.

2.3.2 Components and Procedures

To perform a HS, four key components, including software and hardware, are necessary. These interacting components are shown in Figure 2.13, and are described next.

The first component is a discrete model of the structure to be analyzed on a computer, including the static and the dynamic loadings. The finite element method (FEM) is used to discretize the problem spatially and a time-stepping integration algorithm is then used for the time discretization. The resulting equations of motion for the finite number of discrete degrees of

freedom (DOFs) are a system of second-order ordinary differential equations in time, as shown in Equation (2.1).

$$\begin{aligned} \mathbf{M}\ddot{\boldsymbol{U}}_{i+1} + \mathbf{C}\dot{\boldsymbol{U}}_{i+1} + \boldsymbol{P}_r(\boldsymbol{U}_{i+1}) &= \boldsymbol{P}_{i+1} - \boldsymbol{P}_{0,i+1} \\ \boldsymbol{U}_{i=0} &= \boldsymbol{U}_0 \\ \dot{\boldsymbol{U}}_{i=0} &= \dot{\boldsymbol{U}}_0 \end{aligned} \tag{2.1}$$

In the above equations, $\mathbf{M}$ is the mass matrix assembled from the nodal and element mass matrices, $\ddot{\boldsymbol{U}}$ is the acceleration vector at the structural DOFs, $\mathbf{C}$ is the damping matrix, $\dot{\boldsymbol{U}}$ is the velocity vector at the structural DOFs, $\boldsymbol{P}_r$ is the assembled element resisting force vector (which depend on the displacements), $\boldsymbol{P}$ is the externally applied nodal load vector, $\boldsymbol{P}_0$ is the assembled "equivalent" element load vector, and subscript i indicated the i-th time step.

The second required component is a transfer system consisting of controllers and actuators, so that the incremental displacements determined by the time-stepping integration algorithm can be applied to the physical portions of the structure. Quasi-static testing equipment is typically used for this purpose.

The third major component is the physical specimen test setup. This includes the specimen being tested in the laboratory and the support system (e.g., reaction wall or frame) against which the actuators of the transfer system can react.

The fourth component is a data acquisition (DAQ) system including displacement transducers and load cells. This DAQ system is responsible for measuring the response of the test specimen and returning the resisting forces to the time-stepping integration algorithm to advance the solution to the next analysis step.

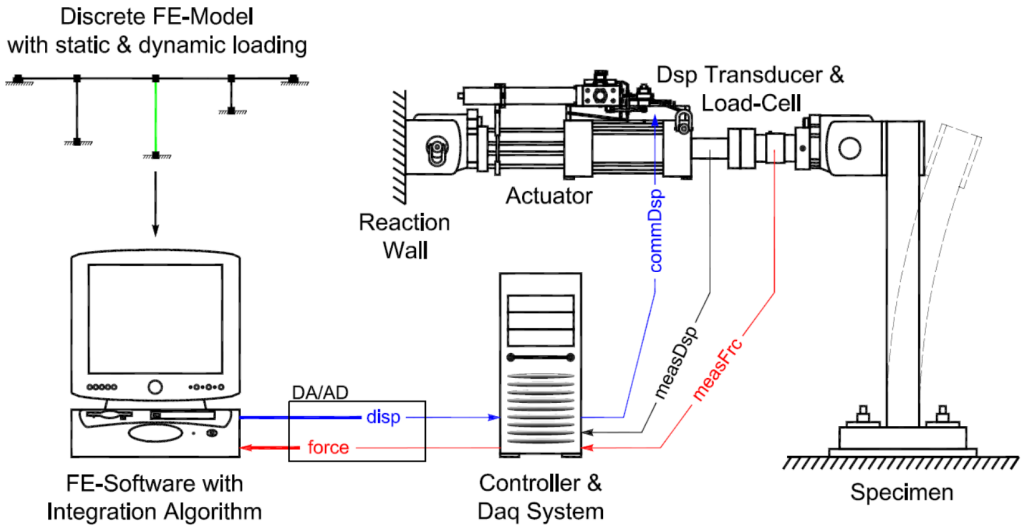

Figure 2.13 Key components of a hybrid simulation system (Schellenberg et al., 2009).

The HS conducted in this study made use of two different hybrid simulation systems. One system is based on the existing platform including the Open System for Earthquake Engineering Simulation (OpenSEES) (McKenna et al., 2000) and the Open-source FRamework for Experimental Setup and COntrol (OpenFRESCO) (Schellenberg et al., 2008). The other system is

a newly developed HSS based on the computation platform Matlab/Simulink (MathWorks, 2015) and the interface platform dSPACE (2017). Details of these two systems, including the components, the communications and the execution procedures can be found in Chapter 5 and 7 of this dissertation.

2.3.3 Integration Methods

The equations of motion that arise in structural dynamics problems are generally solved through the application of numerical time-stepping integration algorithms. Over the years, a vast number of methods have been developed to numerically solve problems in structural dynamics and other engineering disciplines.

2.3.3.1 Explicit vs. Implicit

For an explicit algorithm, the new solution at time $t_{i+1} = t_i + \Delta t$ (assuming a constant time step Δt throughout the time history) can be entirely expressed by known terms such as the current solution state at time t_i and the $k - 1$ previous solution states.

$$\boldsymbol{U}_{i+1} = f\left(\boldsymbol{U}_i, \dot{\boldsymbol{U}}_i, \ddot{\boldsymbol{U}}_i, \ldots, \boldsymbol{U}_{i-k+1}, \dot{\boldsymbol{U}}_{i-k+1}, \ddot{\boldsymbol{U}}_{i-k+1}\right) \tag{2.2}$$

Explicit integration methods are usually conditionally stable, meaning that the time step size has to be smaller than a critical value to yield a stable solution. This critical value is called the stability limit, which is an important property of an algorithm and depends on the integration method. For explicit methods, the new solution at the end of a time step can often be determined in a single calculation step without the knowledge of the tangent stiffness matrix. The advantages of such methods are that they are computationally very efficient, easy to implement, and fast in their execution. However, for structures with very high natural frequencies (stiff or infinitely stiff problems), the integration time step would have to be so small to satisfy the stability condition that the application of explicit methods to HS becomes impractical.

For an implicit algorithm, the new solution at time $t_{i+1} = t_i + \Delta t$ not only depends on the known terms at the current and previous time steps, but also on itself. Because of this, implicit algorithms contain algebraic formulas that need to be solved in order to determine the new solution at the end of a time step.

$$\boldsymbol{U}_{i+1} = f\left(\boldsymbol{U}_{i+1}, \dot{\boldsymbol{U}}_{i+1}, \ddot{\boldsymbol{U}}_{i+1}, \boldsymbol{U}_i, \dot{\boldsymbol{U}}_i, \ddot{\boldsymbol{U}}_i, \ldots, \boldsymbol{U}_{i-k+1}, \dot{\boldsymbol{U}}_{i-k+1}, \ddot{\boldsymbol{U}}_{i-k+1}\right) \tag{2.3}$$

Implicit integration methods are generally unconditionally stable, making them ideal candidates for stiff and infinitely stiff problems. It also means that only the accuracy of the algorithm needs to be considered when determining the time step size. However, they are computationally more demanding because they require iterative solution schemes, and they can introduce spurious loading cycles on the physical parts of the hybrid model.

2.3.3.2 Iterative vs. Noniterative

Another important aspect of the integration method is how many function calls they need to make per time step to determine the new solution at t_{i+1}. For the classic direct integration methods in

structural dynamics, a function call is considered to be the determination of the effective forces $\boldsymbol{P}_{eff}$ for given displacements, velocities and accelerations.

The classic explicit integration methods, which directly solve the second-order differential equations, are noniterative methods because they require only one function call per analysis time step. Implicit algorithms, on the other hand, contain algebraic formulas that need to be solved in order to determine the new solution at the end of a time step. One common approach to solve the nonlinear implicit equations is to utilize the well-known Newton-Raphson algorithm to iteratively determine the solution, see Figure 2.14. The number of function calls is thus directly related to the number of iterations performed per analysis time step. The main disadvantage of implicit methods is that they can be computationally very demanding and far more difficult to implement than explicit methods. For example, each iteration step requires the solution of a system of linear algebraic equations that involves the Jacobian. The formation of the Jacobian and the solution of a large linear system of equations are typically computationally expensive.

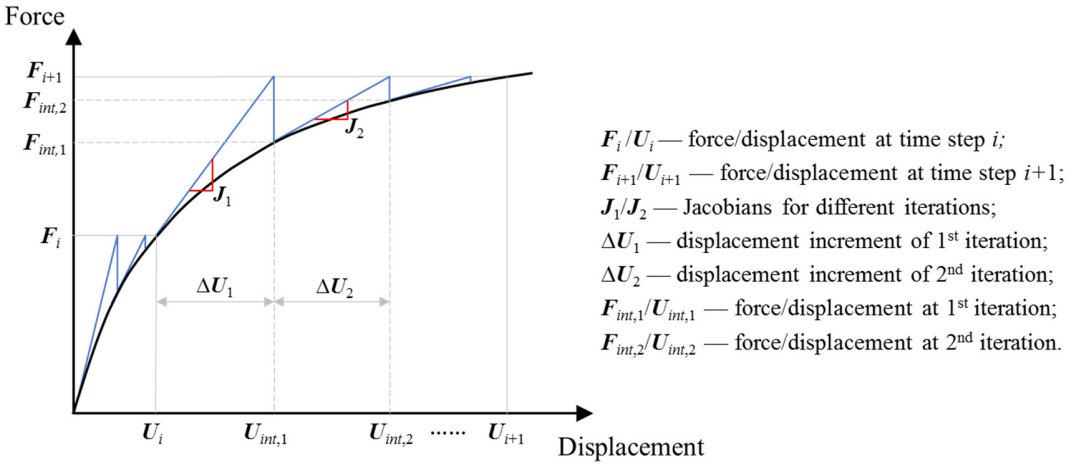

Figure 2.14 Newton-Raphson iterative algorithm.

2.3.3.3 Special Requirements

Since the hybrid model is an aggregation of numerical and experimental portions of a structure, several terms that form the equations of motion are assembled from not only analytical elements but also experimental ones. Because experimental elements represent physical specimens in a laboratory, they behave differently from numerical elements and it is not feasible to execute certain actions that can otherwise be performed on analytical elements. This fact leads to a range of special requirements that need to be provided by the integration methods in order to produce reliable and accurate results in a HS. Among all the requirements, the following two are the most important:

- **As few iterations as possible**: In HS, parts of the resisting force vector $\boldsymbol{P}_r$ is assembled from forces measured in real-time in the laboratory. This leads to the requirement that, for each integration time step, the method should make as few function calls as possible, since every function call triggers the acquisition of the resisting forces from the laboratory setup. The process of acquiring the nonlinear

resisting forces from the test structure means that the calculated displacements need to be applied to the specimen by means of a transfer system and the corresponding forces need to be measured with load cells. This process can be time consuming and introduce experimental errors into the numerical integration algorithm. The classic explicit integration methods, which require only one function call per analysis time step as mentioned previously, would be ideal in this case.

- **Avoid loading-unloading cycles to the experimental elements**: The displacement increments calculated by iterative procedures are required to be strictly increasing or strictly decreasing within an integration time step. While this requirement is not necessary for analytical elements, it is essential for experimental elements that represent physical specimens in a laboratory. Without this restriction, the displacement commands during the iteration process can overshoot the converged displacements. This unintended loading-unloading cycle does not represent the true structural behavior, but is an artifact generated by the numerical algorithm. Contrary to the numerical portions of the hybrid model, for which the response depends on only the committed displacements at convergence, the response of the physical portions is truly path dependent and consequently affected by all iterations.

For the HS conducted in this study, two explicit integration methods — Explicit Newmark method and Alpha Operator-Splitting (Alpha-OS) method — were exploited. Details of these integration algorithms can be found in Chapter 5 and 7 of this dissertation.

2.3.4 History of Development

Starting with the conception of the method in mid-1970s (Takanashi et al., 1975), there has been considerable amount of work related to both development of the methodology and applications on a large variety of problems. A brief discussion on the history of development of the HS method is included herein for completeness.

In HS, proper consideration of substructuring methods to partition the structure into its analytical and experimental substructures is essential. The presence of the experimental substructures in the numerical integration restricts the use of common integration methods utilized in pure analytical simulations. Therefore, adoption of integration methods that meet the requirements of HS introduced by the presence of experimental substructures is needed. Experimental errors are commonly introduced by the presence of a transfer system (controllers, actuators, reaction systems, and DAQ systems) to apply the computed quantities (most commonly displacements) to the experimental substructure and measure the corresponding responses (most commonly forces). These experimental errors require evaluation of their effects and development of methods to eliminate these effects. In addition to the experimental errors, there are inherent errors as part of the simulation errors due to structural modeling and numerical methods. Accordingly, considerable HS research has been conducted on substructuring (e.g., Dermitzakis and Mahin, 1985; Thewalt and Mahin, 1987; Nakashima and Masaoka, 1999; Mosqueda et al., 2010), integration methods (e.g., Shing et al., 1991; Chang, 1997; Combescure and Pegon, 1997; Bonelli and Bursi, 2004; Bonnet et al., 2008; Chen et al., 2009; Schellenberg et al., 2009) and simulation errors (e.g., Shing and Mahin, 1983; Horiuchi et al., 1999; Horiuchi and Konno, 2001;

Mosqueda, 2003; Elkhoraibi and Mosalam, 2007; Chen and Ricles, 2009, 2010; Hessabi and Mercan, 2012, Chae et al., 2013). Furthermore, research has been conducted on geographically distributed HS (e.g., Mosqueda, 2003; Stojadinovic et al., 2006; Schellenberg et al., 2009; Kwon et al., 2008; Kim et al., 2012) and real-time HS (e.g., Nakashima et al., 1992; Lee et al., 2007; Mercan and Ricles, 2007; Bursi et al., 2008; Ji et al., 2009; Günay and Mosalam, 2014, 2015; Mosalam and Günay, 2014), which are extensions of the HS method to cover a broader range of applications.

In addition to the many studies that were geared towards development of the method, HS has been efficiently and effectively used for the evaluation and design of a variety of structures including buildings (e.g., Ji et al., 2009; Hashemi and Mosqueda, 2014; Lai and Mahin, 2013), bridges (e.g., Terzic and Stojadinovic, 2013; Kim et al., 2011) and other structures (e.g., Mosalam and Günay, 2014; Günay and Mosalam, 2014; Whyte and Stojadinovic, 2013). Since new retrofit and design methods require experimental validation and considering that it is not generally possible to test a full-scale structure, HS has been recently used for different protective systems and other new design and retrofit methods (e.g., Karavasilis et al., 2011; Lin et al., 2013; Cha et al., 2013; Friedman et al., 2014; Schellenberg et al., 2017).

3 Development of Experimental Program I: V-connector

This chapter discusses the development of the experimental framework for studying the first proposed bridge subsystem — the V-connector. The test program includes investigation of the structural behavior of the V-connector itself and as part of the bridge system. The design of the test specimen, test setup and boundary conditions, considered loading protocol, specimen construction, material testing and instrumentation techniques used for the experiments are also presented.

3.1 INTRODUCTION

To increase the resilience by enhancing the bridge column behavior as a critical part of the bridge system, a subsystem called "V-connector" was designed, constructed, and tested physically and computationally in collaboration with ACII, Inc. This connection device is expected to absorb and dissipate the energy produced by the earthquake and to be recovered or repaired with minimum efforts. The components of a V-connector are depicted in Figure 3.1. It consists of (1) a V-shaped guiding tube that is embedded inside the bottom part of the connection, e.g., the column or the foundation; (2) a vertical stabilization pin and elastic rod with one end inserted into the V-shape guiding tube (V-pin); (3) a ball-shaped hinge on top of the stabilization pin that is free to rotate when there is a relative motion between the two connection parts; (4) a Teflon washer whose major function is to provide friction-induced energy dissipation when subjected to earthquakes; and (5) a top pad made of stainless steel on top of the Teflon washer. The geometry of the V-tube is specially designed to ensure the V-pin has enough room to deform and to guide the deformation of the V-pin such that the plastic strain will not concentrate at the bottom of the rod and cause failure. The reason for choosing Teflon as the material of the sliding interface is to create a sliding surface with low friction coefficient, isolating the superstructure from earthquake excitation. Another way of seeing the benefit of the sliding surface, which replaces the original connection between the column and deck with a more flexible connection, is that it leads to a reduction in the lateral stiffness and shifts the natural period of the structure to a longer period. For a typical bridge structure, such benefit means that the peak pseudo-acceleration is reduced, and that the demand on the structure is brought down. Because of these response modifications, the bridge components are not expected to experience damage, leading to an improved seismic behavior. Besides, the Teflon pad can provide enough vertical stiffness so that the bridge deck can still accommodate the daily service loads. By on-site assembly of precast structural elements, ABC can also be achieved.

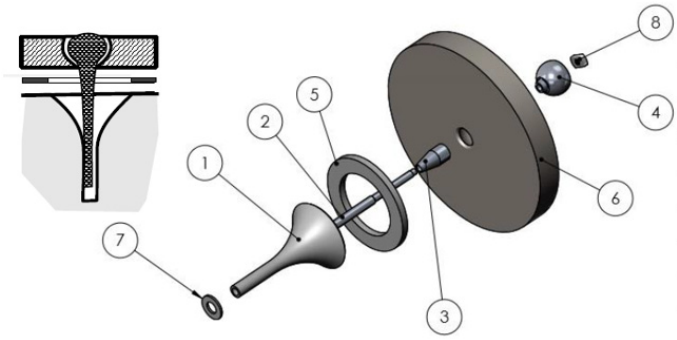

1	V-tube
2	V-pin
3	Shear Reinforcing Ring
4	Ball Hinge
5	Teflon Washer
6	Top Pad
7	Tube Reinforcing Ring
8	Pin-fix Nut

Figure 3.1 Components of a typical V-connector (Hao, 2018).

3.2 SPECIMEN DESIGN

The test specimen in the V-connector study consists of two reinforced concrete blocks and one set of V-connector sandwiched in between, all developed at 1/3-scale from a hypothetical prototypical geometry. The concrete blocks were designed as elastic rigid blocks to apply the lateral displacements to the V-connector. A brief summary of the design and cross section reinforcement of the concrete blocks is presented below.

To calculate the design loads for the concrete blocks, an OpenSEES (McKenna et al., 2000) model of a selected prototype bridge (see Chapter 4 for more details) with a V-connector between the column and the deck was developed and subjected to a set of selected ground motions. The V-connector was modeled by an idealized hysteretic behavior based on its intrinsic behavior. The axial and shear forces of the V-connector obtained from the conducted nonlinear dynamic analysis results were scaled down according to the proper similitude relationships and used to design the concrete blocks. The design included axial and shear design for each block in accordance with ACI 318 (2011) (See Appendix A for details of the specimen design loads and calculations of the required reinforcement). Reinforcement quantities of the top and bottom block are summarized in Table 3.1, and the cross sections of the blocks are shown in Figure 3.2 and Figure 3.3. Several special considerations are taken into account including: (1) In the top block, four 1.5 in. diameter electrical metallic tubing (EMT) conduits were horizontally placed for the prestressing rods; and (2) In the bottom block, four 2 in. diameter vertical EMT conduits and two 2 in. diameter horizontal EMT conduits were used for anchoring and lifting purposes, respectively. In addition, some extra localized reinforcing bars were placed inside the bottom block to strengthen the concrete around the V-tube (see Figure 3.4).

The V-connector set was designed and manufactured by ACII, Inc. according to the design parameters based on the pre-test analysis results. The criteria for choosing the design parameters was to keep the bridge column elastic under a selected set of ground motions. Chapter 4 describes the details of this design procedure.

Table 3.1 Summary of the specimen cross section's reinforcement.

Top Block	40 #7 longitudinal bars
	32 #4 transverse bars with standard hooks at both ends
	4 #4 hoops @7″ spacing
Bottom Block	48 #8 longitudinal bars
	50 #4 transverse bars with standard hooks at both ends
	5 #4 hoops @7″ spacing
	#5 bars surrounding the V-tube

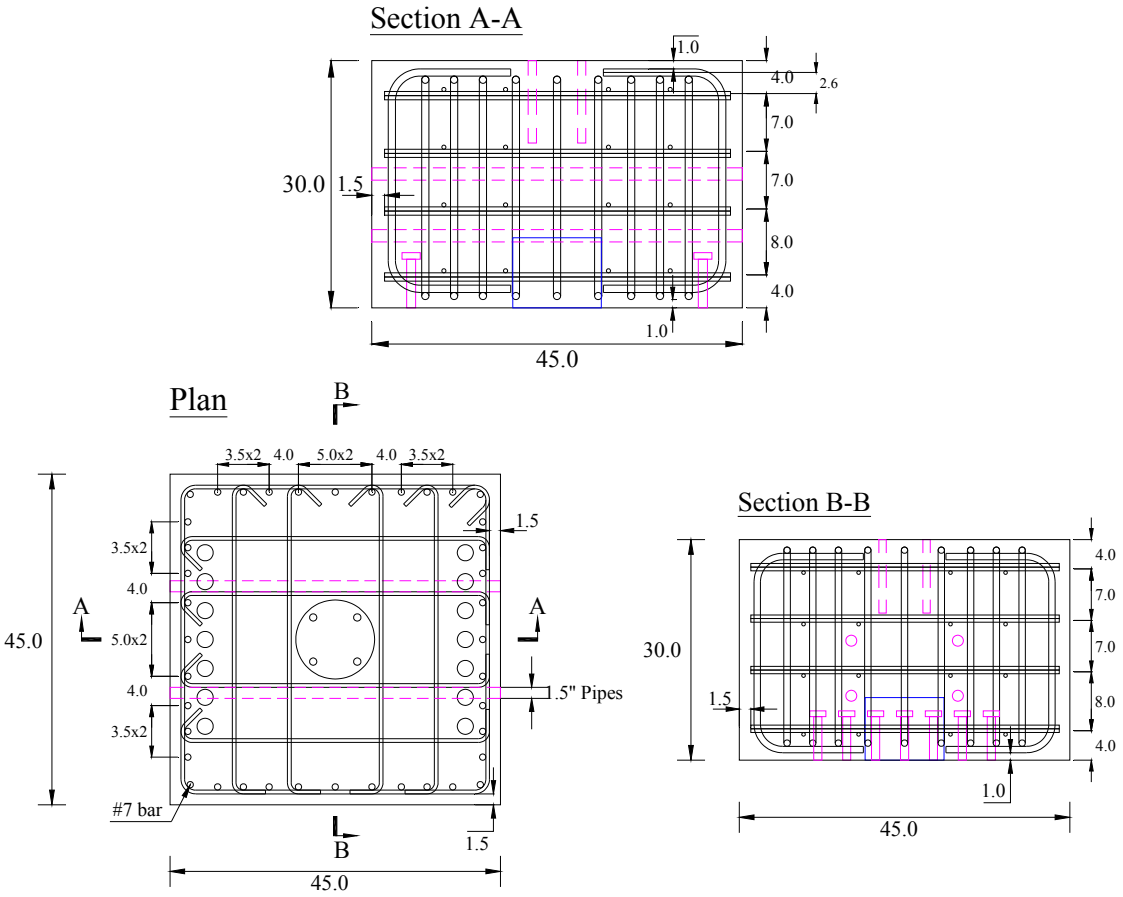

Figure 3.2 Dimensions and reinforcement details for the top block.

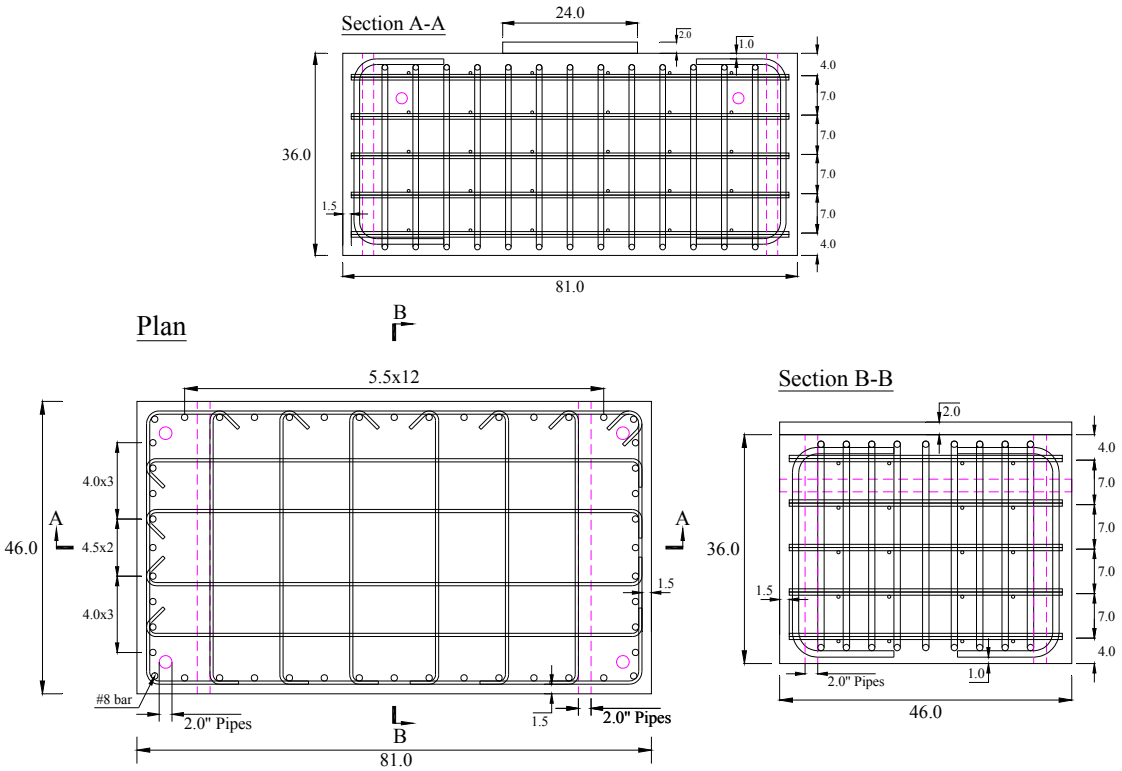

Figure 3.3 Dimensions and reinforcement details for the bottom block.

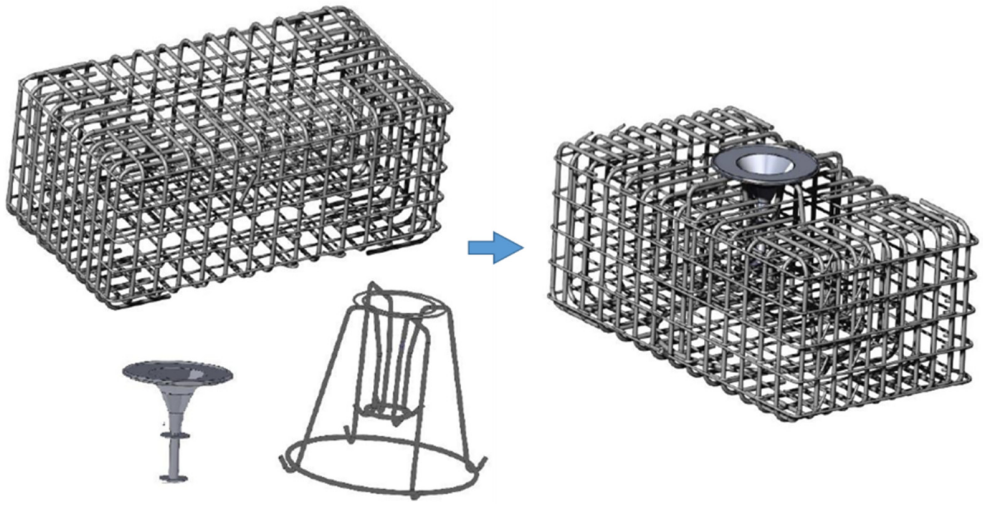

Figure 3.4 Local reinforcement around the V-tube in the bottom block.

3.3 TEST SETUP

The objective of the test was to investigate the behavior of the V-connector under combined vertical and lateral load. Therefore, vertical and lateral loading systems were required. All loads were applied at the top block, while the bottom block was directly anchored to the strong floor. A

schematic representation of the test setup, including the loading systems and boundary supports, is shown in Figure 3.5. The detailed test setup and the relative locations of the loading actuators and supports are shown in different views in Figure 3.6 and Figure 3.7.

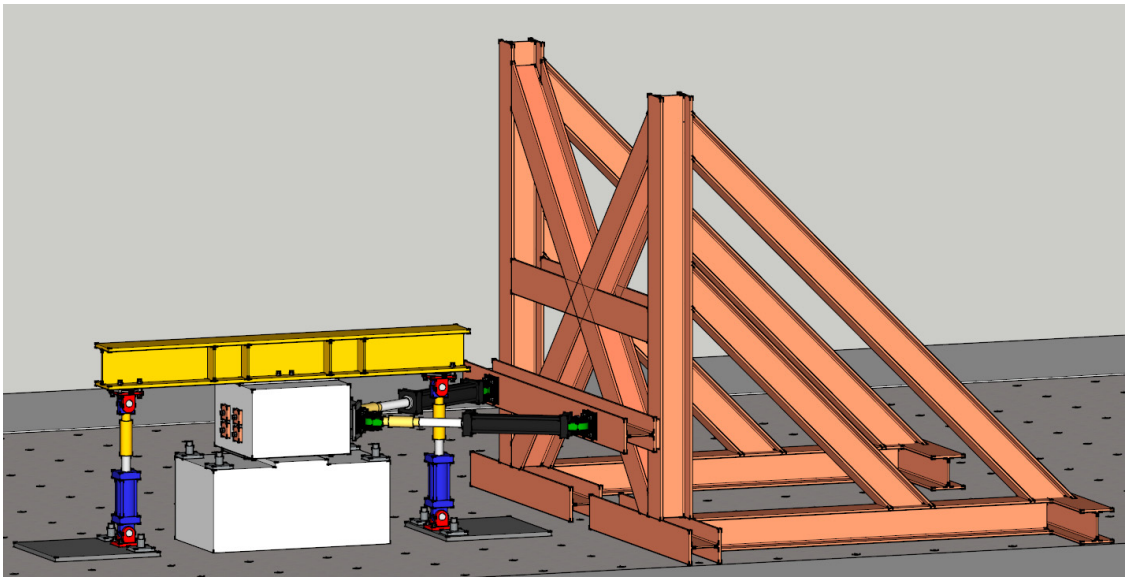

Figure 3.5 Schematic 3D view of the test setup.

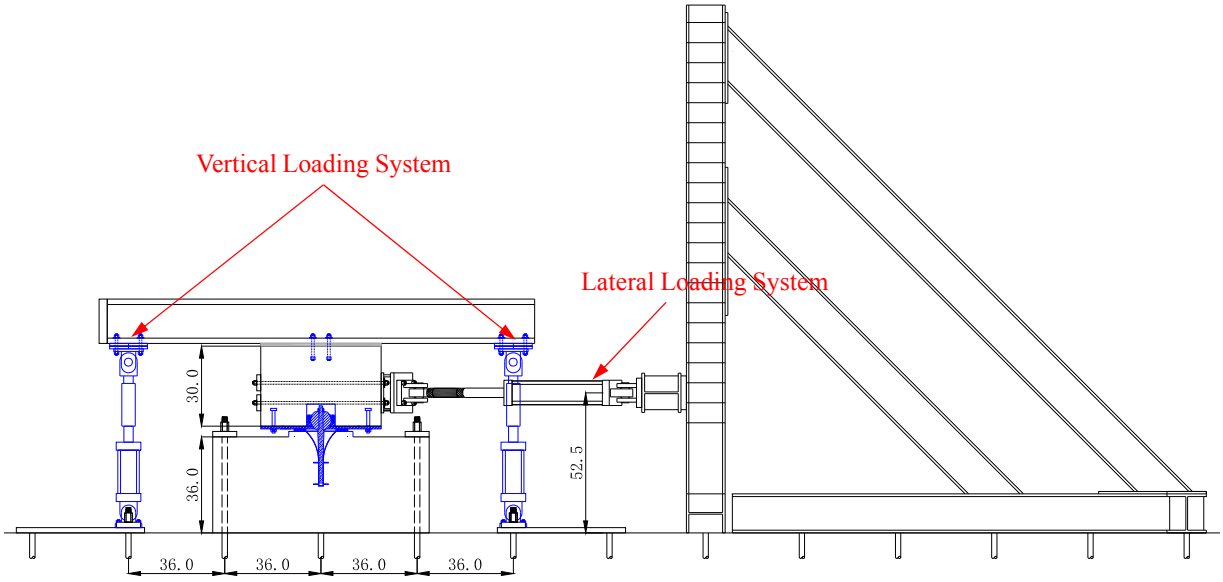

Figure 3.6 Elevation view of the test setup.

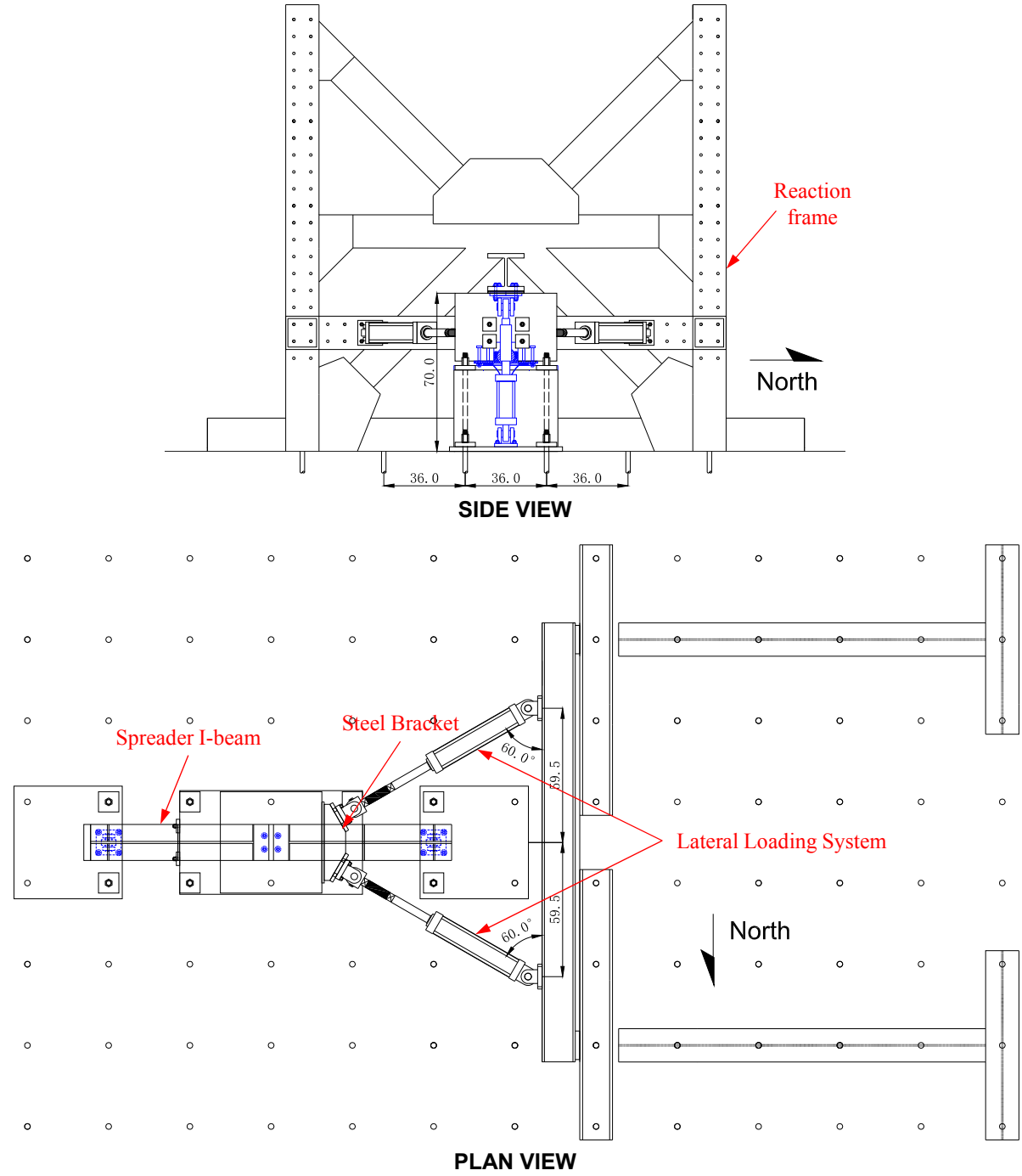

Figure 3.7 Side and plan view of the test setup.

As illustrated in the figures above, the gravity load was applied at the top block through two vertical hydraulic actuators and a steel spreader I-beam bolted to the top block using four rods. The actuators pull downwards on the spreader I-beam through pinned connections from one end and react against the laboratory strong floor, also through pinned connections, at the other end. Due to practical considerations, the span of the spreader beam had to be limited to avoid excessive

flexibility, and to achieve constant and stable vertical load. In addition, a 1 in. hydro-stone layer was applied between the spreader beam and the concrete top block to avoid any stress concentration due to concrete surface imperfections and to achieve a uniform vertical load application.

The lateral load was applied at the top block, using two lateral hydraulic actuators that reacted against the laboratory steel reaction frame, as shown schematically in Figure 3.5. The setting of the lateral actuators allowed for applying both cyclic loading during the quasi-static testing and the computed displacement input during the HS. To provide stability during the unidirectional lateral loading, the actuators were located in one horizontal plane but connected to the top block at two inclined directions. Accordingly, two special considerations were required: (1) Geometric transformation was needed to transform the desired input displacements to the local actuator axes; and (2) A connection device between the top block and the actuators had to be designed to facilitate the two inclined lateral actuators' connections. Based on the attachment points of the actuators to the reaction frame and the distance between the frame and the top block, a steel bracket was designed and fabricated to fulfill the task (see Figure 3.7). The end pin connections of the lateral actuators were achieved through 3D ball-bearing clevises. The pinned nature ensured the application of only lateral forces without any vertical loads or bending moments. The steel bracket and four small steel anchor plates were installed on the two opposite sides of the top block and connected by four prestressing rods running through. The actuators were then bolted to the steel bracket. Thus, when the actuators extended, the force was transferred to the block as bearing on the front face directly. On the other hand, when the actuators retracted, the force was transferred through the prestressing rods to the other face of the block and bearing was achieved from the back side.

As previously discussed, the specimen was directly attached to the laboratory strong floor where a hydro-stone layer was applied between the bottom block and the strong floor. Subsequently, four prestressing rods were used to prestress the specimen down to the strong floor. The hydro-stone and prestressing provided the necessary horizontal and vertical reactions and guaranteed enough friction resistance between the strong floor and the bottom face of the bottom block during lateral loading. The final assembled test setup is shown in the photograph of Figure 3.8.

Figure 3.8 Test setup for the V-connector experiments.

3.4 EXPERIMENTAL PROGRAM

3.4.1 Quasi-Static Testing

The first test on the specimen was conducted under combined constant gravity loading and a pre-defined unidirectional cyclic lateral loading. The goal was to characterize the V-connector's hysteretic behavior under a certain level of axial load. Based on the observed behavior and test results, the prototype bridge was reanalyzed with an updated V-connector modeling, and the scale factors for the ground motions used in the HS test were chosen accordingly. Detailed description of the cyclic test and its results are discussed in Chapter 4.

3.4.2 Hybrid Simulation Trial Testing

The second test on the specimen was a trial HS. The main objective was to verify the HSS that would be used in the real HS test. Two main aspects of the system were verified. The first one was the back and forth communication between the physical and computational components of the hybrid system, including the geometric transformation between global DOFs used in the computational model and local DOFs of the actuators. It was necessary to ensure that the computed input displacements passed to the actuators and the resulting forces fed back to the computational platform as measured by the actuators' load cells were scaled down or up properly according to the length scale factor of 1/3. The second aspect of verification concerned with the actuator's control quality. Both aspects were successfully verified through a test run with one of the three ground motions that were used in the real HS test, but with a reduced scale factor not to induce any damage or nonlinearity to the specimen. The test was conducted using the same constant gravity load as in the quasi-static cyclic test and the real HS test.

3.4.3 Hybrid Simulation Testing

The third and final test in the experimental program was the HS test of the same specimen. The main objective of this test was to investigate the system level performance of the prototype bridge with the usage of the V-connector under earthquake excitations. All bridge components were analytically modeled except for the V-connector, which served as the experimental substructure. A selected set of three ground motions with increasing intensity was applied one by one in a concatenated manner. Through all the HS runs, the constant gravity load, similar to that applied in the cyclic test, was used.

3.5 LOADING PROTOCOL

Two different types of lateral loading techniques were utilized in the experimental program: (1) a quasi-static cyclic loading with a prescribed load pattern; and (2) an online computed earthquake response input signal applied through HS runs (the vertical component of the ground motion was not taken into account for simplicity). While the lateral loading was applied either during a cyclic loading test or a HS run using slow-rate displacement control, a constant gravity load was also applied during all tests through force control. A lateral loading rate of 0.02 in./s was used in the cyclic test while 0.01 in./s was adopted in the HS. For the cyclic test, the lateral loading was an offline signal adopted from the FEMA 461 (2007) guidelines. The input signal for the lateral loading in the HS test, however, was an online signal computed and updated based on a multi-DOF computational model subjected to the three selected earthquake records. More details about the gravity load levels and the FEMA 461 (2007) cyclic load pattern are presented here, while the HS loading details are included in Chapter 5.

3.5.1 Gravity Load

As discussed earlier, a constant gravity load of 200 kips was applied through two vertical actuators and a spreader I-beam placed on the top block. The total gravity load was split evenly between the two actuators. The vertical gravity load was applied first through force control before any lateral loading and remained essentially constant during all tests.

The criteria for choosing the value of the gravity load was based on pre-test analysis results. Since the energy dissipation mechanism of the V-connector is provided by its intrinsic friction which mainly depends on pressure, the axial force of the bridge column under gravity loading was extracted from the analysis. This axial force, after proper scaling, served as the gravity load applied on the V-connector to achieve the desired pressure. It was decided not to vary the gravity load level during the HS test because the axial force fluctuation is negligible without vertical ground excitations.

3.5.2 Cyclic Load Pattern

The parameters of the cyclic loading patterns were the number and amplitude of the cycles in different groups. Several past studies considered cyclic loading histories and patterns for quasi-static tests only (Leon and Deierlein, 1996; Krawinkler, 1996; Clark et al., 1997). Krawinkler (2009) compared several loading histories adopted from different standards and studies for seismic

acceptance testing and performance-based design. Loading histories from ATC-24 Protocol (1992), SAC Protocol (Clark et al., 1997), SPD Protocol (Porter and Cherif, 1987), CUREE (Krawinkler et al., 2000), ISO (1998), and FEMA 461 (2007) were compared. Based on Krawinkler's comparison, these protocols are similar and are expected to produce similar performance assessments. Consequently, the FEMA 461 (2007) loading protocol was adopted in this study because it is the most current and is similar to other loading protocols.

Figure 3.9 presents a conceptual diagram of the recommended loading history in FEMA 461 (2007) section 2.9.1. The loading history consists of repeated cycles of step-wise increasing deformation amplitudes. Two cycles are applied at each amplitude.

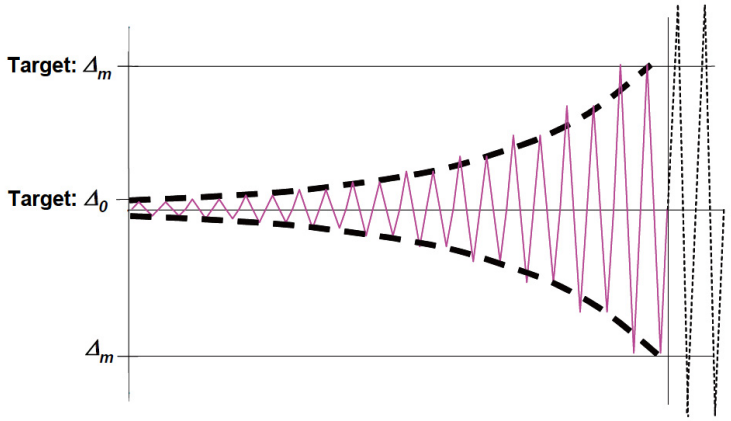

Figure 3.9 Deformation-controlled loading history used in the quasi-static test.

The loading history is defined by the following:

Δ_0 = the targeted smallest deformation amplitude of the loading history. It must be safely smaller than the amplitude at which the lowest damage state is first observed;

Δ_m = the targeted maximum deformation amplitude of the loading history. It is an estimated value of the imposed deformation at which the most severe damage level is expected to initiate;

n = the number of steps (or increments) in loading history, generally 10 or larger; and

a_i = the amplitude of the cycles, as they increase in magnitude, i.e., the first amplitude, a_1, is Δ_0 (or a value close to it), and the last planned amplitude, a_n, is Δ_m (or a value close to it).

The amplitude of step $i + 1$ (not of each cycle, since each step has two cycles) is given by the following equation:

$$a_{i+1} = 1.4a_i \tag{3.1}$$

where a_i is the amplitude of the preceding step; a_n is the amplitude of the step close to the target, Δ_m. If it is desired that the largest amplitude, a_n, be exactly equal to Δ_m, then the ratios a_i / a_n shall be as shown in the following table.

Table 3.2 Relative loading history deformation amplitudes (n = 13).

i	1	2	3	4	5	6	7	8	9	10	11	12	13
a_i /a_n	0.018	0.025	0.035	0.048	0.068	0.095	0.133	0.186	0.26	0.364	0.51	0.714	1.0

Based on the V-connector's V-tube geometry (Figure 3.10), the targeted maximum deformation amplitude Δ_m for the V-connector was 4 in. Therefore, from the information above, the proposed loading protocol is shown in Table 3.3. The first three loading stages were not executed because the deformation amplitudes were too small. An additional loading stage corresponding to $0.875\Delta_m$ was executed in order to better characterize the hysteretic behavior of the V-connector in the intermediate stage. A plot summarizing the lateral loading cycles that were applied during the full quasi-static test is shown in Figure 3.11. A photograph of the loaded specimen during the test is shown in Figure 3.12.

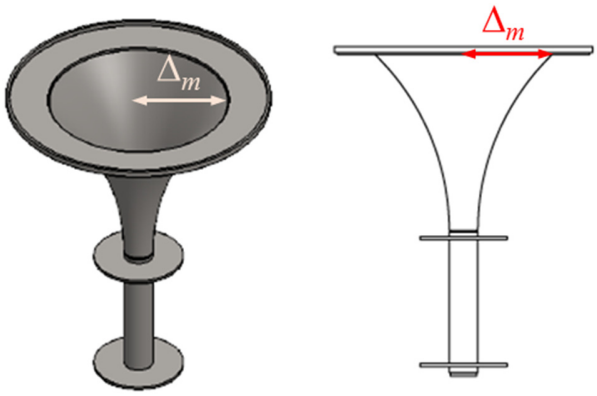

Figure 3.10 V-tube geometry of the V-connector.

Table 3.3 Proposed loading protocol for the V-connector cyclic testing.

Loading Stage	Number of Cycles	Loading Type
$0.048\Delta_m$ = 0.19 in.	2	Displacement-controlled
$0.068\Delta_m$ = 0.27 in.	2	Displacement-controlled
$0.095\Delta_m$ = 0.38 in.	2	Displacement-controlled
$0.133\Delta_m$ = 0.53 in.	2	Displacement-controlled
$0.186\Delta_m$ = 0.75 in.	2	Displacement-controlled
$0.260\Delta_m$ = 1.06 in.	2	Displacement-controlled
$0.364\Delta_m$ = 1.46 in.	2	Displacement-controlled
$0.510\Delta_m$ = 2.00 in.	2	Displacement-controlled
$0.714\Delta_m$ = 2.86 in.	2	Displacement-controlled
$0.875\Delta_m$ = 3.50 in.	2	Displacement-controlled
$1.000\Delta_m$ = 4.00 in.	2	Displacement-controlled

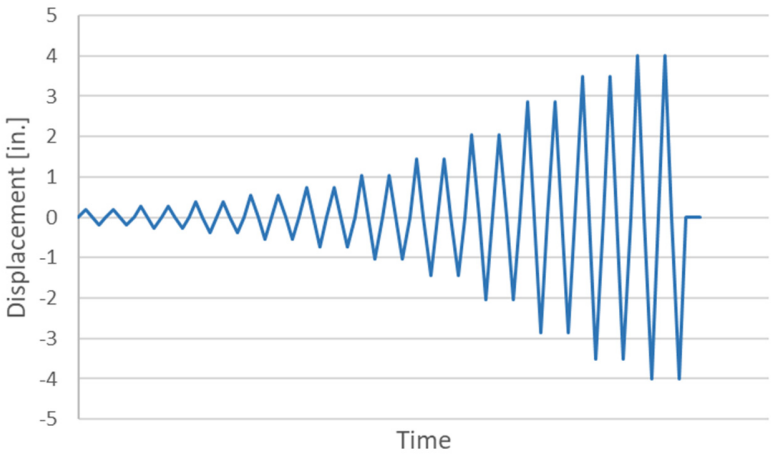

Figure 3.11 Final loading protocol used for the quasi-static cyclic loading test.

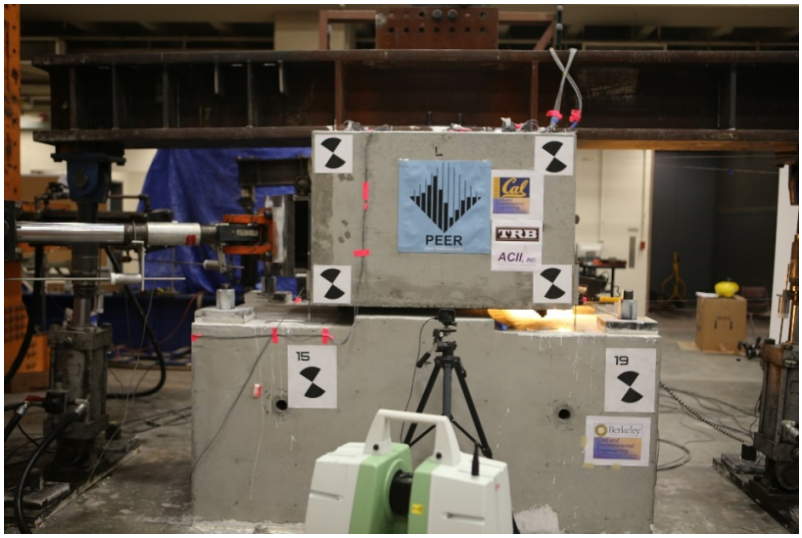

Figure 3.12 A view of test in progress under cyclic loading.

3.6 CONSTRUCTION OF TEST SPECIMEN

The whole specimen construction process was carried out using an on-site assembly of precast structural elements keeping in mind the possibility of achieving the ABC philosophy. The concrete blocks in the test specimen were constructed at the Structural Laboratory on UC Berkeley campus, with ready concrete mix being delivered to the laboratory site in one lift. The V-connector set was designed, manufactured and delivered to the laboratory by ACII, Inc. The specimen was constructed in two phases. Brief description of the different construction phases is presented below.

Phase I of the construction included laying out the formworks for the two concrete blocks, furnishing the transverse and longitudinal reinforcement, constructing the steel cages, placing all the steel cages in place, and casting the concrete. Note that the V-tube was placed inside the bottom block's steel cage with some extra strengthening reinforcement and cast together with the bottom block. Figure 3.13 and Figure 3.14 show the reinforcing bar cages, the formworks and the concurrently concrete casting of the two blocks. Curing blankets in addition to the chemical E-CURE were used for curing during the first week after concrete casting to avoid shrinkage cracks.

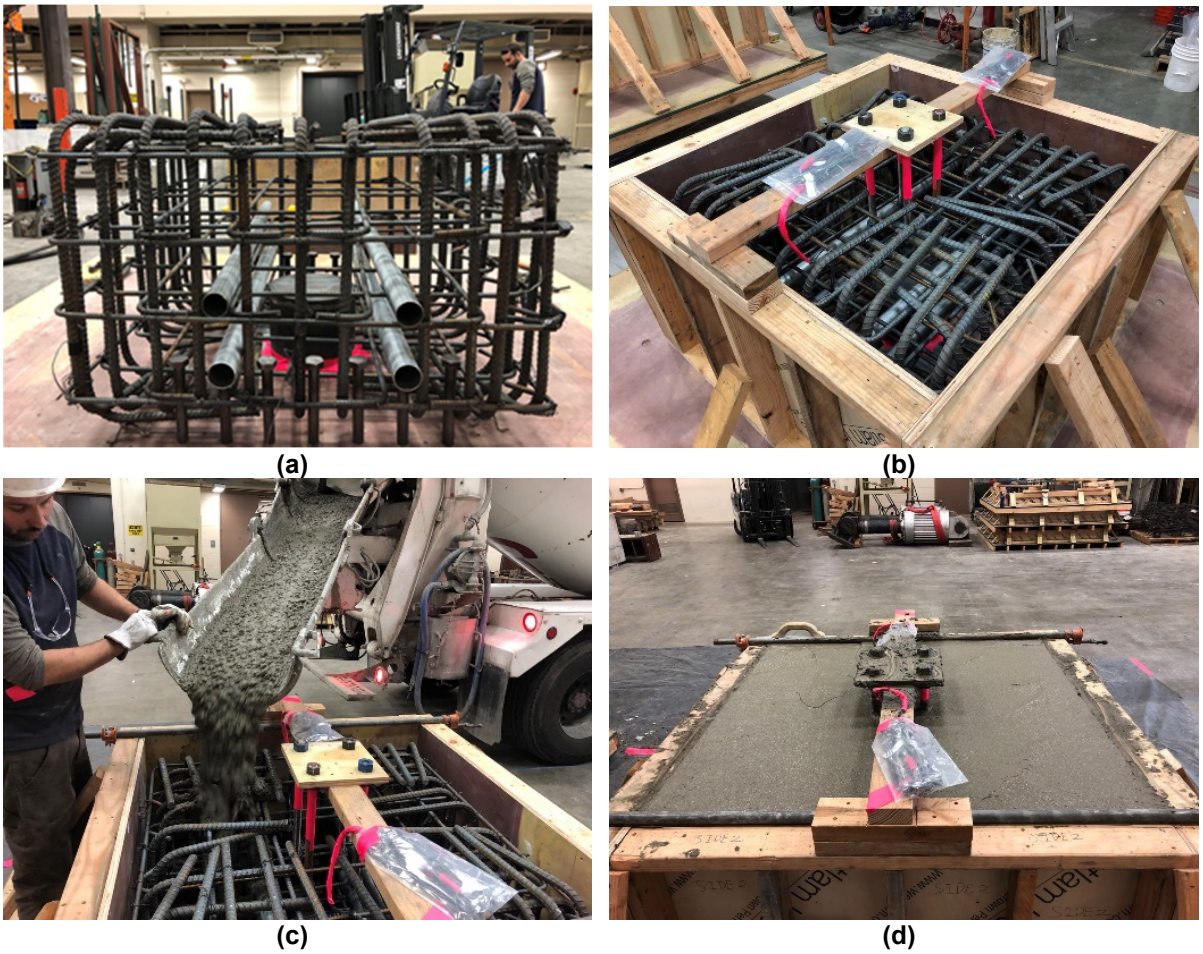

(a) (b)

(c) (d)

Figure 3.13 **(a) Reinforcing bar cage; (b) formwork; (c) concrete casting; and (d) finishing state of the top block.**

Figure 3.14 **(a) Reinforcing bar cage; (b) formwork; (c) concrete casting; and (d) finishing state of the bottom block.**

The second phase involved assembling the V-connector set and putting everything together. First, the Teflon washer was placed on top of the embedded V-tube. The top steel pad with hinge holder was then placed on top of the Teflon washer. Next, the V-pin together with the hinge were inserted into the V-tube. The hinge stop, which was designed to prevent the V-pin from being pulled out during lateral loading, was bolted to the hinge holder. This completed the V-connector assembly procedure. The final step was to set the top block in place and attach the top steel pad to it though a bolt connection. Figure 3.15 shows all the above-mentioned steps for the assembly procedure and Figure 3.16 shows the final specimen configuration before finishing the rest of the test setup.

Figure 3.15 V-connector assembly sequence: (a) place the Teflon washer; (b) put on the top steel pad; (c) insert the V-pin; (d) attach the hinge stop; (e) set up the top block.

Figure 3.16 Completed specimen configuration.

3.7 MATERIAL PROPERTIES

The different sizes of reinforcing steel used in the top and bottom blocks (see Table 3.1) was Grade 60, following the ASTM A706 (2016) standard. The concrete type of the blocks was normal-weight concrete, with a specified strength of 5 ksi. The material for different V-connector parts was Duplex 2205 steel based on the inputs from the manufacturer.

Since the top and bottom blocks were overly-designed (see Appendix A), the material testing is not of major concern for the V-connector study. Therefore, only compressive strength tests of the concrete were conducted using 6 in. diameter by 12 in. height standard cylinders on the 7th day and the day of the cyclic test. The cylinder samples were collected from the same batch of concrete when casting the blocks and were cured in the same indoor laboratory conditions. They were capped with a sulfur compound at both ends before being tested on the Universal Testing Machine in accordance with ASTM C39 (2005). The test results for the concrete are listed in Table 3.4.

Table 3.4 Compressive strength test results for the concrete.

Material	Age [day]	Compressive Strength [ksi]		
		Mean	St. Dev.	COV
Top/bottom block concrete	7	4.665	0.016	0.0035
	40	6.394	0.109	0.017

3.8 INSTRUMENTATION

A wide array of sensors was installed to monitor the response of the specimen during the test. A summary of the different types of instrumentation and their layout is presented in the following. All the sensor data was sampled at 100 Hz.

3.8.1 Load Measurement

Load was measured to assist in the control of both the vertical and lateral actuators and to measure the total forces applied to the specimen for capacity estimation. Four load cells were used to measure the actuator forces: two for the vertical actuators and another two for the lateral ones. The vertical actuators were used to apply the gravity load under load control. Thus, the load cell measurement was indispensable to monitor the level of the applied load. The lateral actuators were running in displacement control. Load cell measurement was a crucial factor in estimating the total applied forces applied during the cyclic test. In addition, the measured lateral resisting forces were used in the HS test as a feedback to perform the numerical integration. The load cells were calibrated in compression using the Universal Testing Machine at UC Berkeley.

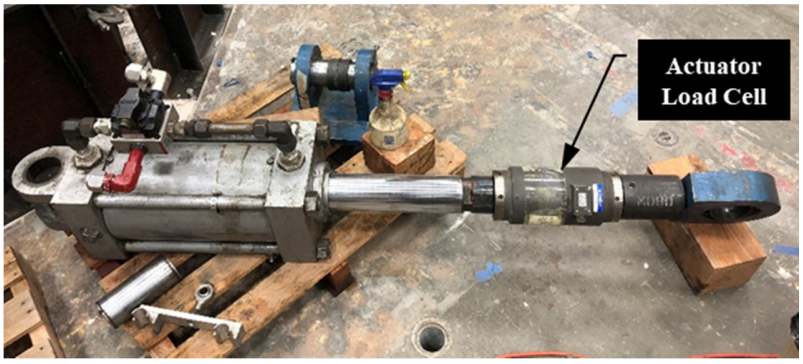

Figure 3.17 Typical actuator load cell.

3.8.2 Displacement Measurement

The displacements were measured using long- and short-range displacement transducers. The long-range displacement transducers were linear wire potentiometers (WPs) with two ranges of stroke, namely ±7.5 in. and ±15 in. Four ±7.5 in. WPs were triangulated to measure the movements of the top block at two elevations in the direction of the applied lateral load. Another two WPs, with a range of ±15 in., were installed on the north side of the top block. These long-range displacement transducers have an accuracy of 0.10% of its full range, i.e., 0.015 in. resolution for a range of ±7.5 in. and 0.03 in. resolution for a range of ±15 in. Thin steel strings (piano wires) were utilized to connect the transducers' cords to the target points mounted on the blocks. Figure 3.18(a) shows a typical example of installation details of the WPs on the instrumentation frame. A typical target point for the WPs on the top block is shown in Figure 3.18(b). The six utilized long-range displacement transducers are presented in Figure 3.19 and Figure 3.20(a).

(a) (b)

Figure 3.18 (a) WPs on the east-side instrumentation frame; (b) target point attached to the reinforced concrete block surface.

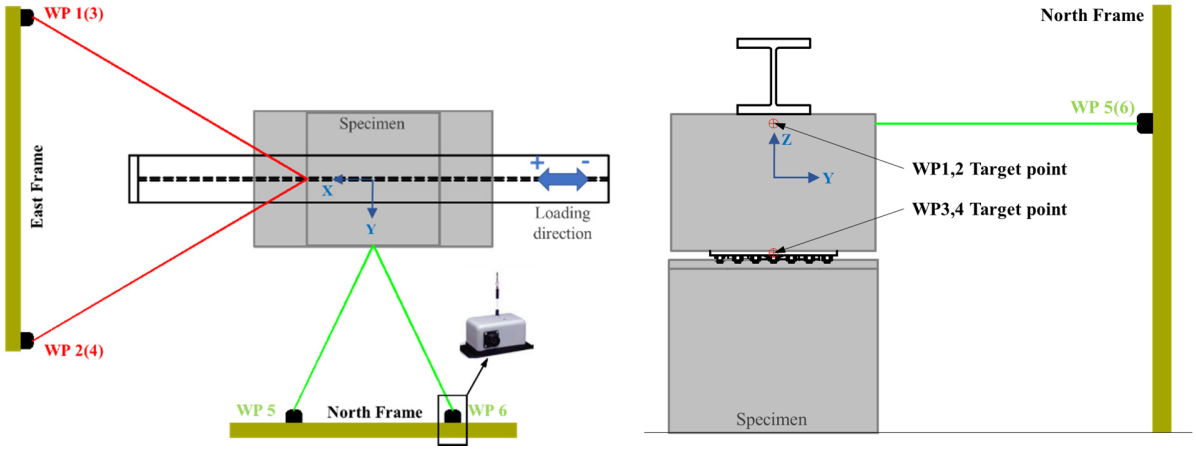

(a) WPs in plan view (b) WPs in N-S elevation view

Figure 3.19 Instrumentation layout for displacement measurements (top & N-S views).

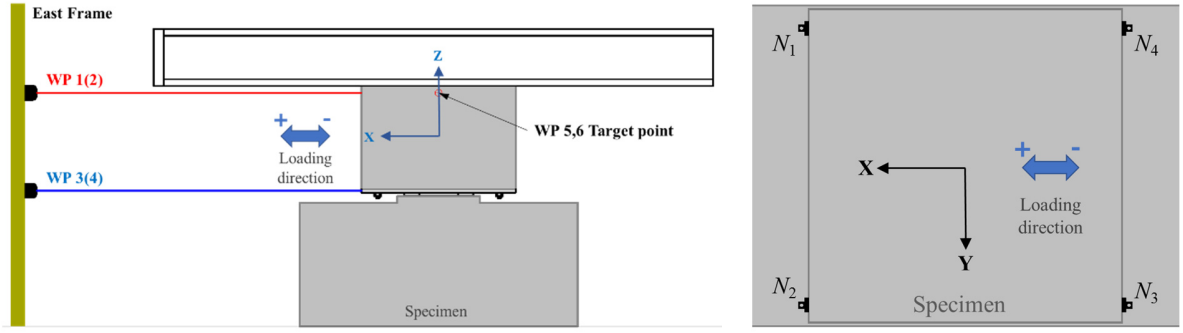

(a) E-W elevation view (b) Plan view of block's vertical instrumentation

Figure 3.20 Instrumentation layout for displacement measurements (E-W & top views).

The short-range displacement transducers were linear variable differential transformers (LVDTs) with range of ±1.5 in. The goal of the use of these transducers was to measure the vertical displacements and rotations, if any, of the top block. The accuracy of these LVDTs is 0.05% of the full range (0.0015 in. resolution), i.e., much better than that of the WPs. They were installed at each corner of the top block as presented in Figure 3.20(b) and Figure 3.21. As shown in Figure 3.22, flat aluminum plates with polished surface were leveled and placed on top of the bottom block such that the spring-loaded tips of the instrument could slide smoothly when the top block moves horizontally relative to the stationary bottom block.

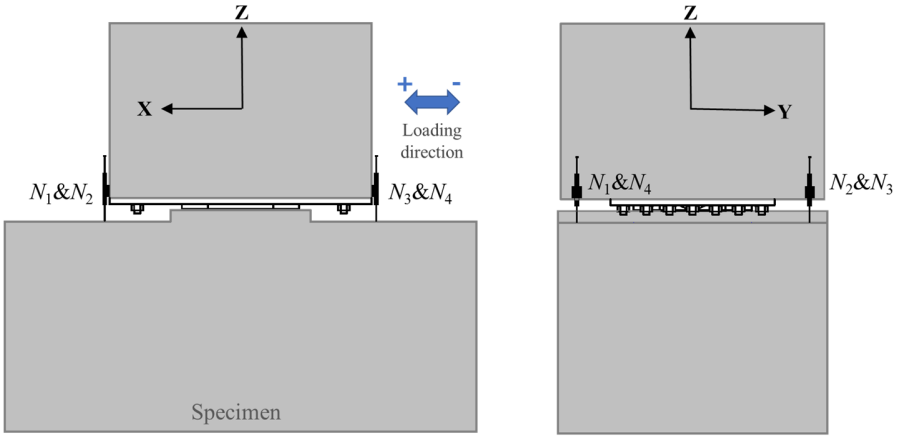

(a) E-W elevation view (b) N-S elevation view

Figure 3.21 Layout schematics of instrumentation for relative vertical displacement of the top block with respect to the bottom block.

(a) (b)

Figure 3.22 Photographs of instrumentation for relative vertical displacement of the top block.

3.8.3 Strain Measurement

Strains of the reinforcing bars were measured using foil gauges mounted on the reinforcement surface. The utilized post-yielding gauge size was 0.20 in.×0.08 in., with a rated deformation

capability of 15%. The reinforcing bar surface deformation in the region surrounding the gauge location was removed and polished. The strain gauge was glued to the surface and covered by three protective coatings: wax, SB tape (made of butyl rubber), and epoxy. Figure 3.23 shows the steps of installing the strain gauges on the reinforcing bars. Note that instrumenting these bars with strain gauges is critical in reinforced concrete components or subassembly testing. Thus, proper attention is required to minimize the chances of losing strain gauges during construction.

A total number of twenty strain gauges, with ten in the top block and ten in the bottom block, were installed. Each block had six strain gauges on the longitudinal reinforcement and four on the transverse. The strain gauge arrangements on the longitudinal and transverse reinforcement of the top and bottom block are shown in Figure 3.24 and Figure 3.25, respectively. Based on the design, the blocks should remain elastic and no reinforcement yielding should be expected. This was verified later on based on the readings from these strain gauges.

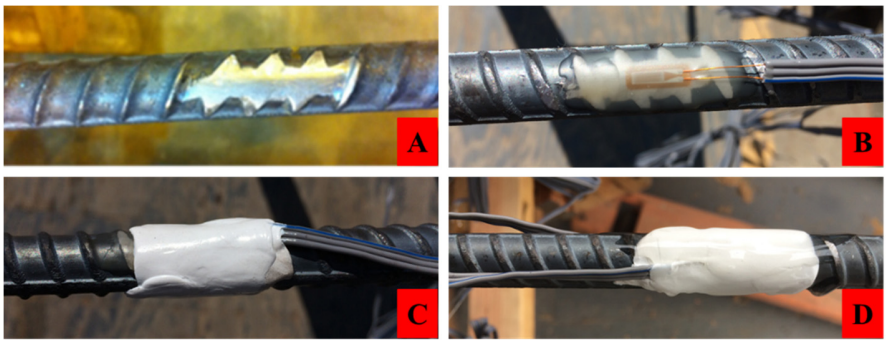

Figure 3.23 **Strain gauges used for reinforcing bars instrumentation where several chemical and mechanical layers were added to protect the gauges.**

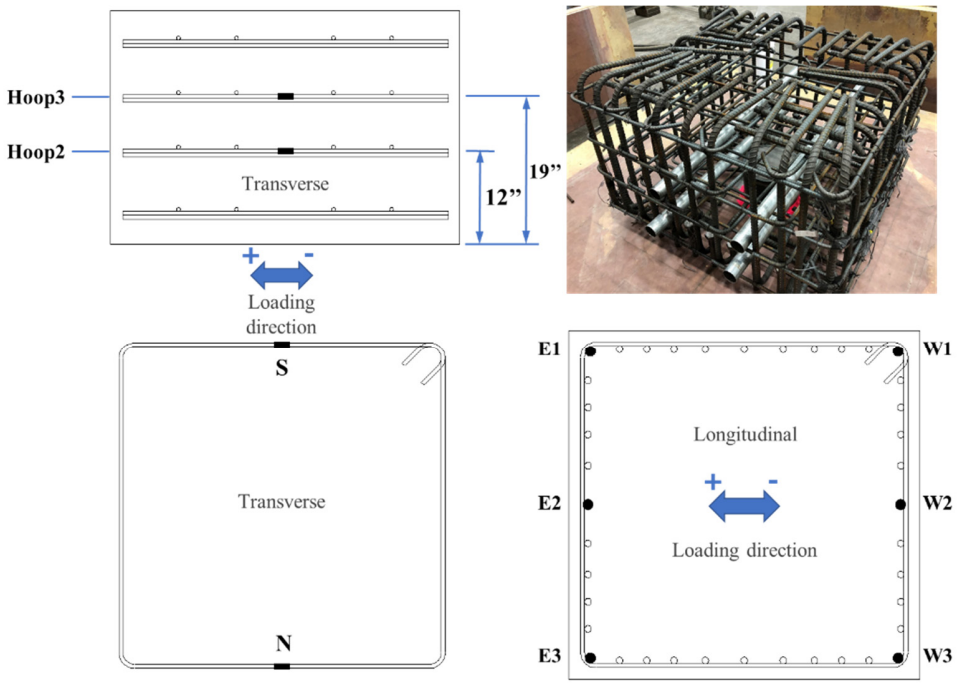

Figure 3.24 **Strain gauges layout of the top block's longitudinal and transverse reinforcement.**

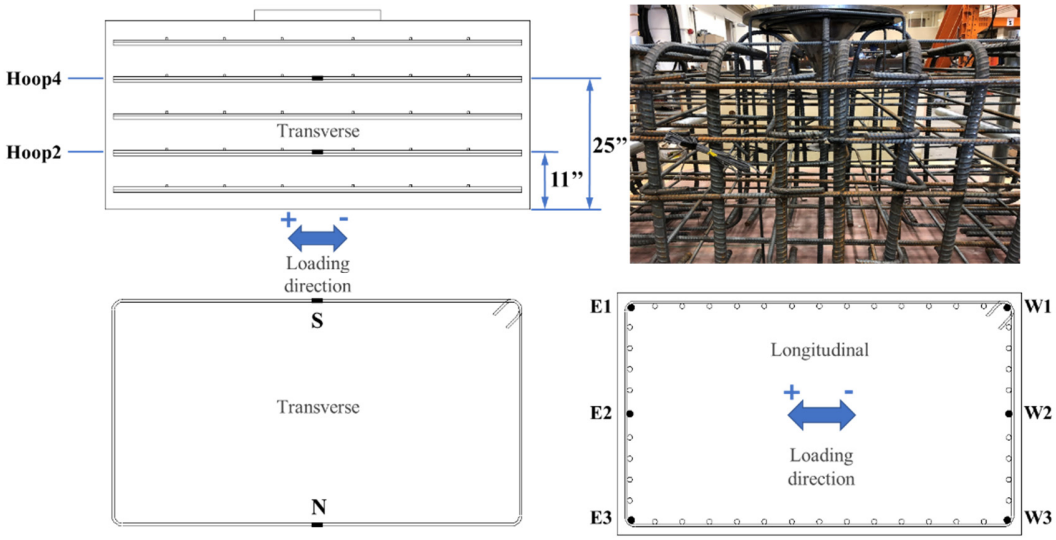

Figure 3.25 **Strain gauges layout of the bottom block's longitudinal and transverse reinforcement.**

3.8.4 Laser Scan Setup

In addition to the conventional instrumentations mentioned above, terrestrial laser scanner was used for displacement and rotation measurements during the quasi-static cyclic test. Laser scanner is an optical instrument that emits laser beams toward objects surrounding the scanner and

measures time-of-flight (TOF) duration of the laser beams reflected back. The distance to each point in space is computed by multiplying this duration by the speed of light. A collection of these points with their spatial coordinates results in the so-called point cloud. ScanStation C10 from Leica Geosystems was used for the point cloud collection. This technology was used in this study to complement and compare conventional instrumentation data to that collected by the laser scanner. While the accuracy of individual point distance acquisition is ±4 mm, this accuracy can be significantly improved by estimating the vertex of a special flat pattern of the high-definition laser target (HDLT), which is commonly used for stitching individual scans into a combined point cloud. In earlier studies, it was shown that the accuracy of the laser target acquisition can be close to ±0.5 mm or better (Takhirov, 2010). The photographs of the previously discussed experimental setup and the details of the point cloud collection are presented in Figure 3.26.

(a) Global view of the setup (also showing 6 HDLTs)

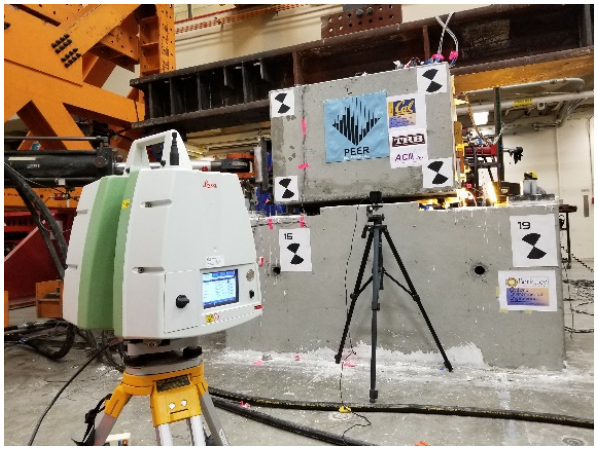

(b) Location of the scanner with respect to the specimen

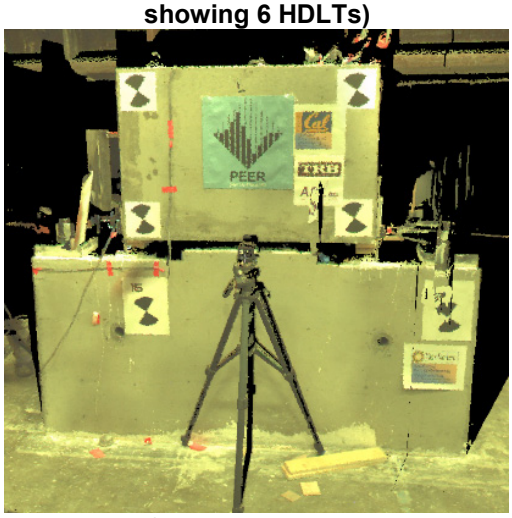

(c) Collected point cloud (real world colors)

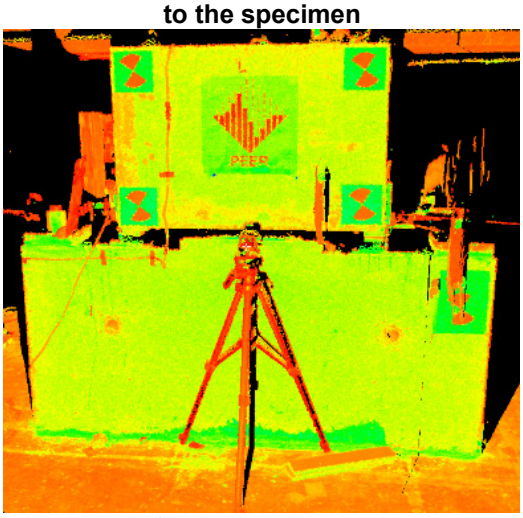

(d) Collected point cloud (intensity colors)

Figure 3.26 Experimental setup and point cloud collection.

The scans were performed from the same location before and during the test. A total of 9 scans were conducted with 3 of them performed before the test. The initial data manipulation was conducted in Cyclone (Leica Geosystems 2018). They were exported as ASCII files and the final

data reduction was conducted in the Matlab (MathWorks, 2018) environment. The vertices of the HDLTs were estimated from the point cloud as presented in Figure 3.27.

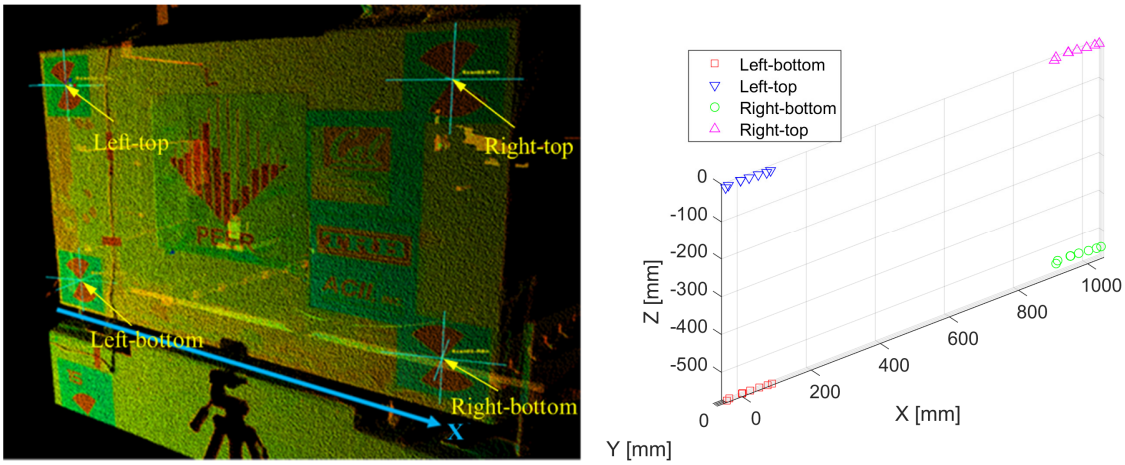

(a) Point cloud of targets and estimated vertices

(b) Vertices imported to the Matlab (MathWorks, 2018) environment

Figure 3.27 Vertices of the high-definition laser targets.

4 V-connector Phase I: Quasi-Static Cyclic Test

This chapter presents the details of the first test conducted on the V-connector: the quasi-static cyclic test. The test was conducted under constant gravity load and 11 unidirectional lateral loading groups. The complete set of all loading groups was achieved in one day of testing.

Before doing the cyclic test, a pre-test finite element analysis was conducted, with two main objectives: (1) Estimate the expected axial and lateral forces during cyclic and HS test and choose the scale factor for the V-connector based on the laboratory limitations; and (2) Come up with a set of expected design parameters for the reduced-scale V-connector manufacturing. The pre-test analysis is divided into three sections. The first section briefly describes the prototype bridge used in this study. The second section is dedicated to the prototype bridge modeling using OpenSEES (McKenna et al., 2000). The third section describes the parametric studies and analysis results of the prototype bridge. These results served as the basis of selecting the design parameters of the V-connector.

The post-processing of the cyclic test results consists of three main parts. Part one discusses the global behavior of the V-connector in terms of lateral forces, displacements, rotations and force-displacement relationship in the loading direction. Some of the response quantities measured by conventional instrumentations were compared against those from the laser scans. Part two focuses on the local behavior of the top and bottom blocks in terms of reinforcement strains. The main purpose of this part is to check if the blocks remained elastic during the test, which was the original design goal. Part three presents an updated V-connector modeling, which is tuned based on the test data. This is an improvement on the idealized model as discussed in the pre-test analysis. The prototype bridge was reanalyzed with the calibrated V-connector modeling, which serves as the basis for selecting the ground motion scale factors in the subsequent HS test.

4.1 PRE-TEST FINITE ELEMENT ANALYSIS

4.1.1 Prototype Bridge Description

The prototype was derived from an existing bridge: the Jack Tone Road On-Ramp Overcrossing (see Figure 4.1) built in 2001, which is located in the city of Ripon, California, at the intersection of Route 99 and Jack Tone Road (identification number 10-SJ-099-2.34-RIP). It has two spans, with a total length of 67.2 m (220.4 ft), and span lengths of 33.105 m (108.58 ft) and 34.095 m (111.82 ft). This bridge is originally about 33° skewed and crosses one lane of traffic on a seven-lane highway. The bridge superstructure is a three-cell continuous prestressed reinforced concrete

box-girder. The bent has a half-cap beam integral with the deck and a single reinforced concrete circular column in the middle. The column of the bent is 1.68 m (5.51 ft) in diameter and is supported on 25 HP 305×79 steel piles. The longitudinal reinforcement ratio ρ_l of the column is approximately 2%. The abutments are seat-type, with four elastomeric bearing pads per abutment. A comprehensive description of the bridge is tabulated in Table 4.1.

The 3D OpenSEES model for the as-built bridge was originally developed in (Kavianijopari, 2011) for identifying the seismic behavior of reinforced concrete bridges with seat-type abutments under earthquake loading, especially with respect to abutment skew angle. In order to represent the bridge behavior in the test, the V-connector was incorporated into the 3D model of the bridge, between the column and the bridge deck, and the dynamic results from this model were used to decide on the key design parameters of the V-connector.

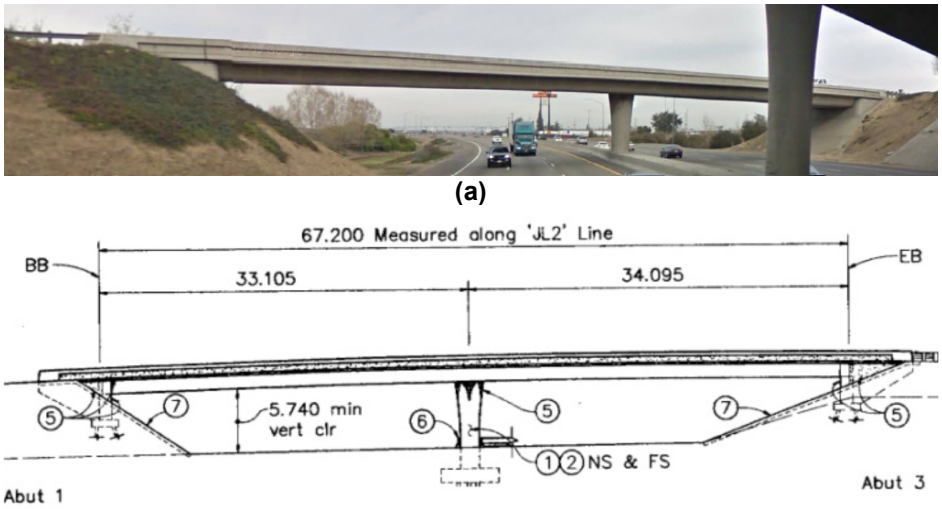

Figure 4.1 The Jack Tone Road On-Ramp Overcrossing: (a) picture (source: Google Maps); (b) elevation (source: Caltrans structural drawings).

Table 4.1 Structural and geometrical information of the prototype bridge.

Parameters	Value/Description
General bridge description	Ordinary standard single-column bridge with 2 spans
Total length of bridge (L_{Total})	220.4 ft (67.2 m)
Number of spans and length of each deck span	2 spans: 108.58 ft (33.105 m) and 111.82 ft (34.095 m)
Total deck width (W_{deck})	27.13 ft (8.27 m)
Deck depth (d_d)	4.64 ft (1.415 m)
Deck cross-sectional geometry*	A = 97.546 ft^2 (9.067 m^2); J = 341.442 ft^4 (2.954 m^4); I_x = 180.328 ft^4 (1.558 m^4); I_y = 3797.9 ft^4 (32.81 m^4); A_{vx} = 18.92 ft^2 (1.759 m^2); A_{vy} = 27.584 ft^2 (2.564 m^2); S_x = 83.35 ft^3 (2.362 m^3); Z_x = 115.143 ft^3 (3.263 m^2); S_y = 279.97 ft^3 (7.934 m^3); Z_y = 521.832 ft^3 (14.788 m^3)
Number and clear height of each column (H_{col})	1 column: 19.68 ft (6 m)
Column diameter (D_c)	5.51 ft (1.68 m)
Deck centroid ($D_{c.g.}$)	2.48 ft (0.756 m) from bottom
Location and size of expansion joints	No expansion joints specified
Support details for boundary conditions	Fixed foundations
Concrete material properties for concrete of superstructure ($f_c^{'}$, E_c)**	Elastic deck: $f_c^{'}$ = 5 ksi (34.5 MPa); E_c = 4030.5 ksi (27800 MPa)
Concrete and reinforcing material properties of the column	Concrete: $f_c^{'}$ = 5 ksi (34.5 MPa); Steel: ASTM A706
Reinforcement details of column cross section***	Longitudinal reinforcement: 44 #11 (bundles of 2), ρ_l = 2% Transverse reinforcement: Spiral. #6 @3.34″
Abutment general geometry	Simplified abutment model
Number and properties of abutment bearing pads	4 elastomeric bearing pads used per abutment

*A is the cross-sectional area;
J is the cross-sectional torsional constant;
I_x & I_y are the second moment of areas w.r.t the weak & strong axes;
A_{vx} & A_{vy} are the shear areas along the weak & strong axes;
S_x & S_y are the elastic section moduli w.r.t the weak & strong axes;
Z_x & Z_y are the plastic section moduli w.r.t the weak & strong axes.
**$f_c^{'}$ and E_c are the compressive strength and the elastic modulus of the concrete.
***ρ_l is the longitudinal reinforcement ratio of the column.

4.1.2 Model Description

In the 3D spine-line model of the prototype bridge developed in OpenSEES (McKenna et al., 2000), the line elements were located at the centroid of the cross sections following the alignment of the bridge. A representative bridge model used in the analysis is displayed in Figure 4.2. The model comprises of the seat type abutments, the column, the superstructure and the V-connector.

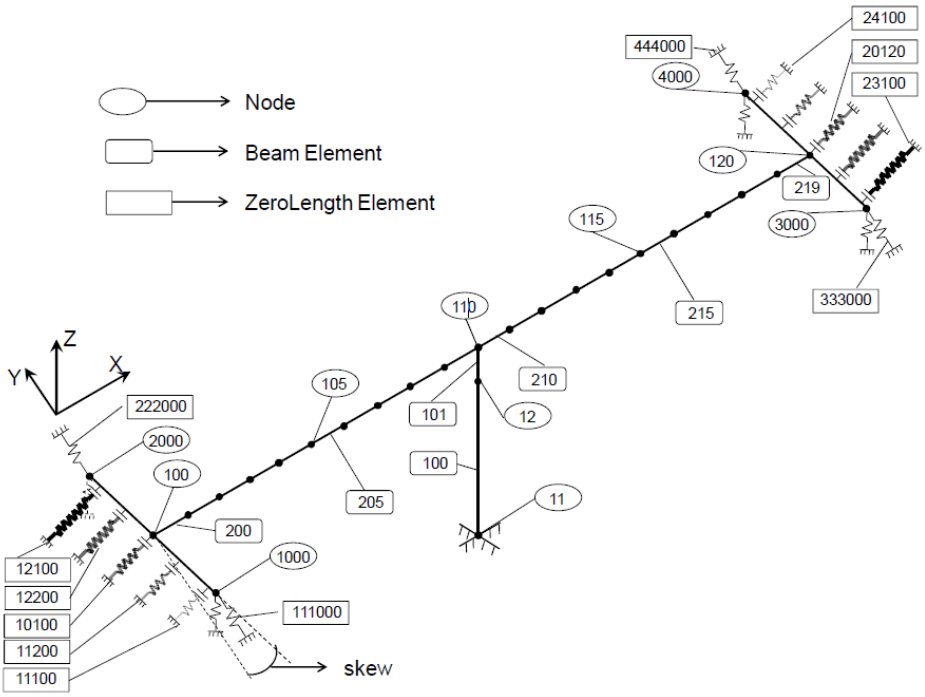

Figure 4.2 Nodal and element designation of the prototype bridge (Kavianijopari, 2011).

4.1.2.1 Bridge Component Modeling

The prestressed concrete box girder system was modeled using elastic beam-column elements along the spine of the bridge deck as flexural yielding of deck during seismic response is not expected. On the contrary, progression of column yielding and damage are expected under strong ground motions. Thus, one single nonlinear force-based beam-column element with 5 quadrature points and fiber section was used to represent the column. This is usually deemed to provide adequate accuracy. As mentioned earlier, all components were modeled in the centerline of the elements. Therefore, a rigid element with length equal to the distance between the superstructure's cross section centroid and the column top was assigned on top of the nonlinear element to model the portion of the column embedded in the superstructure, see Figure 4.3.

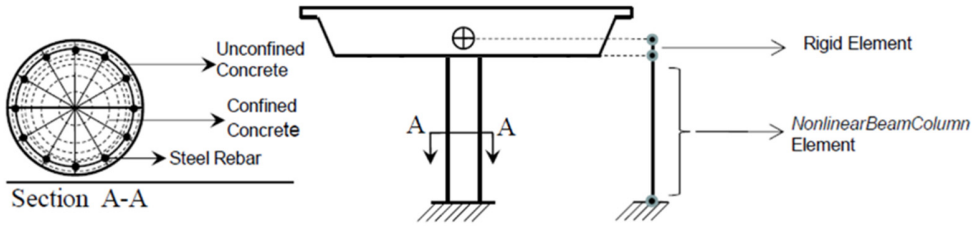

Figure 4.3 Column modeling scheme (Kavianijopari, 2011).

The abutment model consists of several zero-length springs modeled both in series and in parallel to approximate the behavior in each direction. The longitudinal response was modeled using five nonlinear springs in series with gap elements as shown in Figure 4.4. The nonlinear springs and the gap elements represent the passive backfill response and the expansion joint, respectively. In the transverse direction, a strut-and-tie model was employed to simulate the shear key component. The vertical response was modeled by two parallel springs, simulating the elastomeric bearing pads and the stem wall. Details of the abutment modeling techniques can be found in (Kavianijopari, 2011).

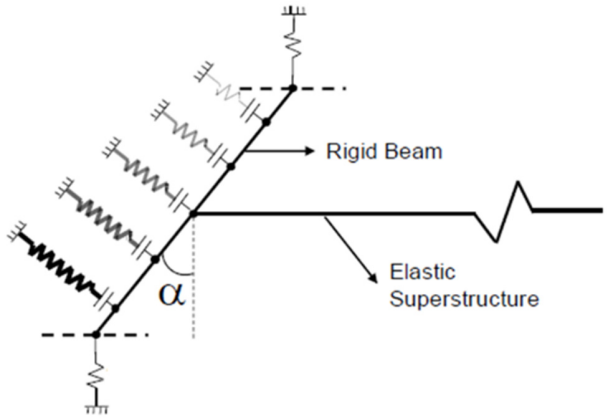

Figure 4.4 Abutment modeling detail: backfill soil springs (Kavianijopari, 2011).

4.1.2.2 V-connector Modeling

The V-connector was added to the prototype bridge between the column and the rigid link connecting the column and the superstructure, as shown in Figure 4.5. It was modeled using translational zero-length springs along the longitudinal and transverse directions of the bridge with an idealized bilinear hysteretic response. Assuming the V-connector's response to be decoupled in the longitudinal and transverse directions, the zero-length springs were added in these two directions independently.

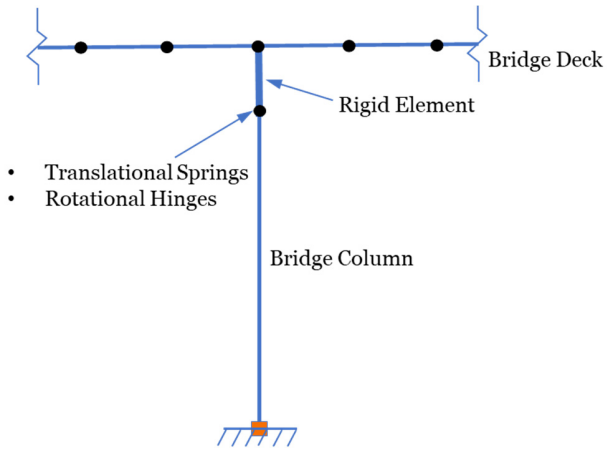

Figure 4.5 Schematic representation of the V-connector location.

The idea of using a bilinear model to approximate the behavior of the V-connector was inspired by the friction pendulum bearing. The typical response of a friction pendulum bearing under cyclic loading is shown in Figure 4.6. As can be seen from the figure, the behavior of the friction pendulum system is essentially a bilinear model with an initial stiffness K_1 and a post-yielding stiffness K_2. When u_y is close to zero, this hysteresis loop can approximate the expected behavior of the V-connector. It can be decomposed into two components: the linear elastic component provided by the lateral stiffness of the V-pin, and the kinematic friction component between the Teflon washer and the top steel plate. Therefore, the force-displacement relationship of the translational zero-length spring was represented by a linear elastic component in parallel with an elastic-perfectly plastic (EPP) component with a very high tangent stiffness for loading and unloading (see Figure 4.7), which becomes essentially rigidly plastic. To account for the moment release due to the hinge connection inside the V-connector, rotational hinges about the X and Y axis (refer to Figure 4.5) were added between the column top and the rigid element.

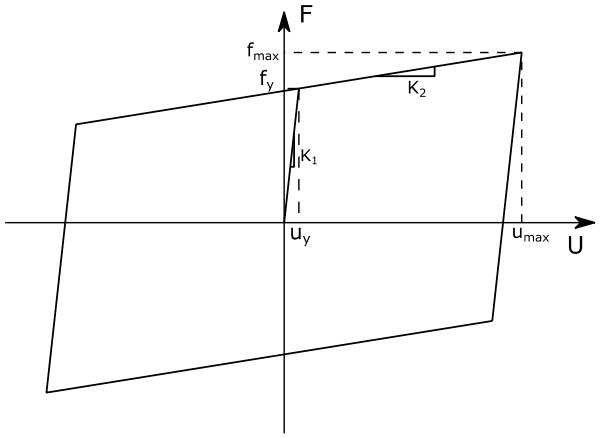

Figure 4.6 Hysteresis loop of a friction pendulum system.

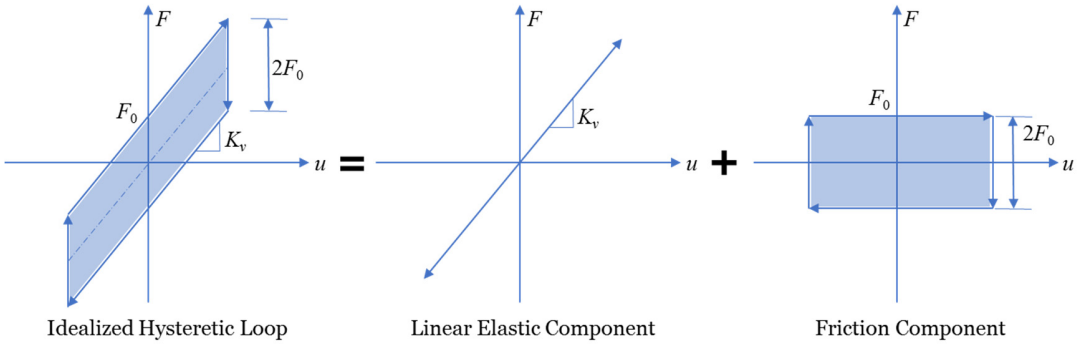

Figure 4.7 Idealized hysteretic response of the V-connector and its decomposition.

4.1.3 Prototype Bridge Analysis

As stated before, the goal for conducting parametric studies on the prototype bridge is to find the key design parameters for the V-connector manufacturing. In case of the idealized hysteretic behavior in Figure 4.7, the design parameters are the intrinsic friction F_0 and the stiffness K_v of the V-pin. The criterion for choosing these parameters is to keep the bridge column elastic during the earthquake excitation.

4.1.3.1 Ground Motions

The same set of eight ground motions for studying the seismic response of composite concrete-dual steel shell columns (Guerrini and Restrepo, 2013), with the same scale factors, were applied to the prototype bridge in a concatenated manner to perform nonlinear time history analysis. Only two horizontal components of each motion were considered. The chosen records and the corresponding scale factors are summarized in Table 4.2.

Table 4.2 Selected ground motion records and scale factors.

Test	Event	Date	Station	Scale Factor
EQ1	Coalinga	1983/05/09	Harris Ranch-Hdqtrs (temp)	2.50
EQ2	Imp. Valley	1979/10/15	EC Meloland Overpass FF	0.80
EQ3	Morgan Hill	1984/04/24	Coyote Lake 4Dam (SW abut)	0.70
EQ4	Northridge	1994/01/17	Rinaldi Receiving Station	0.56
EQ5	Northridge	1994/01/17	Sylmar-Olive View Med FF	-0.80
EQ6	Northridge	1994/01/17	Rinaldi Receiving Station	0.90
EQ7	Kobe	1995/01/16	Takatori	0.77
EQ8	Kobe	1995/01/16	Takatori	-0.90

4.1.3.2 Design Parameters

The intrinsic friction F_0 depends on the friction coefficient and the pressure, and the pressure is related to the axial force on the column top. Since no vertical ground excitation is applied in any of the V-connector tests, axial force fluctuation is negligible and a value of 1986.4 kips from pure gravity analysis can be used and treated as constant. The friction force was obtained through the kinematic friction coefficient using Coulomb friction model. With the friction coefficient μ equal to 0.1 for typical Teflon/stainless steel interface as suggested by the V-connector manufacturer, the friction force was around 200 kips. Therefore, F_0 = 200 kips was used as the first design parameter.

The stiffness of the V-pin, K_v, was sought by trial and error method. The general trend is to reduce K_v because: (1) Reducing the stiffness increases the period of the bridge, therefore reducing the accelerations and the inertia forces acting on the bridge; and (2) Smaller K_v reduces the maximum force in the V-connector, which then reduces the maximum force transmitted to the column due to equilibrium. The flow chart for the proposed trial and error method is shown in Figure 4.8.

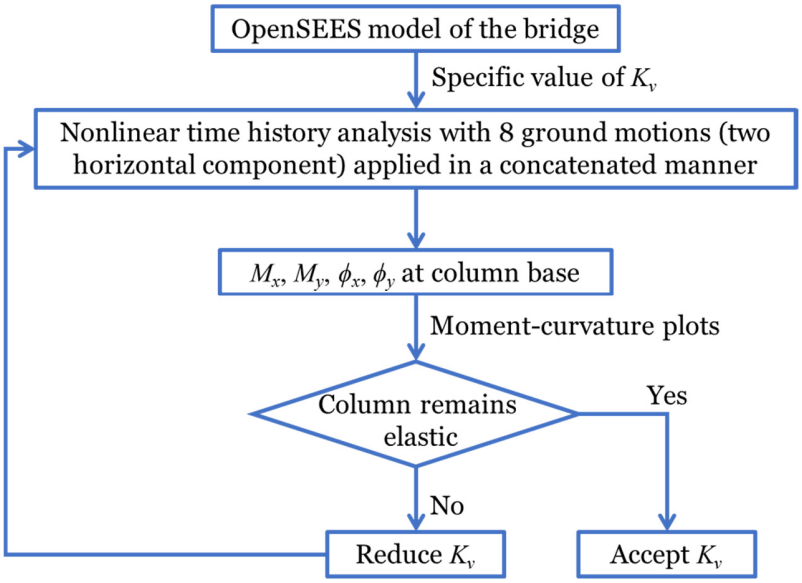

Figure 4.8 **Flow chart for seeking acceptable V-pin stiffness K_v (M_x & ϕ_x and M_y & ϕ_y are the respective bending moments and corresponding curvatures about X and Y axes).**

4.1.3.3 Analysis Results

Following the flow chart in the previous section, different values of K_v were explored. The moment-curvature relationships of the bridge column as well as the force-displacement curves of the V-connector were checked. The results corresponding to three typical values of K_v are compared in Figure 4.9 and Figure 4.10. These plots show that using K_v = 30 kips/in. leads to the elastic behavior of the bridge column. The deformation demand on the V-connector is around 17 in. and the developed maximum shear force V_{max} is about 720 kips.

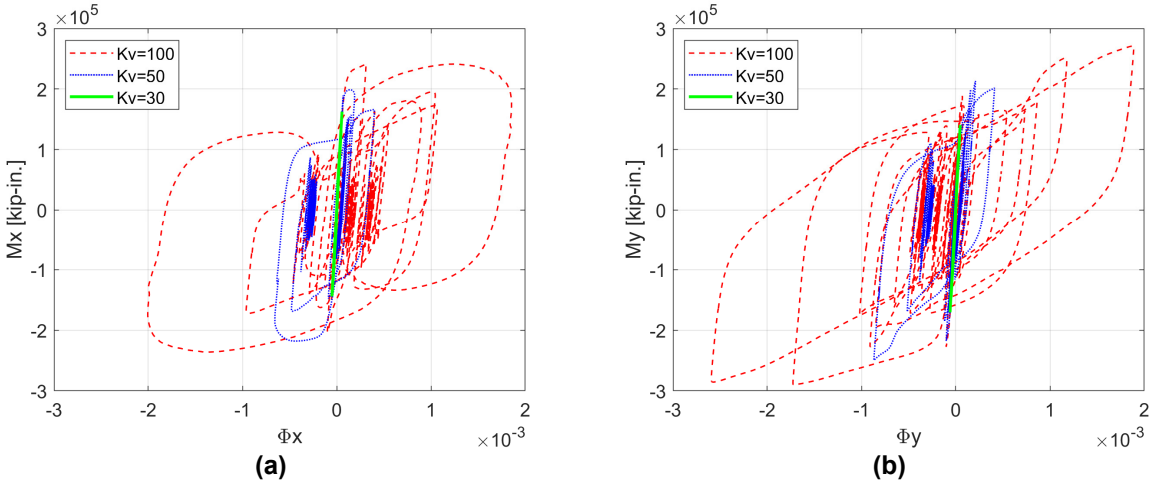

Figure 4.9 **Column moment-curvature relationships in (a) longitudinal direction (X); and (b) transverse direction (Y).**

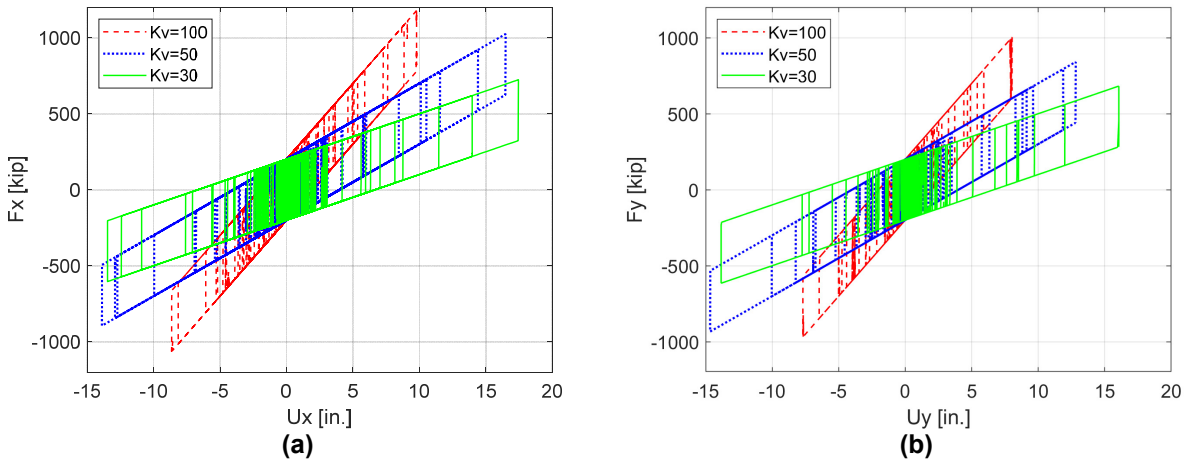

Figure 4.10 Hysteretic behavior of the V-connector in (a) longitudinal direction (X); and (b) transverse direction (Y).

Based on the analysis results, a reduced-scale V-connector needs to be manufactured due to the large shear force and deformation demands. A length scale factor $S_L = 3$ was chosen, leading to the similitude relationships of the V-connector's design parameters and concrete blocks' design forces summarized in Table 4.3. The reduced-scale V-connector and the blocks were designed accordingly. Although from the subsequent quasi-static cyclic test these design parameters of the V-connector were not exactly satisfied, probably because of practical considerations during the fabrication or because the utilized hysteretic behavior was highly idealized in the pre-test analysis, these numbers still provided guidance for the design.

Table 4.3 Similitude relationships for design parameters and design forces.

Elements		Full-Scale	Reduced 1/3-Scale	Scale Factor
Design Parameters	V-pin stiffness K_v [kip/in.]	30	10	3
	Friction coefficient μ	0.1	0.1	1
	Deformation capacity [in.]	17.0	5.7	3
Design Forces	Shear force V [kip]	723.7	80.4	9
	Axial force P [kip]	1986.4	220.7	9

4.2 QUASI-STATIC CYCLIC TEST

4.2.1 Progression of Testing

The cyclic loading test involved unidirectional loading in the global X direction. Figure 4.11 shows the test setup and progression of the loading. Throughout this study, the loading in the global X direction refers to loading in the east-west direction as defined in Figure 4.11. Whenever loading is pushing towards the east, it is designated as the positive loading direction, and, in turn, the

negative loading direction is pulling towards the west. The global X direction defined this way is consistent with the longitudinal direction of the prototype bridge when performing the HS test.

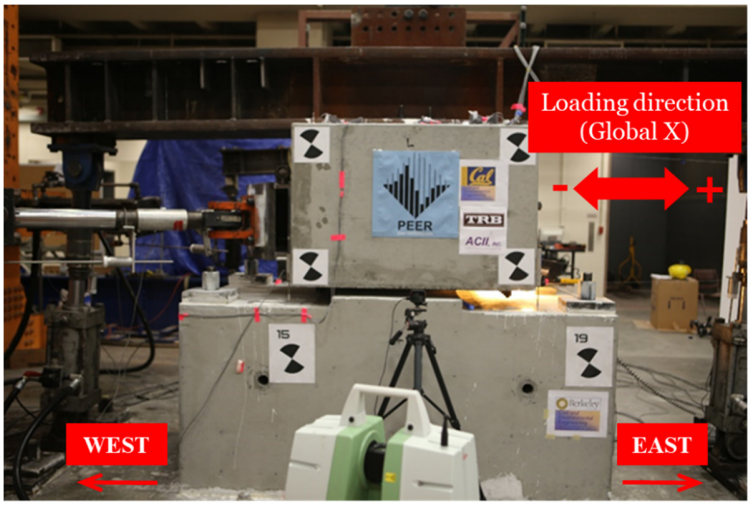

Figure 4.11 Cyclic test setup and progression of loading in the global X direction.

4.2.2 Test Results

4.2.2.1 Force Measurement

The progressive cyclic loading groups are fractions of the targeted maximum displacement amplitude of 4 in. as recommended by FEMA 461 (2007). On the other hand, gravity load of 200 kips was applied and kept constant during all cycles of lateral loading. Details of selected loading protocol can be found in Chapter 3.

The time history of the total gravity loading, together with the forces measured from each vertical actuator are shown in Figure 4.12. Although some fluctuations were observed in each single actuator, the total gravity load of 200 kips was well maintained throughout the test.

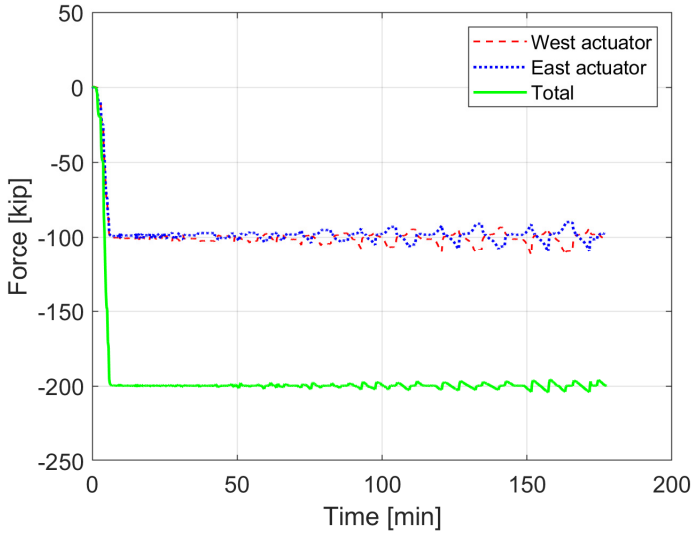

Figure 4.12 Time history of the gravity load applied during the cyclic test.

The forces developed in the lateral actuators with a prescribed displacement were laterally applied. The resultant force F_x in global X direction, which was computed from the actual recorded forces in the load cells of the lateral actuators based on exact geometry and configuration, was utilized to estimate the V-connector's resisting force during the lateral loading cycles. Figure 4.13 shows the time history plots of the measured forces in the two lateral actuators, designated as north and south actuators according to their location relative to the test setup, and the resultant force F_x. Note that the actuator forces have approximately similar values and directions during the unidirectional lateral loading cycles, which is to be expected.

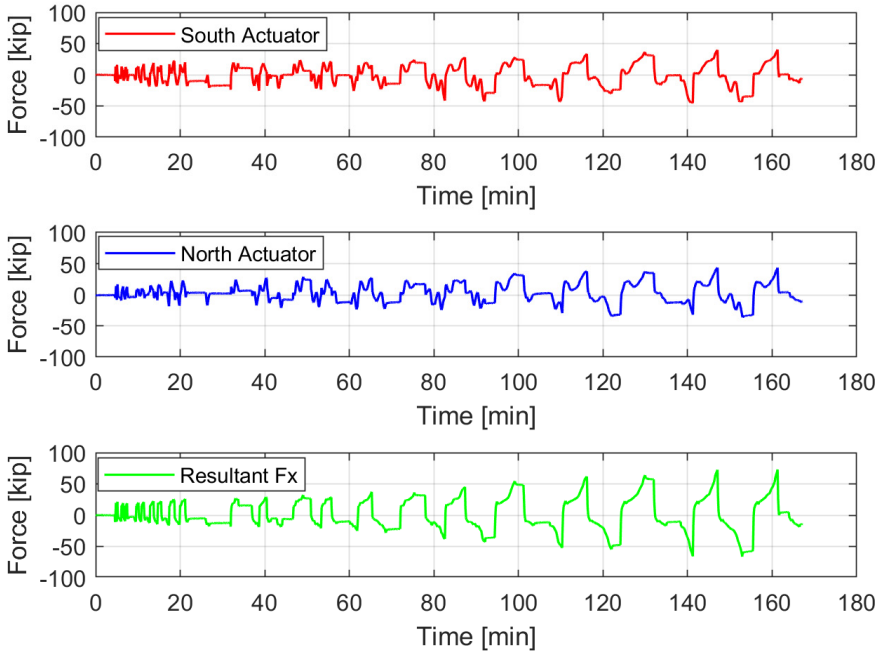

Figure 4.13 **Time history of both north and south lateral actuators load cells measurements and the corresponding resultant forces in the global X direction (F_x) for all cyclic loading groups.**

4.2.2.2 Displacement and Rotation Measurements

Lateral Displacement

For a cyclic loading test under displacement control, prescribed displacements are the primary input commands to the actuators. For practical reasons, the actuators were installed at about 30° to the loading direction. Accordingly, the displacement input from the actuators was transformed such that the resulting movement of the top block agrees with the desired lateral displacement (U_x in the global coordinate system). The obtained displacements during the test were tracked in the actuators' local directions from the feedback provided by the Temposonic transducers of the actuators, and in the global coordinate system through the WPs by performing triangulation. The geometry and configuration of the actuators were used to transform their local motion to the corresponding global directions. The transformed actuators' Temposonic measurements were compared to the WPs to check the accuracy of the measurements and transformations. It was found that the displacements computed from the exact actuators' geometry and Temposonic measurements were the most accurate, although the computed displacements from the WPs were also quite close to those from the actuators (see Figure 4.14). Therefore, only the displacements obtained from transformed Temposonic measurements were used in later discussions.

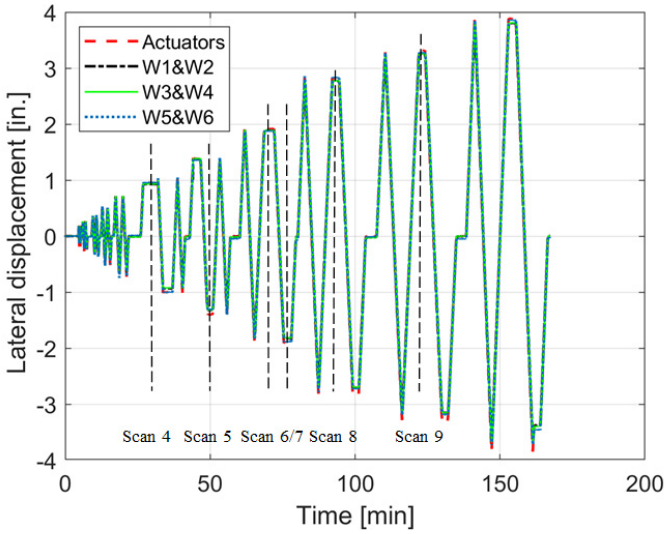

Figure 4.14 Lateral displacement time history computed from different measurements.

Figure 4.15 shows the time history plots of the recorded Temposonic measurements of the north and south actuators along with the resulting displacements in both the global X (U_x) and the global Y (U_y) directions. Two observations can be made: (1) The Temposonic measurements in the actuators' local axes are the same; and (2) The resulting displacements U_y are close to zero. This gives another evidence showing the correctness of the geometric transformation. The flat parts of the plots at given displacement peaks represent the pause in time when the laser scanning was performed and the specimen's condition was visually inspected. The target input displacements and the actual applied displacements based on Temposonic measurements are summarized in Table 4.4. The displacement tracking was well controlled, as can be seen from the table where the maximum relative error is about 5%.

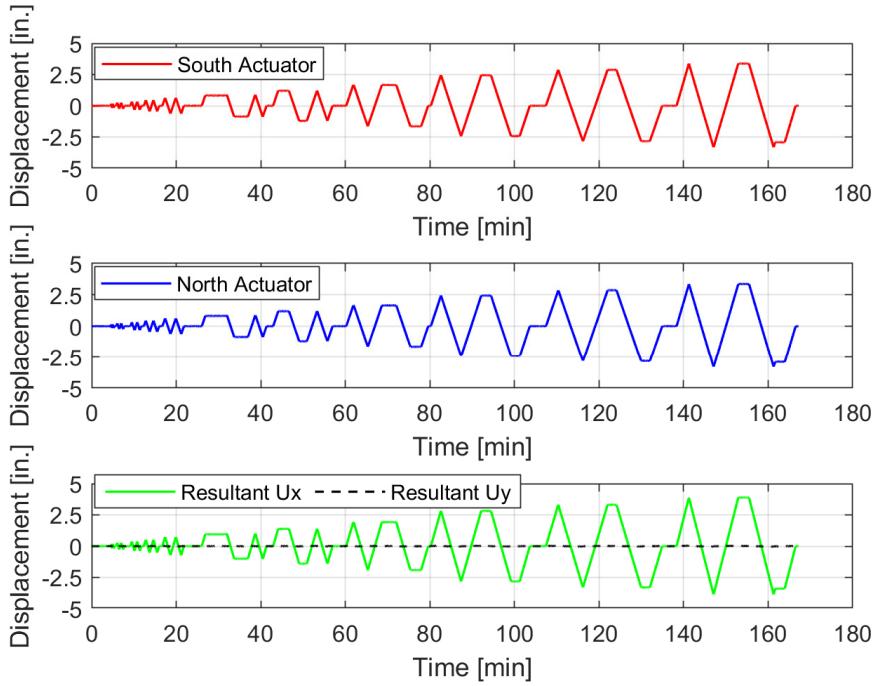

Figure 4.15 **Time history of the Temposonic measurements of both north and south actuators and the resultant displacement in the global X and Y directions (U_x & U_y) for all cyclic loading groups.**

Table 4.4 **Target and actual obtained displacements with relative errors.**

Target Disp. [in.]	0.19	0.27	0.38	0.53	0.75	1.06	1.46	2.00	2.86	3.50	4.00
Obtained Disp. [in.]	0.187	0.271	0.37	0.514	0.73	1.02	1.40	1.92	2.83	3.32	3.89
Relative Error [%]	-1.6	0.4	-2.6	-3.0	-2.7	-3.8	-4.1	-4.0	-1.0	-5.1	-2.8

The lateral displacement was also measured by tracking the displacements of the vertices of the HDLTs using laser scans. The displacements of the vertices in the lateral direction are presented in Figure 4.16. As noted earlier, the first three scans were performed before the test with no vertical preload. As a result, all vertex displacements for these 3 scans were very close to zero. The plot shows excellent agreement between conventional and laser scan measurements.

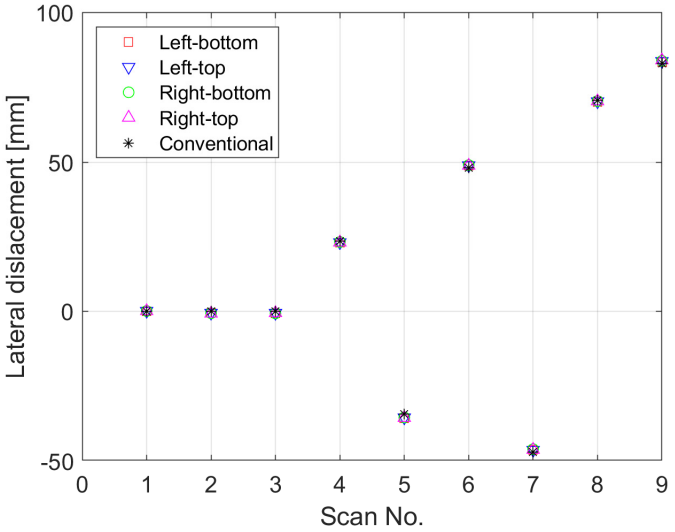

Figure 4.16 Comparison between laser scan data and conventional (Temposonic) measurements.

Vertical Displacement

The vertical movement of the top block relative to the bottom block was measured by four short-range position transducers mounted near the corners. In order to compare with the laser scan results, transformation or correction was needed, because the locations of the measurements were not exactly at the top block's south surface where the HDLTs were located. Based on the geometry shown in Figure 4.17, the transformation was performed by the following:

$$\frac{D_s - D_{23}}{D_{14} - D_{23}} = \frac{a}{b} \Rightarrow D_s = \frac{a}{b}(D_{14} - D_{23}) + D_{23} \tag{4.1}$$

where

D_s = south surface vertical displacement;

D_{14} = average value of the readings from N_1 and N_4 vertical transducers; and

D_{23} = average value of the readings from N_2 and N_3 vertical transducers.

Figure 4.18(a) presents the vertical displacement of the top block during the test, which clearly shows that the top block was gradually sinking under the constant vertical load. The same trend was observed from the laser scan data as presented in Figure 4.18(b). The plots show good agreement between the displacements measured by the conventional instruments and those from the displacements of HDLTs' vertices.

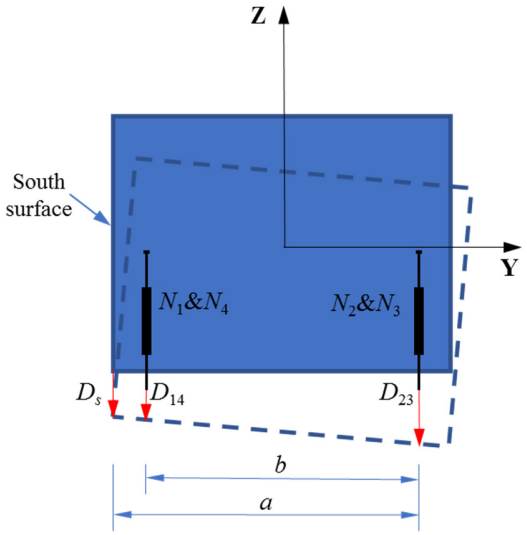

Figure 4.17 Transformation of the vertical displacement.

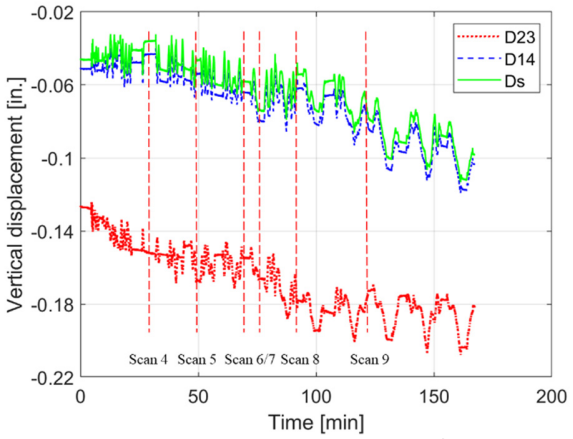

(a) Time when scans were performed

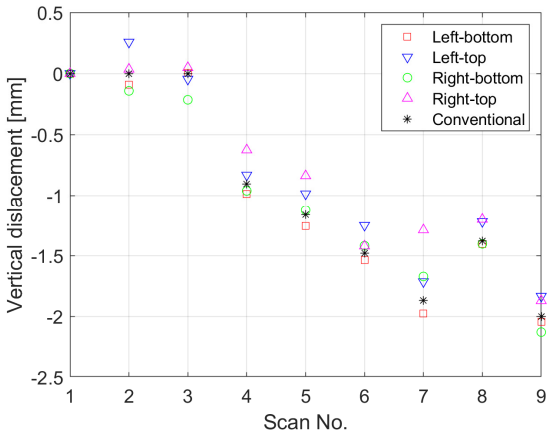

(b) Vertical displacements comparison

Figure 4.18 Vertical displacement from laser scans compared to conventional measurements.

Rotations of Top Block

Rotation of the top block, especially the rotation around the global Y axis is one of the concerns in this study, because the V-connector is not expected to experience any rotations on top in the real installation of a bridge system. Hence, specific attention was paid to the control of the vertical actuators to minimize the artificial rotation caused by the test setup limitation. The top block's rotation can also be measured by the four short-range position transducers mounted near the corners. Based on the geometry shown in Figure 4.19, the block rotation can be calculated as follows:

$$R_x = \frac{D_{14} - D_{23}}{L_2};\ R_y = \frac{D_{12} - D_{34}}{L_1} \tag{4.2}$$

where

D_{14} = average value of the readings from N_1 and N_4 vertical transducers;

D_{23} = average value of the readings from N_2 and N_3 vertical transducers;

D_{12} = average value of the readings from N_1 and N_2 vertical transducers;

D_{34} = average value of the readings from N_3 and N_4 vertical transducers;

L_1 = distance between N_2 and N_3 (that was the same as between N_1 and N_4); and

L_2 = distance between N_3 and N_4 (that was the same as between N_1 and N_2).

The rotations of the top block during the test are presented in Figure 4.20. Since the block rotation around the global Y axis was controlled by two vertical actuators together with the spreader I-beam, the maximum rotation was limited to 0.0006 radian (0.03°) as shown in Figure 4.20(b). Conversely, the rotation of the top block around the global X axis was not controlled, resulting in relatively larger rotations which did not exceed 0.0032 radian (0.18°). In both cases, the rotations were well below the practical rotation thresholds set by any test setup of the size considered herein.

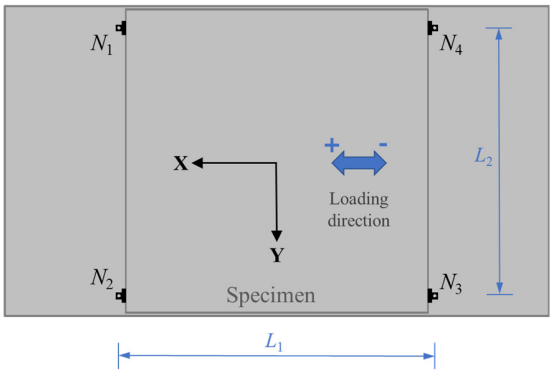

Figure 4.19 Geometry of the top block for performing the rotation calculations.

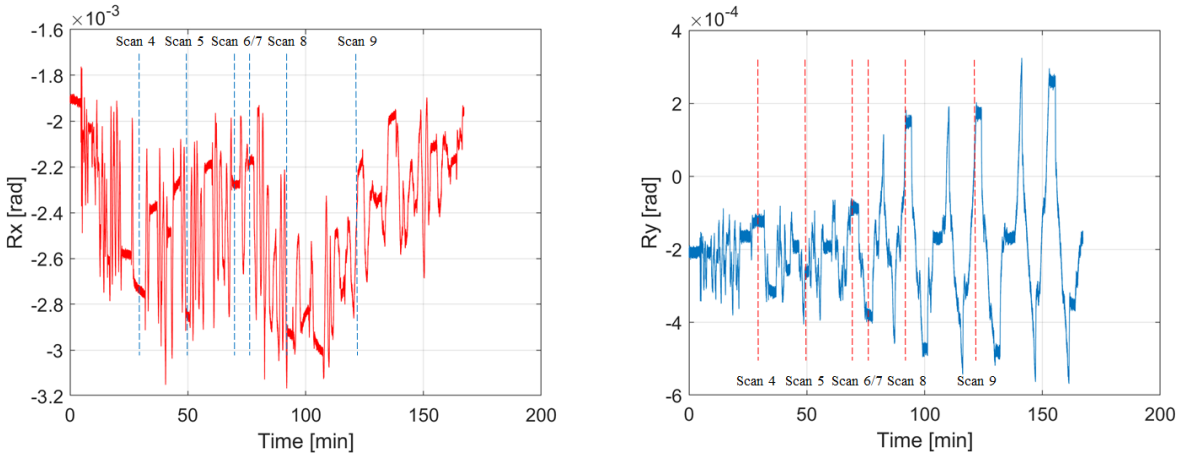

(a) Rotation around X axis **(b) Rotation around Y axis**

Figure 4.20 Top block's rotation time history plots.

The rotation measurements of the block from the conventional instrumentations are compared against the laser scan results in Figure 4.21. Both plots clearly demonstrate a very close match between the conventional measurements and those obtained from the laser scans by estimating the location of the HDLTs in space.

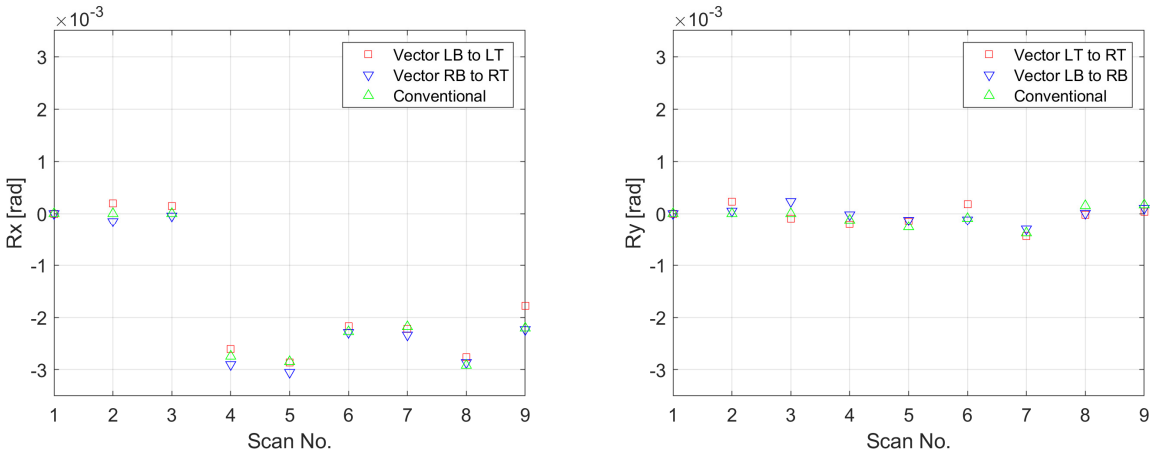

(a) Rotation around X axis **(b) Rotation around Y axis**

Figure 4.21 Rotation comparison of the top block (L: Left, R: Right, B: Bottom, T: Top).

Summary of Errors

The results above are summarized in Table 4.5 and Table 4.6, with the error being the difference between the average value of the laser scan measurements and the conventional measurements. From the tables, it can be clearly seen that the error for the displacement measurements is within 1.3 mm while for rotation measurements is less than 9.0%. The relative error for the rotation around the Y axis is not shown here because the rotation around the Y axis was so small (as discussed above) that the measurement itself is fluctuating around zero, leading to difficulties in the relative error quantification.

Table 4.5 Errors in the displacement measurements.

Scan #	Lateral Displacement [mm]			Vertical Displacement [mm]		
	laser scan average	conventional	error	laser scan average	conventional	error
1	0.000	0.000	0.000	0.000	0.000	0.000
2	-0.698	0.000	-0.698	0.015	0.000	0.015
3	-0.733	0.000	-0.733	-0.052	0.000	-0.052
4	23.254	23.647	-0.393	-0.852	-0.906	0.054
5	-35.608	-34.315	-1.293	-1.052	-1.163	0.111
6	48.909	48.057	0.852	-1.408	-1.481	0.073
7	-46.273	-47.142	0.869	-1.663	-1.869	0.206
8	70.272	70.663	-0.391	-1.308	-1.380	0.072
9	83.692	83.007	0.685	-1.970	-2.002	0.032

Table 4.6 Relative errors in the rotation measurements.

Scan #	Rotation about X [$\times 10^{-3}$ radian]		Error [%]
	laser scan average	conventional	
1	0.0	0.0	-
2	0.02	0.0	-
3	0.05	0.0	-
4	-2.75	-2.74	-0.38
5	-2.96	-2.85	-3.82
6	-2.23	-2.27	1.98
7	-2.28	-2.18	-4.57
8	-2.81	-2.92	3.63
9	-2.01	-2.21	8.97

4.2.2.3 Force-Displacement Relationship

The obtained resultant forces and displacements in the global X direction (loading direction) were used to obtain the force-displacement relationship of the V-connector. The force-displacement plot for all the cyclic loading groups in the loading direction (F_x vs. U_x) is shown in Figure 4.22. The high initial stiffness can be clearly observed as the V-connector has to overcome the static friction force before it starts to move. The average friction force was around 16 kips for each cycle and had the tendency to increase as the number of cycles increased. This is mainly because: (1) The interface between the Teflon pad and the top steel plate tends to get rougher after many cycles due to the abrasion. This leads to a larger value of the friction coefficient μ and increases the friction force; and (2) The

rotation of the top block, even if it is small, changes the pressure distribution, which also affects the friction force.

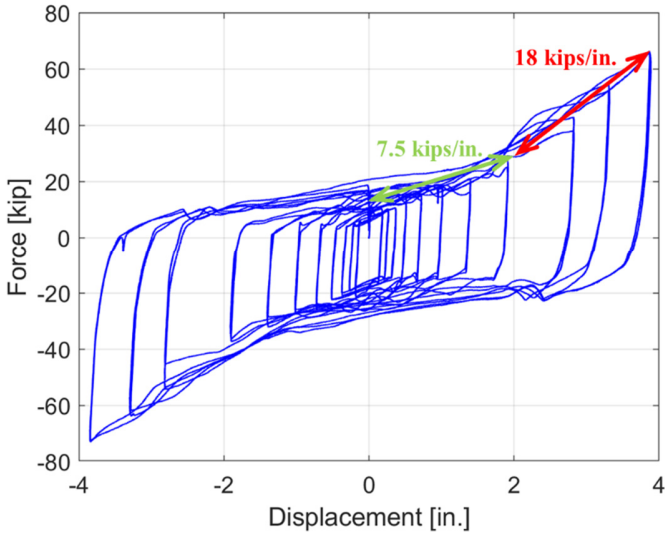

Figure 4.22 Force-displacement relationship for all cyclic loading groups in the loading direction.

Another observation is that the lateral stiffness of the V-pin was not constant as assumed in the idealized model. The initial stiffness was around 7.5 kips/in. at the beginning, which then increased to about 18 kips/in. when the lateral displacement was larger than 2 in. If the V-pin is treated as a cantilever column and the inner surface of the V-tube is treated as an additional lateral support when the pin touches the inner surface, this increase in the lateral stiffness can be explained by the reduction of the V-pin's free length. Besides, possible friction between the ball hinge and the hinge holder introduces a restriction at the top of the V-pin, leading to a sudden change of the stiffness.

4.2.2.4 Strain Behavior

Several strain gauges were installed on the longitudinal and transverse reinforcing bars of the top and bottom blocks to monitor the bar strains during the test. The longitudinal strain gauges were placed at six outermost bars that experienced the largest strain values on the east and west sides according to the adopted E-W loading direction. The transverse strain gauges were placed at two layers of the transverse bars to measure the shear strains, if any. The notation of loading direction is presented along with all the instrumented longitudinal and transverse bars of the two blocks in Figure 4.23 and Figure 4.24. The time histories of the measured strains in each block can be found in Figure 4.25 and Figure 4.26. These figures indicate that the reinforcing bars did not experience any significant strains during the test, because the strain gauges were only measuring noise. Meanwhile, the amplitude of the strains was much smaller than the yielding strain (assuming 2000 microstrain) of the reinforcement, meaning that the blocks remained perfectly elastic throughout the test.

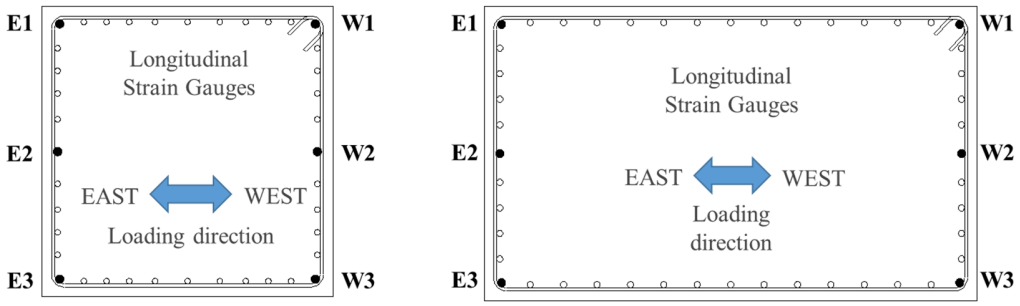

(a) Top block (b) Bottom block

Figure 4.23 Notation of loading direction and layout of instrumented longitudinal bars.

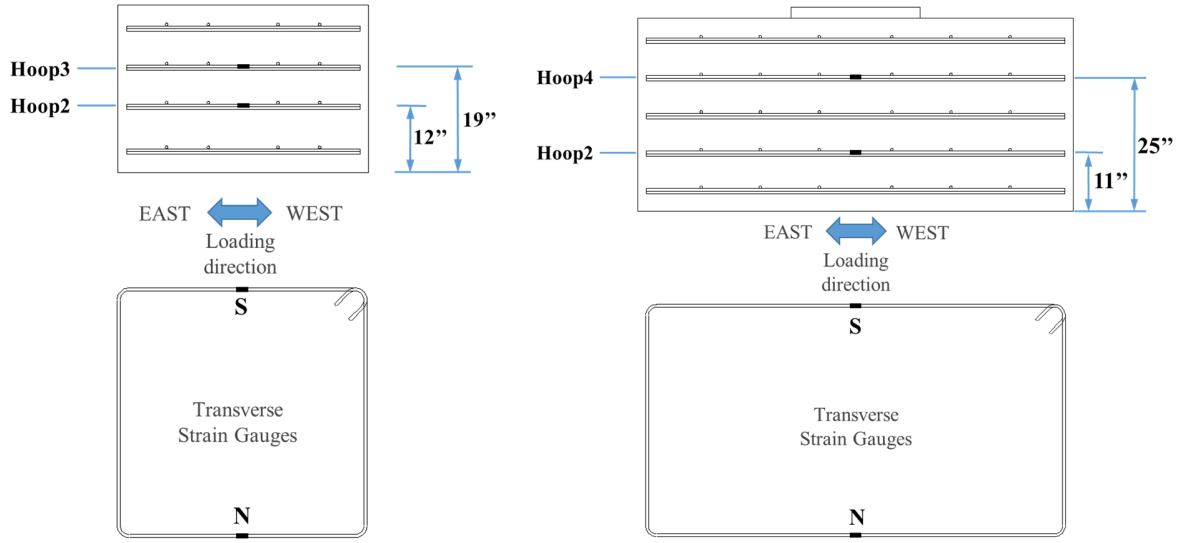

(a) Top block (b) Bottom block

Figure 4.24 Notation of loading direction and layout of instrumented transverse bars.

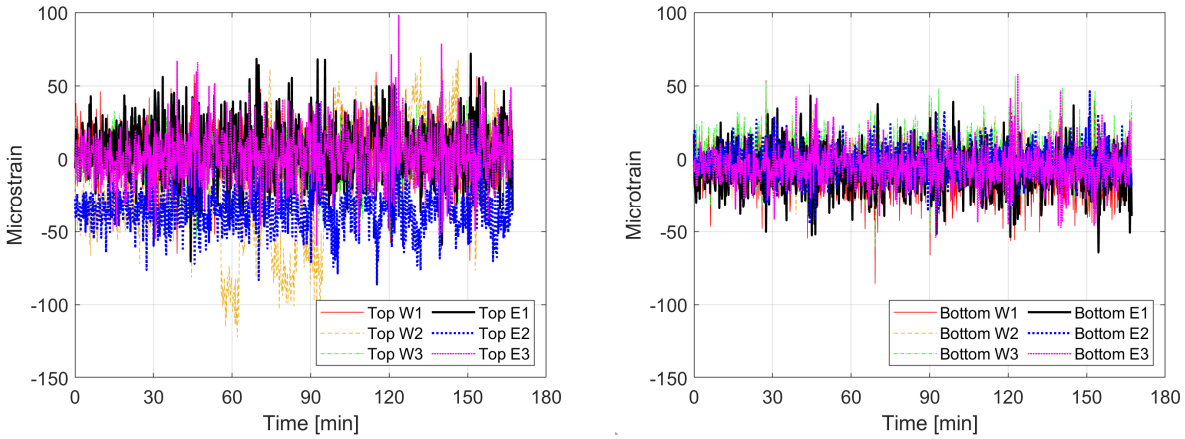

(a) Top block (b) Bottom block

Figure 4.25 Time histories of the strains in longitudinal reinforcing bars for all loading cycles.

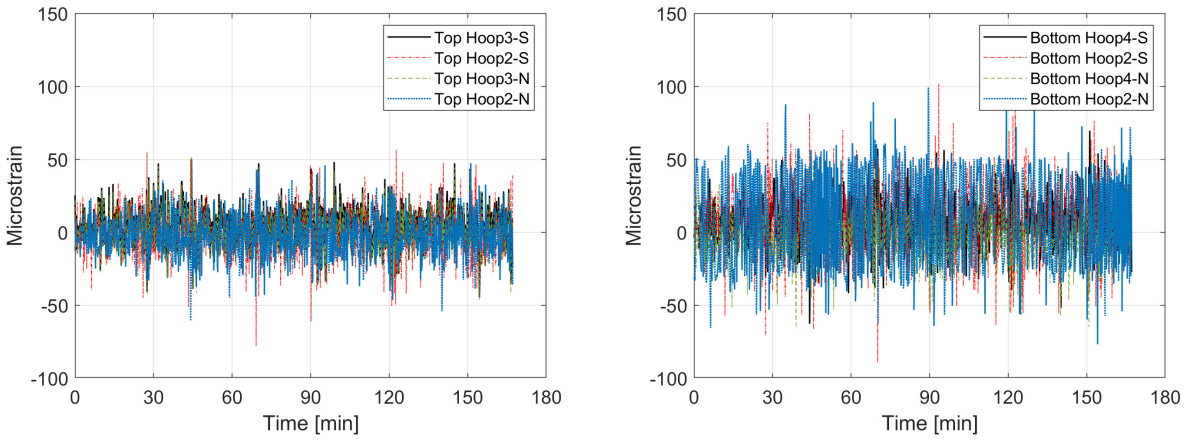

(a) Top block **(b) Bottom block**

Figure 4.26 Time histories of the strains in transverse reinforcing bars for all loading cycles.

4.3 MODEL CALIBRATION

It is obvious that the idealized hysteretic response of the V-connector failed to capture the fluctuation in the friction force as well as the observed stiffness increase during the quasi-static cyclic test. Therefore, the adopted model for pre-test analysis needs to be calibrated to better represent the actual behavior of the V-connector. Two different models, each with their own advantages and disadvantages, are presented in the following sections. The V-connector was again modeled using a translational zero-length spring element in OpenSEES, whose force-displacement relationship is characterized by different materials. Displacement histories measured directly from the cyclic test were applied to the zero-length spring, and the resisting forces were calculated accordingly. The measured and the calculated force-displacement relationships were then compared to check the validity of the selected model.

4.3.1 Hysteretic Material Model

In the first proposed model, the hysteretic material in OpenSEES (McKenna et al., 2000) was considered to represent the hysteretic behavior of the V-connector. The points on the envelope were picked from the hysteresis curve of the quasi-static test, while the remaining material parameters were selected to have the best match between the model and the test results. Figure 4.27 gives a schematic representation of the hysteretic material and the parameters that need to be determined. This type of material can be used to construct a uniaxial bilinear hysteretic material object with pinching of force and deformation, damage due to ductility and energy dissipation, and degraded unloading stiffness based on ductility. Besides the six points that describe the envelope of the hysteresis loop, there are 5 other parameters controlling the shape of the hysteresis loop. The parameters *$pinchX* and *$pinchY* are the pinching factors for deformation and force during reloading. These two parameters describe the modified slope in the X and Y axes of the plot. The two strength-reducing damage parameters, *$damage1* and *$damage2*, are respectively ductility and energy dependent. These two parameters are determined according to the strain level and energy dissipation by inelastic strain. Generally, a larger strain level and more energy dissipation

give larger values of these parameters. The parameter *$beta* is the power used to determine the degraded unloading stiffness, which is zero here since there was no observed stiffness degradation during unloading.

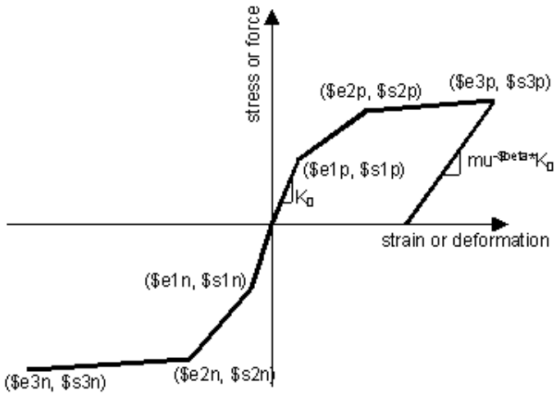

Figure 4.27 Hysteretic material in OpenSEES.

The plot comparing the force-displacement relationships is shown in Figure 4.28. It can be observed that the hysteretic material model captures the global response of the V-connector very well. It shows excellent match in terms of the friction and the unloading behavior. However, the reloading process is not following the hardening path until it approaches the yield surface of the previous smaller cycles. As a result, the pinching effect in the middle part of the hysteretic loop is missing and the model overestimates the energy dissipation when subjected to large displacements.

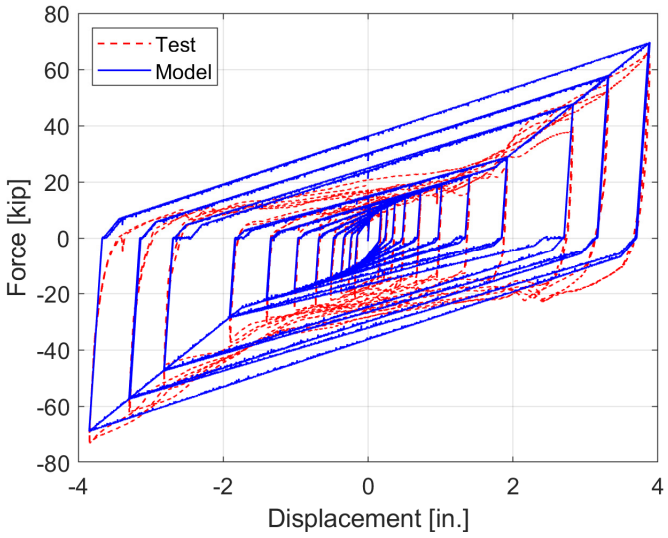

Figure 4.28 Comparison of hysteresis curves from the test and the hysteretic material modeling approach.

4.3.2 Parallel Material Model

In this model, the bilinear steel01 material with isotropic hardening was used in parallel with the EPP gap material in OpenSEES (McKenna et al., 2000) to simulate the hysteretic behavior of the V-connector (see Figure 4.29). The parameters of steel01 bilinear material were selected to represent the friction and the initial stiffness of the system after overcoming the static friction force, which are around 16 kips and 7.5 kips/in., respectively, as previously mentioned. The isotropic hardening parameters were selected to achieve the best match between the model and the test results. The parameters of the EPP gap material need to reflect the stiffness increase of the V-pin when subjected to large displacements. Specifically, the positive/negative gap value was chosen to be 2 in. to capture this change.

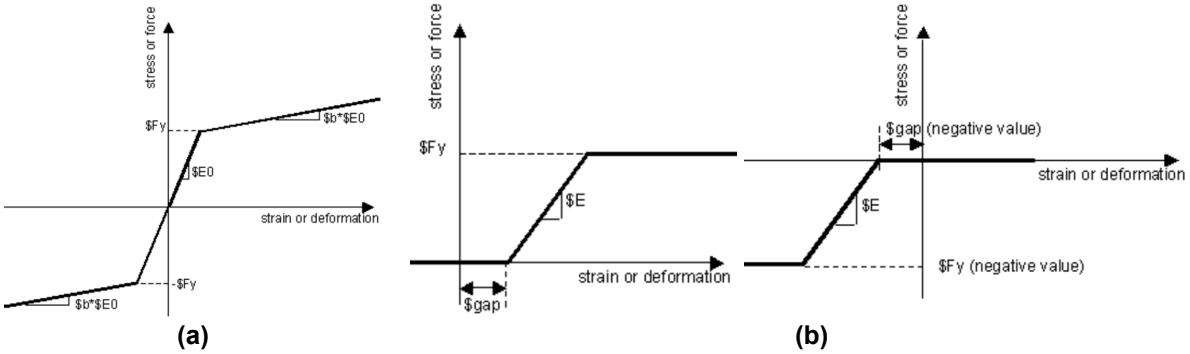

Figure 4.29 Components of the parallel material: (a) steel01 material with isotropic hardening; and (b) elastic-perfectly plastic gap material.

The comparison of the force-displacement relationships between the parallel spring model and the experimental results is given in Figure 4.30. The bilinear parallel model is another a good representation of the V-connector's hysteretic response. It shows excellent match in terms of the friction and the hardening behavior of the stiffness. It is also capable of capturing the pinching effect in the middle of the hysteresis loop. However, this hysteretic curve misses the soft corner during the unloading phase.

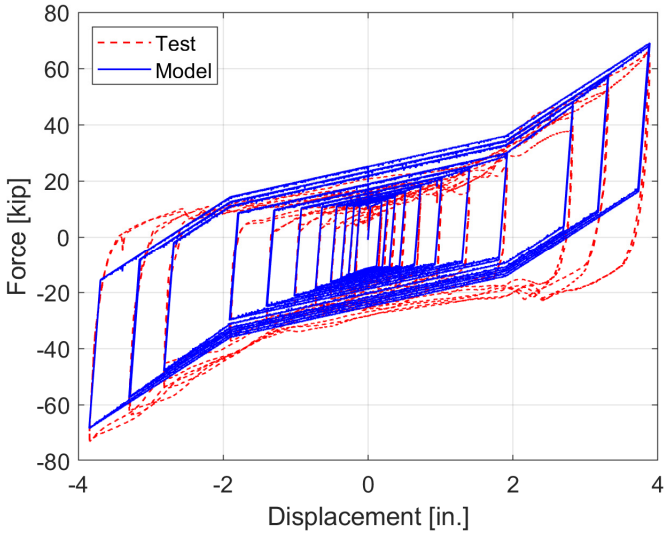

Figure 4.30 Comparison of hysteresis curves from the test and the parallel material modeling approach.

5 V-connector Phase II: Hybrid Simulation

The experimental program conducted in the V-connector study mainly comprised of the quasi-static cyclic test and the HS runs. The behavior of the V-connector under cyclic loading has already been discuss in Chapter 4. Discussions of the HS runs are the focus of this chapter.

This chapter starts with a description of the utilized HSS. Several detailed aspects of the conducted HS, including substructuring, integration methods and the necessary geometric transformation, are explained. This is followed by a complete discussion of the HS trial test for validating the whole system, and the real HS test conducted on the same V-connector set with test results presented. Before testing, the same prototype bridge with a calibrated V-connector model as described at the end of Chapter 4 was reanalyzed to predict the behavior of the V-connector and to choose the ground motion inputs for both the trial and the real HS runs. This chapter concludes with a brief discussion on the effectiveness of the V-connector by comparing different behaviors of the bridge column with and without utilizing the V-connector.

5.1 HYBRID SIMULATION DETAILS

5.1.1 Hybrid Simulation System

As described in Chapter 2, a typical HSS is made up of four parts: a discrete finite element model of the structure, a transfer system consisting of controllers and actuators, a physical specimen being tested with proper boundary conditions, and a DAQ system. A vital feature of the HSS is to connect the above four components together to achieve effective two-way communication for sending the displacement input and receiving the force feedback.

Figure 5.1 illustrates the main components of the considered HSS to conduct the V-connector's HS test at the Structures Laboratory of the University of California, Berkeley. It includes: (a) the computational platform OpenSEES (McKenna et al., 2000) which conducts the state determination of the analytical substructures and performs the numerical integration; (b) the middleware OpenFRESCO (Schellenberg et al., 2008), which provides the communication between OpenSEES and the PI660HybridSim; (c) PI660HybridSim, a new interface software developed within the Pacific Instruments (PI) DAQ system that communicates with OpenFRESCO through a TCP/IP connection; (d) the digital signal processing (DSP) card which establishes the communication between the PI660HybridSim and the controllers; and (e) the MTS 407 controllers that controls the hydraulic actuators. It is noted that the *GenericTCP* experimental control was used in OpenFRESCO to establish the PI660HybridSim-OpenFRESCO communication. It is also

noted that the employed HSS is capable of communicating with computational platforms other than OpenSEES, which was utilized herein for its relevance to the studied bridge system and its modeling from (Kavianijopari, 2011).

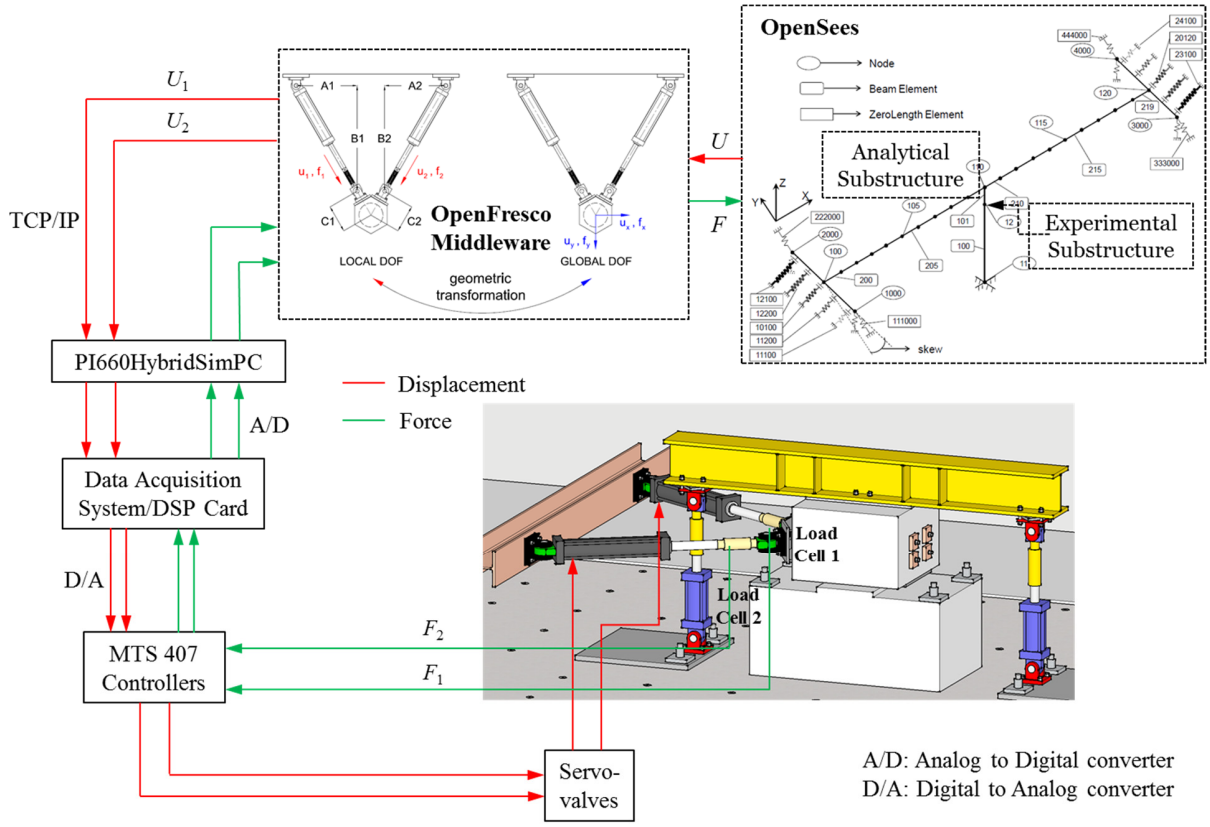

Figure 5.1 Employed hybrid simulation system in the V-connector study.

5.1.2 Substructuring

The hybrid nature of the tested model is attributed to the fact that part of the model is a computational analytical model, whereas the rest of the model is a physical experimental substructure. Analytical substructures are generally those that can be modeled with confidence, while experimental substructures are those that are difficult to model analytically. For the HS test considered herein, the same 1/3-scale V-connector used in the quasi-static cyclic test was treated as the experimental substructure, while the remainder of the bridge model based on the study by (Kavianijopari, 2011) was simulated as the analytical substructure (see Figure 5.2). OpenSEES (McKenna et al., 2000), previously used in the nonlinear dynamic analysis, was used again in the HS test as the finite element software to analyze the bridge structure and solve the equations of motion for the displacement at each time step. OpenFRESCO (Schellenberg et al., 2008) was used as a middleware to connect the finite element software with the experimental substructure in the laboratory. Accordingly, a single OpenSEES/OpenFRESCO input file prepared by the Tool Command Language (TCL) was used to define the computational model and the communication settings. The V-connector was represented in OpenSEES using the *twoNodeLink* experimental element type.

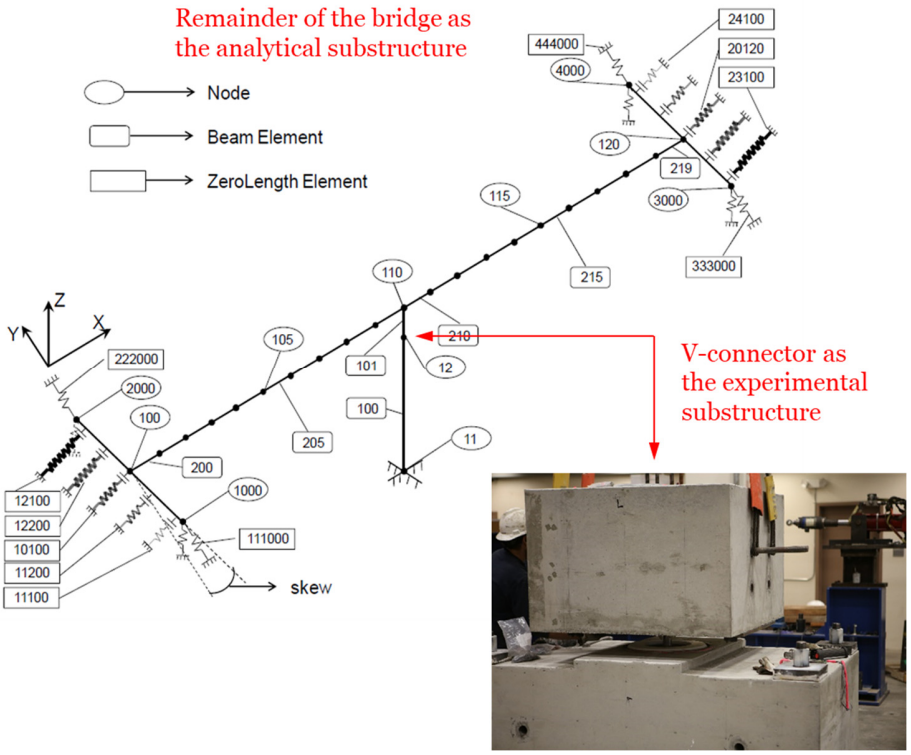

Figure 5.2 Experimental and analytical substructures.

5.1.3 Numerical Integration

In HS, the governing equations of motion are solved using numerical integration methods. The presence of the experimental substructures restricts the use of standard numerical integration methods (e.g., Implicit Newmark integration) in HS, because unlike analytical substructures in the computer, it is not suitable to perform certain actions such as loading and unloading introduced by iterations on the physically tested substructures as explained in Chapter 2.

The Alpha-OS is a predictor-corrector integration method that is commonly used in HS (Combescure and Pegon, 1997; Elkhoraibi and Mosalam, 2007; Nakashima et al., 1990; Schellenberg et al., 2009). Detailed steps of the Alpha-OS integration algorithm are provided in Figure 5.3. This algorithm was chosen for the study because of its HS-compatible features as listed below:

- It is an explicit method that consists of a prediction and a correction. Therefore, as opposed to an implicit method, it does not require any iterations. Because iterations are not suitable in HS due to the presence of the experimental substructure, the noniterative nature of this algorithm makes it appropriate for HS;
- It does not require the use of tangent stiffness matrix as shown in Figure 5.3. This feature is also appealing for HS, because it is difficult, if not impossible, to obtain the tangent stiffness matrix of an experimental substructure that consists of multiple DOFs; and

- It is unconditionally stable as long as the tangent stiffness is smaller than the initial stiffness (Combescure and Pegon, 1997).

1. Determine the initial values of response variables: $\boldsymbol{u}_1 = 0$, $\dot{\boldsymbol{u}}_1 = 0$, $\ddot{\boldsymbol{u}}_1 = 0$, $\tilde{\boldsymbol{u}}_1 = 0$;
2. Calculate the effective mass: $\mathbf{m}_{eff} = \mathbf{m} + (1-\alpha)\Delta t\gamma\mathbf{c} + (\Delta t)^2\beta(1-\alpha)\mathbf{k}_I$;

   Δt: integration time step;

   α, γ, β: integration parameters; and

   $\mathbf{k}_I$: initial stiffness matrix.
3. Compute the predicted displacements at the second step: $\tilde{\boldsymbol{u}}_2 = \boldsymbol{u}_1 + \Delta t\dot{\boldsymbol{u}}_1 + (\Delta t)^2[(1-2\beta)\ddot{\boldsymbol{u}}_1]/2$;
4. For each time step i: $1 \le i \le N-1$; N: total number of steps

   a1. Compute the resisting forces from the analytical substructure corresponding to the predicted displacements using methods of state determination (Spacone et al., 1996);

   a2. Apply the corresponding predicted displacement to the experimental substructure and measure the corresponding resisting forces;

   a3. Determine the resisting force vector $\boldsymbol{p}_r(\tilde{\boldsymbol{u}}_{i+1})$ by combining the contributions from the analytical and experimental substructures;

   b. Compute the effective force:
   $\boldsymbol{p}_{eff} = (1-\alpha)\boldsymbol{p}_{i+1} + \alpha\boldsymbol{p}_i - (1-\alpha)\boldsymbol{p}_r(\tilde{\boldsymbol{u}}_{i+1}) - \alpha\boldsymbol{p}_r(\tilde{\boldsymbol{u}}_i) - \left[(1-\alpha)\mathbf{c}\Delta t(1-\gamma) + \alpha(\Delta t)^2\beta\mathbf{k}_I\right]\dot{\boldsymbol{u}}_i - \mathbf{c}\dot{\boldsymbol{u}}_i$;

   c. Compute the acceleration by solving the linear system of equations: $\mathbf{m}_{eff}\ddot{\boldsymbol{u}}_{i+1} = \boldsymbol{p}_{eff}$;

   d. Compute the corrected displacements: $\boldsymbol{u}_{i+1} = \tilde{\boldsymbol{u}}_{i+1} + (\Delta t)^2\beta\ddot{\boldsymbol{u}}_{i+1}$;

   e. Compute the velocities: $\dot{\boldsymbol{u}}_{i+1} = \dot{\boldsymbol{u}}_i + \Delta t[(1-\gamma)\ddot{\boldsymbol{u}}_i + \gamma\ddot{\boldsymbol{u}}_{i+1}]$;

   f. Compute the next predicted displacements: $\tilde{\boldsymbol{u}}_{i+2} = \boldsymbol{u}_{i+1} + \Delta t\dot{\boldsymbol{u}}_{i+1} + (\Delta t)^2[(1-2\beta)\ddot{\boldsymbol{u}}_{i+1}]/2$;

   g. Increment i and go to step a1.

Figure 5.3 Alpha Operator-Splitting integration algorithm for the conducted HS test of the V-connector.

5.1.4 Test Setup and Geometric Transformation

The test setup for the HS is exactly the same as the one used in the quasi-static cyclic test (see Chapter 3 for more details). The two horizontal actuators used for applying the lateral load were arranged in a planer triangular configuration. The *ExperimentalSetup* object named *TriangularActuators*, previously developed by Moustafa (2015), was used in OpenFRESCO (Schellenberg et al., 2008) to perform the geometric transformation between the two model (global) DOFs, designated as *x* and *y*, and the two actuator (local) DOFs, designated as 1 and 2, as shown in Figure 5.4. The TCL syntax input for the experimental setup is as follows:

expSetup TriangularActuators *$tag* -control *$ExpControltag $B1 $B2 $A1 $A2 $C1 $C2*

where *$ExpControltag* is the defined tag for the used experimental control object, which is the *GenericTCP* in this case, and *$B1*, *$B2*, *$A1*, *$A2*, *$C1*, and *$C2* are geometric input parameters that describe the relative locations of the two actuators, as identified in Figure 5.4. Further verification of the geometric transformation achieved through the experimental setup element was conducted as discussed in section 5.2.1.

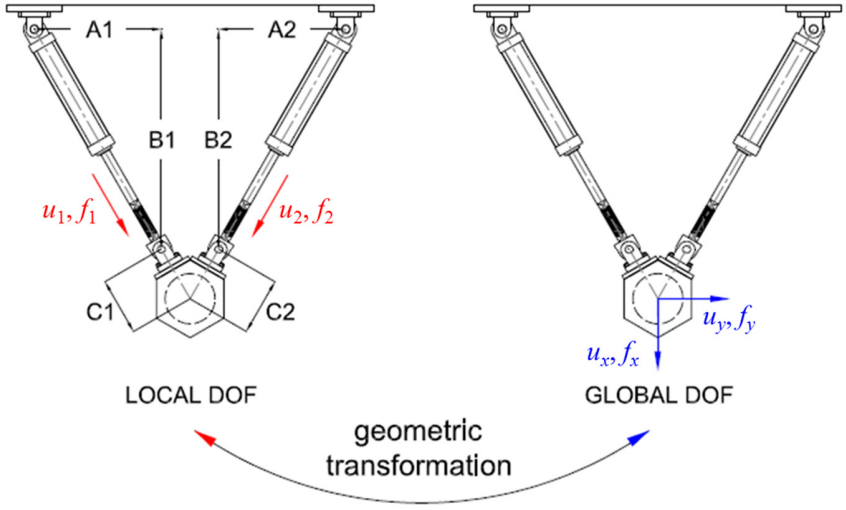

Figure 5.4 Geometric transformation of input displacements and measured forces between the global and local DOFs (Moustafa, 2015).

For each integration time step, the dynamics of the discrete model of the bridge structure was used to compute the displacement that is to be imposed to the test specimen. To obtain the command displacement for each actuator, the scaled value of the computed displacement first underwent geometric transformation from the global coordinate system *x*-*y* to the local coordinate system 1-2 (see Figure 5.4). The scale factor for the lateral displacement was $1/S_L = 1/3$. The transformed displacements in each actuator's local DOF were delivered to the corresponding controller for execution. After applying the scaled computed displacement to the specimen, the corresponding reactions (resisting forces) were measured using the load cell in each actuator's local DOF and passed to the DAQ system. The measured forces underwent a set of geometric transformations and were then scaled up by a factor of $S_L^2 = 9$ before they were passed to the time-stepping integration algorithm to advance the solution to the next analysis step.

5.1.5 Simulation Errors

The HS test was conducted slower than real time as the force-displacement relationship of the V-connector was assumed not to be rate dependent. Computed displacement was applied with a constant velocity of 0.01 in./s. As this rate was quite slow, reasonable actuator tracking was achievable with proper tuning of the actuators (see section 5.2.2 for details).

5.1.6 Loading

During the HS test, the bridge model was subjected to two sequences of loading in the following order: (1) gravity load; and (2) recorded ground motions (one horizontal component). As stated before, a gravity load of 200 kips was used and kept constant throughout both the trial and the real HS test. For the ground motion selection, response spectrum analysis of the prototype bridge with an updated V-connector model (described in section 4.3) was conducted, using the eight ground motions from the pre-test analysis (see Table 4.2). Note that only the horizontal component that corresponds to the longitudinal direction of the prototype bridge was considered because of the large demand in that direction (Figure 4.10). Also note that the modeling parameters based on the test results from Chapter 4 need to be scaled up by a factor of 3 in the updated V-connector modeling of the prototype bridge, since the V-connector being tested is a reduced-scale one. From the eight candidate motions, three were selected to represent the service level (SLE), design basis (DBE) and maximum considered (MCE) earthquakes. Figure 5.5 shows the response spectra of the eight ground motions with their original scale factors. Two vertical lines in the plot represent the fundamental period of the bridge with two different V-connector models. The results are summarized in Table 5.1.

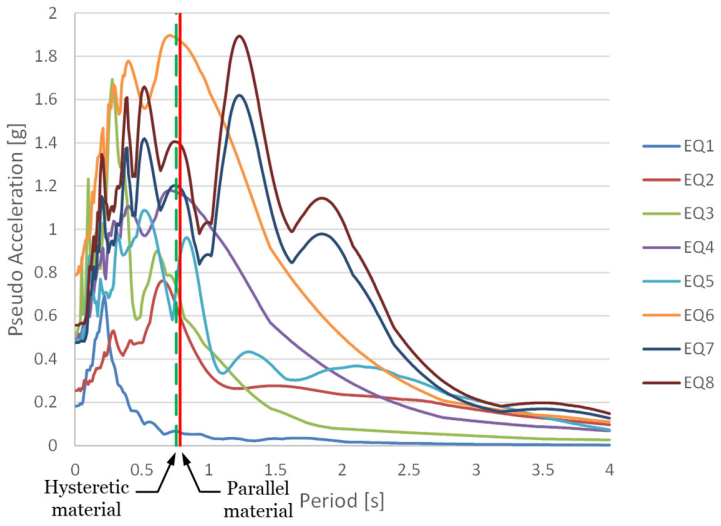

Figure 5.5 Response spectra of the ground motions used in the pre-test analysis.

Table 5.1 Summary of the response spectrum analysis results of the prototype bridge.

V-connector Model	Period [s]	Spectral Coordinate [g]							
		EQ1	EQ2	**EQ3**	**EQ4**	EQ5	**EQ6**	EQ7	EQ8
Hysteretic Material	0.758	0.066	0.646	**0.737**	**1.172**	0.738	**1.884**	1.202	1.404
Parallel Material	0.787	0.060	0.597	**0.673**	**1.165**	0.875	**1.872**	1.192	1.393

Based on the response spectrum analysis results, EQ3, EQ4 and EQ6 were selected, representing the small, medium and large earthquake scenarios. To predict the behavior of the 1/3-scale V-connector during the HS test and make sure the displacement applied to the V-connector is within the 4 in. limit set by the V-tube geometry, nonlinear time history analysis was conducted.

The selected ground motions were applied in a concatenated manner with increasing magnitude and the deformation amplitudes of two different V-connector modeling were checked. It was observed that by reducing the scale factor of EQ6 from 0.9 to 0.75, the deformation amplitudes of the full-scale V-connector using the hysteretic material and parallel material models were 11.5 in. and 11.2 in., respectively (see Figure 5.6). Therefore, the displacement that needs to be applied during the HS was expected to be in the range of 3.7~3.8 in., with a small safety factor being considered. The information of the selected ground motion records for the HS test can be found in Table 5.2.

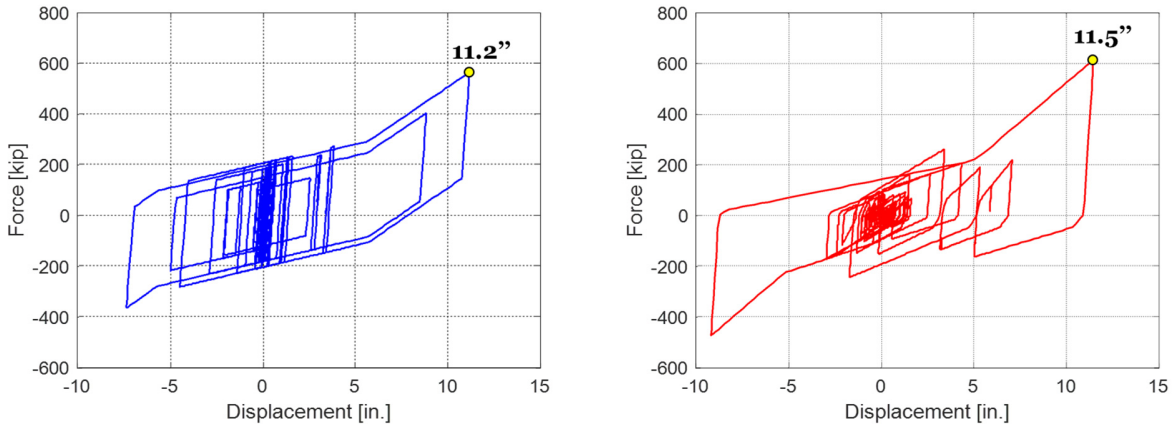

(a) Parallel material (b) Hysteretic material

Figure 5.6 Deformation amplitudes of the full-scale V-connector using different models.

Table 5.2 Ground motions used in the hybrid simulation test of the V-connector.

EQ #	Event	Date	Station	Scale Factor
EQ3	Morgan Hill	1984/04/24	Coyote Lake 4 Dam (SW abut.)	0.70
EQ4	Northridge	1994/01/17	Rinaldi Receiving Station	0.56
EQ6	Northridge	1994/01/17	Rinaldi Receiving Station	0.75

5.2 HYBRID SIMULATION TRIAL TEST

To confirm the performance of the whole HSS that would be utilized for the real HS test, a low-level HS trial test making use of the selected horizontal component of EQ4 was conducted. The scale factor was reduced to 0.275 based on the analysis results to limit the applied displacement to be around 1.5 in.

5.2.1 Geometric Transformation and Scaling Check

The first verification was the back and forth communication between the physical and computational components of the HSS. Since the V-connector being tested is 1/3-scale, it was necessary to ensure that the computed input displacements passed to the actuators and the resulting forces that need to be sent back to the computational platform as measured by the load cells of the

actuators were respectively scaled down or up properly. Specifically, based on similitude relationships, the ratio between OpenSEES (McKenna et al., 2000) computed displacement and the actual applied displacement (after geometric transformation) should be 3, while the ratio between the resisting forces that passed on to the computational platform and the resisting forces measured by the actuator load cells (after geometric transformation) should be 9.

Before performing any complicated verification, a very intuitive check for the geometric transformation is that if a global longitudinal direction only motion (u_x in Figure 5.4) is required, the two actuators should have identical input along the local DOFs. This anticipated geometric transformation was verified as shown in Figure 5.7.

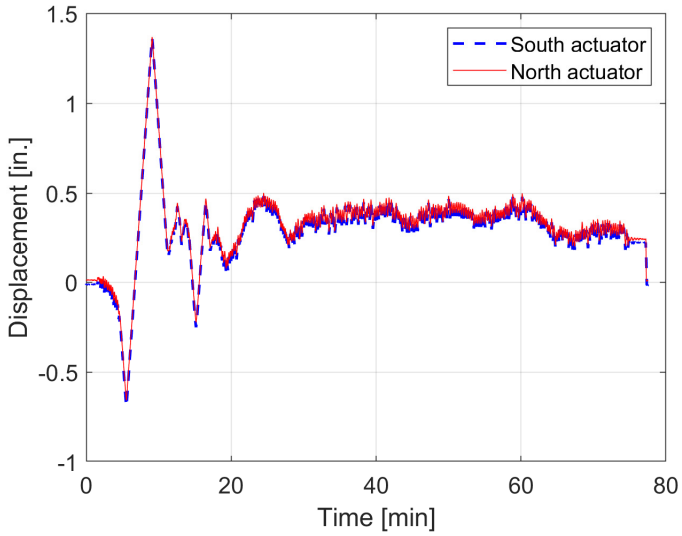

Figure 5.7 Actuator displacement history plots for the longitudinal direction only ground motion test.

Figure 5.8(a) compares the computed displacement from OpenSEES and the transformed feedback displacement of the actuators multiplied by $S_L = 3$ in the loading direction. The feedback displacements were provided by the position Temposonic transducers of the actuators. Figure 5.8(b) compares the V-connector forces from the OpenSEES recorder and the transformed forces of the actuators multiplied by ${S_L}^2 = 9$ in the loading direction. In both plots, the curves do not coincide because of the differences in the time scale. The timeline for the actuator feedbacks is based on the testing time (or real time), while the timeline for OpenSEES is obtained by stretching the ground motion duration in the real world for a more intuitive comparison. However, the trend and the peaks in both plots showed perfect match, which verifies the geometric transformation and the scaling between the physical and computational components of the HSS. It should be noted that the noisy part in the force plot represents the high frequency component caused by the friction, because of the small displacement oscillation towards the end of the earthquake.

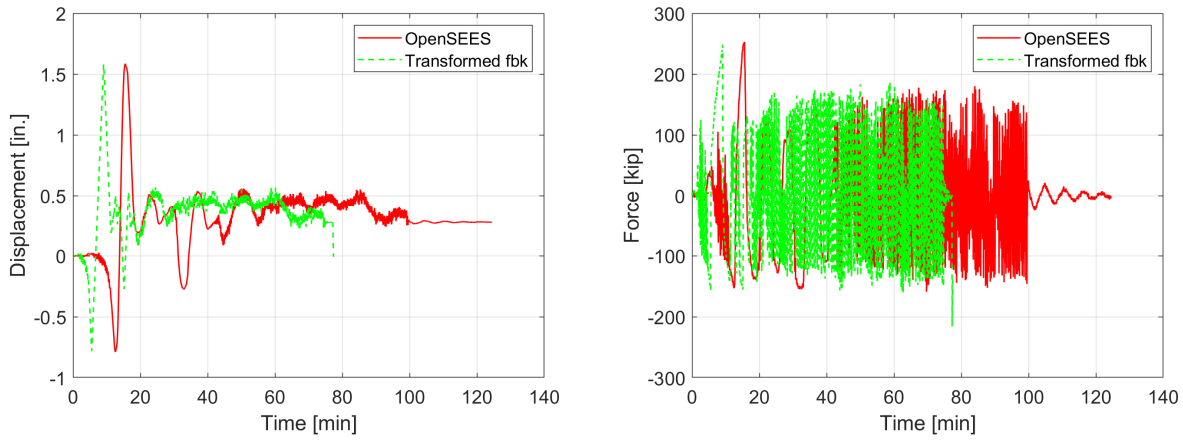

(a) Displacement check **(b) Force check**

Figure 5.8 Geometric transformation and scaling check of the hybrid simulation system.

5.2.2 Control Quality Check

The second aspect of the verification was the control quality of the actuators. For good control quality, the command displacement from the controller and the feedback displacement measured by the position transducer should be as close as possible with minimum time delay. Figure 5.9 shows the command and feedback displacements in the loading direction after geometric transformation, representing the effect of the two horizontal actuators working together. Figure 5.10 shows the separate check for each horizontal actuator. The perfect match shown in these plots proves that the quality of the used controllers is reliable.

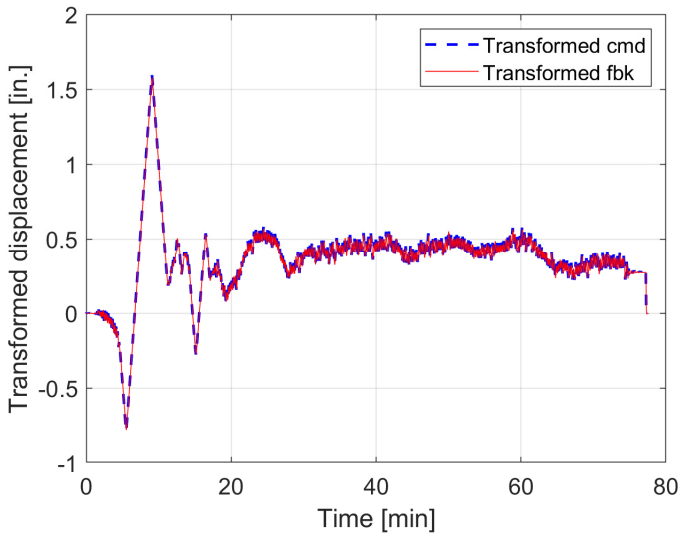

Figure 5.9 Transformed command (cmd) vs. feedback (fbk) displacements of the actuators in the loading direction.

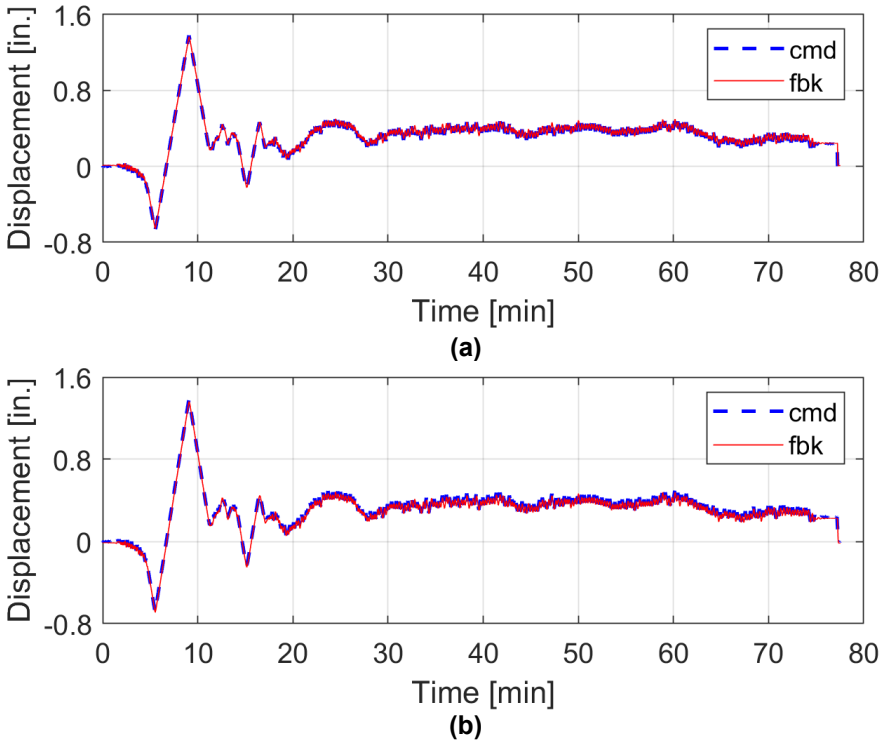

Figure 5.10 **Command (cmd) vs. feedback (fbk) displacement for (a) north actuator; and (b) south actuator.**

5.3 HYBRID SIMULATION TEST

During the real HS test, the V-connector was subjected to a constant gravity load of 200 kips, followed by the three ground motions running back to back with increasing magnitude. Same as the cyclic test, the loading towards east is designated to be the positive global X direction, while the loading towards west is negative. The loading direction defined this way is consistent with the longitudinal direction of the prototype bridge. In addition, the same set of instrumentation previously used in the cyclic test was also used for the HS test, except that no laser scan was performed. The test results are presented below.

5.3.1 Test Results

5.3.1.1 Displacement History

Similar to the quasi-static cyclic test, WPs were used to capture the global specimen displacements. Temposonic transducers were installed along the actuators axes to capture and control the actual movement for each actuator. The displacements of the actuators were geometrically transformed to the global directions and compared with the WP measurements, as shown in Figure 5.11. According to the observation made in the cyclic test, the transformed displacements based on Temposonic measurements were the most accurate. Moreover, the reliability of the geometric transformation was successfully verified in the HS trial test. Thus, the displacements of the V-

connector in the loading direction were deduced from the transformed Temposonic measurements. Figure 5.12 shows the time history plots of the measured displacements in the north and south actuators' local DOFs along with the resulting displacements in both global longitudinal (U_x) and transverse (U_y) directions. The fact that the two actuators moved together in the same pattern and that the corresponding U_y was almost zero when only U_x was applied proves the good control quality.

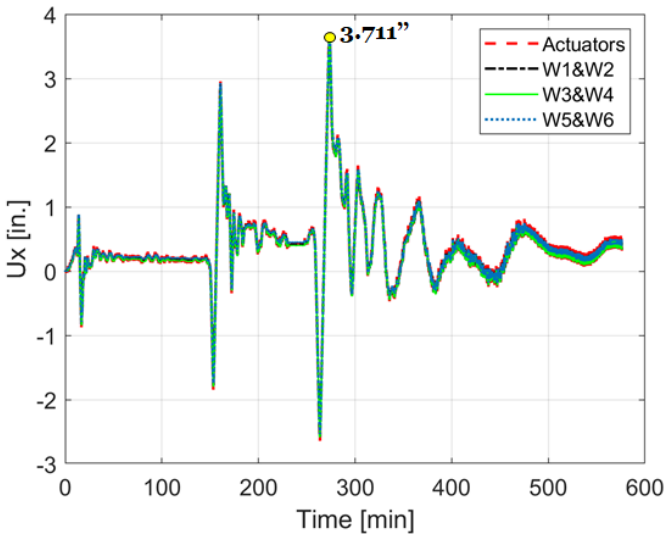

Figure 5.11 Lateral displacement time history plots computed from different measurements.

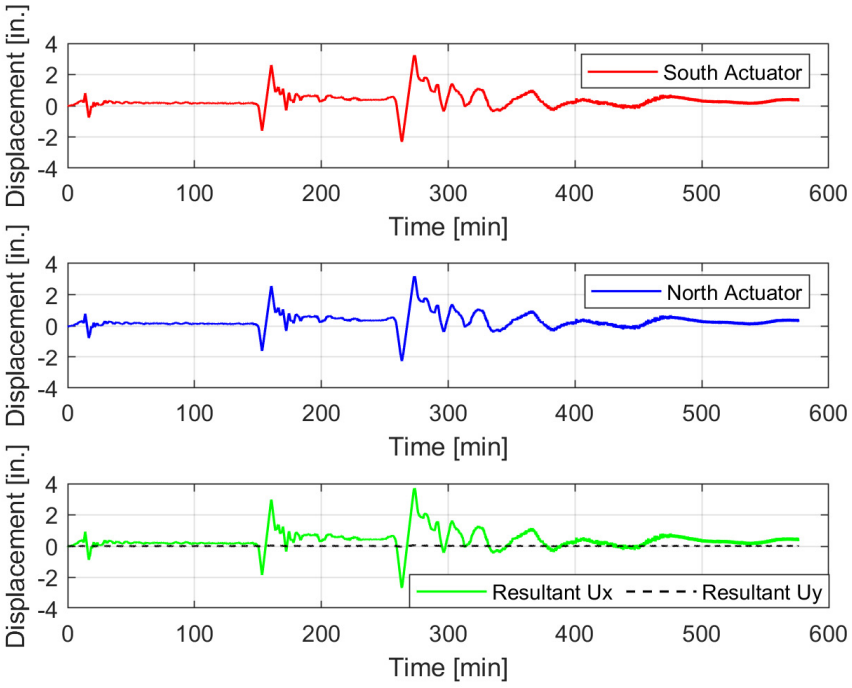

Figure 5.12 **Time history plots of both north and south actuators Temposonic measurements and the resultant displacements in the global longitudinal and transverse directions (U_x & U_y) for the HS test.**

One observation from the above two plots is that the maximum displacement value applied to the V-connector was 3.711 in., which falls into the predicted range of 3.7~3.8 in. when choosing the ground motion scale factors for the HS test. This justifies the usage of the calibrated V-connector models in performing the nonlinear time history analysis. Another important observation from the displacement time history plots is the residual displacement at the end of the earthquakes. The residual displacement was around 0.4 in. (about 11% of the maximum displacement), resulting in a residual displacement of 1.2 in. if a full-scale V-connector was used. This is most likely caused by the friction force that prevented the V-connector from going back to its starting position. In addition, the residual plastic deformation of the V-pin may have also added to the observed residual displacement. In terms of resiliency, this is acceptable. However, future works should be focused on how to improve the V-connector's design to further reduce the residual deformation.

In addition to the lateral displacements, the vertical movements and the rotations of the top block were also measured by using the short-range displacement transducers, similar to those in the cyclic test. It turned out that both the vertical movements and the rotations were negligible.

5.3.1.2 Force History

For displacement-controlled HS test, it is crucial to monitor the displacements because that is the only way to know what deformation the specimen has gone through during the test. However,

lateral forces are even more important to monitor because it is the force feedback that affects the next-step solution of the governing equations of motion, Equation (2.1), and in turn, the new displacement input. A constant vertical gravity load was applied by two vertical actuators and maintained throughout the tests under force control. The time history of the total gravity loading is shown in Figure 5.13, together with the forces measured from each vertical actuator. The 200 kips gravity load remained very stable, as can be seen from the plot.

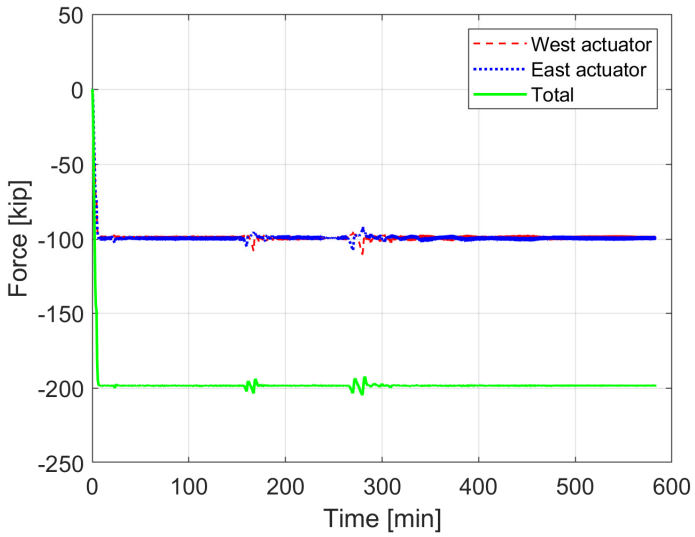

Figure 5.13 Time history plots of the applied gravity load during the HS test.

Similar to the displacement discussion, the horizontal forces measured in the local DOFs of the actuators through load cells were compared to the resulting force in the global longitudinal direction. Figure 5.14 shows the full histories of the north and south actuator forces along with longitudinal force resultant F_x. The high frequency component of the plotted forces caused by friction has already been filtered out. Again, the actuator forces have approximately similar values and direction, which should be expected because of the longitudinal-only loading.

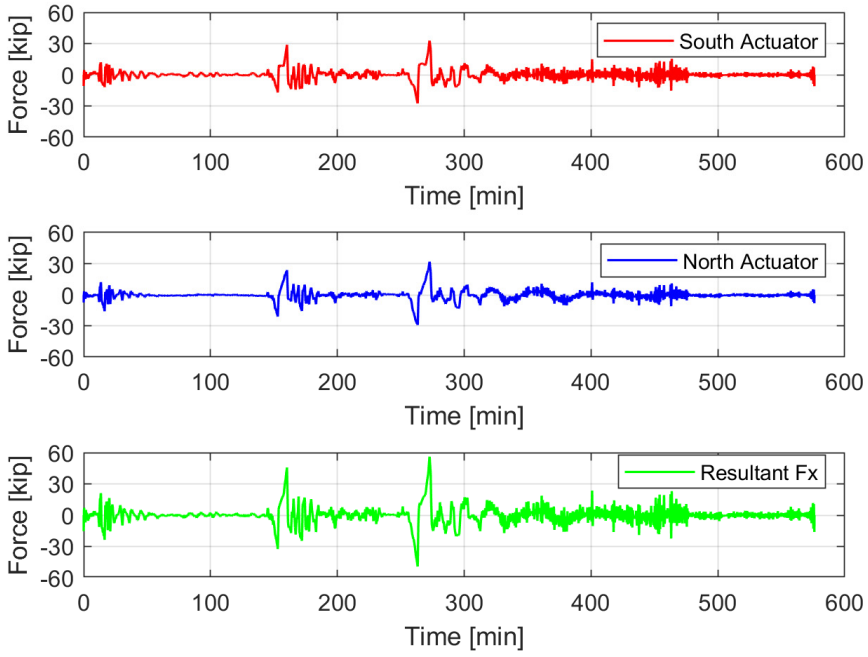

Figure 5.14 **Time history plots of both north and south actuators load cell measurements and the resultant forces in the global longitudinal direction (F_x) for the HS test.**

5.3.1.3 Force-Displacement Relationship

The relationship between the global feedback forces and the applied displacements in the loading direction from the HS test is shown in Figure 5.15(a). The congested part in the middle of the plot reflects the friction forces caused by the small amplitude of displacement oscillations. The curve obtained from the HS test was also plotted against that from the quasi-static cyclic test, see Figure 5.15(b). The good fit of the HS test curve inside the cyclic test curve indicates that there was no degradation in terms of force-displacement relationship during the realistic HS runs up to the MCE level and that the V-connector's behavior was consistent after undergoing large deformation amplitudes. This is a very important aspect in terms of resiliency because the replacement of the V-connector can be costly and time-consuming in practice.

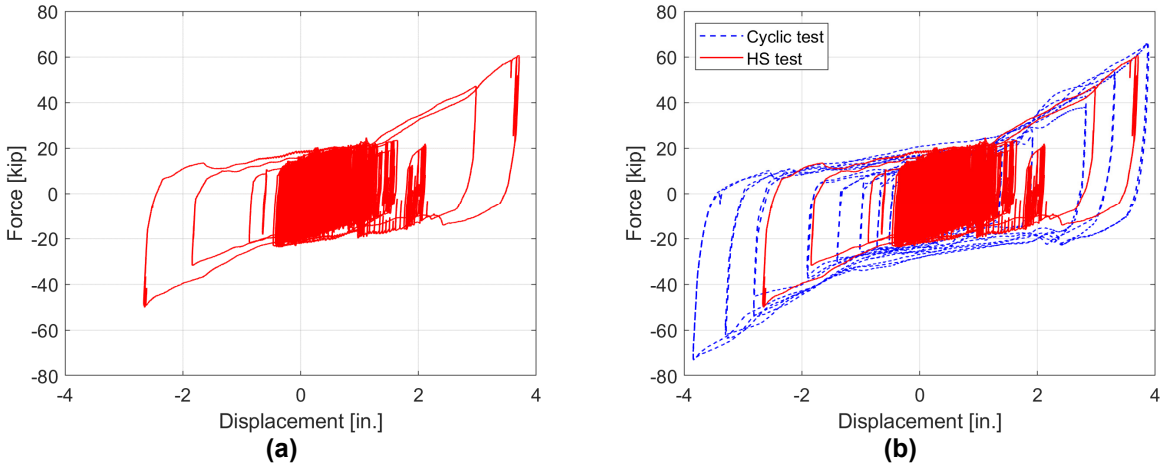

Figure 5.15 **(a) Force-displacement relationship obtained from the HS test; (b) comparison of force-displacement relationships from the HS and the quasi-static cyclic tests.**

5.3.1.4 Damage Inspection

The damage condition of the V-connector was assessed after the HS test. Figure 5.16 and Figure 5.17 show the damage conditions of the different components of the V-connector. It can be observed that the components of the V-connector went through different levels of damage during the tests.

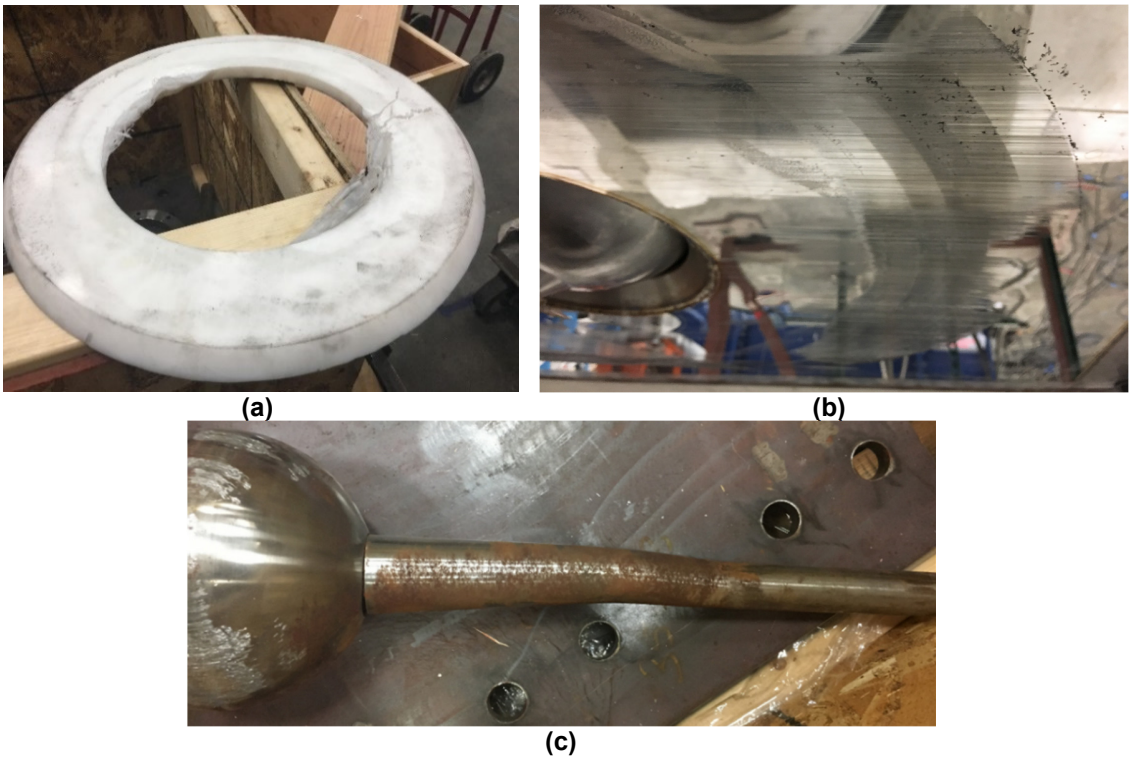

Figure 5.16 **Damage conditions of the different V-connector components: (a) Teflon washer; (b) bottom surface of the stainless steel plate; and (c) V-pin.**

Figure 5.17 **Damage conditions of the different V-connector components: (a) ball hinge; (b) hinge holder.**

Figure 5.16(a) and (b) show the abrasion damage caused by the friction between the stainless steel plate and the Teflon washer. This damage was expected because the friction is the main source of energy dissipation. Figure 5.16(c) shows the deformed shape of the V-pin. Some residual plastic deformations distributed along the rod can be clearly observed. Such deformed shape means that the response of the V-pin cannot be treated as elastic during the test, especially

when subjected to large displacement amplitudes where geometric and material nonlinearities need to be considered. Figure 5.17 shows the damage caused by friction between the ball hinge and the hinge holder. This type of damage was unexpected since the ball hinge was originally designed to be able to rotate frictionlessly. The development of friction force can be explained by the geometric nonlinearity of the V-pin during the tests. Since the hinge holder was only allowed to move horizontally instead of vertically, the vertical movement of the V-pin was constrained. Therefore, the V-pin had to elongate to accommodate the horizontal displacements at the top. When the displacement amplitude was large, this elongation was no longer negligible and tension force developed in the V-pin, leading to an increased pressure between the ball hinge and the hinge holder. As a result, the friction force between these two surfaces occurred. To reduce the friction force, it is recommended to provide certain types of lubrication between the two steel surfaces in order to lower the friction coefficient μ.

5.3.2 The Effectiveness of the V-connector

The resiliency of the bridge system with the V-connector being used is achieved in terms of the elastic behavior of the bridge components (mainly the columns) that would otherwise show significant inelastic behavior using conventional designs. The response quantities of the bridge column were recorded in OpenSEES (McKenna et al., 2000) recorders during the HS test and its elastic behavior was confirmed by the moment-curvature relationship at the bottom of the column as shown in Figure 5.18(a).

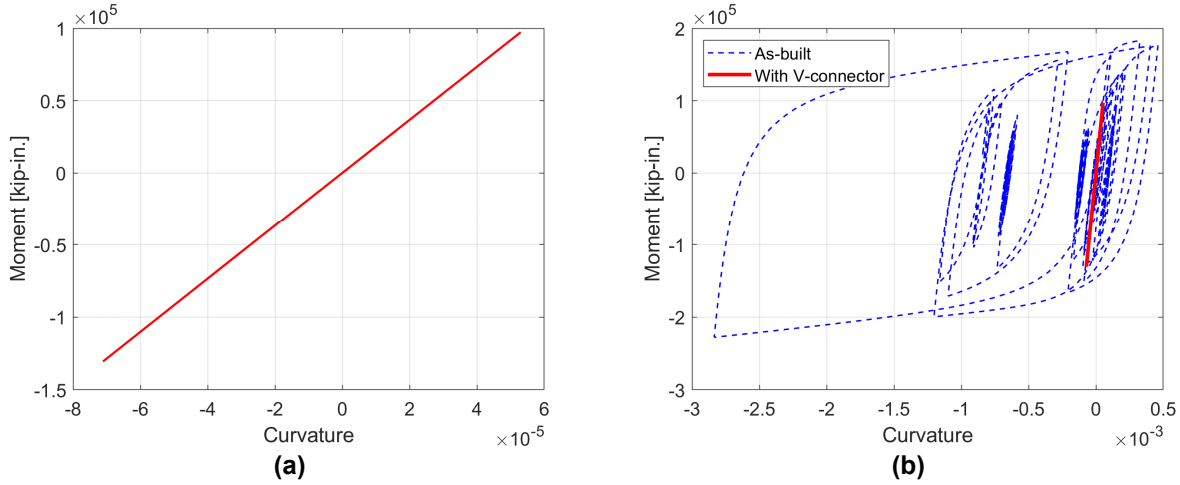

Figure 5.18 **(a) Moment-curvature relationship at the bottom of the bridge column during the HS test; (b) comparison of column response with and without the V-connector.**

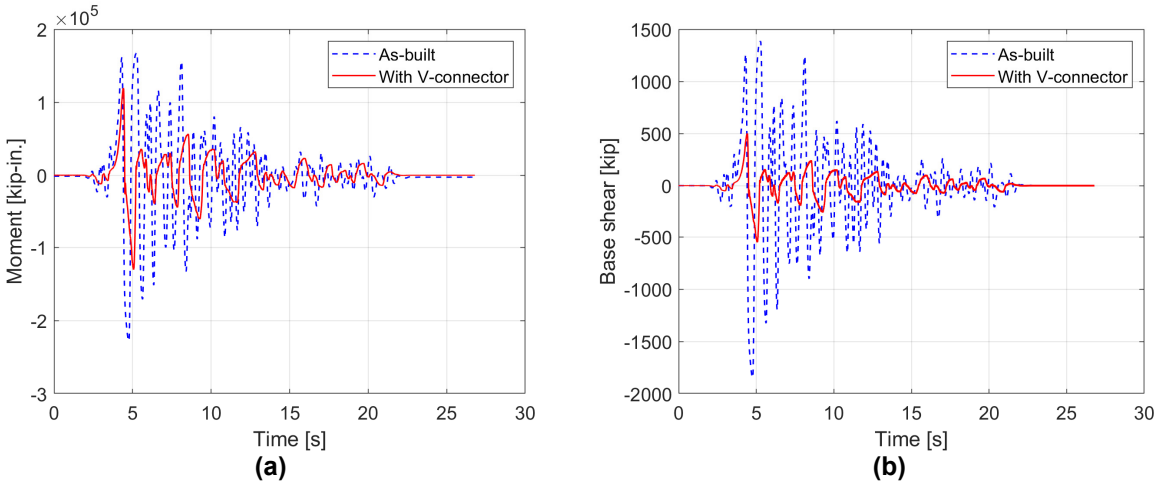

Figure 5.19 Comparison of (a) column base overturning moment; and (b) base shear during the MCE (EQ6) with and without the V-connector.

To further demonstrate the effectiveness of the V-connector and the superiority of the bridge with the V-connector being used, nonlinear time history analysis of the as-built prototype bridge (without V-connector) was conducted using the same set of three ground motions in the HS runs. The obtained column moment-curvature behavior was then compared to that obtained from the OpenSEES recorders during the HS test, see Figure 5.18(b). The as-built bridge column experienced significant damage as illustrated by the moment-curvature plot, while the bridge column with the V-connector remained essentially elastic. In addition, as shown in Figure 5.19, the usage of V-connector significantly reduces the reactions (base overturning moment and base shear) at the column base. The period elongation is also quite obvious. These results clearly demonstrate the effectiveness of the V-connector in protecting the key bridge components (the column in this case) and assuring the resiliency for the whole bridge system.

6 Development of Experimental Program II: Resilient Bridge Bent

Starting from this chapter, the discussion focuses on the second bridge subsystem — the resilient bridge column. This chapter begins with a brief introduction of the innovative features and how these features can lead to superior seismic response and ABC aiming towards a more resilient bridge system. The rest of the chapter follows the same style as Chapter 3. All the physical preparations before the test, including the specimen's design/construction/assembly, material testing, test setup and the instrumentation can be found in this chapter. Besides, the three-part experimental program and the loading protocol are briefly discussed to complete the description of the experimental framework. Detailed executions of the experimental program are provided in later chapters.

6.1 INTRODUCTION

The developed bridge subsystem (Figure 6.1) utilizes an innovative self-centering bridge column technology for application in seismic regions. It combines precast, post-tensioned, composite steel-concrete columns with supplementary energy dissipation, in such a way to simplify the off- and on-site construction burdens and minimize earthquake-induced residual deformations, damage and associated repair costs and time. The column consists of reinforced concrete cast inside a segmented cylindrical steel jacket, which acts as both the formwork and confinement to concrete and serves as transverse reinforcement. The pre-cast end beams (a cap beam and a footing in case of a bridge system) have corrugated duct lined sockets, where the columns are placed and grouted on-site to form the column-beam joints. Large inelastic deformation demands in the structure are concentrated at the column-beam interfaces, which are designed to accommodate these demands with minimal structural damage through a rocking behavior. Gaps are allowed to open at these locations and to close upon load reversals. Longitudinal post-tensioned (PT) high strength steel threaded bars, designed to respond elastically, in combination with gravity forces ensure re-centering behavior. Internal mild steel reinforcing bars, debonded from the concrete at the interfaces, provide energy dissipation and impact mitigation.

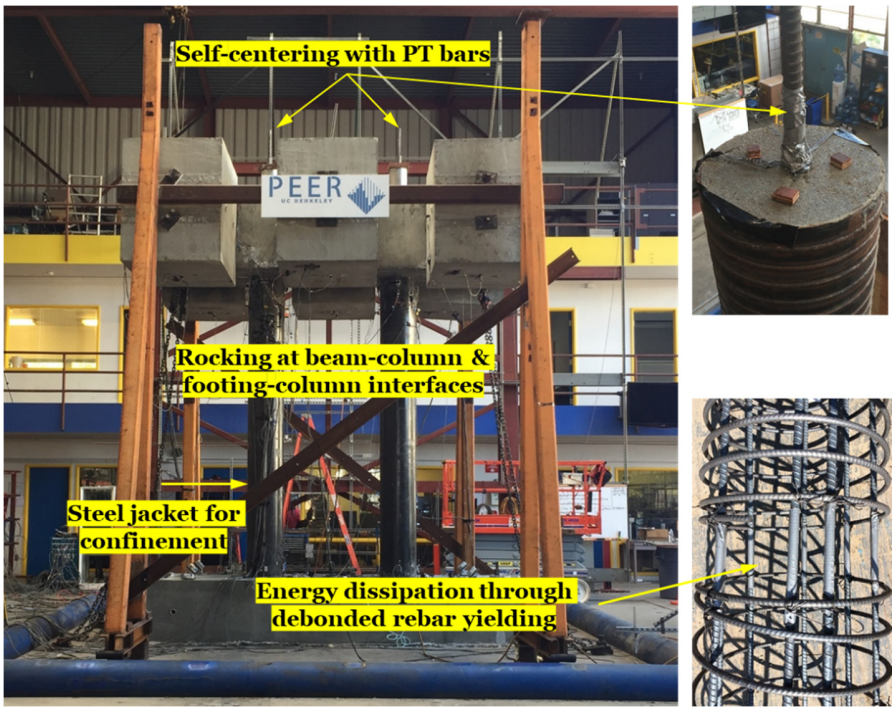

Figure 6.1 Innovative design features of the investigated bridge subsystem.

6.2 SPECIMEN DESIGN

As stated previously, one of the main objectives for the second half of the resilient bridge bent study was to compare the HS results against a previously conducted shaking table test (Nema, 2018). Therefore, the test specimen utilized here was almost identical to that of the shaking table test, except that the mass blocks on top of Figure 6.1 were removed as the inertia mass can be simulated in the computer. The columns followed the exact same design while for the cap beam and the foundation, some minor non-structural changes were made in order to accommodate the new test setup (see section 6.3). Complete information of the original design can be found in (Nema, 2018). Details and changes made on the original design of the columns, the foundation and the cap beam are presented in the following subsections.

6.2.1 Columns

The columns were designed by scaling down the prototype columns to 35% (description of the prototype columns can be found in section 7.1.1). Each column of the test specimen has an external diameter of 16 in. Ten #4 ASTM A706 (2016) Grade 60 bars provide the longitudinal reinforcement with a 6 in. length of each bar debonded from the surrounding concrete using duct tape at the rocking interfaces. Three separate #3 ASTM A706 (2016) Grade 60 spiral segments were used to hold the longitudinal reinforcement together. The splitting of the spirals was to prevent them from contributing to the energy dissipation by yielding at the rocking interfaces. The use of spirals was only for construction purpose as the majority of the shear and confinement reinforcement was provided by the column outer shell.

Due to the difficulty in sourcing 3/8 in. strands as required in the specimen representing the scaled prototype, the strands were replaced by a single 1-3/8 in. ASTM A722 (2012) Grade 150 threaded PT bar, which has a yield strength capacity equal to the required ten 3/8 in. strands. The PT bar anchorage was embedded inside the bottom of the column before the placing of concrete, and the PT bar itself was enclosed inside a 2 in. inner diameter (ID) PVC sleeve to debond from the concrete. The top end of the bar was allowed to extend from the top of the column for setting up the prestressing equipment later on. This extension was also proved helpful in guiding the cap beam in place during the specimen assembly in the test setup. Figure 6.2 shows the reinforcement details of the column design.

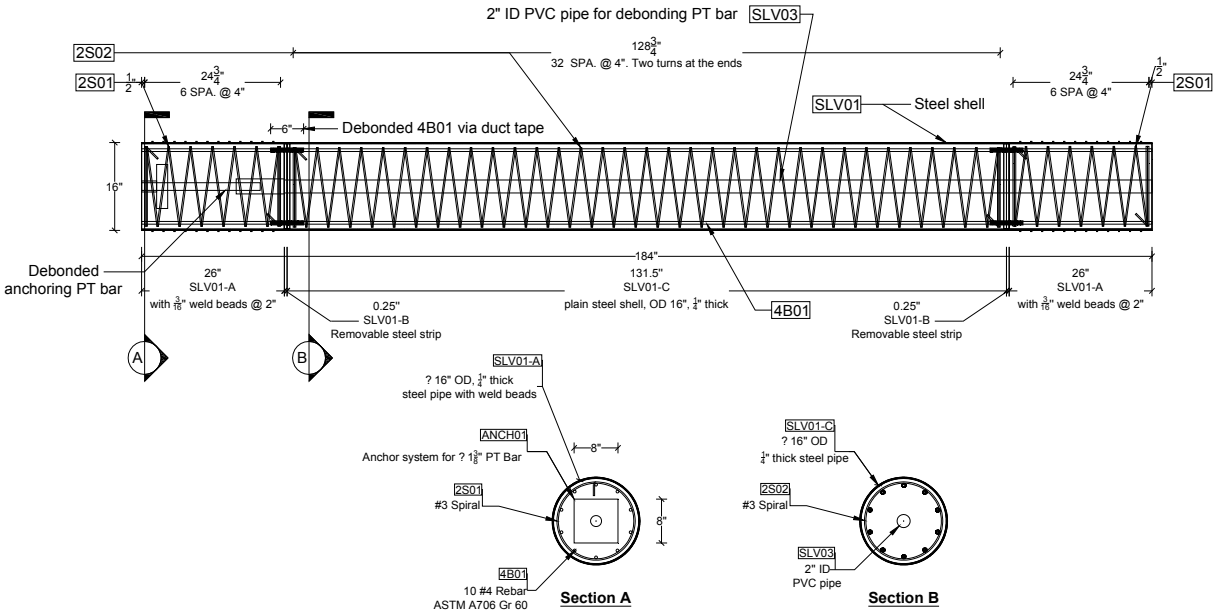

Figure 6.2 Dimensions and reinforcement details for the column (Nema, 2018).

6.2.2 Foundation/Cap Beam

The foundation, with dimension 178 in. (length) by 38 in. (width) by 26 in. (height), was designed around the socket connection. The socket for accommodating each column was formed out of a 21 in. ID, 26 in. deep corrugated metal pipe (CMP). Primary reinforcement design was conducted following the strut-and-tie method (Nema, 2018) as prescribed in section 5.6.3 of AASHTO (2012). The column axial load was assumed to be transferred directly to the strong floor of the laboratory, while the lateral load was assumed to be first transferred to the top and bottom of the sockets by lateral bearing, which eventually also went to the strong floor. The strut-and-tie model indicates that the socket type of joint requires extra cross ties around the connection to prevent splitting in the longitudinal direction due to the bearing forces arising from the transfer of column shear to the foundation. Additional reinforcement was provided around the socket to prevent any splitting due to out-of-plane forces. This reinforcement, while not necessary for the specimen, is necessary in the case of real bridge foundations.

No structural changes were made in the foundation design for the HS. The main change was to accommodate the connection of the bottom clevis of the vertical actuator. For this purpose,

a total number of eight 1.5 in. diameter EMT conduits were aligned with the connection holes on the bottom clevis and placed inside the foundation reinforcing bar cage. Figure 6.3 shows the reinforcement details of the foundation design, with the modification mentioned above highlighted in the drawing.

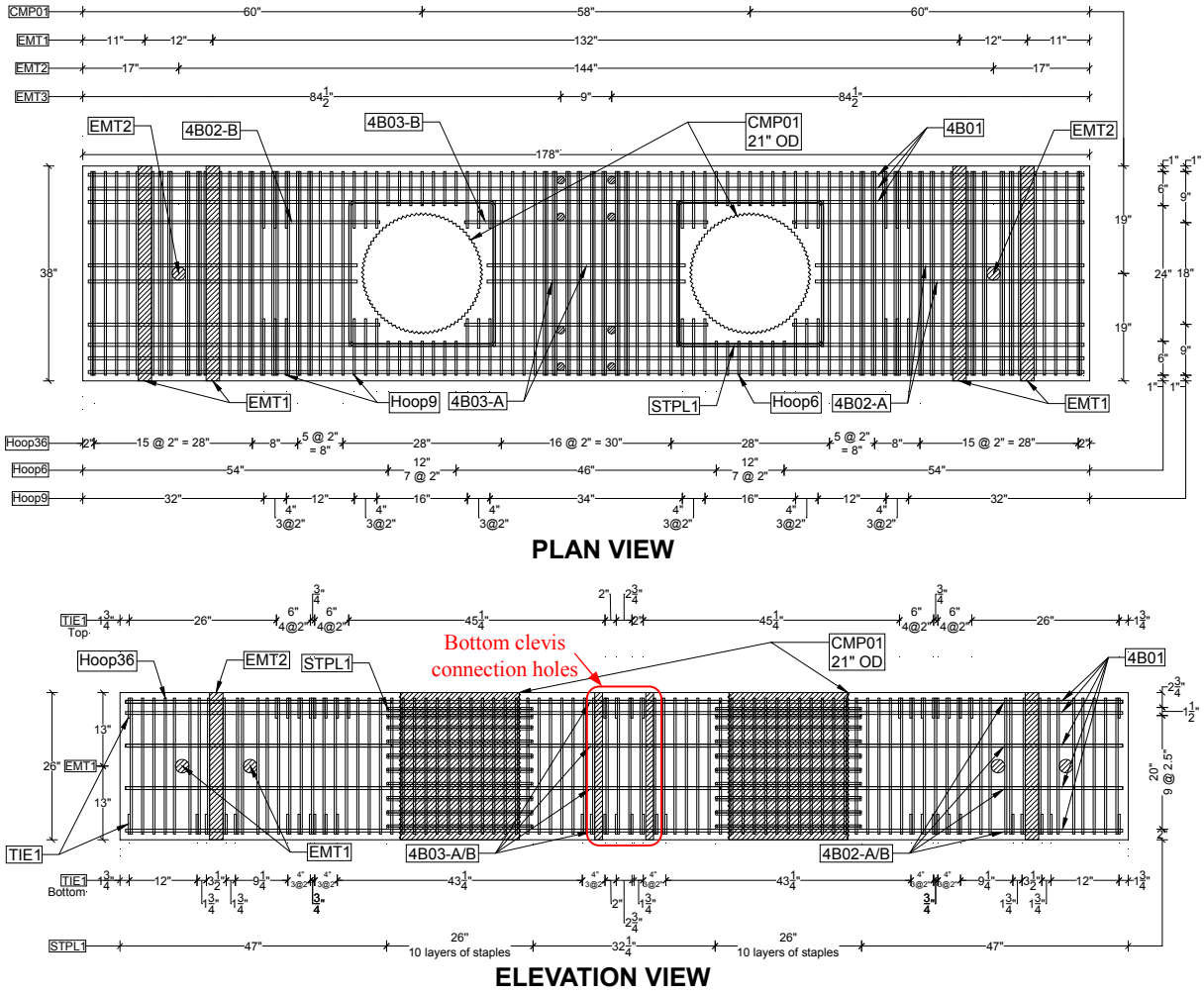

Figure 6.3 Dimensions and reinforcement overview for the foundation (Nema, 2018, with modifications).

Similar to the foundation, the original design of the cap beam with dimension 164 in. (length) by 38 in. (width) by 32 in. (height), revolved around the socket connection. The socket was again formed by 21 in. ID, 26 in. deep CMP. The reinforcement design was also conducted using the strut-and-tie method. Unlike the foundation, the vertical load needs to be transferred from the cap beam to the columns. For this purpose, a 6 in. thick layer of reinforced concrete was placed on top of the column sockets and was strengthened by overhanging stirrups to prevent punching shear failure. Same as the foundation, additional reinforcement was provided to avoid splitting in the longitudinal and transverse direction. A 2 in. ID opening was allowed above each socket for the PT bars to pass through.

No structural changes were made in the design of the cap beam. However, some minor adjustments and accommodations were made and summarized as follows: (1) The size and the number of grouting holes near the socket periphery were increased to allow for easier grouting; (2) A total of ten 1.5 in. diameter EMT conduits were aligned with the connection holes on the top clevis of the vertical actuator for actuator connection; and (3) Three steel plates were embedded into the cap beam reinforcing bar cage for the lateral support of the test setup. Figure 6.4 shows the reinforcement details of the cap beam design, with modifications mentioned above highlighted in the drawing.

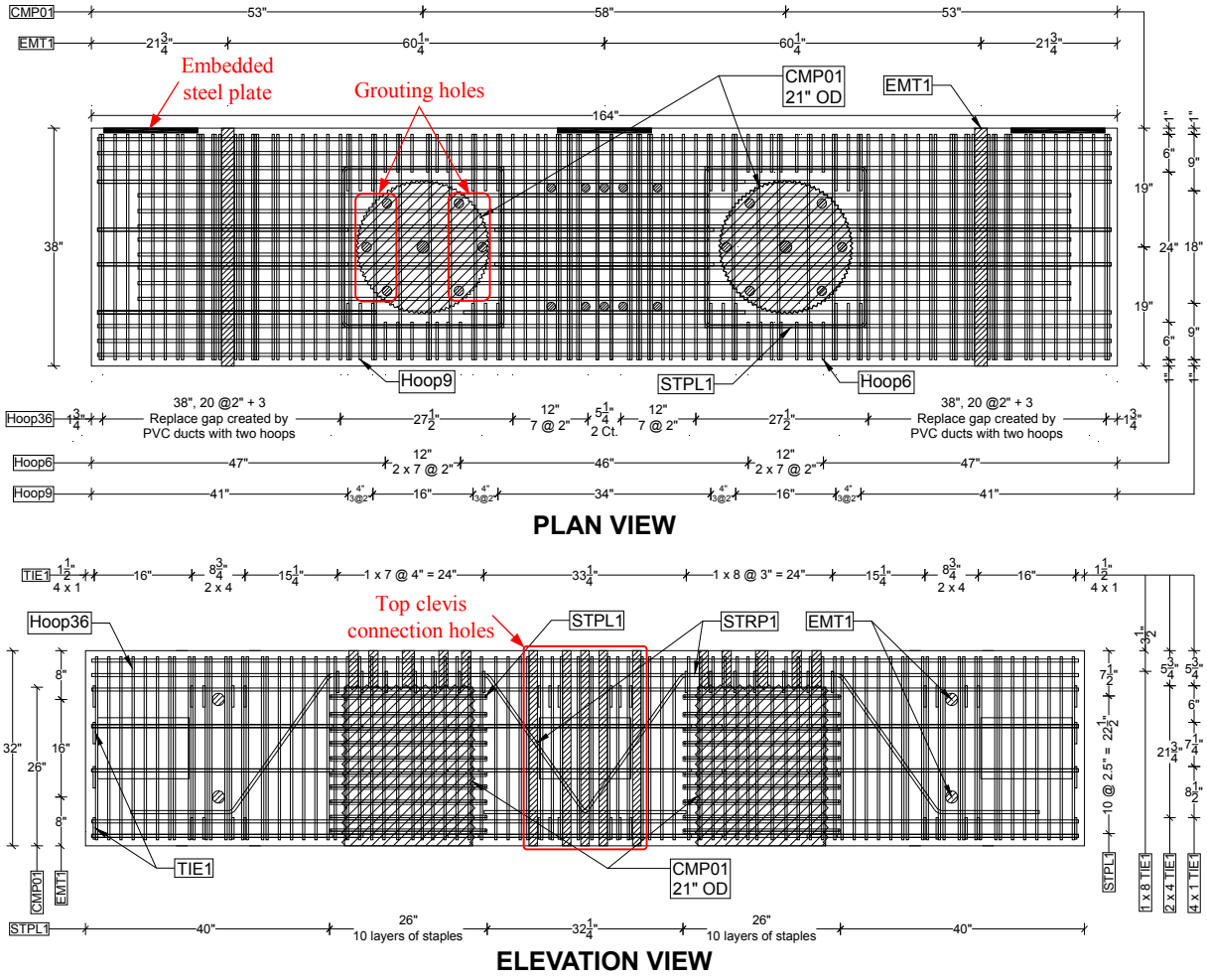

Figure 6.4 Dimensions and reinforcement overview for the cap beam (Nema, 2018, with modifications).

6.3 TEST SETUP

The experimental investigation consists of two phases, with the objective to: (1) Compare the test results from the HS test and the shaking table test; and (2) Do a system level performance evaluation of a representative highway bridge with resilient bridge bent design. In both phases,

two-directional ground motion inputs were considered, one horizontal and the vertical component. Therefore, lateral and vertical loading systems were required to be carefully arranged.

Because of its experimental nature, the test specimen during the HS experiment needs to interact with the analytical substructure modeled in the computer. Figure 6.5 depicts the substructuring in phase I of the HS test. The interaction between the experimental substructure and the analytical substructure was achieved through the forces and the moments at the center of the cap beam. For the experimental substructure, these quantities are external and need to be applied through actuators. One key issue in determining the test setup was the layout of the horizontal actuator(s), refer to Figure 6.6. If the external moment is negligible, then it is sufficient to use only one layer of actuator(s). Otherwise, two layers of horizontal actuators are needed and the force in each actuator needs to be carefully controlled to apply the desired forces and bending moments.

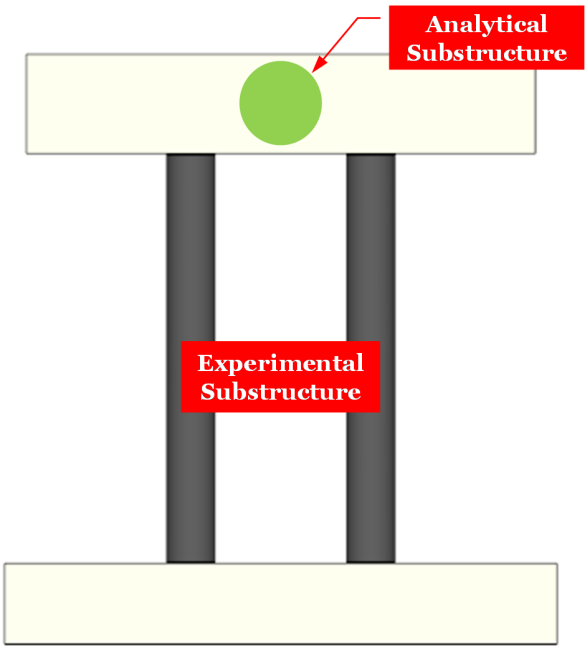

Figure 6.5 Substructuring in phase I of the hybrid simulation.

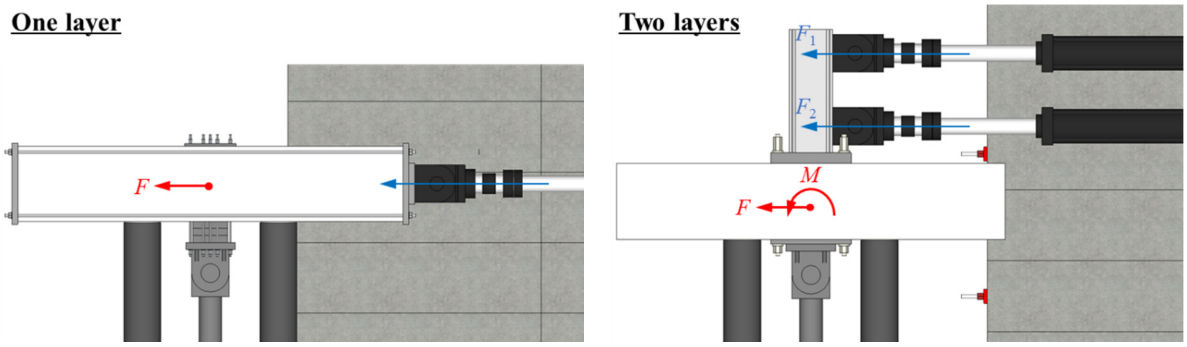

Figure 6.6 Different layout of the horizontal actuator(s).

The criterion to judge whether the bending moment is negligible or not was to check the demand to capacity ratio (DCR) of the base overturning moment of the bridge bent from the

shaking table test results. The moment capacity M_C and demand M_D of the bridge bent were calculated by Equation (6.1).

$$M_C = F_{\max} \times H$$
$$M_D = \ddot{\theta}_{\max} \times I \tag{6.1}$$

$$\ddot{\theta} = (\ddot{a}_2 - \ddot{a}_1)/d$$
$$I = 2I_1 + 4(I_1 + m_{block}d^2/4) \tag{6.2}$$

Figure 6.7 is a schematic illustration of the above calculation where relevant terms are defined by the following:

$F_{\max}$ = maximum lateral inertia force, measured from the shaking table test;

H = center-to-center distance between the bent cap and the foundation;

$\ddot{\theta}_{\max}$ = maximum angular acceleration above the columns;

I_1 = rotational inertia for one single inertia block;

m_{block} = mass for one single inertia block;

$\ddot{a}_1$ & $\ddot{a}_2$ = vertical accelerations of the inertia blocks measured from the shaking table test; and

d = distance between the inertia blocks, as shown in Figure 6.7.

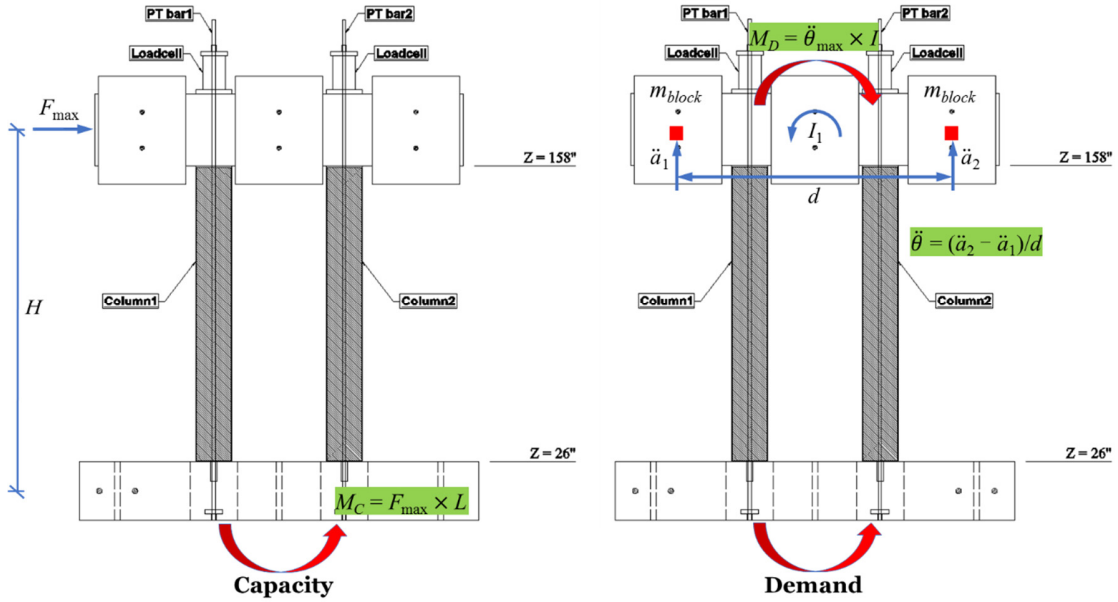

Figure 6.7 Moment capacity and moment demand calculations of the bridge bent from the shaking table test.

By referring to the data from the shaking table test, the maximum lateral inertia force was 70 kips, resulting in M_C to be 940 kip-ft. The maximum angular acceleration was found to be 2.2 rad/s^2, leading to M_D = 81.4 kip-ft. Therefore, the DCR ratio M_C/M_D is about 0.087, meaning that

the moment at the center of the cap beam was negligible. For this reason, the test setup with only one horizontal actuator is selected for practicality. A 3D sketch of the test setup, including the loading systems and boundary supports, is shown in Figure 6.8. Detailed test setup is shown in different views in Figure 6.9 and Figure 6.10.

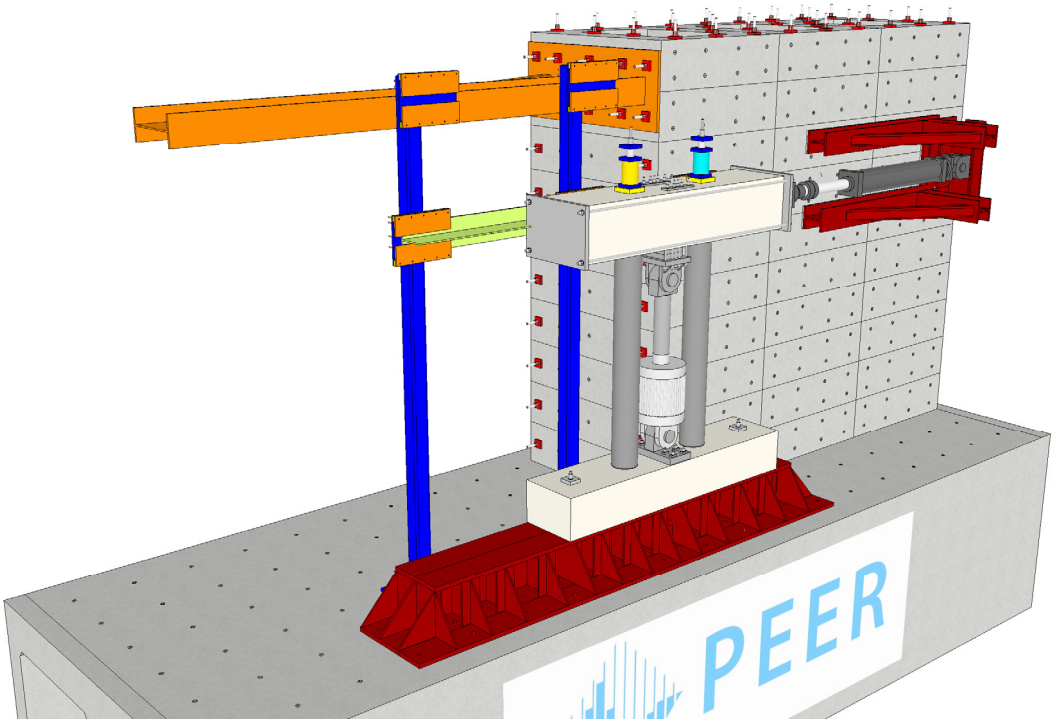

Figure 6.8 Schematic 3D view of the test setup of the HS experiments.

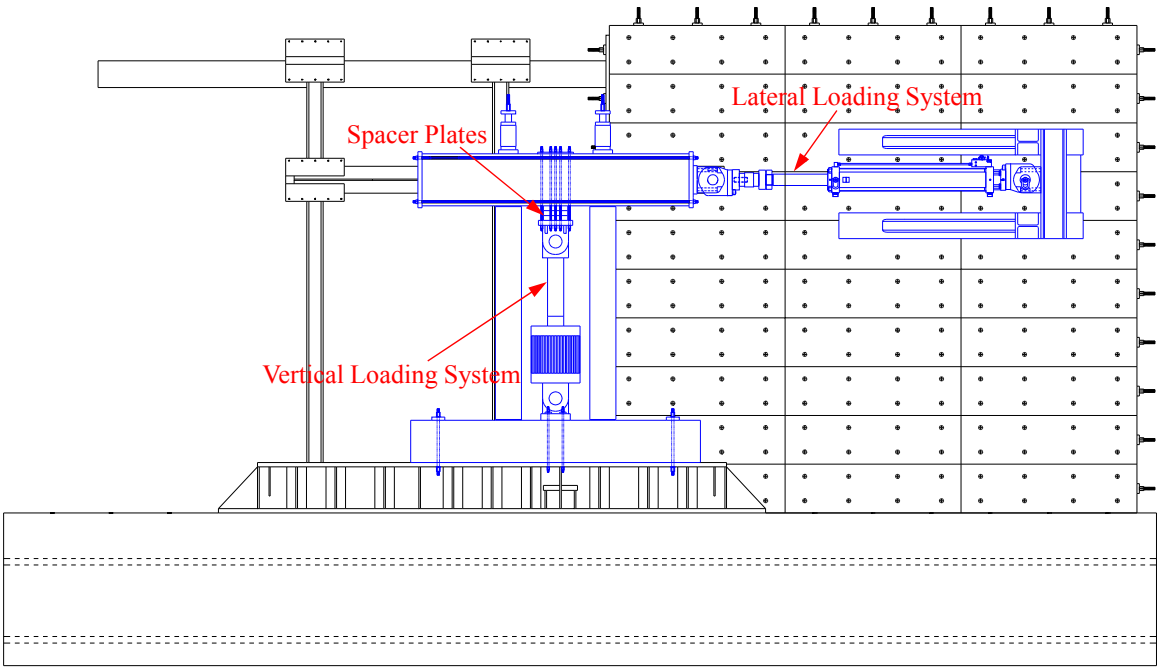

Figure 6.9 Elevation view of the test setup of the HS experiments.

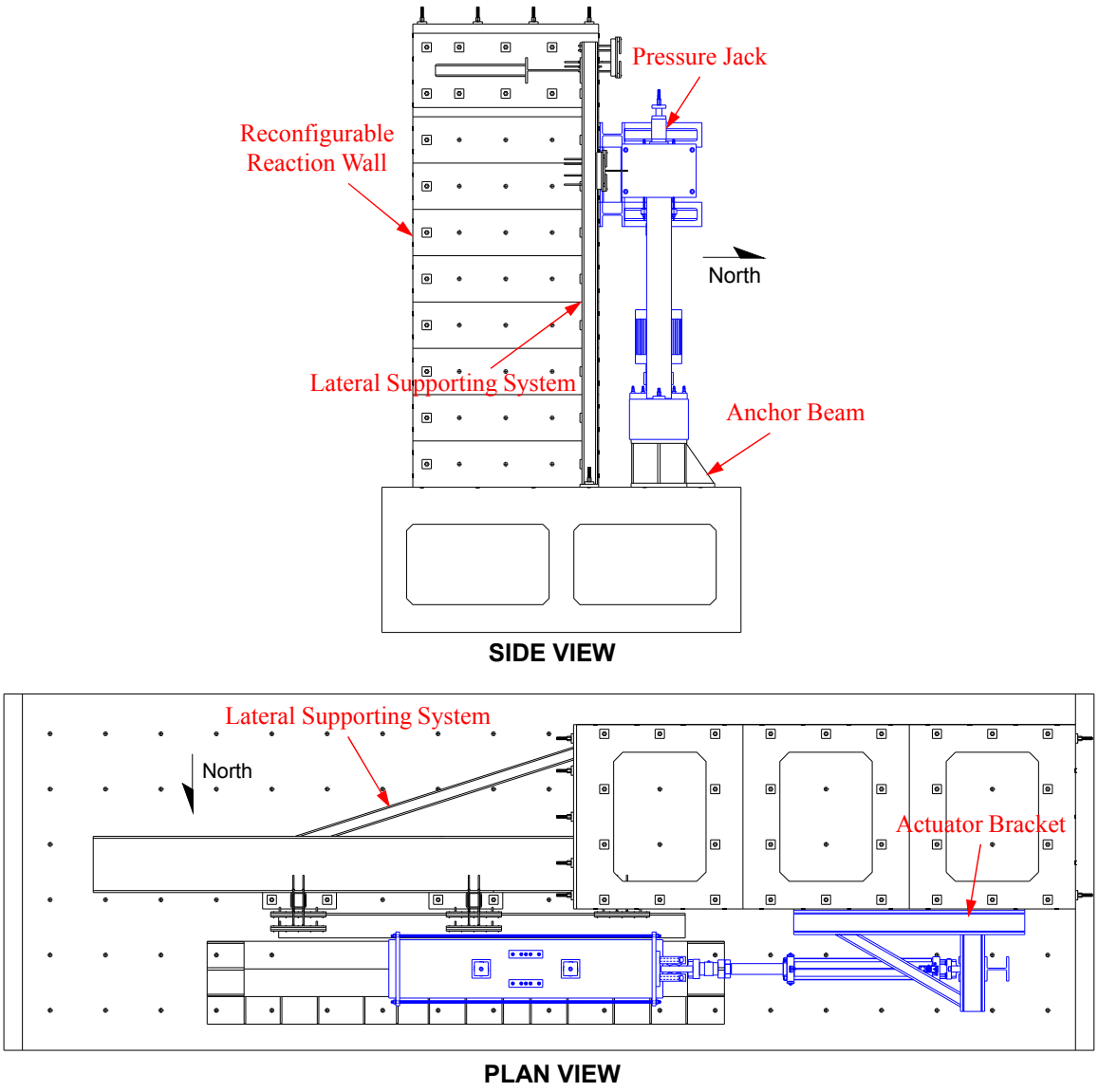

Figure 6.10 Side and plan view of the test setup of the HS experiments.

As can be seen from the test setup drawings, the foundation of the test specimen was hydro-stoned and prestressed to the steel anchor beam attached to the strong floor of the laboratory. A vertical actuator was placed in the middle of the specimen between the two columns to apply the gravity load as well as the vertical force fluctuation caused by the vertical ground motion component. The respective connections between the top and bottom clevises of the vertical actuator and the cap beam and foundation of the test specimen were achieved through William rods. Ten 1 in. diameter rods, with one end bolted to the top clevis, were anchored to the top surface of the cap beam after being prestressed. Similarly, eight 1 in. rods connecting the bottom clevis and the foundation were prestressed and anchored to the top flange of the underlying steel beam. This way, the vertical actuator pulls downwards or pushes upwards on the cap beam from the top and reacts against the stationary steel beam at the bottom. To make the actuator close to mid-stroke

before starting the test, three 3 in. thick spacer plates were added between the vertical actuator and the cap beam.

The lateral load was applied to the cap beam using one horizontal actuator that reacted against the steel bracket on the reaction wall, as schematically shown in Figure 6.8. Two steel end plates sandwiching the cap beam were fabricated and connected by four prestressing rods. The horizontal actuator was then bolted to the near end plate. This way, when the actuator extended, the force was directly applied to the cap beam as bearing on the near end. When the actuator retracted, the force was transferred through the prestressing rods to the other side of the cap beam and bearing was achieved at the far end. Similar to the shaking table test, to prevent the cap beam from the out-of-plane movement when applying the lateral load, a lateral supporting system was employed. Figure 6.11 shows the out-of-plane restraining system details. Three steel plates, embedded inside the cap beam before casting the concrete, were welded to a T-beam. The T-beam, even if being restrained by the adjustable brackets from moving sideways, was allowed to slide frictionlessly along the loading direction by greasing the contact surfaces.

The complete test setup is shown in Figure 6.12. Throughout the study, the loading in the horizontal direction (also referred to as the transverse direction of the bridge) is along the east-west direction. Whenever the horizontal actuator is pushing towards the east, it is designated as positive, and, in turn, the negative loading direction is when the actuator retracts, i.e., moving towards the west. The positive and negative directions for the vertical loading are quite axiomatic.

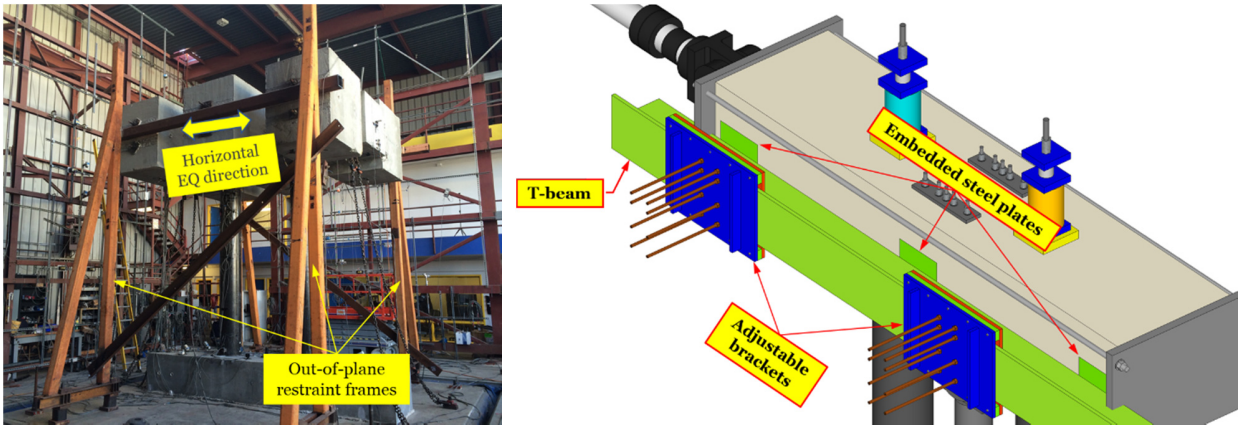

Figure 6.11 **The lateral supporting system for (a) the shaking table test; and (b) the hybrid simulation experiments.**

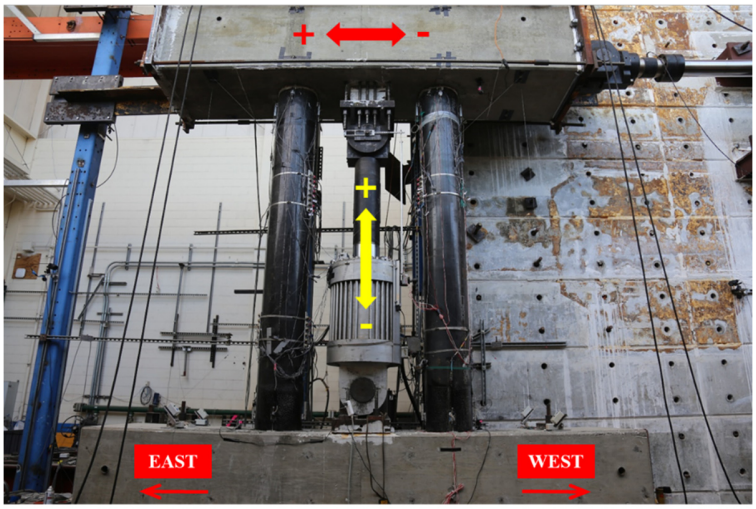

Figure 6.12 Completed test setup and loading directions for the hybrid simulation experiments.

6.4 EXPERIMENTAL PROGRAM

6.4.1 Hybrid Simulation System Verification Test

Before starting the actual HS experiments, a verification test is indispensable to check the three key aspects of the newly developed HSS. The first one is the correctness of the numerical integration and the displacement interpolation algorithm. At each time step, the numerical integration takes the measured force as an input and calculates the displacement to be imposed to the test specimen as an output. The displacement interpolation is aiming for a smooth transition between two displacement values from subsequent time steps. The second one is the proper back and forth communication between the physical and computational components of the hybrid system. During the test, the computed displacement (in a digital format) needs to be converted to an analog voltage such that the controller can recognize before imposing it to the physical specimen, while the measured resisting force (in an analog format) needs to be converted to a digital value to be sent back to the numerical integration algorithm. These conversions are achieved by the built-in Simulink blocks and their proper functionalities are key to the simulation execution. The third aspect is related to the control quality of the actuators. Good displacement tracking is crucial to the HS because the measured resisting force from the physical component is directly related to the computed applied displacement. In addition, the displacement overshooting, or undershooting can lead to either a damping increase or instability issues, see Figure 6.13. All aspects were successfully verified through a HS verification test with free actuators detached from the test specimen.

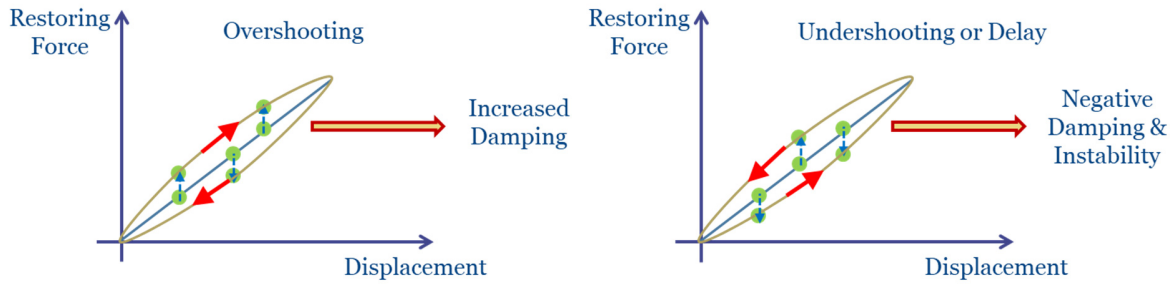

Figure 6.13 Improper actuator tracking and its consequences (Mosalam and Günay, 2013).

6.4.2 Hybrid Simulation Phase I

The objective of phase I HS experiments was to compare the test results with the shaking table test. For this purpose, the two-column bridge bent was simulated as the experimental substructure while the horizontal/vertical mass and the corresponding mass-proportional damping were modeled in the computer. The modeling parameters were obtained by analyzing the test data from the shaking table. Same ground motion records, consisting of one horizontal and the vertical component measured directly by the accelerometers mounted on the shaking table, were applied as the input excitations to the equations of motion in the HS. This is to eliminate any possible errors between the target signals and the actually obtained signals in the shaking table test. More details regarding phase I of the HS are presented in Chapter 7.

6.4.3 Hybrid Simulation Phase II

The third part of the experimental program was the system level performance evaluation of a representative bridge with the innovative bridge bent design under seismic loading. The selected prototype bridge is the same as the one used in the V-connector study, the Jack Tone Road On-Ramp Overcrossing (see Figure 4.1). In this HS phase, the analytical substructure was changed from a single mass and dashpot in phase I HS to the superstructure of the bridge, including the end abutments. The experimental substructure remained the same as in phase I. Unlike the HS test of the V-connector which focused on the longitudinal direction of the bridge, here the focus is on the transverse direction. Some ground motions from phase I testing were repeated to check the effect of different analytical substructures on the specimen and entire bridge system responses. Followed by that, a set of three ground motions with increasing intensity was selected from the NGA West2 ground motion database (Bozorgnia et al., 2014) based on the target spectrum of a high seismicity site. These ground motions were applied to the full bridge system for the system level study.

6.5 LOADING PROTOCOL

6.5.1 Gravity Load

For the two HS phases, two different values of gravity load were selected. In phase I, a gravity load of 47 kips corresponding to the total weight of six inertia mass blocks attached to the cap beam in the shaking table test was applied to the test specimen before starting the HS experiment.

This way the same initial value of the column axial forces could be achieved in both the shaking table test and the HS experiment. This is a very important aspect as the specimen response can be heavily dependent on the level of the column axial force.

In phase II HS, the applied gravity load represented the weight of the prototype bridge's superstructure. A gravity analysis of the prototype bridge with the inclusion of a full-scale bridge bent was conducted, with the force on top of the bridge bent being extracted (see section 8.1.6.3 for more details). This force, after proper scaling, served as the gravity load (172 kips, i.e., about 3.6 times that of phase I of the HS) applied to the test specimen before the HS experiment.

6.5.2 Earthquake Load

In both HS phases, the applied earthquake loadings were based on the computed responses in the horizontal and vertical directions after the gravity loading. The horizontal loading was applied using a slow-rate displacement control, with a loading rate of 0.05 in./s. For the vertical direction, the original plan was also to conduct a slow-rate displacement control according to the computed displacement. However, a decision was made to switch from a displacement control to a force control due to the limitation of the test setup (see section 7.4.1 for more details). The vertical force was obtained by multiplying the calculated vertical displacement with the estimated vertical stiffness of the specimen, under the assumption that the specimen will remain essentially elastic in the vertical direction. Again, a slow-rate force control was utilized in the vertical direction with a loading rate of 2 kips/s.

6.6 CONSTRUCTION OF THE TEST SPECIMEN

The test specimen was constructed in two phases following the same steps as those in the shaking table test (Nema, 2018), except for some minor changes mentioned in section 6.2. Brief description of the different construction phases in presented below. Appendix B provides additional details of the construction process.

Building the columns was the main focus of phase I construction. The two bridge columns were constructed together with those used in the shaking table test by a professional construction company and then delivered to the laboratory. The use of a dry-socket connection between the columns and the end beams allowed for an innovative construction method. The entirety of each column was formed by inserting the reinforcement cage inside a segmented steel shell that was assembled from 0.25 in. thick ASTM A53 (2012) Grade B pipe, followed by the placing of concrete with nominal compressive strength of 6 ksi. The steel pipe served as both the permanent formwork and the transverse confinement for the column concrete. It also provided a force transfer mechanism between the columns and the end members (cap beam and foundation). To allow rocking at the beam-column and column-foundation interfaces, the steel shell was segmented into five sections: two embedded end sections with weld beads outside and inside for developing composite action, one central section over the column clear height, and two thin removable open strips between the central section and the two end sections. The five segments were spot welded together at a few locations to form the single pipe unit for the concrete casting. During the specimen assembly, the spot welds were grinded off and the thin strip segments were removed to

form the rocking interfaces (see Appendix C). Some photographs from the column construction process are shown in Figure 6.14 to Figure 6.16.

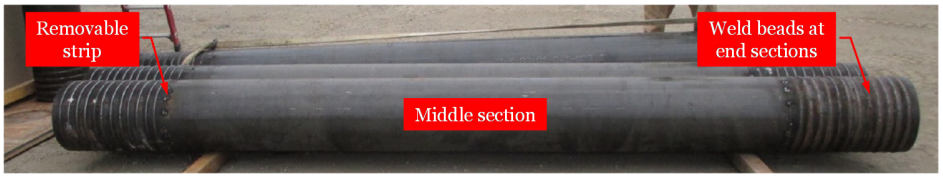

(a)

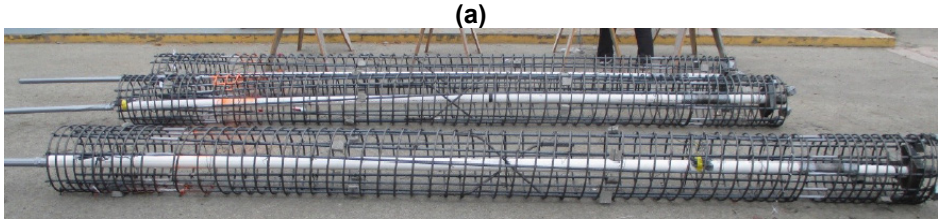

(b)

Figure 6.14 **(a) Segmented column steel shells; (b) finished column reinforcing bar cages.**

(a) (b)

Figure 6.15 **Concrete placing setup: (a) erect the column steel shells; (b) column reinforcing bar cages installation.**

Figure 6.16 Final completed columns.

Phase II of the construction included laying out the formworks for the foundation and the cap beam, furnishing the transverse and longitudinal reinforcement, constructing the reinforcing bar cages, placing these cages and other supplementary parts (including the CMP, EMT conduits and the embedded steel plates) in place, and casting the concrete. All these steps in this study were completed in the local laboratory with the help of several students and laboratory technicians. Figure 6.17 to Figure 6.19 show this phase II of the construction process for the foundation and the cap beam. Curing blankets in addition to the chemical E-CURE were used for concrete curing during the first week after concrete casting to avoid shrinkage cracks.

(a) (b)

Figure 6.17 (a) Completed foundation reinforcing bar cage; (b) completed cap beam reinforcing bar cage.

Figure 6.18 **(a) Reinforcing bar cages and formworks before concrete casting; (b) concrete curing using curing blankets.**

Figure 6.19 **Final completed foundation (left) and cap beam (right).**

6.7 MATERIAL PROPERTIES

Extensive material testing was conducted for steel and concrete as part of the research program on resilient bridge bent. These material tests are presented in the following subsections.

6.7.1 Steel

6.7.1.1 Reinforcing Steel

The reinforcing steel used in the columns serving as the energy dissipator was ASTM A706 (2016) Grade 60, size #4. Three reinforcing bar coupons, each 18 in. long, were tested using a Universal Testing Machine under monotonic tension to characterize the material properties. All coupons were tested until rupture occurred. The stress and strain were calculated by dividing the total load

by the nominal cross-sectional area of the reinforcing bar and the deformation by the gauge length. Test results are summarized in Table 6.1. The stress-strain curves obtained from all coupons together with the average curve are shown in Figure 6.20. Note that the 0.2% offset yield point was utilized to find the yield stress and the corresponding yield strain.

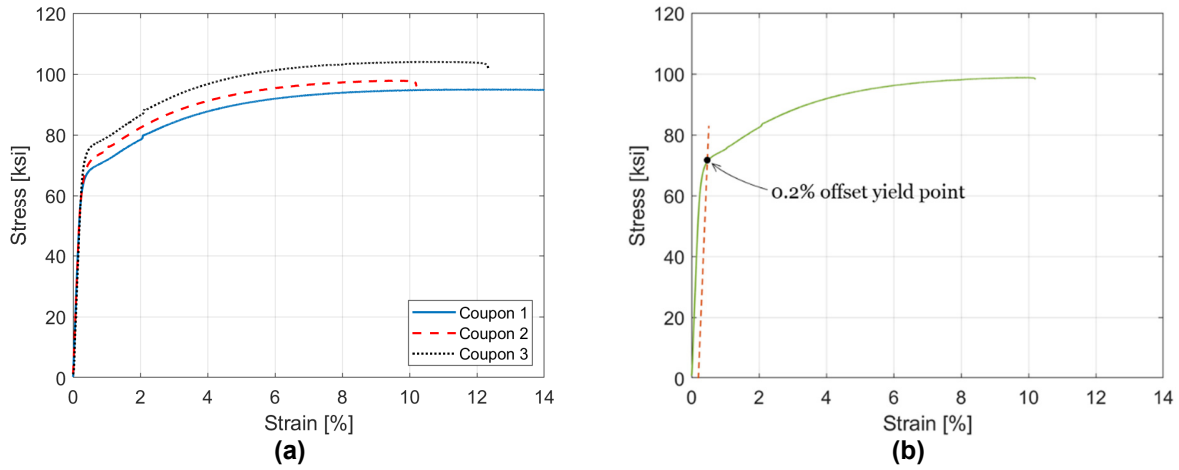

Figure 6.20 **(a) Stress-strain curves for all three reinforcing bar coupons; (b) average stress-strain relationship and yield point.**

6.7.1.2 Prestressing Steel

The prestressing steel used for post-tensioning the columns was ASTM A722 (2012) Grade 150 threaded bar with 1-3/8 in. nominal diameter. Three PT bar coupons, each 24 in. long, were tested under monotonic tension to characterize the material. The test results can be found in Table 6.1. The stress-strain curves obtained from all three coupons together with the average curve are shown in Figure 6.21. The 0.2% offset yield point was again utilized to determine the yield stress and the corresponding yield strain.

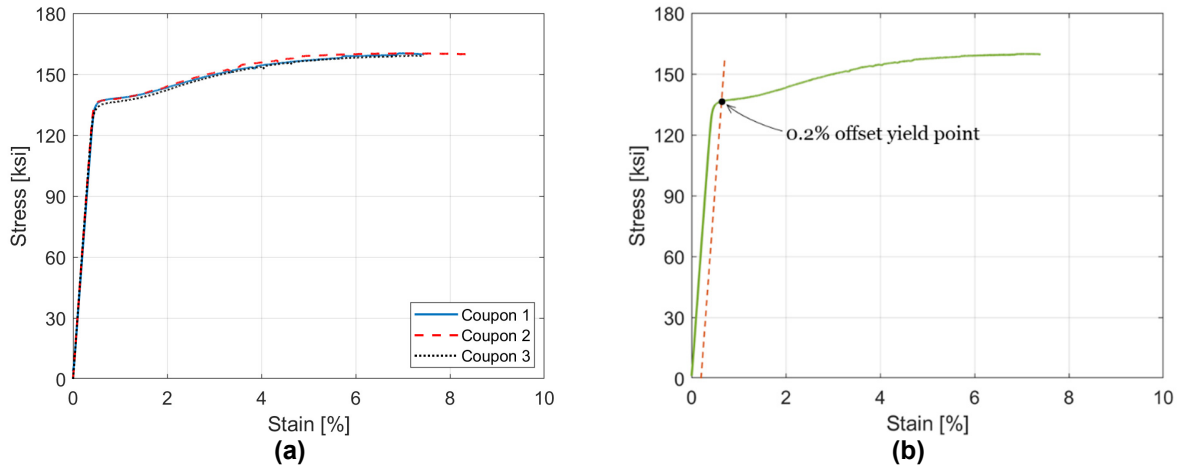

Figure 6.21 **(a) Stress-strain curves for all three PT bar coupons; (b) average stress-strain relationship and yield point.**

6.7.1.3 Shell Steel

The column shell was made from ASTM A53 (2012) steel. Three steel coupons were made out of the 0.25 in. strips removed from the column outer steel shell at the rocking interfaces (see Figure 6.22) and were tested under monotonic tension. Figure 6.23 shows the test setup. All coupons were tested until rupture occurred. The average properties are reported in Table 6.1. The stress-strain curves obtained from all three coupons together with the average curve can be found in Figure 6.24. For the strips, the strain recording was stopped at 1.8%, and only the ultimate strength was reported beyond that point. Again, the 0.2% offset yield point was used to find the yield stress and the corresponding strain values.

(a) (b)

Figure 6.22 Test coupons made from the removed strips.

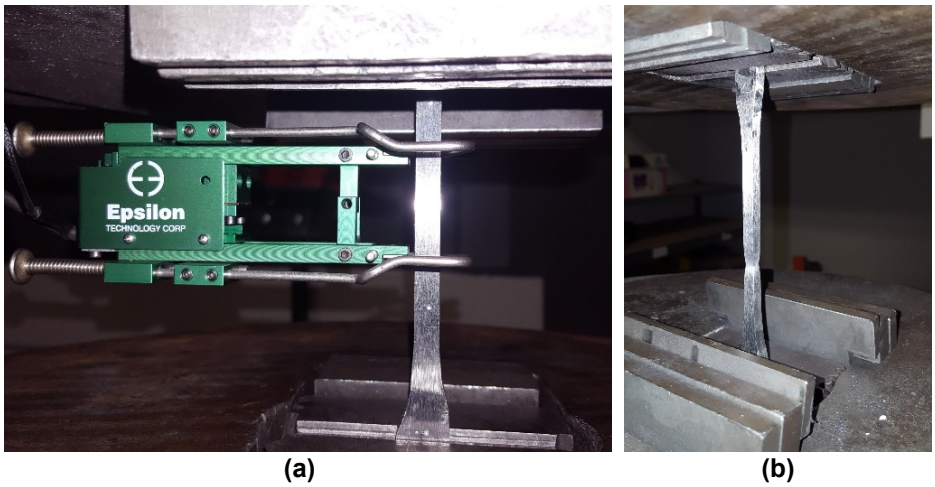

(a) (b)

Figure 6.23 (a) Material property test setup for shell steel; (b) observed necking during the test.

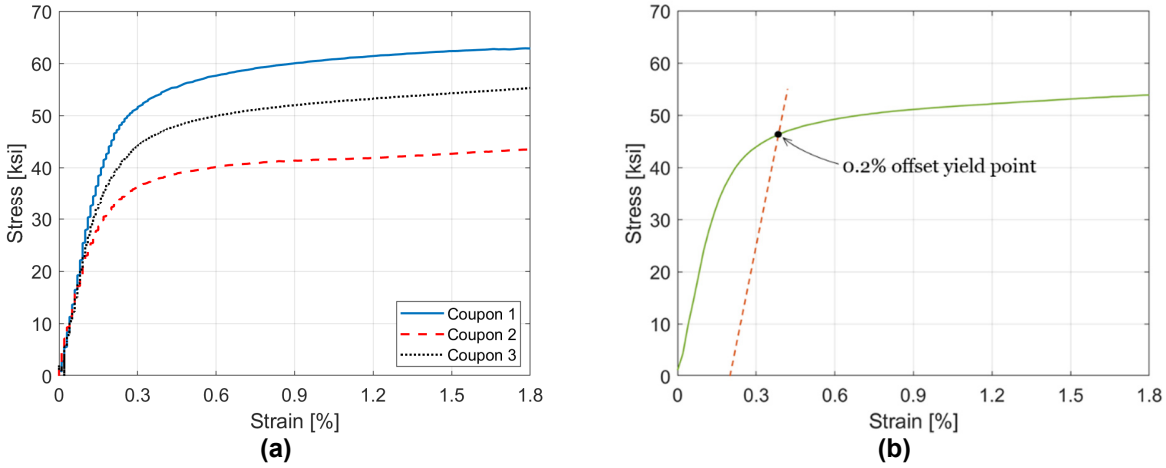

Figure 6.24 **(a) Stress-strain curves for all three shell steel coupons; (b) average stress-strain relationship and yield point.**

Table 6.1 **Measured mechanical properties of the steel.**

Material	A706 Grade 60			A722 Grade 150			A53		
	Mean	St. Dev.	COV	Mean	St. Dev.	COV	Mean	St. Dev.	COV
Elastic Modulus [ksi]	26,900	573	0.021	31,400	194	0.006	25,200	2,344	0.093
Yield Stress [ksi]	71.272	3.857	0.054	136.613	1.097	0.008	46.263	9.157	0.198
Yield Strain	0.0047	0.0001	0.021	0.0064	0.0001	0.016	0.0038	0.0004	0.105
Peak Stress [ksi]	98.958	4.609	0.047	159.959	0.652	0.004	63.914	10.473	0.164
Ultimate Strain	0.1365	0.0427	0.313	0.0777	0.0059	0.076	-	-	-

6.7.2 Grout

BASF MasterFlow® 928 non-shrink grout, mixed at fluid consistency with a large percentage of water (17% by weight) was used for grouting the top and bottom gaps between the columns and the CMP socket walls. Compressive strength tests were conducted to check the strength of the grout on the first day of phase I HS testing. For this test, a total number of twelve 2 in. diameter by 4 in. height cylinders were taken from the top and the bottom grout, six for each batch, and were placed next to the test specimen in the same indoor laboratory conditions. The cylinders were capped with a sulfur compound at both ends before being tested on a Universal Testing Machine at the Concrete Laboratory of University of California, Berkeley. The test setup and a typical tested and crushed grout cylinder are shown in Figure 6.25. Test results are summarized in Table 6.2.

(a) (b)

Figure 6.25 (a) Compressive strength test setup for grout; (b) typical mode of failure.

Table 6.2 Compressive strength test results for the grout.

Material	Age [day]	Compressive Strength [ksi]		
		Mean	St. Dev.	COV
Bottom Grout	122	6.859	1.133	0.165
Top Grout	85	5.662	1.183	0.209

6.7.3 Concrete

Normal-weight concrete was used for the foundation, the cap beam and the columns, with a specified strength of 6 ksi and maximum aggregate size of 3/4 in. A minimum slump of 6 in. was required to ensure proper workability and flowability of the concrete inside the congested reinforcing bar cages. A slump test was performed, and slump value was verified before accepting the concrete lift to avoid any construction problems, see Figure 6.26(a).

(a) (b)

Figure 6.26 (a) Slump test; (b) sample concrete cylinders for material testing (cap beam and foundation).

To monitor the strength gain of concrete with time at standard ages (7, 14, 21, and 28 days) and the first day of testing (DOT), compressive strength tests were conducted using 6 in. diameter by 12 in. height standard cylinders. Two sets of cylinder samples were collected, one from the end members (cap beam and foundation) and the other from the columns, as the concrete was placed on separate days (see Figure 6.26(b)). Each set of cylinder samples was collected from the same batch of concrete when casting different parts of the specimen and were cured in the same indoor laboratory conditions. Similar to the grout testing, the cylinders were capped with a sulfur compound at both ends before being tested on the same Universal Testing Machine in accordance with ASTM C39 (2005). The test results for the concrete at all different ages are listed in Table 6.3.

Table 6.3 Compressive strength test results for the concrete.

Material	Age [day]	Compressive strength [ksi]		
		Mean	St. Dev.	COV
Column Concrete	7	4.421	0.290	0.066
	22	5.023	0.129	0.026
	48	6.187	0.374	0.060
	DOT	6.793	0.676	0.099
Foundation/ Cap beam Concrete	7	3.534	0.071	0.020
	14	4.867	0.243	0.050
	21	5.316	0.484	0.091
	28	5.840	0.263	0.045
	DOT	6.789	0.610	0.090

In additional to the regular compressive tests, the same test setup was used for a compressive stress-strain test under force control to determine the constitutive behavior of the

concrete. The only difference from regular compressive tests was the usage of an axial extensometer around the cylinder to measure the strain (see Figure 6.27). To obtain the stress-strain curve up to the failure point, six sample cylinders from each set were instrumented with the axial extensometer and tested on the first DOT. The axial extensometer consists of two displacement transducers attached to the opposite side of the cylinder to measure the average strain based on the readings from both transducers. The plots showing the stress-strain curves can be found in Figure 6.28 and the results are summarized in Table 6.4. For most of the sample cylinders under stress-strain testing, the post-peak constitutive behavior could not be captured. This is because the axial extensometer fell off the cylinder surface as the concrete reached the peak strength and spalling occurred, leading to unreliable data afterwards.

(a) (b)

Figure 6.27 **(a) Stress-strain compressive test setup for the concrete; (b) the typical mode of failure of the tested cylinders.**

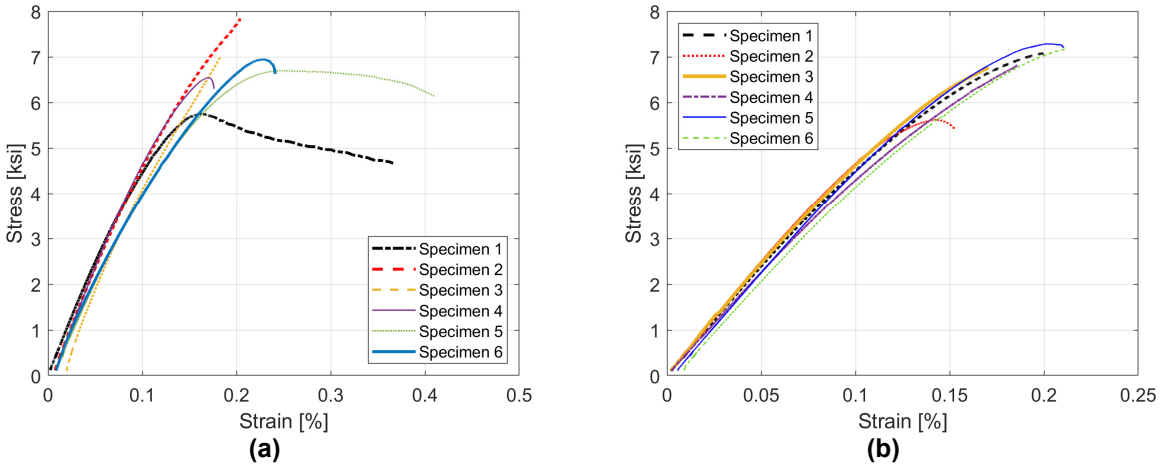

Figure 6.28 **Stress-strain curves for (a) column concrete; and (b) foundation/cap beam concrete.**

Table 6.4 Stress-strain compressive test results for the concrete.

Material	Age [day]	Stress at peak [ksi]			Strain at peak		
		Mean	St. Dev.	COV	Mean	St. Dev.	COV
Column Concrete	DOT	6.793	0.676	0.099	0.0020	0.0003	0.164
End member (foundation/cap beam) Concrete	DOT	6.789	0.610	0.090	0.0018	0.0003	0.137

6.8 INSTRUMENTATION

Different types of instruments were installed to monitor different aspects of the response, including forces, displacements and strains, during the test. All the sensor data was sampled at 20 Hz.

6.8.1 Load Measurements

Two different types of equipment were used to measure the load during the test. These include the load cell and the hydraulic pressure jack.

6.8.1.1 Load Cell

As described in section 3.8.1, load cells are essential for the actuator control and for measuring the total forces applied to the test specimen. Two load cells, one for each actuator, were used to measure the actuator forces (see Figure 6.29). The vertical actuator was used to apply the gravity and the earthquake loads under force control. The horizontal actuator was running in displacement control and the resisting forces measured by the load cell were directly used in the numerical integration to advance the calculations. Thus, the load cell measurements were indispensable in both directions. The load cells were calibrated before the test.

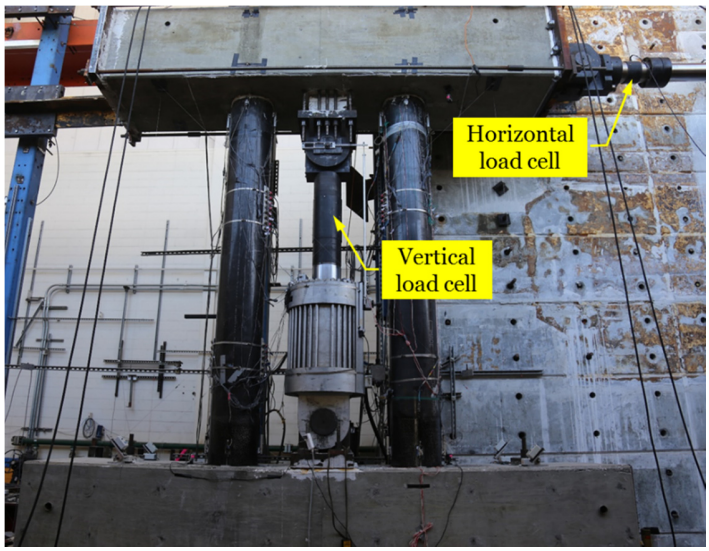

Figure 6.29 Horizontal and vertical actuator load cells.

6.8.1.2 Pressure Jack

The hydraulic pressure jacks in this study have two tasks: prestress the PT bars and obtain the PT bar forces. Two pressure jacks were used, each one being connected to an individual two-stage pump (see Figure 6.30). During the prestressing stage, the pump pushed the oil into the reservoir of the jack and drove the piston up. This way the PT bar also got extended and the prestressing force was developed accordingly. When the prestressing force reached the target value of 40% guaranteed ultimate tensile strength (GUTS), the returning valve of the pump was locked to prevent the backflow of the oil and to maintain the oil volume during the test.

(a) (b)

Figure 6.30 (a) Hydraulic pressure jacks on top of the test specimen; (b) the two-stage pump.

The PT bar forces were not measured directly. Instead, a pressure transducer with maximum measuring range of 10 ksi was installed on each pressure jack to measure the oil pressure,

which then gets converted into forces by multiplying the pressure value with the jack's piston area. To make sure the conversion is reliable, the pressure jacks were calibrated on the Universal Testing Machine to obtain the load-pressure curves. Two cycles of loading-unloading were conducted and the obtained curves for each jack are shown in Figure 6.31. The linear relationship for each jack is a good indication of the conversion reliability.

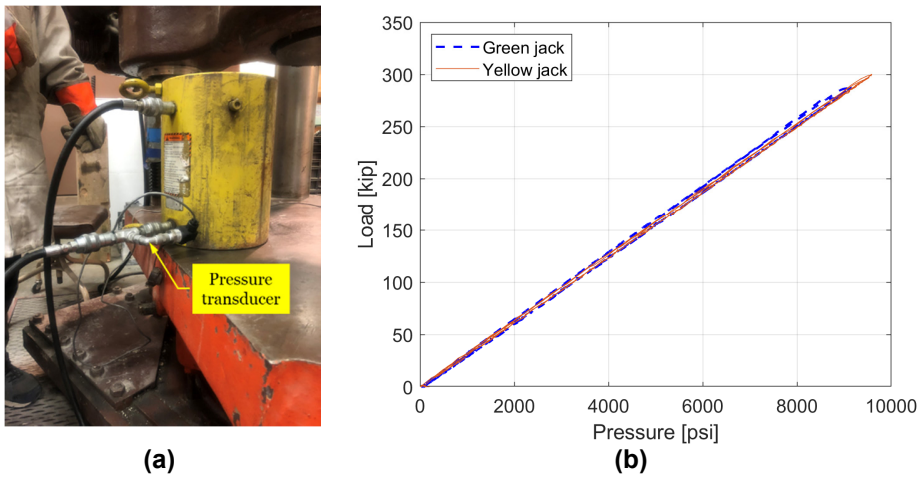

Figure 6.31 **(a) Pressure jack calibration setup; (b) load-pressure curves for the two used pressure jacks.**

6.8.2 Displacement Measurements

Similar to the V-connector study, the displacements were measured using long- and short-range displacement transducers. The long-range displacement transducers were linear WPs with ±20 in. stroke. Six WPs were installed on the instrumentation frames away from the test specimen, with two in the direction of the lateral loading to measure the relative displacements between the two end members (cap beam and foundation) and four on the north side of the cap beam to monitor the out-of-plane displacements and rotations, if any. In addition, four diagonal and four vertical WPs were triangulated in pairs between the cap beam and the foundation to provide redundant measurements of the relative displacements. Note that since the foundation is fixed, the obtained relative displacements are in fact the applied displacements to the cap beam. Thin steel strings (piano wires) were utilized to connect the cords of the transducers to the target points mounted on the test specimen. Figure 6.32 shows some details of the WPs installation. The layout of all WPs is schematically represented in Figure 6.33 and Figure 6.34.

(a) (b)

Figure 6.32 (a) WPs on the north-side instrumentation frame; (b) WPs between the cap beam and the foundation.

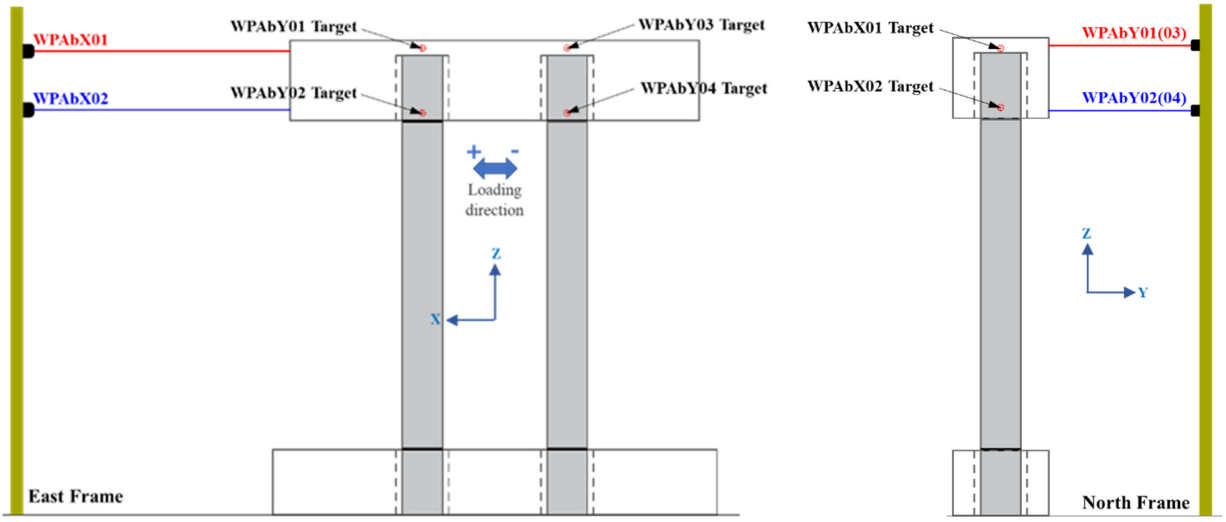

(a) E-W elevation view (b) N-S elevation view

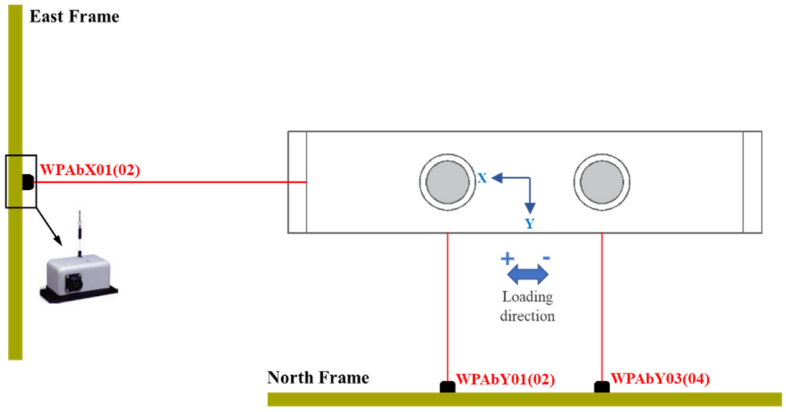

(c) Plan view

Figure 6.33 Layout of WPs on the instrumentation frames.

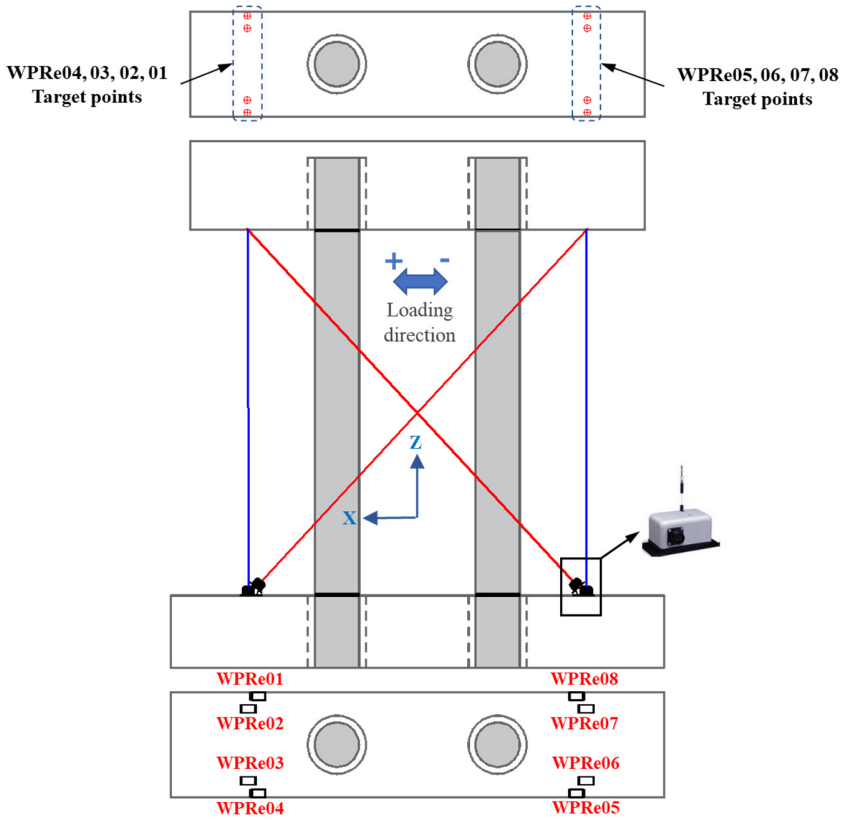

Figure 6.34 Layout of WPs between the two end members (cap beam and foundation).

The short-range displacement transducers were LVDTs with two ranges of stroke: ±1.0 in. and ±2.0 in. The goal was to measure the gap opening and the rocking behavior. Four LVDTs were installed at each rocking interface, with two longer ones along the lateral loading direction where the main rocking behavior is expected to take place, and two shorter ones orthogonal to the loading direction. Flat aluminum plates with polished surfaces were placed underneath the tips of the LVDTs, see Figure 6.35. Figure 6.36 shows the layout of all sixteen LVDTs being installed.

(a) (b)

Figure 6.35 (a) LVDTs installed at the bottom interface; and (b) those at the top interface.

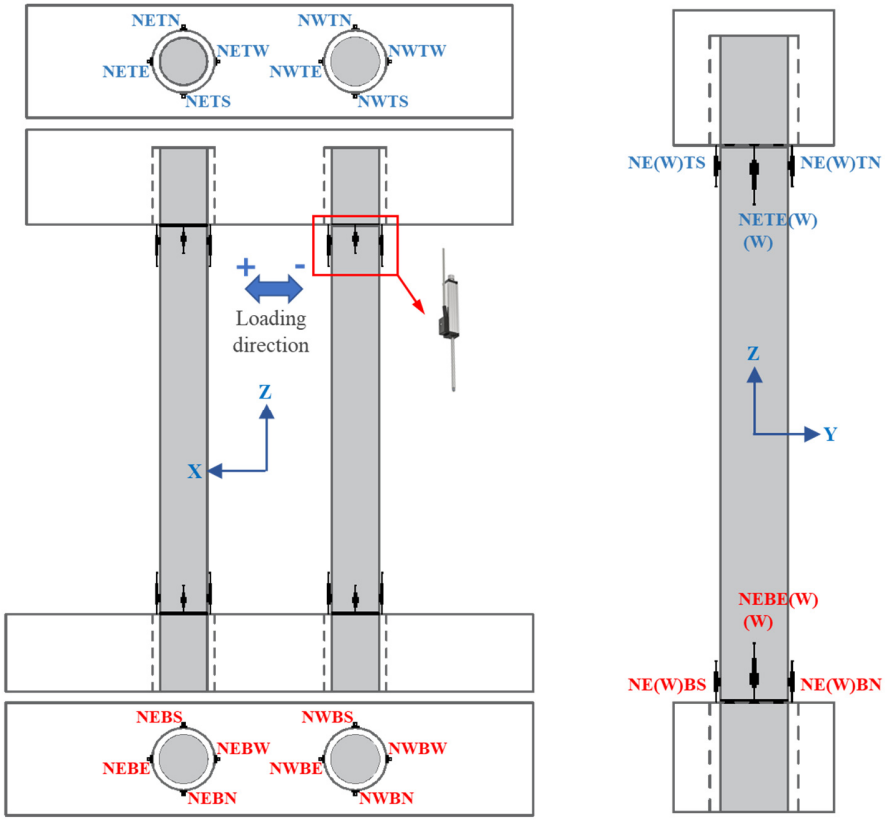

(a) E-W elevation view (b) N-S elevation view

Figure 6.36 Layout of the LVDTs at the rocking interfaces.

6.8.3 Strain Measurements

Different types of strain gauges were extensively installed to measure strains on the reinforcing bars and the column steel shells. The steps for strain gauge installation can be found in section 3.8.3.

6.8.3.1 Columns

Figure 6.37 and Figure 6.38 depict the strain gauges layout for the columns. Ten regular strain gauges were installed in the debonded lengths of three energy dissipaters at each rocking interface and in each column to measure the strains experienced during the test. Eight additional strain gauges were installed outside the debonded lengths of the longitudinal reinforcement in the east column to determine the strain distribution.

For both columns, four strain gauges were vertically installed on the top embedded steel shell segment orthogonal to the loading direction, to measure the strains produced by the transfer of the axial forces between the columns and the cap beam. Eight horizontal strain gauges were also installed on diametrically opposite points that are 2.5 in. and 8.5 in. away from each rocking

interface along the loading direction to estimate the circumferential strain behavior of the steel shell.

For the west column, the steel shell segments embedded inside the sockets were fitted with four rosette gauges at each end: one gauge at each point 2 in. from the end of the embedded segment and on diametrically opposite points along the loading direction (see Figure 6.39). Finally, two strain gauges were installed on both PT bars at the same location above the cap beam but within the portion being post-tensioned to measure the PT bar strains.

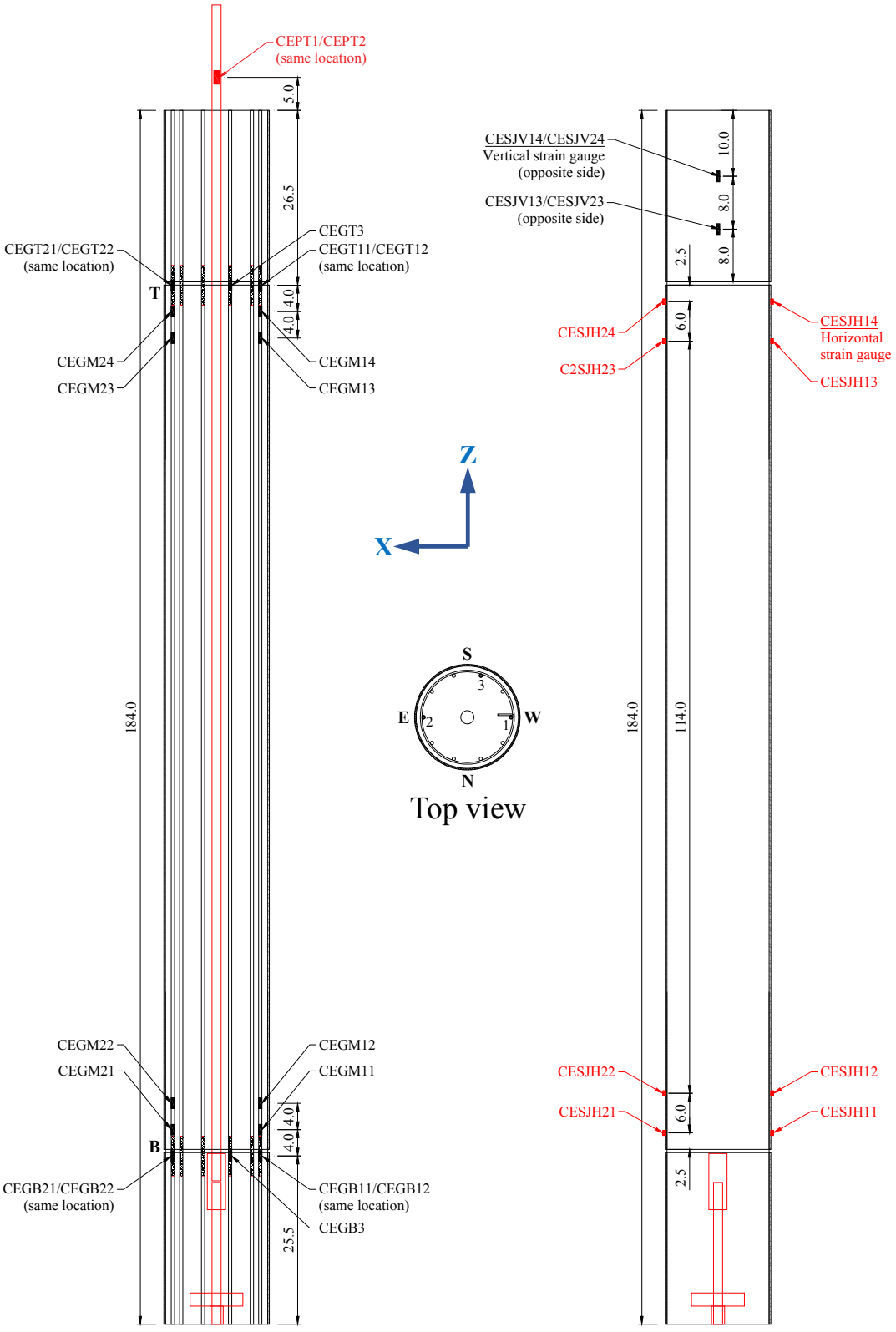

Figure 6.37 Strain gauges layout of the east column.

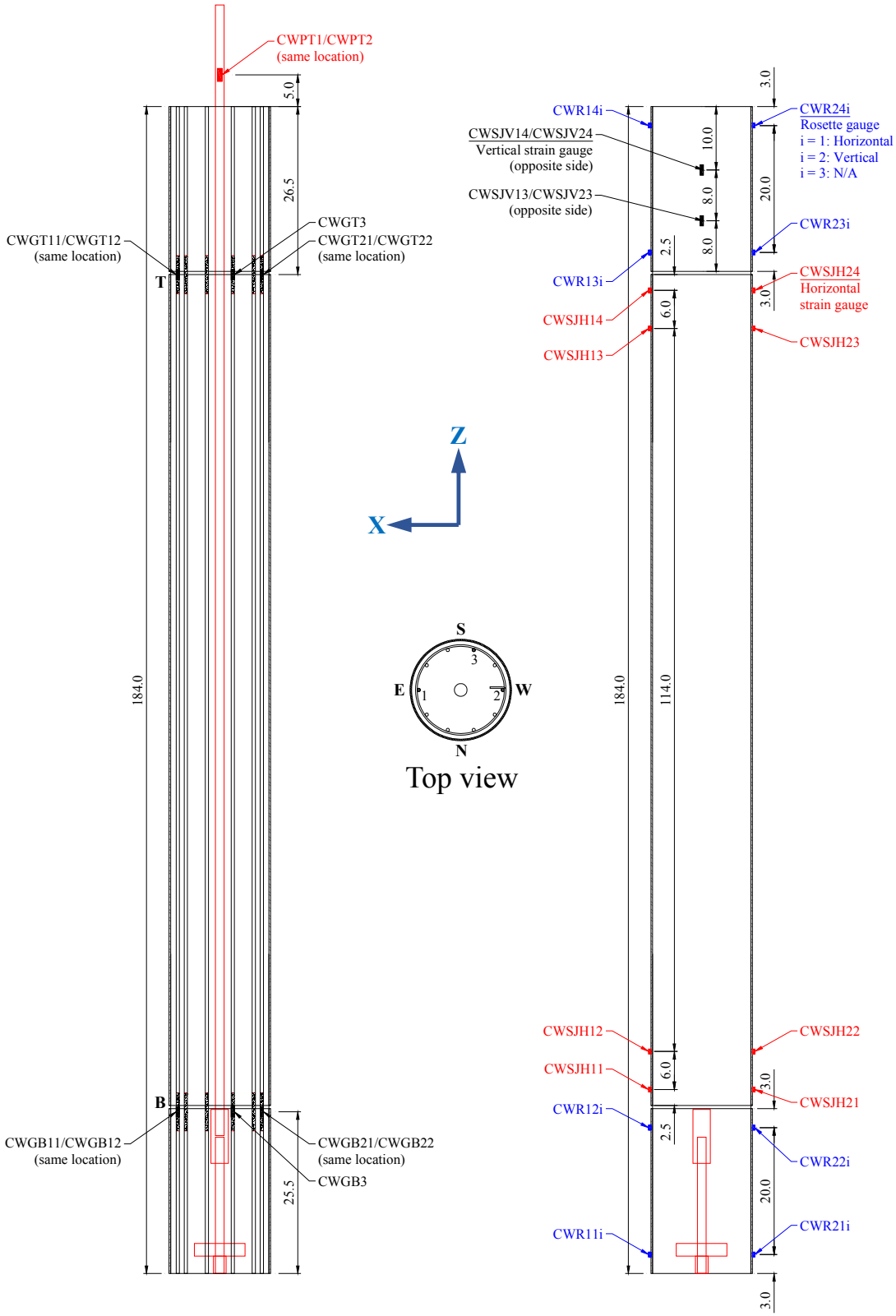

Figure 6.38 Strain gauges layout of the west column.

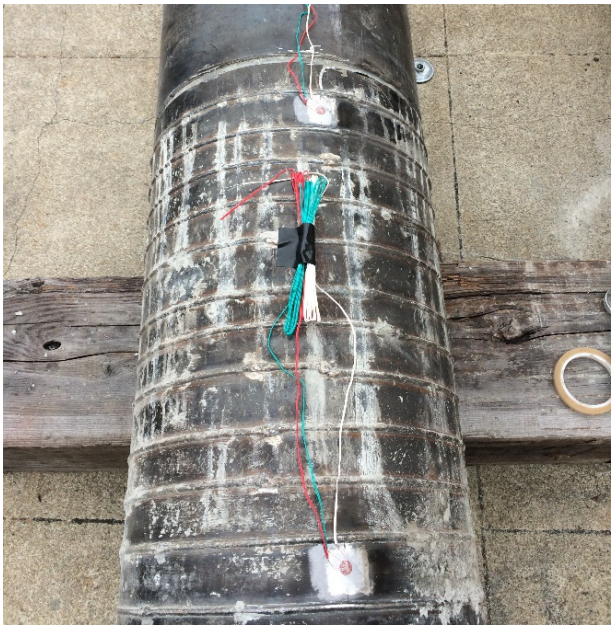

Figure 6.39 Rosette strain gauges on the steel shell.

6.8.3.2 Cap Beam

A total number of sixteen strain gauges were installed in the cap beam, with eight on the stirrups and eight on the top/bottom layer of the longitudinal reinforcement. As shown in Figure 6.40 and Figure 6.41, the stirrup strain gauges were placed above each socket to monitor any possible strains caused by the punching shear effect, while the strain gauges on the longitudinal reinforcing bars were placed at locations where the maximum positive/negative bending moments are expected to occur. Based on the design, the cap beam should remain essentially elastic and no reinforcement yielding should be expected.

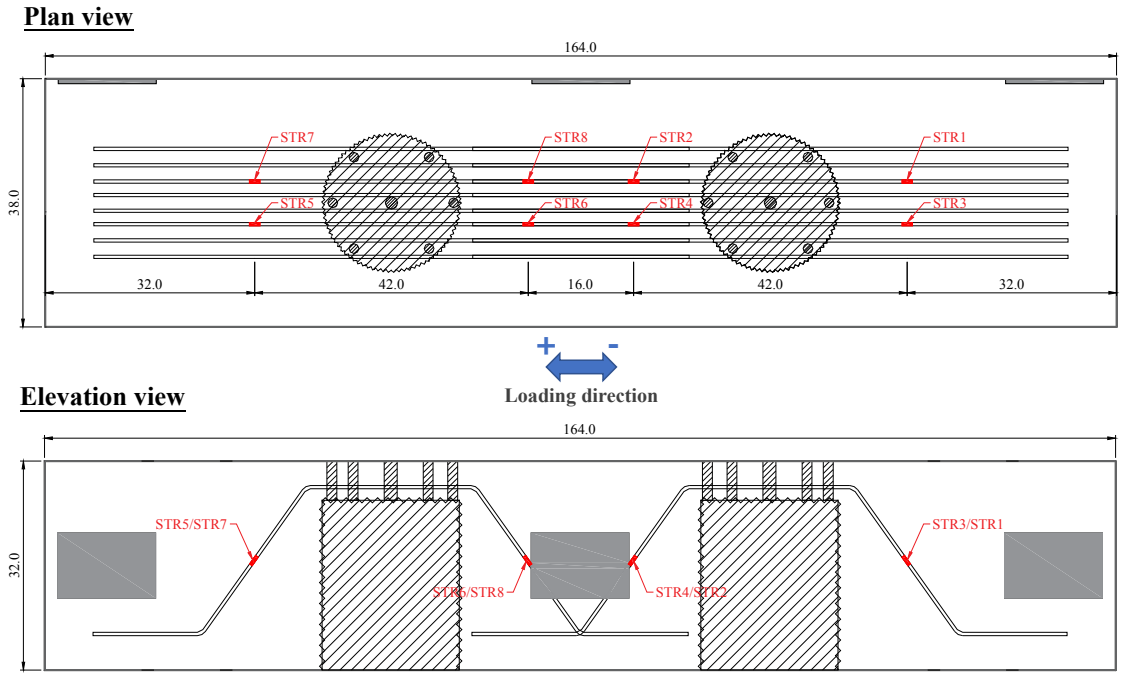

Figure 6.40 Strain gauges layout on the stirrups of the cap beam.

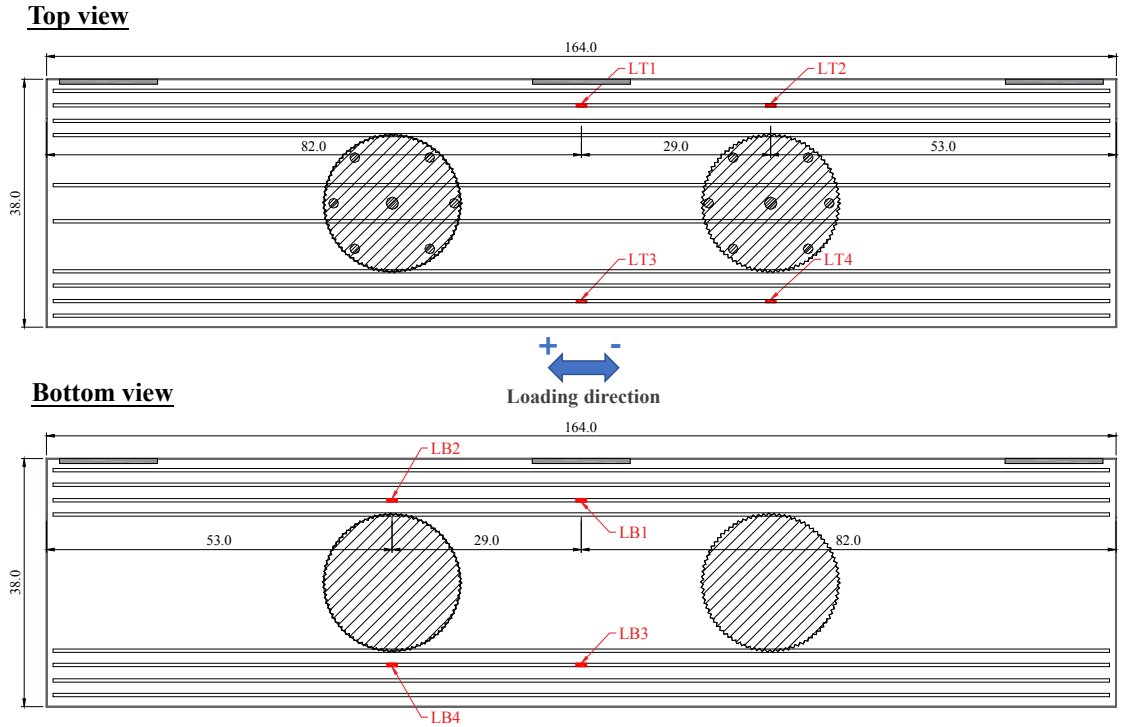

Figure 6.41 Strain gauges layout on the longitudinal reinforcement of the cap beam.

6.8.4 Cameras

Cameras were used extensively throughout the experimental study. Figure 6.42 shows the arrangement of various cameras used during the test. For all the test runs, a Canon EOS 6D digital single-lens reflex (DSLR) camera was placed on the north side of the test specimen to capture the overall response. In addition, three GoPro cameras were mounted at the rocking interfaces to capture the opening and closing of the gaps. All cameras performed time-lapse photography, taking high-quality pictures at 10 second intervals because of the slow test speed.

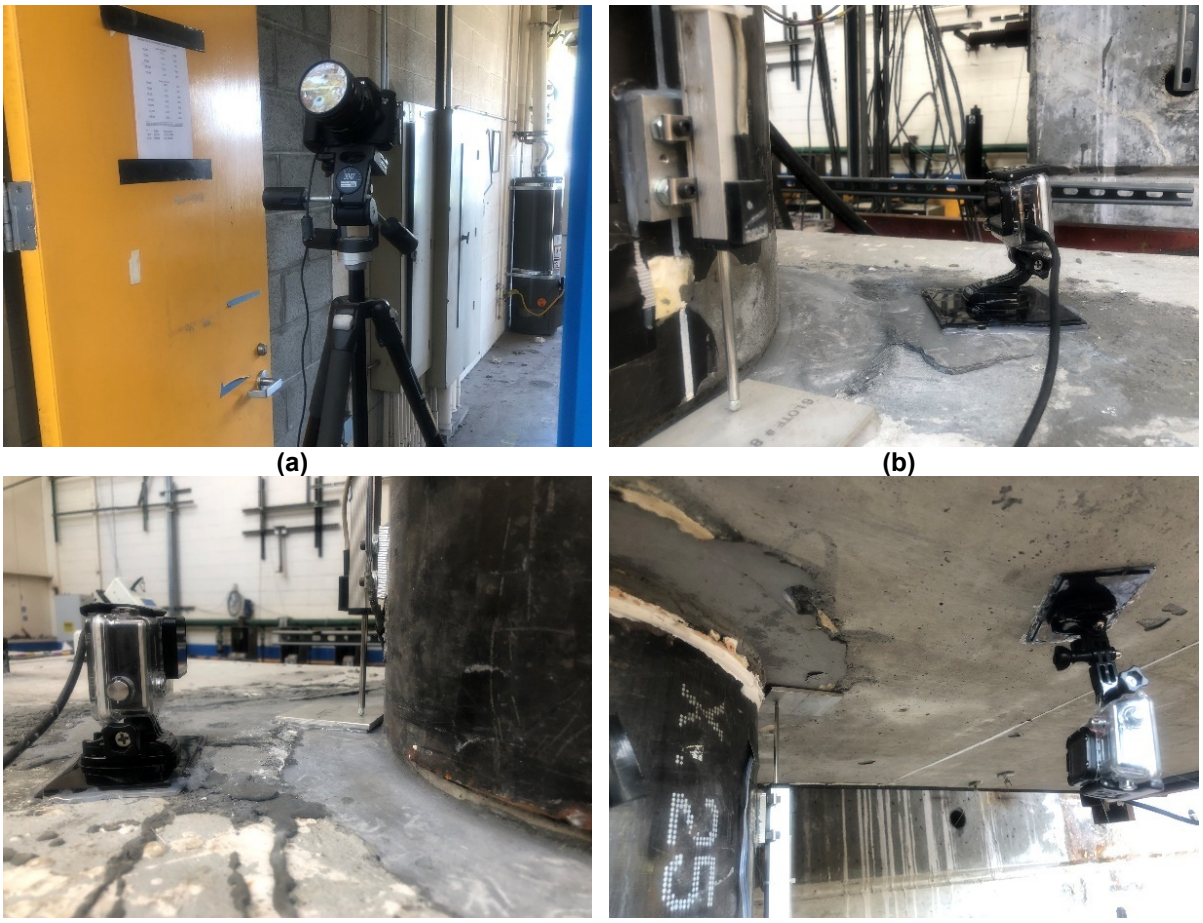

(a) (b)

(c) (d)

Figure 6.42 **(a) DSLR camera on the north side and GoPro cameras at (b) west column bottom; (c) east column bottom; (d) west column top.**

7 Hybrid Simulation of a Resilient Bridge Bent Design: Phase I

As mentioned in Chapter 2, since HS combines the benefits of the quasi-static testing method and the shaking table test (real-time HS is not considered here as traditional facilities for quasi-static tests are insufficient), it can be as cost-effective as the quasi-static test while at the same time providing sufficient realism comparable to the shaking table test. If rate-dependency of the material response is not of major concern, the results of the HS experiment and those from a shaking table test performed on the same structural system should be reasonably close. However, to the author's best knowledge, few researchers have been focused on the comparison between these two test methods.

This chapter describes the phase I HS of the resilient bridge bent, with the intent to fulfill the abovementioned comparison. Before discussing the HS results, the previously conducted shaking table test (Nema, 2018) is briefly recapped, including the derivation of the test specimen, the selected input ground motions and the main test results. Next, the detailed implementation of a new HSS in Matlab/Simulink (MathWorks, 2015) environment is provided. This HSS was successfully verified by a HS trial run for various aspects, e.g., the actuator control quality, the implemented numerical integration and interpolation, and the back and forth communication. The parameters in the HS test were estimated from the shaking table test results for a more reliable representation of the dynamic system.

Six ground motion records measured directly from the accelerometers on the shaking table were repeated in this phase of the HS experiments, i.e., phase I HS. The main part of the post-processing herein is dedicated to the comparison between the HS test and the shaking table test results. Some other relevant response quantities are also presented.

7.1 SHAKING TABLE TEST SUMMARY

An early study on the proposed bridge subsystem was conducted in 2017 at the PEER Earthquake Simulation Laboratory (Nema, 2018). The test specimen represents a 35% scale (i.e., length scale factor S_L = 2.857), two-column bridge bent originated from an existing bridge located in a high seismicity region. It was tested under dynamic loads arising from simulated ground motions produced by a shaking table. Inertia forces were provided by six concrete blocks (47 kips) post-tensioned to the cap beam and the cap beam itself (22 kips) for a combined weight of 69 kips, simulating the portion of the bridge superstructure weighing 573.3 kips over two columns. The

scale factor for the weight S_W was chosen to be S_L^2 instead of S_L^3 in an attempt to match the stresses of the columns. Figure 7.1 shows the setup and specimen configuration from the shaking table test. Several ground motions with one horizontal and the vertical component were applied. The ground motions were selected and scaled according to targeted lateral displacement demands as predicted by preliminary numerical simulations. The dynamic response of the specimen was monitored using a dense instrumentation setup. Verification of the system's re-centering capabilities and accuracy of the analysis methods were of primary interest in the shaking table test study.

(a) View from northeast (b) View from northwest

Figure 7.1 Test setup used for the shaking table test (photo credit: Robert Cerney, laboratory technician).

7.1.1 Prototype Bent Development

The prototype bent used in the planning of the shaking table test was derived from an existing bridge: the Massachusetts Avenue Over Crossing (MAOC) located in San Bernardino, California near the I215/HW210 interchange in close proximity to the San Andreas Fault. It is noted that this prototype bridge was used for developing the test specimen for the shaking table test, but the same prototype bridge employed in the HS test of the V-connector (i.e., the Jack Tone Road On-Ramp Overcrossing) was used in phase II HS of the bridge bent as described later. There are two main reasons for this change in the prototype bridge: (1) to explore the two studied systems (V-connector and resilient bridge bent) using the same prototype; and (2) the modifications of the prototype bent by considering only the edge columns (described below) make the application of HS on the MAOC bridge inconvenient to explore the system level response.

The as-built MAOC bridge consists of five asymmetric spans of lengths 15.0 m, 28.8 m, 28.0 m, 30.4 m, and 23.8 m for a total bridge length of 126 m (415 ft). The four bent caps are skewed with respect to the bridge post-tensioned box girders to match the roadway underneath it. Each bent cap is supported on four 1.22 m diameter reinforced columns with 22 No.36 (#11) mild steel. The girder ends rest on isolated shear keys formed by bearing pads placed between the

girders and the abutments. The elevation view and plan view of the bridge are shown in Figure 7.2, while a typical bridge bent is shown in Figure 7.3.

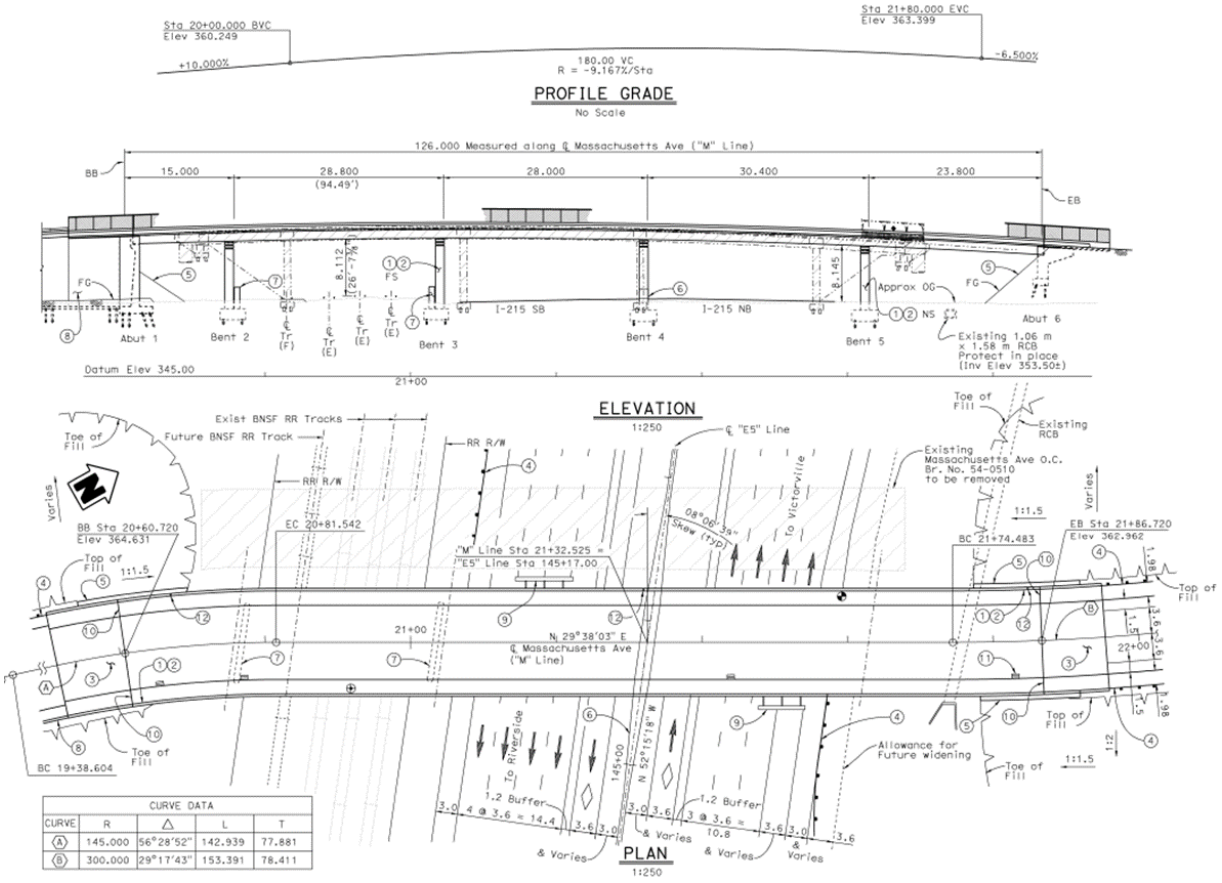

Figure 7.2 Elevation and plan views of the MAOC bridge (source: Caltrans structural drawings).

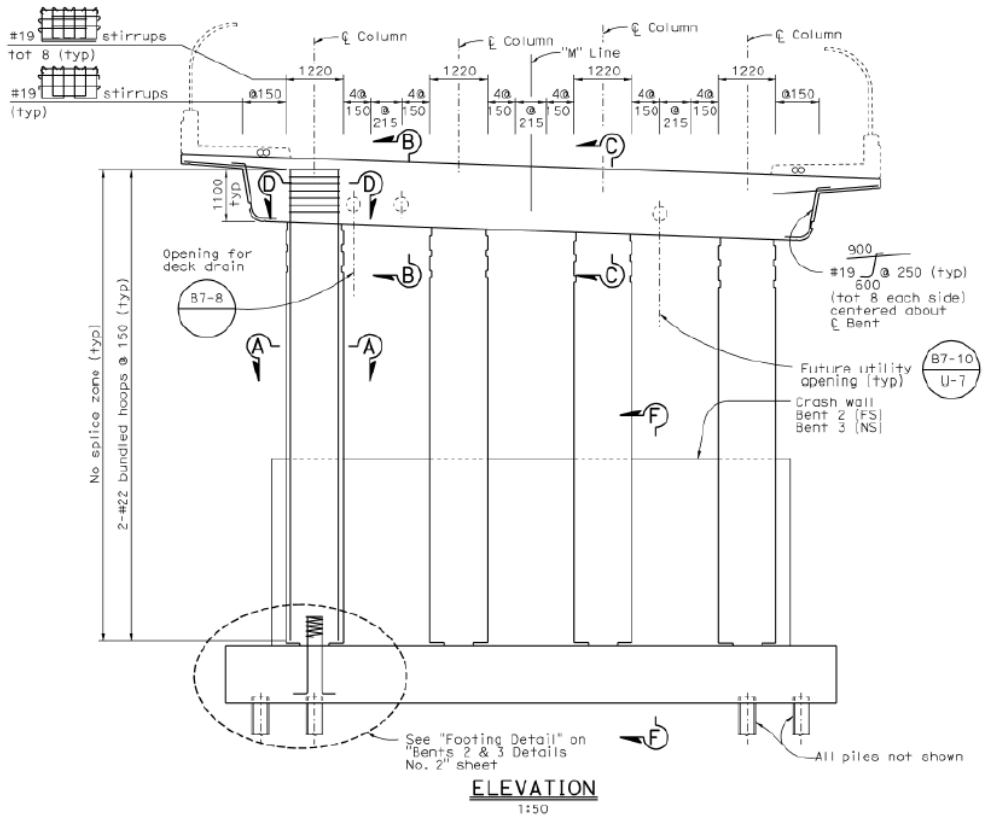

Figure 7.3 Elevation view of a typical bent of the MAOC bridge (source: Caltrans structural drawings).

In order to better represent the bridge behavior in the test, resilient columns were incorporated into a 3D OpenSEES (McKenna et al., 2000) model of the bridge by replacing the as-built bridge columns. The 3D bridge model was originally developed for studying the seismic response with several types of shear keys (Beckwith, 2015). The modeling of the resilient column was developed and validated against several test results (Guerrini et al., 2015).

For the redesign of the bridge utilizing resilient columns, a portion of the mild reinforcing steel in the conventional design was replaced with PT reinforcement. The aim for the replacement was to maintain similar strength between the conventional and the new design. This was achieved by matching the combined yield strength of mild and PT steel in the hybrid design to the yield strength of mild steel in the conventional design. The resilient column consists of ten No. 36 (#11) mild steel bars and 8×4 15 mm Grade 270 strands stressed at 40% GUTS. A representation of the cross sections of the as-built conventional column and the resilient column is shown in Figure 7.4. An effective mild steel debonded length of 1.22 m was used for the resilient column configurations, which was equal to 0.5 m applied debonding and additional 20 bar diameters (0.72 m) to account for the development length on either side of the interface. A 12.7 mm thick steel jacket was used to confine the entire column. The column clear height was assumed to be precast, and the column-beam interface was assumed to be made of a 25.4 mm thick layer of high-strength mortar. Finally, the debonded PT strands were assumed to terminate 0.78 m away from the column ends, which is at the location of the center of gravity of the bent cap.

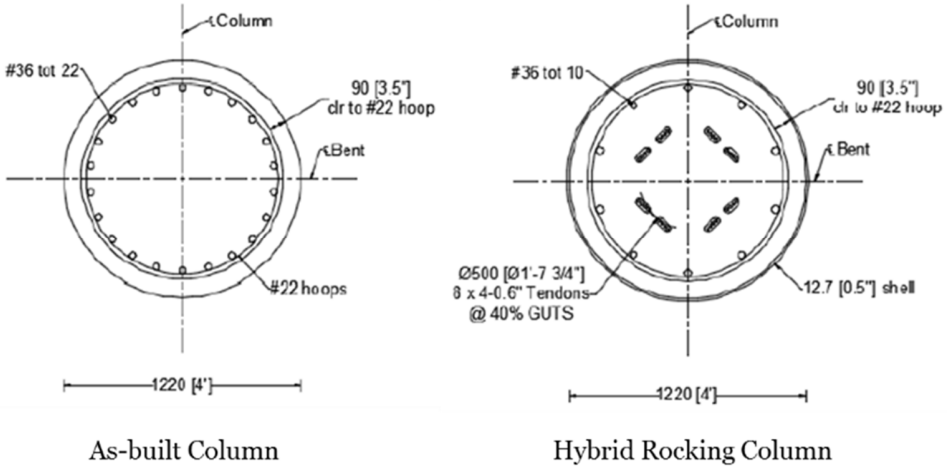

Figure 7.4 **Cross section representation of the as-built column (left) and the re-centering column (right) (Nema, 2020).**

With the details of the resilient columns established above, a full-scale prototype bridge bent was developed representing the specimen to be tested on the shaking table. This prototype, derived from bent #3 of the MAOC bridge, contains two resilient columns instead of four (see Figure 7.5). This change was made to maximize the utilization of the shaking table in terms of force and displacement capacities, and to optimize the experimental cost. The modification necessitated further changes in the prototype's geometry, specifically the distance between the columns, to improve similarity (in terms of column axial stresses) between the two columns in the prototype bent and the two marked edge columns in the MAOC bridge bent, refer to Figure 7.5.

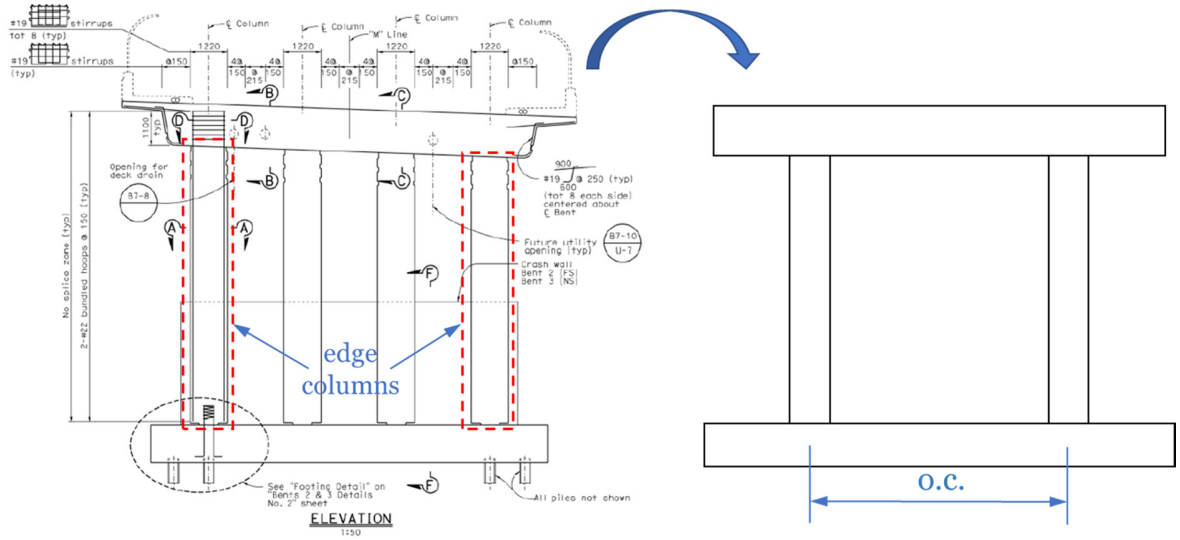

Figure 7.5 **Prototype bent derived from the MAOC bridge for designing the test specimen.**

The analytical modeling of the prototype bent starts with two resilient columns separated by a distance of 9.2 m, same as the center-to-center distance between the two edge columns in bridge bent #3. The columns were modeled in the exact same way as those in the updated MAOC bridge with a clear height of 9.6 m, the average clear height of the columns in bent #3. The foundation and cap beam dimensions were assumed to be the same as those in the MAOC bridge. The effective inertia and gravity load corresponding to the two columns were inferred to be 2.55 MN (573.3 kips) for the prototype bent from the analysis of the as-built MAOC bridge. To obtain comparable results from the modified prototype bent and the original bridge, the bridge's skew angle was chosen to be zero and only transverse and vertical excitations were used. This is because the modified prototype to be used for scaling to the specimen size contains only one single bent and no actual girders providing constraints in the longitudinal direction are present. The parametric study for investigating the column distance in the modified prototype bent utilized the fault normal and vertical components of the ground motions measured at the Sylmar-Olive View Medical Center station during the 1994 Northridge earthquake. The axial loads in the columns of this modified prototype bent were compared to those in the outer columns of bent #3 in the as-built bridge for different column distances. Figure 7.6 shows the responses for a few selected distance values. The "initial load" in the plot is the axial load of the column due to gravity. On the basis of these results, a column center-to-center distance of 4.2 m was finally selected for the modified prototype bent configuration to be used for designing the shaking table test specimen.

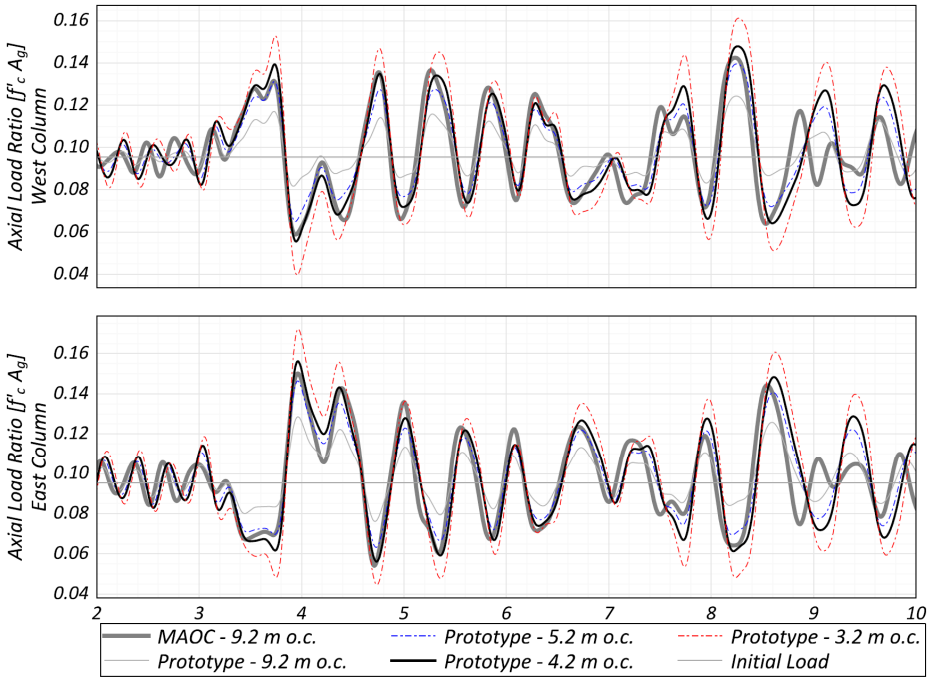

Figure 7.6 Comparison of axial loads between the edge columns in the MAOC bridge and the columns in the modified prototype bent (Nema, 2018).

7.1.2 Input Ground Motions

The numerical model for the test specimen, after proper scaling down of the modified prototype bent presented in previous section, was used to select a set of near fault earthquakes to be imposed

on the specimen for dynamic testing. The selection was made based on expected peak drift as calculated by the numerical model, in comparison with the design drift capacity of the system defined by the yielding of the PT bars and calculated to be 7%. The selected motions represent very small (0.6% drift), small (1.8% drift), moderate (4% drift) and large (> 5% drift) events.

Nine ground motions were planned in the initial loading protocol. To investigate the effect of lower intensity aftershocks, the test was not conducted with continuously increasing demands; instead, a larger motion was followed by smaller intensity of shaking until a peak drift of 4% was reached. For larger drifts, ground motion polarity was occasionally switched to avoid damaging the specimen in only one direction. Significant structural integrity remained after the initially planned sequence and the scope was expanded with three additional tests. Details of the final ground motion sequence are listed in Table 7.1 in the order they were imposed onto the specimen.

Table 7.1 Input ground motion sequence for the shaking table test.

EQ #	Event Name	Station Name	Unscaled PGA [g]	Scale Factor	Expected Drift [%]
01	Landers, 1992	Lucerne	0.72	0.90	0.6
02	Landers, 1992	Lucerne	0.72	0.90	0.6
03	Tabas, 1978	Tabas	0.85	-0.90	1.8
04	Kocaeli, 1999	Yarimca	0.30	1.00	0.6
05	Northridge, 1994	RRS	0.85	0.81	4.0
06	Duzce, 1999	Duzce	0.51	1.00	1.8
07	Northridge, 1994	NFS	0.72	-1.20	4.0
08	Kobe, 1995	Takatori	0.76	-0.80	5.0
09	Kobe, 1995	Takatori	0.76	0.90	7.0
10	Tabas, 1978	Tabas	0.85	-0.90	-
11	Northridge, 1994	RRS	0.85	0.81	-
12	Kobe, 1995	Takatori	0.76	-0.80	-

7.1.3 Test Results

The testing took place over two days, with EQ1 to EQ4 on day one and the remaining excitations on day two. Some key test results are presented below.

7.1.3.1 Hysteretic Responses

The hysteretic responses during the tests are shown in Figure 7.7. Note that the lateral forces were normalized by the specimen inertia weight and expressed as base shear coefficients. The pinched shape or the "flag-shape" of the hysteresis loop is the characteristic behavior of re-centering systems, with very small residual displacement but peak capacity comparable to that of a conventional ductile system.

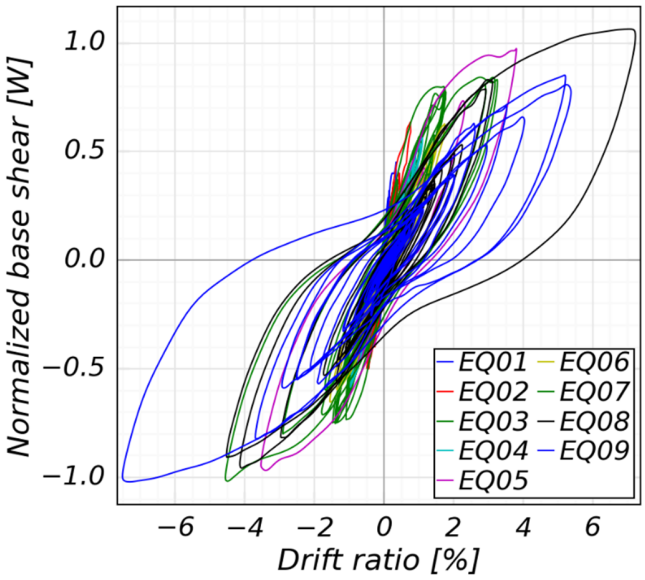

Figure 7.7 Overlaid hysteretic responses from EQ1 to EQ9 (Nema, 2018).

7.1.3.2 Drift Ratios

The peak and residual drifts from different excitations are shown graphically in Figure 7.8. Rotations measured at the rocking interfaces of the south column can be found in Figure 7.9. The re-centering behavior of the system is evident in the residual drift and rotation at the end of each motion. Additionally, the rotation time histories at column interfaces of the south column from EQ8 and EQ9 are shown in Figure 7.10. It can be seen that the rotation closely followed the drift, indicating that the column behaved nearly like a rigid body over the clear height.

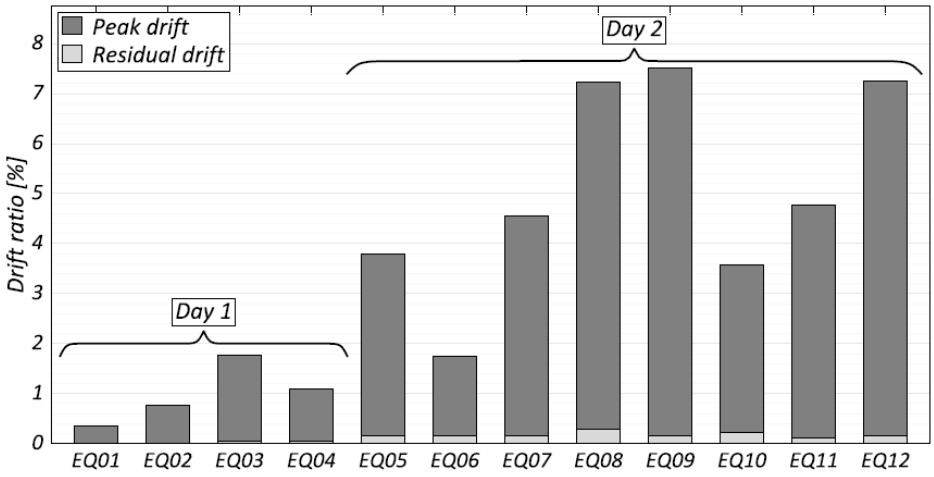

Figure 7.8 Peak and residual drift ratios (Nema, 2018).

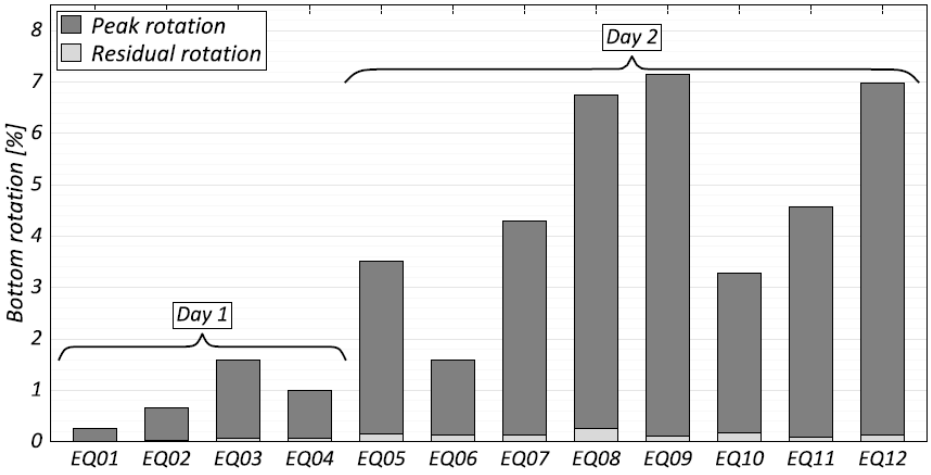

(a) South column bottom

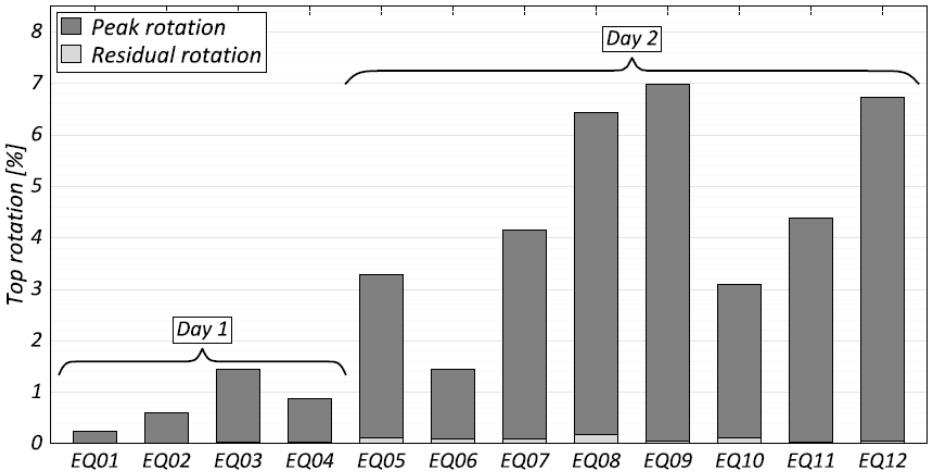

(b) South column top

Figure 7.9 Peak and residual interface rotations of the south column (Nema, 2018).

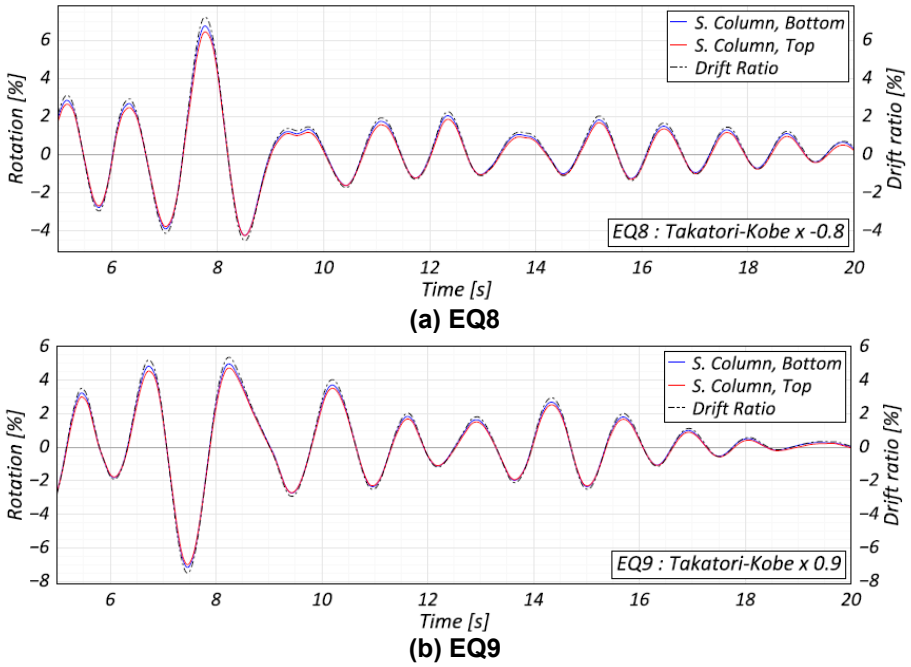

Figure 7.10 South column interface rotations in EQ8 and EQ9 (Nema, 2018).

7.1.3.3 Deformations

The maximum and the residual gap opening at the bottom interface of the south column from EQ9 are shown in Figure 7.11. Also shown below are the overall deformations of the test specimen at the instance of maximum gap opening. It can be seen that the rocking interface naturally formed near the location where the thin strip segment of the steel shell was removed, and that the gap closed completely at the end of each excitation, with only minor concrete spalling.

(a) South column interface, north side;
Δ = 5.4%

(b) South column interface, south side;
Δ = -7.5%

(c) South column interface, north side;
end of excitation

(d) South column interface, south side;
end of excitation

(e) Specimen deformation;
Δ = 5.4%

(f) Specimen deformation;
Δ = -7.5%

Figure 7.11 Specimen response in terms of gap openings at the bottom interface of the south column and the overall deformations at the peak drifts (EQ9).

7.2 DEVELOPMENT OF THE NEW HSS

7.2.1 System Description

The core of the HSS described in section 5.1.1 is the computational platform OpenSEES (McKenna et al., 2000) and the middleware OpenFRESCO (Schellenberg et al., 2008). These two platforms are nowadays among the most popular tools in conducting HS tests around the world. However, not only these two software programs have a steep learning curve, but also they may require some new developments for a specific experimental task, e.g., developing the PI660HybridSim interface software and the *TriangularActuators* experimental setup described previously in Chapter 5. In addition, some complicated experimental control methods in OpenFRESCO put high demands on the testing capacities in terms of both software and hardware for the available laboratory. Even if the idea of HS is quite straightforward, all these features make HS not so readily accessible to researchers in the Structural Engineering communities and set barriers to the development and popularity of the HS techniques. With the intent to make HS back to its easily understandable and tractable essence, a new HSS was developed, utilizing commonly available software and hardware components in most structural engineering laboratories.

Figure 7.12 shows the newly developed HSS. It consists of: (a) the computational platform Matlab/Simulink (MathWorks, 2015) which performs the numerical integration and the displacement interpolation; (b) dSPACE (2017), an interface hardware/software platform, which establishes the communication between the computational platform Simulink and the controller by performing digital to analog (D/A) and analog to digital (A/D) conversions; and (c) two MTS 407 controllers that drive the vertical and the horizontal hydraulic actuators. The execution steps are as follows: (1) For each integration time step, the two uncoupled single-degree-of-freedom (SDOF) equations are numerically solved in the Simulink model to compute the horizontal and the vertical displacements to be imposed to the test specimen; (2) The computed command displacements, after interpolation, are sent to the controllers using a built-in DAC (digital to analog conversion) Simulink block that comes with dSPACE. The DAC block (Figure 7.13) is used to convert the digital displacements to analog voltages that can be recognized by the controllers; (3) After applying the computed displacements to the specimen, the corresponding reactions (resisting forces) are measured by the load cell in each actuator and passed on to the controllers as analog voltages; and (4) The measured forces are sent to the computational platform though another built-in ADC (analog to digital conversion) Simulink block. The ADC block (Figure 7.13) converts the analog voltages to the digital force values before they are passed on to the time stepping integration algorithm to advance the solution to the next analysis time step.

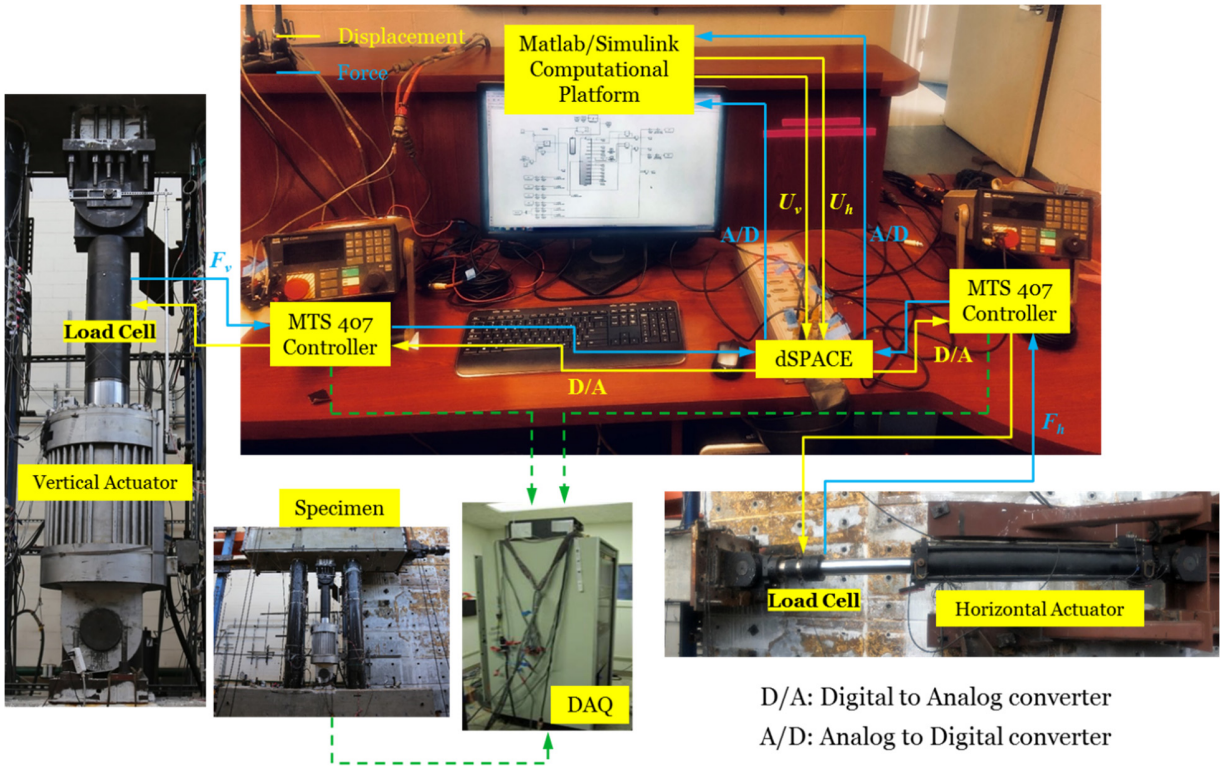

Figure 7.12 Main components and connectivity of the developed hybrid simulation system.

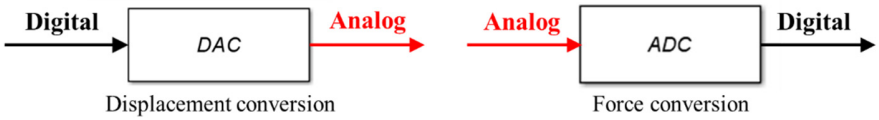

Figure 7.13 Built-in Simulink DAC and ADC blocks.

The hardware components of the dSPACE (2017) are the DS1104 R&D Controller Board that is installed in the PCI slot of the host PC and the CP1104 Connector Panel with 8 ADC and 8 DAC channels (Figure 7.14). The Simulink model used in the computations is developed in the host PC and compiled on the DS1104 R&D Controller Board for deterministic (i.e., fixed sample timed) real-time execution (Figure 7.15). Figure 7.16 shows the configuration settings for the Simulink compilation. The software component of the dSPACE is the ControlDesk which provides an interface to the developed Simulink model. The selected response quantities can be recorded for post-processing and plotted for real-time monitoring in the ControlDesk, see Figure 7.17.

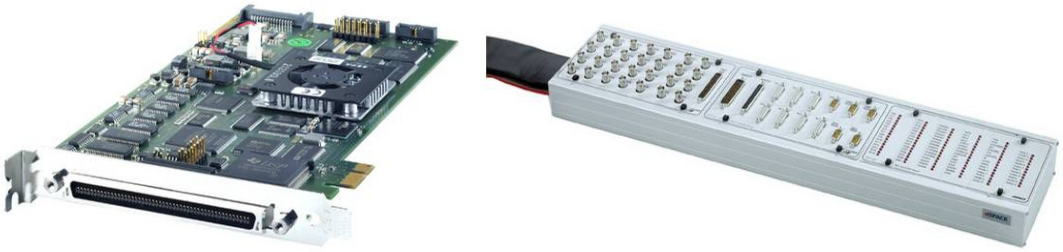

(a) (b)

Figure 7.14 **(a) DS1104 R&D Controller Board; (b) CP1104 connector panel with ADC and DAC channels (source: Internet).**

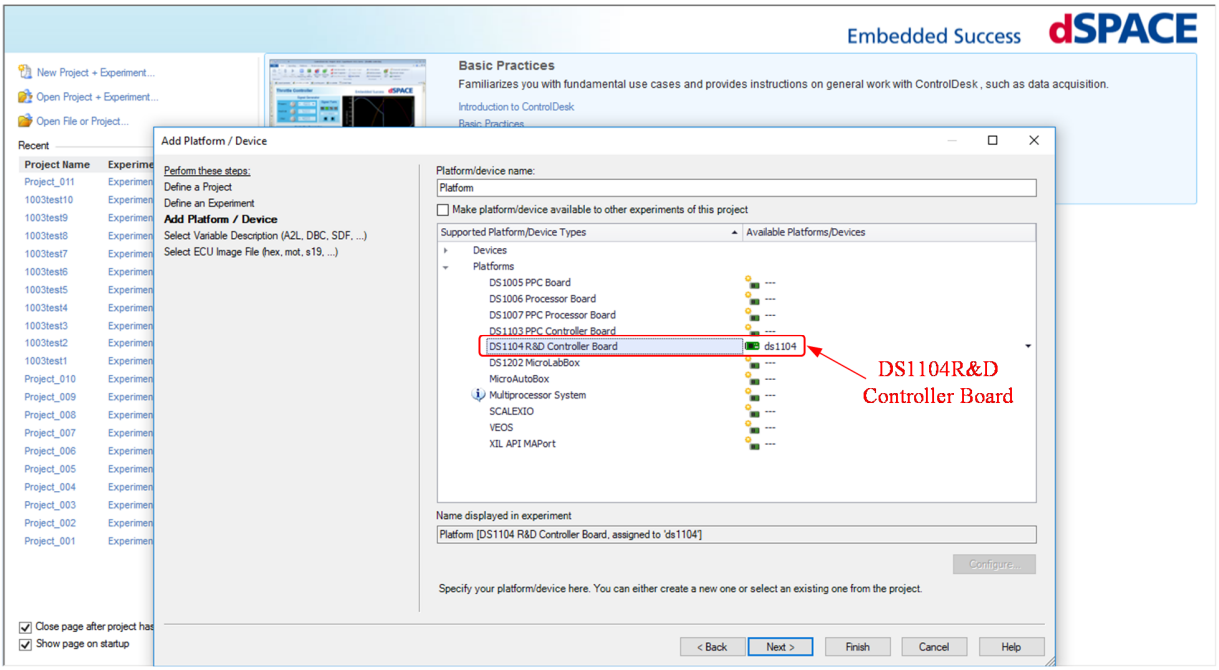

Figure 7.15 **Selection of DS1104R&D Controller Board for real-time execution.**

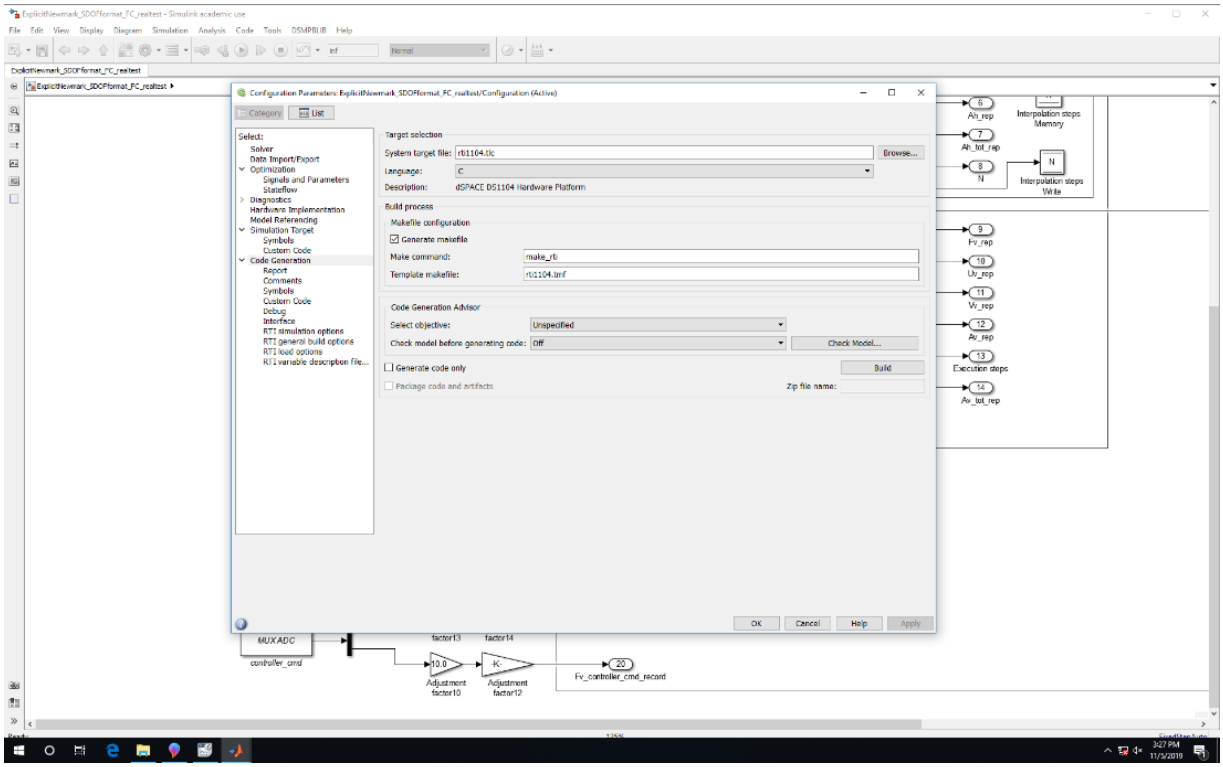

Figure 7.16 Simulink configuration settings.

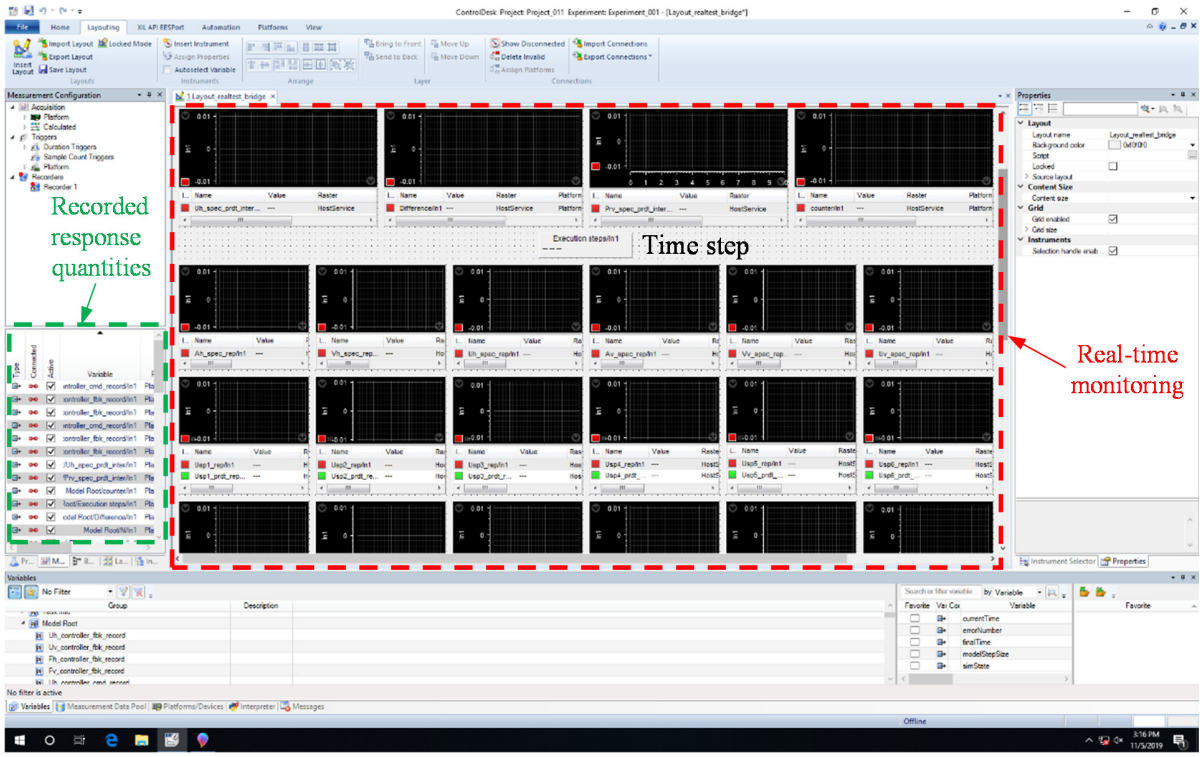

Figure 7.17 Screenshot of the ControlDesk software interface.

7.2.2 Substructuring

The simulated hybrid structure in phase I HS is described in Figure 7.18. The bridge bent with two self-centering columns was considered as the experimental substructure, while the inertia mass blocks attached to the top of the test specimen were removed and replaced by an analytical mass modeled in the computer along with the viscous damping. Considering the two-directional ground motion inputs in the shaking table test and that the responses from these two directions can be represented by two independent and uncoupled differential equations of motion, the horizontal and the vertical DOFs were formulated separately.

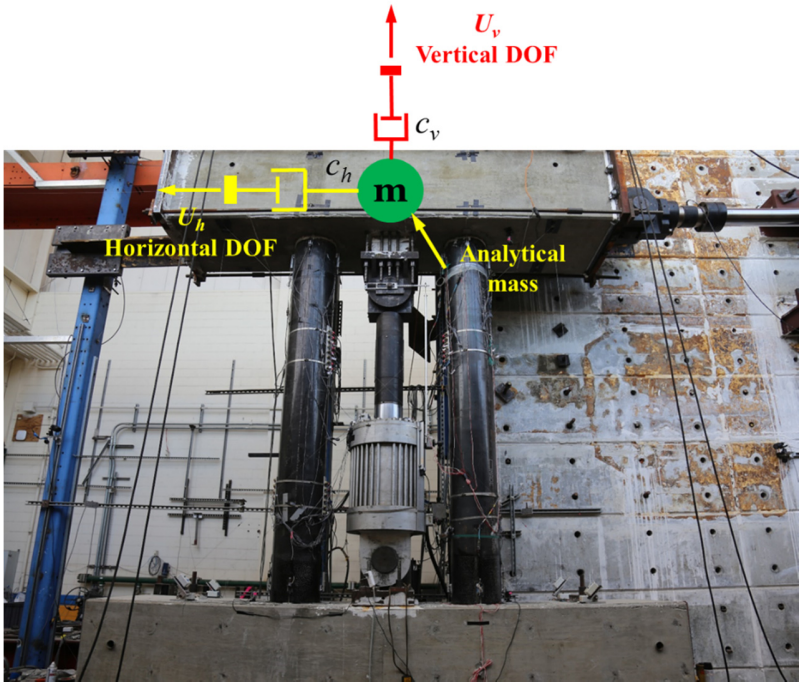

Figure 7.18 Experimental and analytical substructures for phase I HS.

7.2.3 Simulink Implementation

As mentioned before, two main tasks were accomplished on the Matlab/Simulink (MathWorks, 2015) computational platform: the numerical integration and the displacement interpolation. The developed Simulink model for phase I testing is shown in Figure 7.19, together with the roles of different parts of the model. The key component is the "if" action box highlighted in dashed line. The communication with controllers, response quantities output, and the displacement interpolation were implemented outside the "if" statement while inside the "if" action box, the implementation was related to numerical integration (see Figure 7.20). Details are presented in the following subsections.

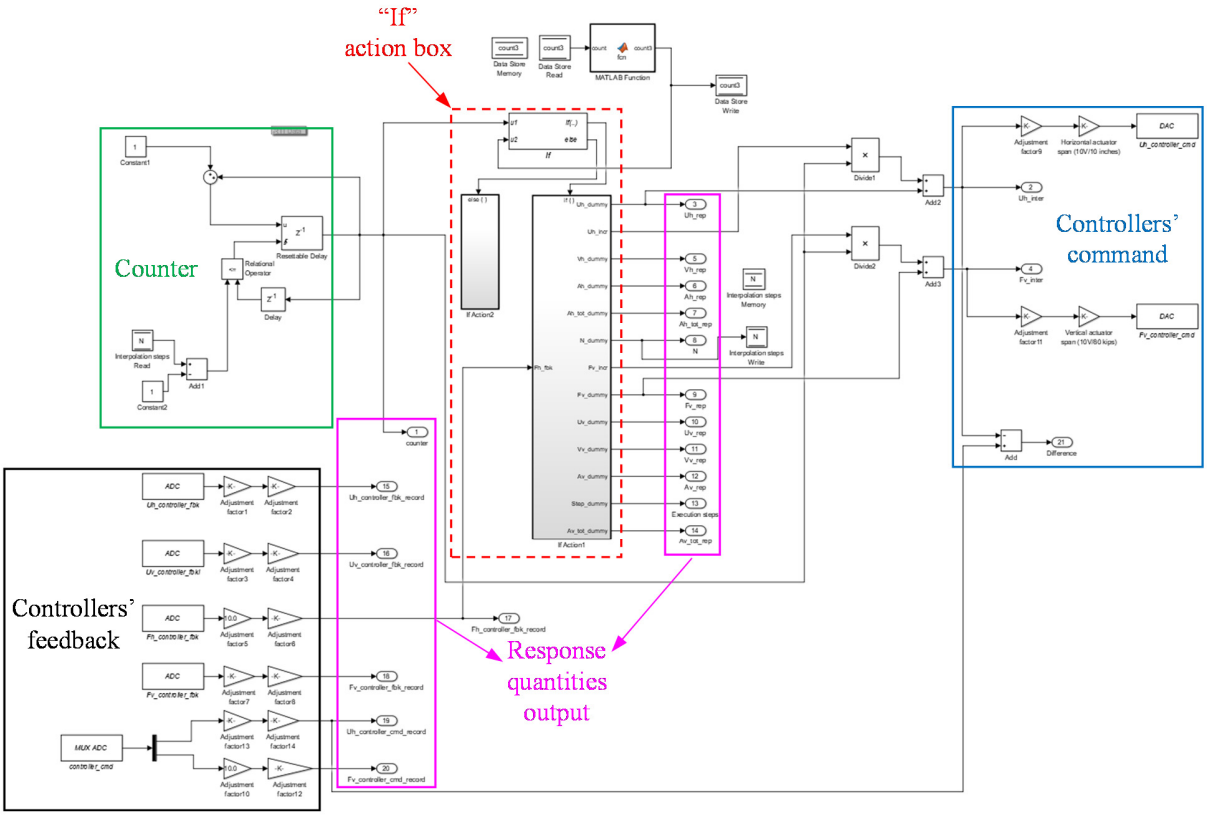

Figure 7.19 Developed Simulink model for phase I HS test.

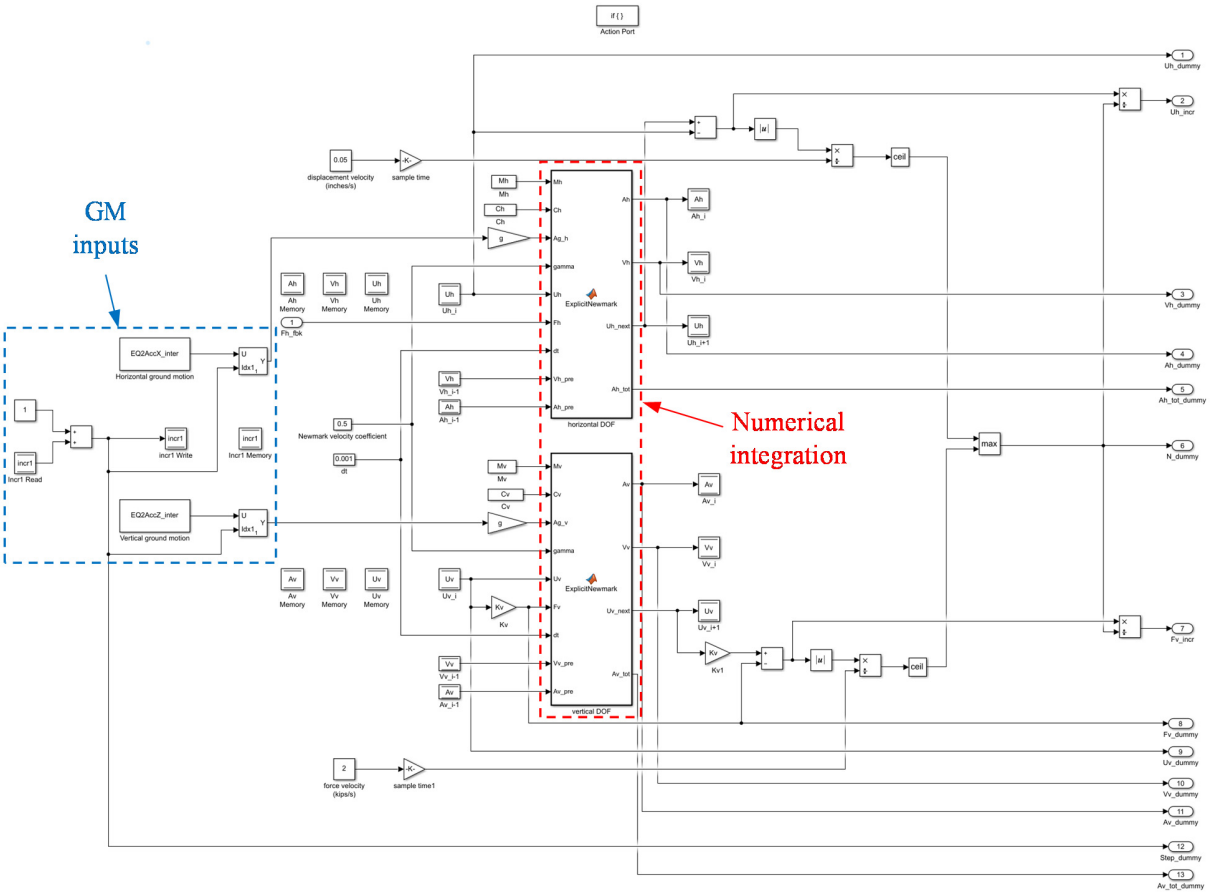

Figure 7.20 Detailed implementation inside the "If" action box.

7.2.3.1 Numerical Integration

The first task for the computational platform is the numerical integration. The Explicit Newmark integration method, which was proposed in HS (pseudo-dynamic testing at that time) for the first time in (Mahin and Williams, 1980), was selected and implemented, with detailed steps provided in the algorithmic box of Figure 7.21. Besides the noniterative characteristic obtained by its explicit nature, some additional advantages of the Explicit Newmark method are listed below:

- It is a self-starting method, meaning that it does not require any response quantities before $t = 0$. The velocities and accelerations are directly obtained as part of the solution algorithm and do not need to be separately calculated;
- The resisting forces are required only once per each time step, meaning that no more than one force acquisition from the experimental substructure of the hybrid model is necessary per each integration step; and
- The stiffness of the structure is not required in the solution algorithm.

=>Initialize: $\boldsymbol{u}_0 = 0$, $\dot{\boldsymbol{u}}_0 = 0$, $\ddot{\boldsymbol{u}}_0 = 0$;

$$\boldsymbol{u}_1 = \boldsymbol{u}_0 + \Delta t\dot{\boldsymbol{u}}_0 + \frac{(\Delta t)^2}{2}\ddot{\boldsymbol{u}}_0 = 0$$

Starting from $i = 1$

1. Impose $\boldsymbol{u}_i$ to the test specimen and measure the corresponding force $\boldsymbol{f}_i$;
2. Compute the current step accelerations:

   $[\mathbf{m} + \Delta t\gamma\mathbf{c}]\ddot{\boldsymbol{u}}_i = \boldsymbol{p}_i - \boldsymbol{f}_i - \mathbf{c}[\dot{\boldsymbol{u}}_{i-1} + \Delta t(1-\gamma)\ddot{\boldsymbol{u}}_{i-1}]$

   $\boldsymbol{m}_{eff}\ddot{\boldsymbol{u}}_i = \boldsymbol{p}_{eff}$
3. Compute the current step velocities:

   $\dot{\boldsymbol{u}}_i = \dot{\boldsymbol{u}}_{i-1} + \Delta t[(1-\gamma)\ddot{\boldsymbol{u}}_{i-1} + \gamma\ddot{\boldsymbol{u}}_i]$
4. Compute the next step displacements:

   $$\boldsymbol{u}_{i+1} = \boldsymbol{u}_i + \Delta t\dot{\boldsymbol{u}}_i + \frac{(\Delta t)^2}{2}\ddot{\boldsymbol{u}}_i$$
5. Increment i;

Figure 7.21 Implemented Explicit Newmark integration algorithm in the HSS.

It can be shown that the Explicit Newmark method with $\gamma = 0.5$ yields the same solutions as the well-known central-difference method. Because of its numerical equivalence, the Explicit Newmark method inherits the order of accuracy and the stability condition of the central-difference method. It is conditionally stable with the following stability limit:

$$\Delta t \leq \frac{T_n}{\pi} \tag{7.1}$$

where Δt is the step size of the integration method and T_n is the shortest natural period of the structure that is being analyzed. Considering the high stiffness of the test specimen in the vertical direction, the shaking table ground motion records were interpolated to reduce the step size from 0.005 s to 0.001 s to avoid any possible stability issues and to increase the accuracy of the numerical integration.

The numerical integration for both DOFs was performed through the Matlab function block in Simulink (MathWorks, 2015). A typical numerical integration block is shown in Figure 7.22. Per the Explicit Newmark integration algorithm shown above, the function block takes as inputs the mass $\boldsymbol{m}$, the damping coefficient $\boldsymbol{c}$, the ground acceleration $\ddot{\boldsymbol{u}}_{gi}$ (in the unit of in./s^2) at the current time step i, the Newmark velocity coefficient γ, the displacement $\boldsymbol{u}_i$ at the current time step, the measured force $\boldsymbol{f}_i$ corresponding to $\boldsymbol{u}_i$, the discrete time step dt, and the velocity $\dot{\boldsymbol{u}}_{i-1}$ and acceleration $\ddot{\boldsymbol{u}}_{i-1}$ at previous time step $i - 1$, and outputs the acceleration $\ddot{\boldsymbol{u}}_i$, the velocity $\dot{\boldsymbol{u}}_i$, the total acceleration at the current time step i, and the displacement $\boldsymbol{u}_{i+1}$ at the next time step $i + 1$. The calculated quantities from the current calculations are written and stored using the Simulink

blocks “DataStoreWrite” and “DataStoreMemory”, and are read by the Simulink block “DataStoreRead” to be used in the next step calculations.

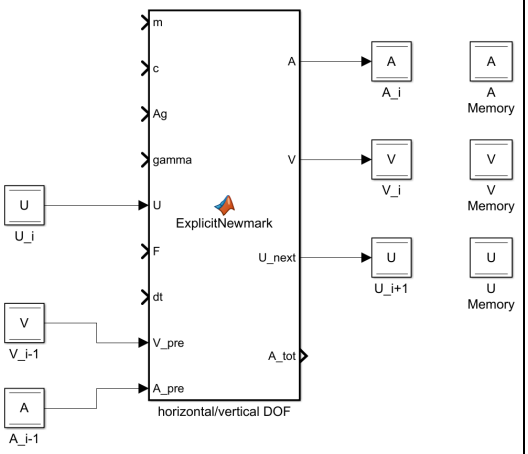


```
function [A,V,U_next,A_tot] =
ExplicitNewmark(m,c,Ag,gamma,U,F,dt,V_pre,A_pre)
% Explicit Newmark algorithm for SDOF system
% Inputs: m - mass corresponds to SDOF system
%         c - damping ratio
%         Ag - ground acceleration at step i
%         gamma - Newmark velocity coefficient
%         U - displacement at step i
%         F - measured resisting force at step i
%         dt - time step, deltaT
%         V_pre - velocity at step i-1
%         A_pre - acceleration at step i-1
% Outputs: A - acceleration at step i
%          V - velocity at step i
%          U_next - displacement at step i+1
%          A_tot - total acceleration at step i
%% compute acceleration A at step i
P = -m*Ag;
m_eff = m + dt*gamma*c;
P_eff = P - F - c*(V_pre + dt*(1 - gamma)*A_pre);
A = P_eff/m_eff;
%% compute velocity V at step i
V = V_pre + dt*((1 - gamma)*A_pre + gamma*A);
%% compute displacement U_next at next step i+1
U_next = U + dt*V +0.5*(dt^2)*A;
%% compute total acceleration A_tot at step i
A_tot = A + Ag;
```

Figure 7.22 Matlab function block for performing the Explicit Newmark numerical integration in the HSS.

7.2.3.2 Displacement Interpolation

The second task for the computational platform is the displacement interpolation. Between the current step displacement $\boldsymbol{u}_i$ and the next step displacement $\boldsymbol{u}_{i+1}$, interpolation of displacements is needed to generate commands for the controller. This is because: (1) The operation of the MTS 407 controller is based on receiving a command displacement at every 10 milliseconds; (2) The HS test is conducted slower than real-time; and (3) The actuator velocity is limited to 0.05 in./s in order to achieve good control quality. Therefore, the maximum allowed displacement increment between two commands is 0.05 in./s × 10 millisecond = 0.0005 in. The Simulink blocks used to determine the number of interpolations between the two integration time steps is shown in Figure 7.23. In both horizontal and vertical directions, the absolute values of the displacement increment $\Delta\boldsymbol{u}$ between two adjacent steps are obtained and divided by the maximum allowed displacement increment. The resulting two numbers are rounded up to the nearest integers and the larger of the two is selected to be the number of interpolation steps for both directions. The horizontal and vertical displacements are then linearly interpolated accordingly using the number of interpolation steps.

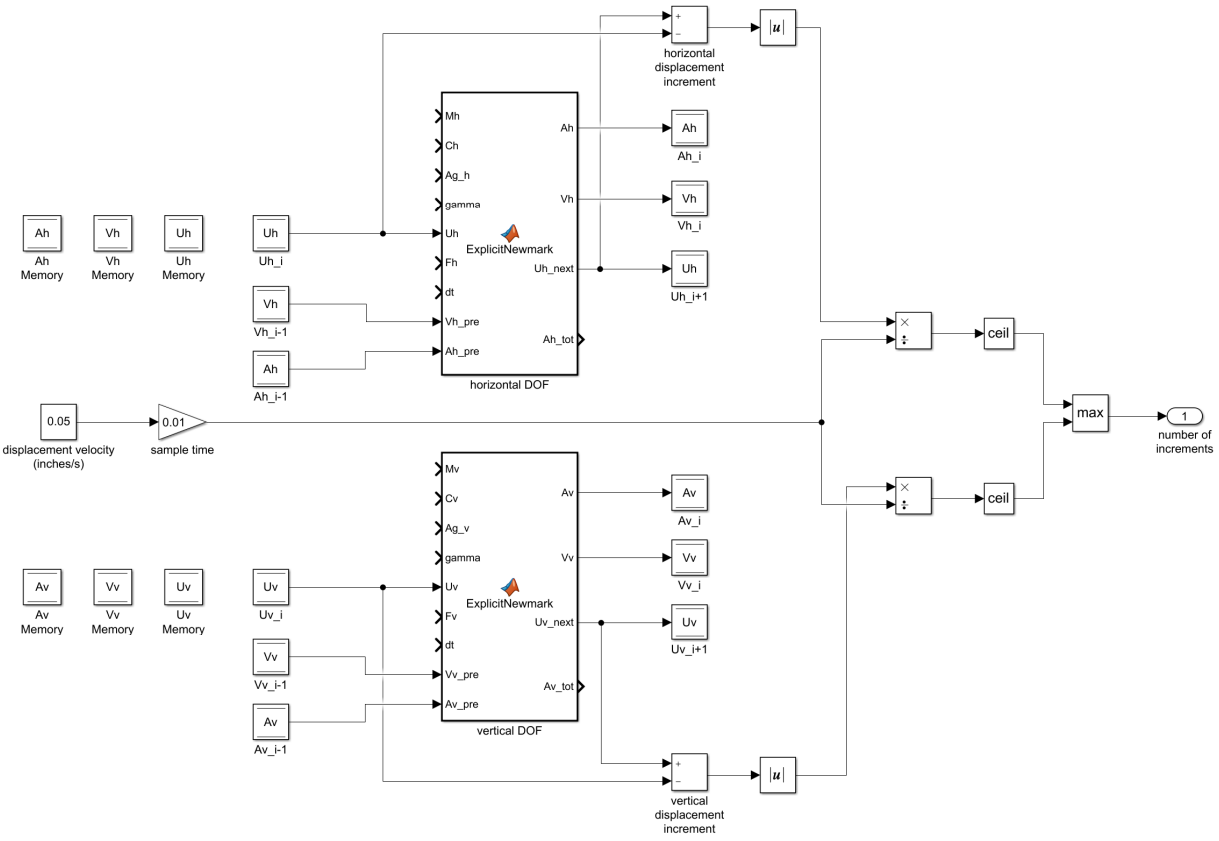

Figure 7.23 Simulink blocks for calculating the number of interpolation steps between two time steps in the HSS.

Another important issue that needs to be addressed in the developed Simulink model is that while performing the displacement interpolation, the numerical integration needs to "hold on". That is, the integration algorithm should not advance to the next time step until the displacement interpolation has been completed. During the displacement interpolation, the actuator is continuously moving at a constant velocity and the load cell is continuously measuring the resisting forces corresponding to different displacement values from the test specimen. However, only the resisting force that corresponds to the displacement value at the beginning of the interpolation, namely $\boldsymbol{f}_i$, is the one that should be utilized by the integration algorithm. This requirement is achieved in Simulink by defining a "resettable counter" and making use of the "if" statement block, shown in Figure 7.24. At the end of each time step, the number of interpolation steps, denoted with "N" is obtained and passed on to the counter. The counter takes values from 0 to $N-1$ and its value is multiplied by the displacement increment $\boldsymbol{u}_{incr}$ in each direction (the displacement increment in different directions can be different) and then added to the current step displacement $\boldsymbol{u}_i$ to obtain the intermediate values $\boldsymbol{u}_i + 0 \times \boldsymbol{u}_{incr}$, $\boldsymbol{u}_i + 1 \times \boldsymbol{u}_{incr}$, $\boldsymbol{u}_i + 2 \times \boldsymbol{u}_{incr}$,…, $\boldsymbol{u}_i + (N-1) \times \boldsymbol{u}_{incr}$ to be converted by the DAC block for the controller (see Figure 7.25 and Figure 7.26). Once the counter reached the value $N-1$, it is reset to 0 and the numerical integration is activated according to the "if" condition. The time step i is then increased by 1 and the displacement value becomes $\boldsymbol{u}_{i+1}$. The resisting force corresponding to $\boldsymbol{u}_{i+1}$, denoted with $\boldsymbol{f}_{i+1}$, is measured and converted by the ADC block before it is passed to the numerical integration to

advance the solution to the next time step and to start the next round of displacement interpolation between $\boldsymbol{u}_{i+1}$ and $\boldsymbol{u}_{i+2}$.

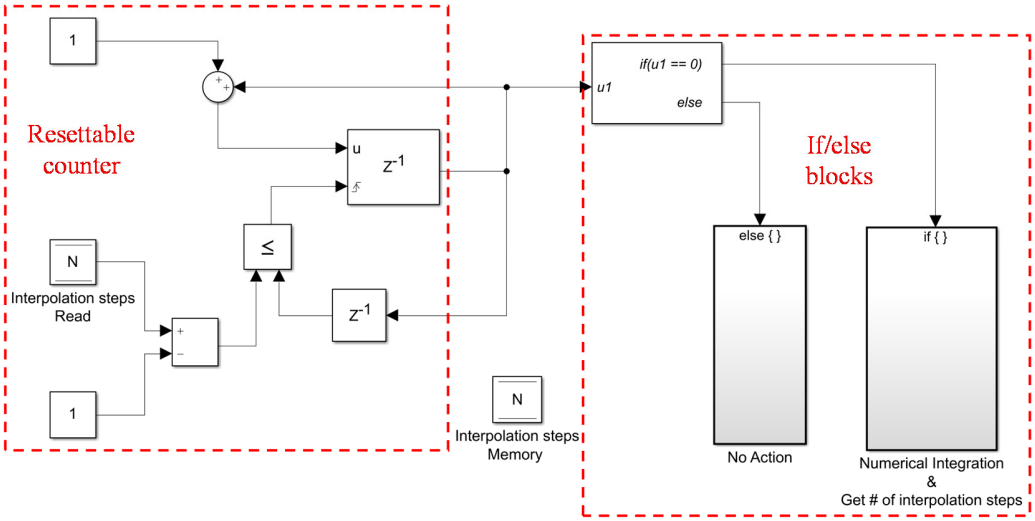

Figure 7.24 Simulink blocks for resettable counter and "if" actions in the HSS.

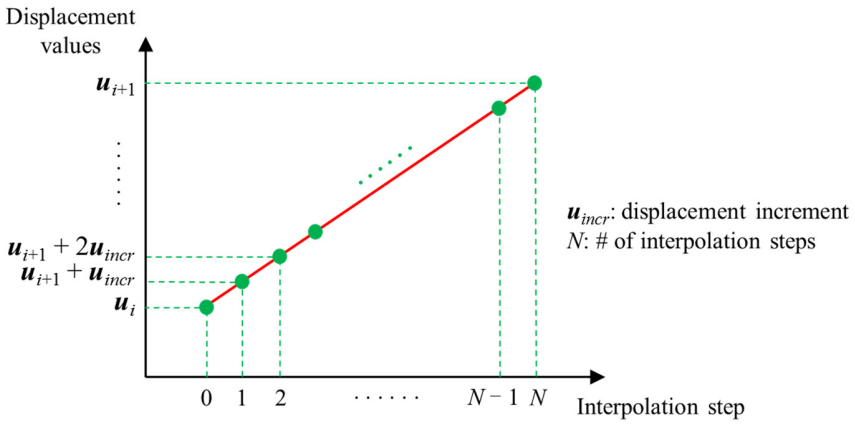

Figure 7.25 Typical displacement interpolation between time step *i* and *i* + 1 in the HSS.

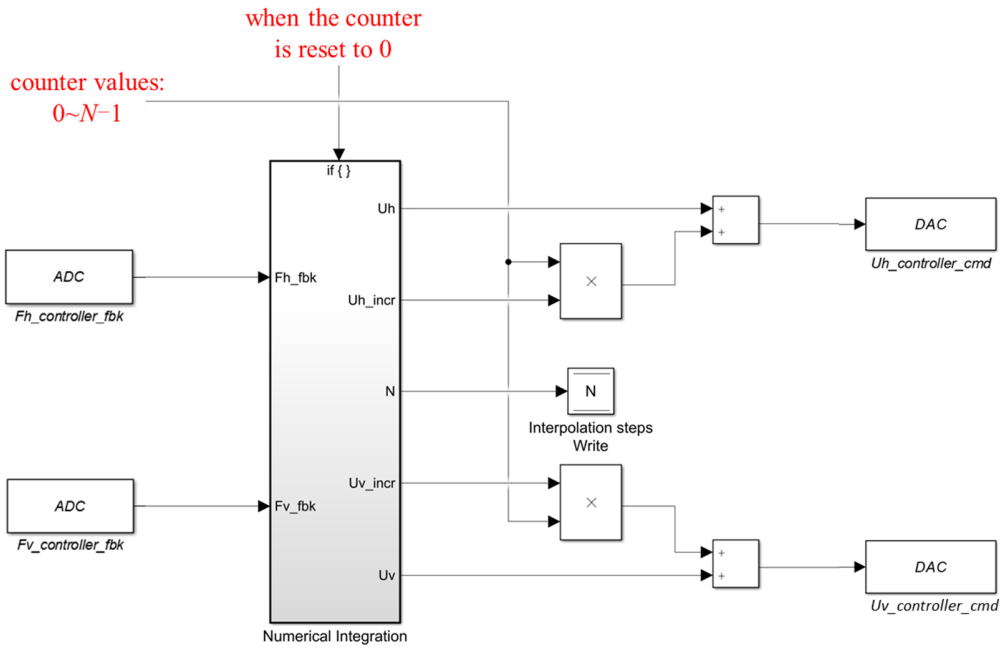

Figure 7.26 Calculation of intermediate displacement values in the HSS.

7.3 HYBRID SIMULATION SYSTEM VERIFICATION TEST

To confirm the performance of the implemented developments and validate the whole HSS together with the proper actuator tracking, a HSS trial run was indispensable before proceeding further. The trial run was conducted on free horizontal and vertical actuators detached from the test specimen. Two-way communication is necessary in HS: one way is for sending the displacement command and the other is for receiving the force feedback. A free actuator that is not attached to any specimen reports zero force feedback or only the load cell noise. Thus, for the free actuator trials, a multiplier (stiffness) of the displacement feedback was used as the virtual force feedback. The constant multiplier reflected the stiffness of a hypothetical linear elastic force-displacement relationship. A schematic representation of the HS trial run is shown in Figure 7.27. The advantage of this virtual feedback is that it allows for comparison with pure simulation results where an elastic element with a constant stiffness replaces the actuator's displacement/force feedback. The computational model for the pure simulation was a linear elastic system with two uncoupled DOFs, with some selected representative parameters (mass, stiffness and damping ratio). The ground motion record measured by accelerometers mounted on the shaking table during EQ2 was used as the ground motion input. For comparison with the pure simulation case, the horizontal and vertical stiffness in the pure simulation were used as multipliers for the displacement feedback to the computational platform to reflect an assumed linear elastic behavior in both directions.

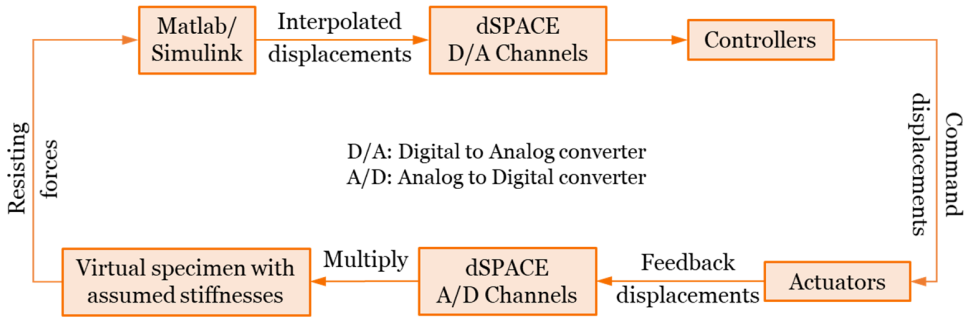

Figure 7.27 Schematic representation of the HS trial run.

7.3.1 Control Quality Check

Figure 7.28 and Figure 7.29 check the control quality of the horizontal and vertical actuators by plotting the controller's command displacement vs. the actuator's feedback displacement. Both actuators delivered good control quality as the command and the feedback plots overlapped with little time delay. The displacement feedback from the vertical actuator, however, was noisy. As a multiplier of the feedback displacement, the virtual feedback force would also be noisy. This might raise issues in the vertical direction during the system verification, especially at the beginning of the ground motion where the resisting force is expected to be small. This concern is addressed in later HS runs corresponding to phases I and II by switching from displacement control to force control for the vertical actuator.

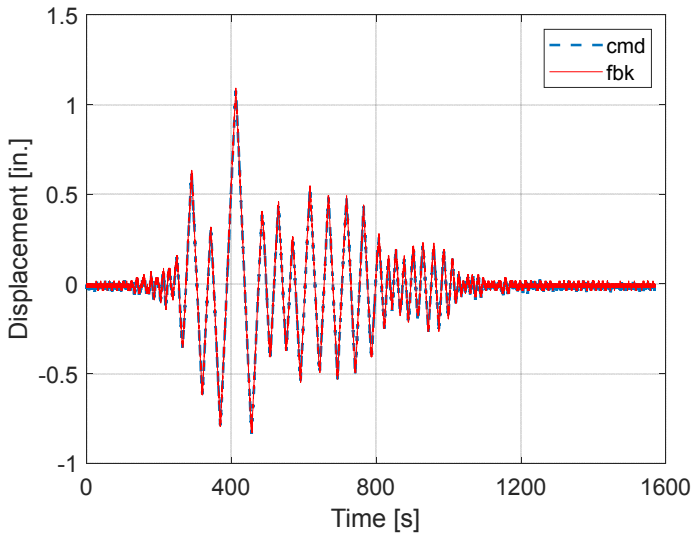

Figure 7.28 Command (cmd) vs. feedback (fbk) displacements for the horizontal actuator.

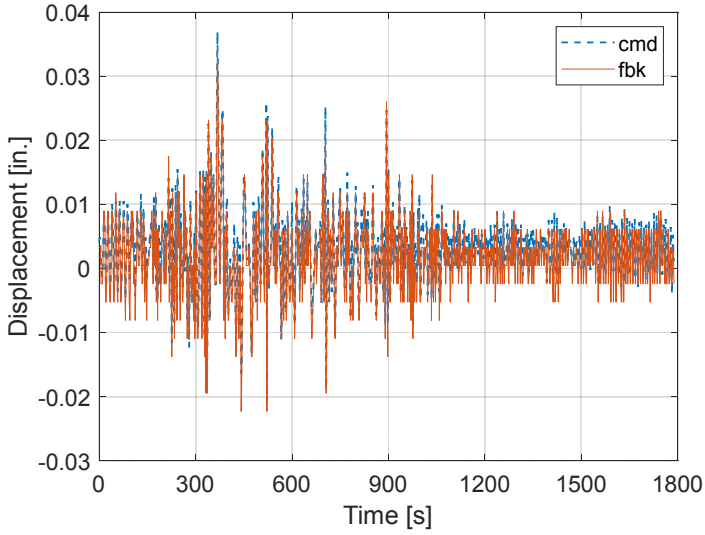

Figure 7.29 Command (cmd) vs. feedback (fbk) displacements for the vertical actuator.

7.3.2 Interpolation Check

If the displacement interpolation algorithm is implemented correctly, the displacement time histories before and after the interpolation should be exactly the same. The only expected difference is that the interpolated displacement time history will have more data points between two subsequent time steps. Figure 7.30 and Figure 7.31 show the original and interpolated time histories from both directions, plotted in the real execution time. As can be seen from the zoom-in views on the right sides of these figures, the interpolation algorithm performed well as intended.

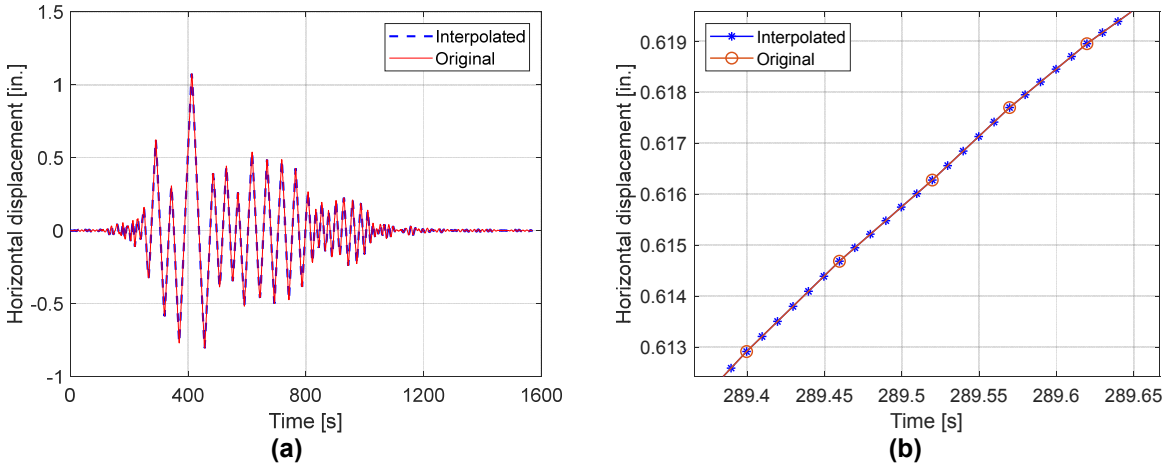

Figure 7.30 (a) Original and interpolated (with $N = 6$) displacement time histories from the horizontal direction; (b) zoom-in view.

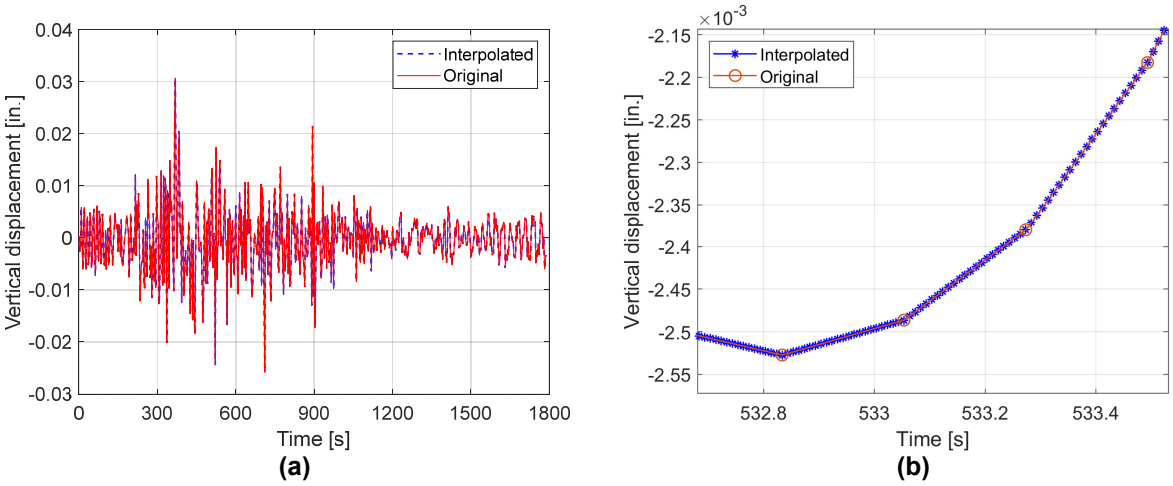

Figure 7.31 **(a) Original and interpolated (with *N* = 22) displacement time histories from the vertical direction; (b) zoom-in view.**

7.3.3 Overall Check

The horizontal and vertical displacement time histories recorded by the dSPACE (2017) ControlDesk software during the HS trial run were compared against those obtained from a pure simulation conducted with the same mass, damping coefficient, and stiffness. Perfect match between the HS trial run and the pure simulation (as is the case for the horizontal direction, refer to Figure 7.32(a)) indicates proper functioning of the computation, the communication between the HS components, and proper actuator control and displacement tracking. The high-frequency displacement oscillation in the vertical direction at the beginning and the end of the HS trial run, refer to Figure 7.32(b), was due to the noisy displacement feedback from the vertical actuator, as explained in section 7.3.1. However, the oscillation amplitude was very small, i.e. below 0.01 in.

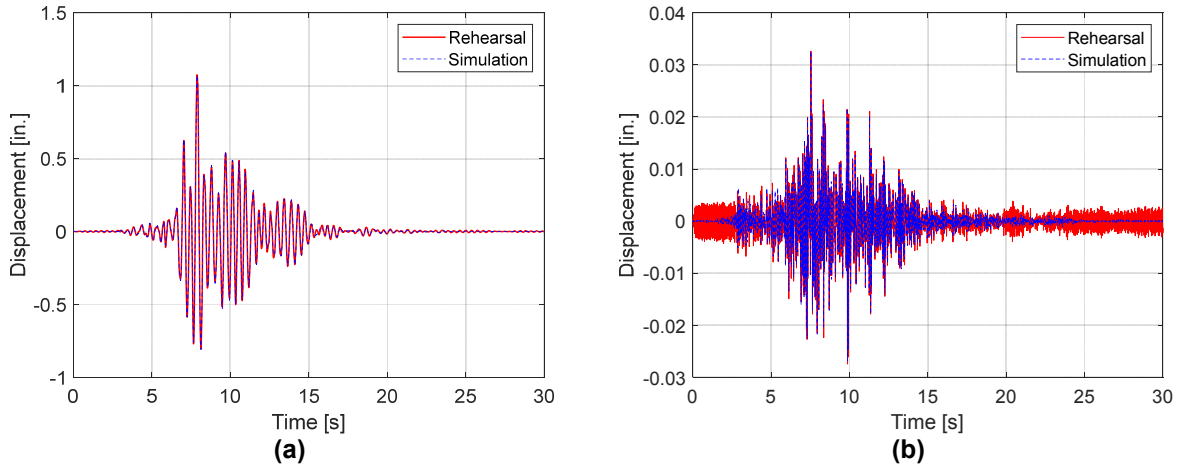

Figure 7.32 **Hybrid simulation verification test in (a) horizontal direction; and (b) vertical direction.**

7.4 HYBRID SIMULATION TEST

7.4.1 Gravity Loading

During the HS test, the hybrid structure was subjected to two sequences of loading. These are applied in the following order: (1) gravity load; and (2) two-directional ground motion inputs measured by accelerometers mounted on the table during the shaking table test.

As stated before, a gravity load of 47 kips representing the total weight of the six mass blocks was applied through the vertical actuator before starting each HS run. Note that as the gravity load from the cap beam (22 kips) is already present physically, it does not need to be applied again. With the applied gravity load of 47 kips from the vertical actuator and the 22 kips weight of the cap beam, the total gravity load on the columns was 69 kips. Figure 7.33 shows the force-displacement relationship in the vertical direction during the gravity loading application. The stiffness change during gravity loading can be clearly observed from the plot. This was caused by compression of the grout between the top clevis connection anchorage plate of the vertical actuator and the top surface of the cap beam, as shown in Figure 7.34. When the vertical actuator pulled down, it first squeezed the grout before starting to engage the complete vertical stiffness of the test specimen. Therefore, the stiffness was small during the compression of the grout. After that, the vertical actuator started acting against the specimen and the response became much stiffer, representing the correct vertical stiffness of the test specimen. In order to eliminate this problem due to the test setup limitation, it was decided to switch from displacement control to force control for the vertical actuator. The forces were computed by multiplying the vertical displacements with the estimated vertical stiffness of the specimen, assuming linear elastic behavior in the vertical direction.

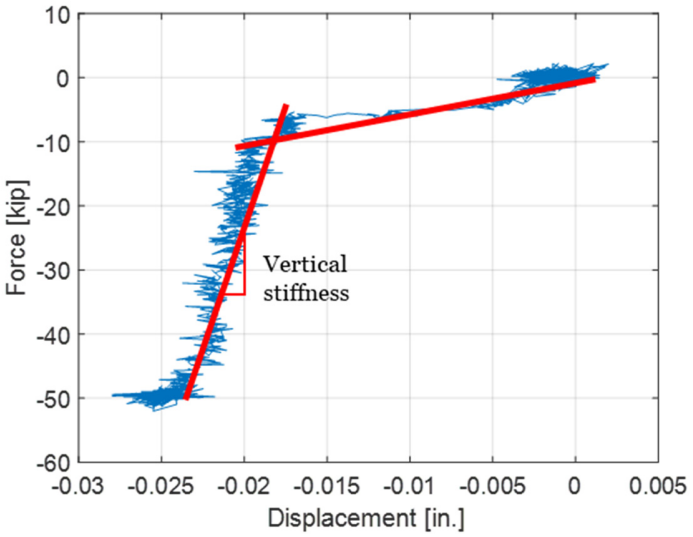

Figure 7.33 Force-displacement plot during the gravity loading.

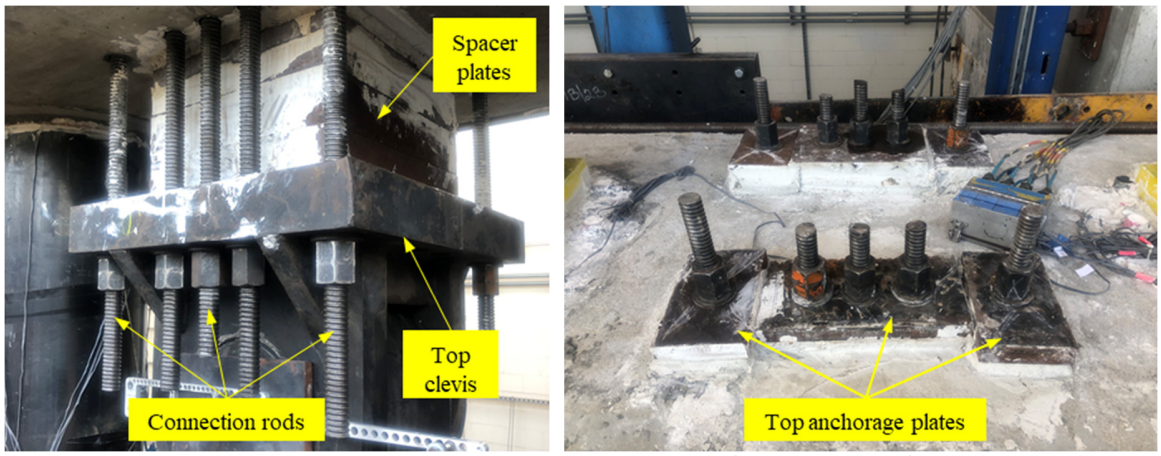

(a) Top clevis connection (b) View from the top of the cap beam

Figure 7.34 Connection detailing of the vertical actuator's top clevis to the cap beam.

Because of the change in the vertical actuator control, the displacement interpolation in the vertical direction as described in section 7.2.3.2 needs to be changed to force interpolation. The vertical actuator's force velocity was limited to 2 kips/s and the maximum allowed force increment between two commands was 2 kips/s × 10 millisecond = 0.02 kips. The number of interpolation steps between two subsequent time steps was obtained as discussed before but in this modified version based on the horizontal displacement increment and the vertical force increment.

7.4.2 Selected Parameters

The parameters used in the HS are chosen for proper representation of the dynamics of the two uncoupled SDOF systems. The response of a SDOF system in the linear elastic range is completely defined by its period and damping. To match the results from the shaking table test, it was important to identify the correct period and damping of the test specimen from the shaking table test. The test results from EQ2 of the shaking table test were used for this purpose because the specimen remained mostly in the linear elastic range during this test. EQ1 shaking table test was not considered here, since one of the inertia blocks was found to be not seated properly and the restraint frame was found to be bearing against the specimen, providing lateral resistance during EQ1, an issue that was corrected in subsequent shaking table test runs.

7.4.2.1 Horizontal Direction

The period of the test specimen in the horizontal direction was investigated by taking the Fast Fourier Transformation (FFT) of the measured horizontal acceleration time history from the top of the specimen during the shaking table test EQ2. There were a total number of 16 accelerometers measuring the horizontal acceleration on top and the average value was considered. The FFT result is shown in Figure 7.35(a). The frequency corresponding to the peak is 2.3 Hz, which results in the horizontal period to be 0.43 s.

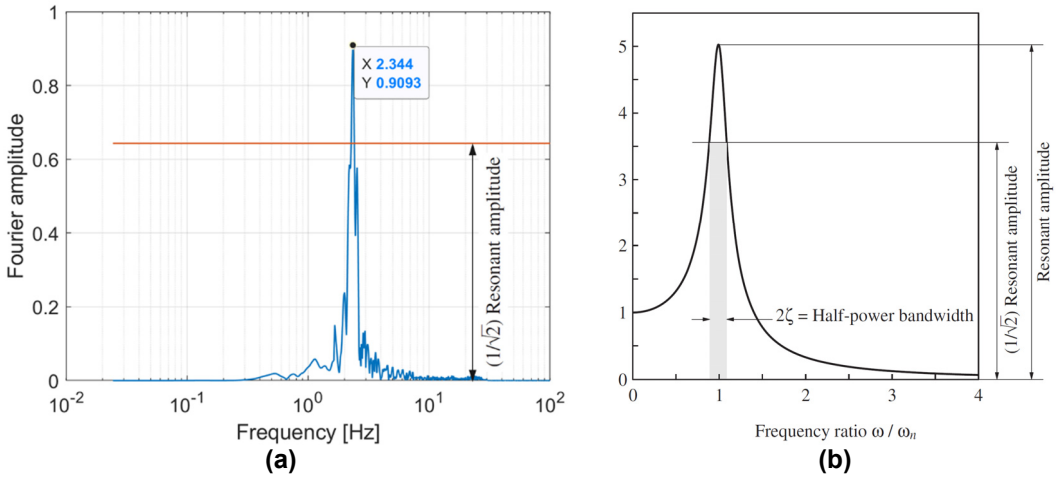

Figure 7.35 (a) FFT and half-power bandwidth results in the horizontal direction; (b) illustration of the half-power bandwidth method (Chopra, 2011).

The damping ratio was found by the half-power bandwidth method (Figure 7.35(b)). This method states that if ω_a and ω_b are the frequencies on either side of the resonant frequency, ω_n, at which the amplitude is $1/\sqrt{2}$ times the resonant amplitude, then for small damping ratio ζ, $\zeta = (\omega_b - \omega_a)/2\omega_n$. Based on this calculation, the damping ratio was found to be around 3%. A damping ratio of 2% was used in the HS for horizontal direction to account for any additional energy dissipation from the test specimen resulted from any potential damping that can be introduced due to simulation errors as explained before in section 6.4.1.

The horizontal stiffness of the specimen was computed from a low-level test with two small cycles. The mass m_h and the damping coefficient c_h, were computed to match the period and damping ratio identified above from the shaking table test. The horizontal inertia mass considered in the shaking table test includes six mass blocks and the cap beam, which resulted in a total mass of 69 kips/g, while the horizontal mass used in the HS test was estimated to be 81 kips/g. This was mainly due to the larger strength and stiffness of the older concrete in the test specimen because the HS test was conducted one year after the shaking table test.

7.4.2.2 Vertical Direction

To determine the parameters in the vertical direction, initially, the method described above for the horizontal direction was adopted. In order to avoid any possible effect on the vertical response due to the shaking table flexibility, the FFT of the measured vertical acceleration time history from the top of the specimen was divided by the FFT of the measured vertical ground motion input from the table to obtain the transfer function. It turned out that the frequency that corresponds to the peak of the transfer function agrees with the one that corresponds to the vertical response. There were a total number of 8 accelerometers measuring the vertical (Z) accelerations on top of the specimen, but only the two mounted on the mass blocks at the center of the cap beam (AZM21 and AZM51 in Figure 7.36) were considered. This is because the deformations at both ends of the cap beam during the ground shaking might have led to inaccurate acceleration measurements due to the vibration mode of the cantilevered portion of the cap beam. The FFT result is demonstrated

in Figure 7.37. The frequency corresponding to the peak is 15.48 Hz, resulting in the horizontal period to be 0.065 s. The damping ratio based on the half-power bandwidth method was estimated to be 0.36%, which was questionable as it is much smaller than the damping ratios of typical structures in engineering practice.

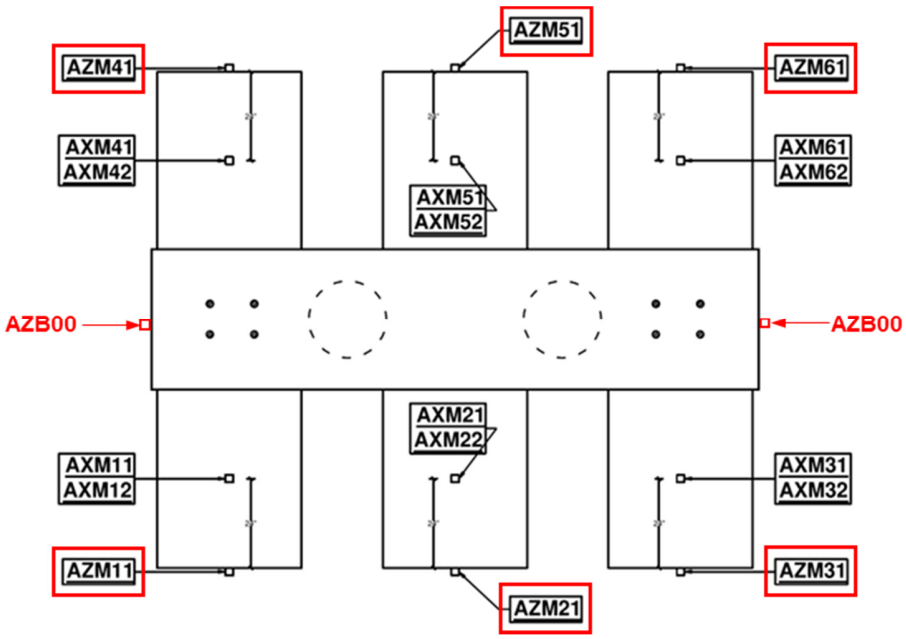

Figure 7.36 Accelerometers measuring vertical accelerations on top of the test specimen in the shaking table test (Nema, 2018).

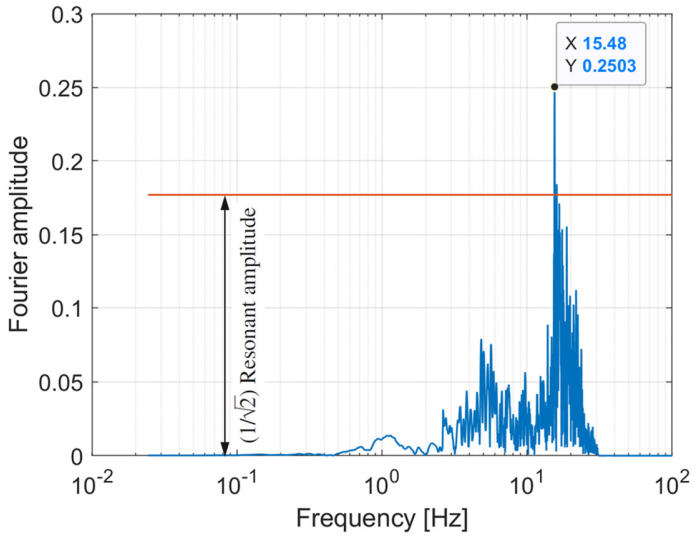

Figure 7.37 FFT and half-power bandwidth results in the vertical direction.

As indicated earlier, because of the unrealistic small vertical stiffness at small displacements, it was decided to switch from displacement control to force control. Considering that the response in the vertical direction would remain essentially elastic and that the vertical load

could influence the overall response of the specimen in the horizontal direction through the level of the column axial load, another approach for seeking the parameters in the vertical direction was taken by matching the shaking table test results from EQ2. For this purpose, the response of a linear elastic SDOF system was investigated by varying the period and the damping ratio in a certain range of interest. The investigated period range was selected to be 0.04~0.08 s so that the potentially correct period could be included, while the range of the damping ratio was selected to be 1~15% to cover the practical range. The root-mean-square (RMS) error was computed by comparing the acceleration response of the SDOF system against the shaking table test results and the parameter combination which yielded the smallest RMS error was selected. It was found that the period of 0.076 s (which is comparable to the 0.065 s from the previous approach) and damping ratio of 11.1% (which is much higher than the questionable 0.36% from the previous approach) gave the best match between the analysis and the shaking table results (see Figure 7.38). These parameters were used to compute the mass m_v and damping coefficient c_v in the vertical direction. The vertical mass was found to be very close to that of the shaking table test. Therefore, the same value 69 kips/g was used. It is noted that the damping ratio identified this way was higher than expected. However, this was considered to be more realistic, especially considering the possible friction between the lateral supporting frame and the mass blocks during the shaking table test, see Figure 7.1.

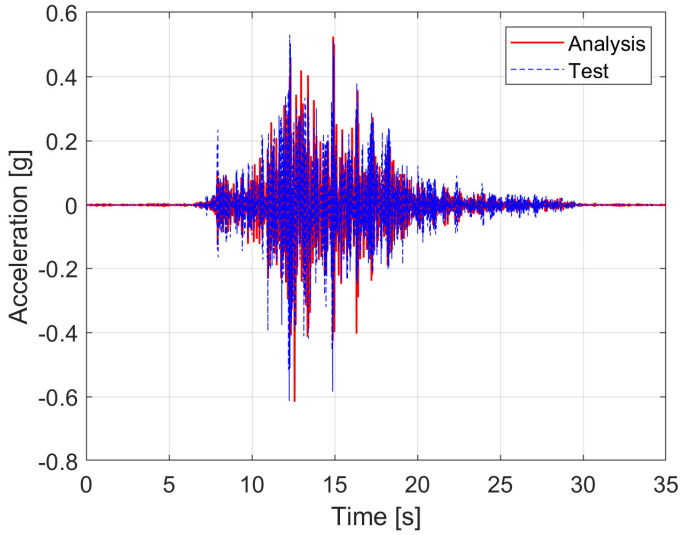

Figure 7.38 Vertical acceleration comparison with T_v = 0.076 s and ζ = 11.1%.

7.4.3 Test Results

A total number of six ground motions, from EQ2 to EQ7 in Table 7.2, were completed in the HS test. Considering that the remaining two ground motions (EQ8 and EQ9) are two different scales of the Takatori station's recording of the 1995 Kobe Earthquake, which is a motion characterized by the presence of a very strong pulse, it was thought that the completed motions are sufficient for the comparison purpose between the HS phase I and the shaking table test results. This comparison represents the main part of this section. Moreover, some other important response quantities are presented herein.

Table 7.2 Ground motions used in phase I of the hybrid simulation experiment.

EQ #	Event Name	Station Name	Unscaled PGA [g]	Scale Factor	Expected Drift [%]
01	For shaking table test checking and not used in HS				
02	Landers, 1992	Lucerne	0.72	0.90	0.6
03	Tabas, 1978	Tabas	0.85	-0.90	1.8
04	Kocaeli, 1999	Yarimca	0.30	1.00	0.6
05	Northridge, 1994	RRS	0.85	0.81	4.0
06	Duzce, 1999	Duzce	0.51	1.00	1.8
07	Northridge, 1994	NFS	0.72	-1.20	4.0

7.4.3.1 Comparison of Results

Figure 7.39 to Figure 7.44 give the displacement time history, force time history, acceleration time history, and force-displacement relationship comparisons between the shaking table test and the HS experiment in the horizontal direction. These results show very good overall matching in terms of the amplitude of the response quantity, the time history pattern, and the hysteretic behavior of the test specimen, although there are some discrepancies in some of the runs towards the end. This might have been caused by two reasons: (1) the possible friction force from the lateral support system in the HS setup; and (2) the small level of rate dependency of reinforced concrete (Moehle, 2014). Another observation is that the matching is better for larger earthquakes than smaller ones.

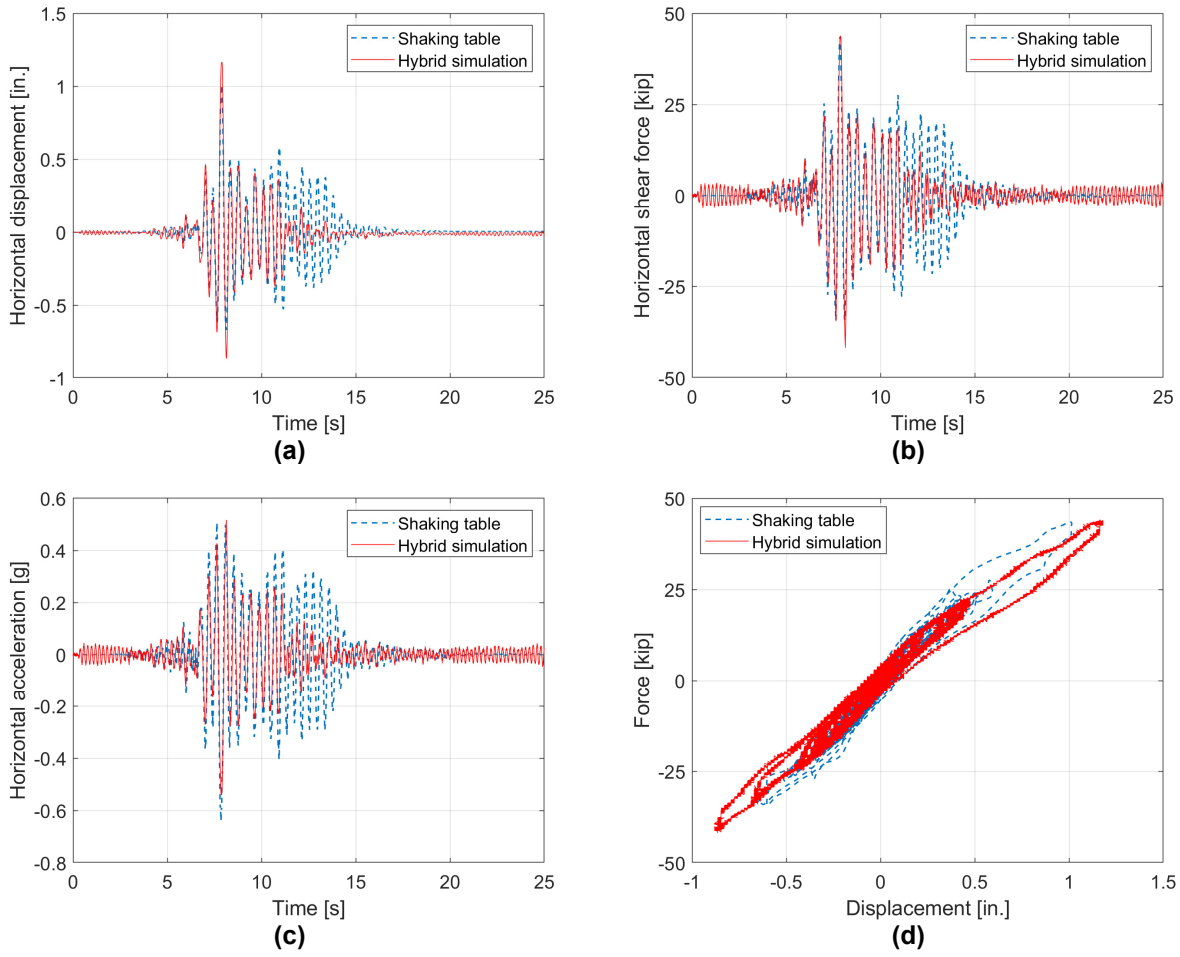

Figure 7.39 **(a) Displacement time history; (b) resisting force time history; (c) acceleration time history; and (d) force-displacement relationship comparisons of EQ2 in the horizontal direction.**

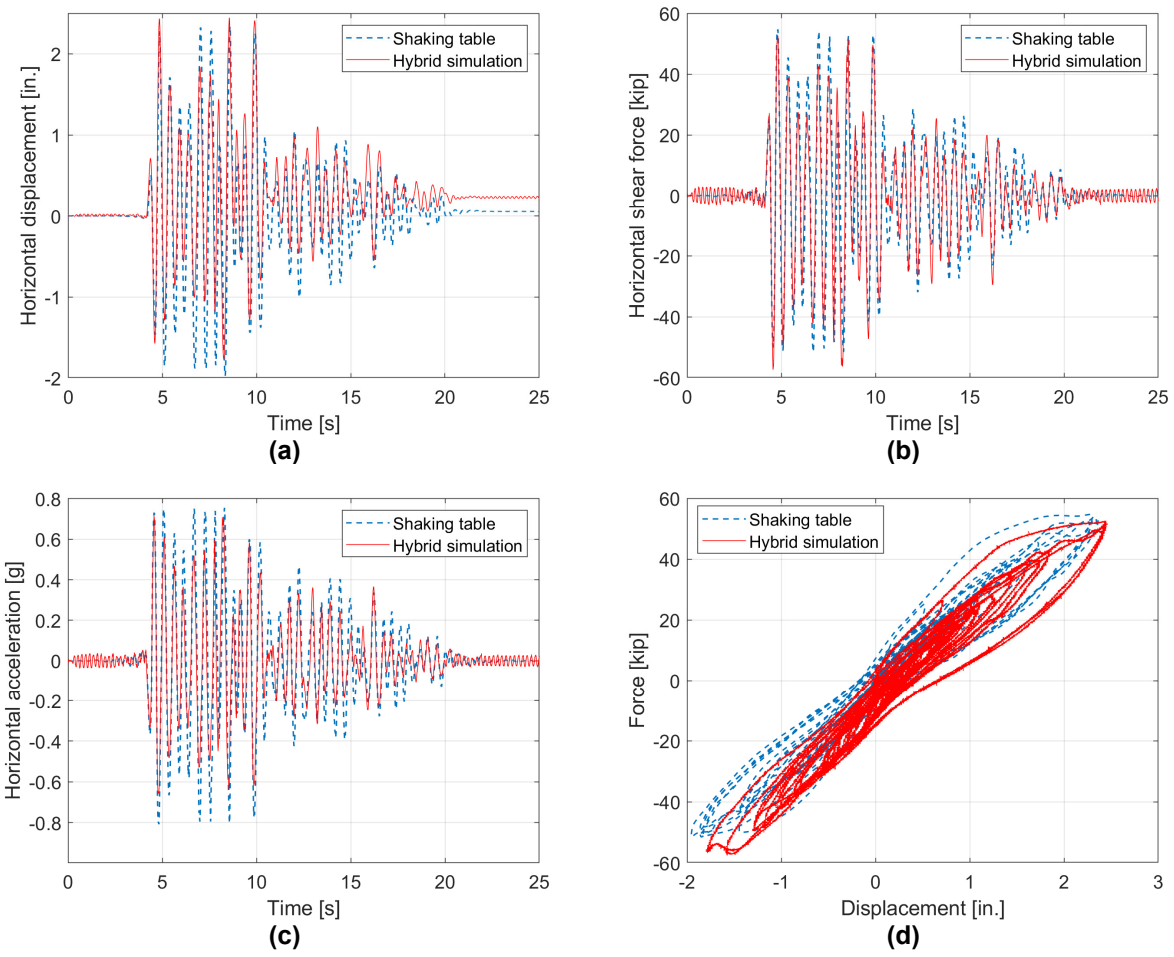

Figure 7.40 **(a) Displacement time history; (b) resisting force time history; (c) acceleration time history; and (d) force-displacement relationship comparisons of EQ3 in the horizontal direction.**

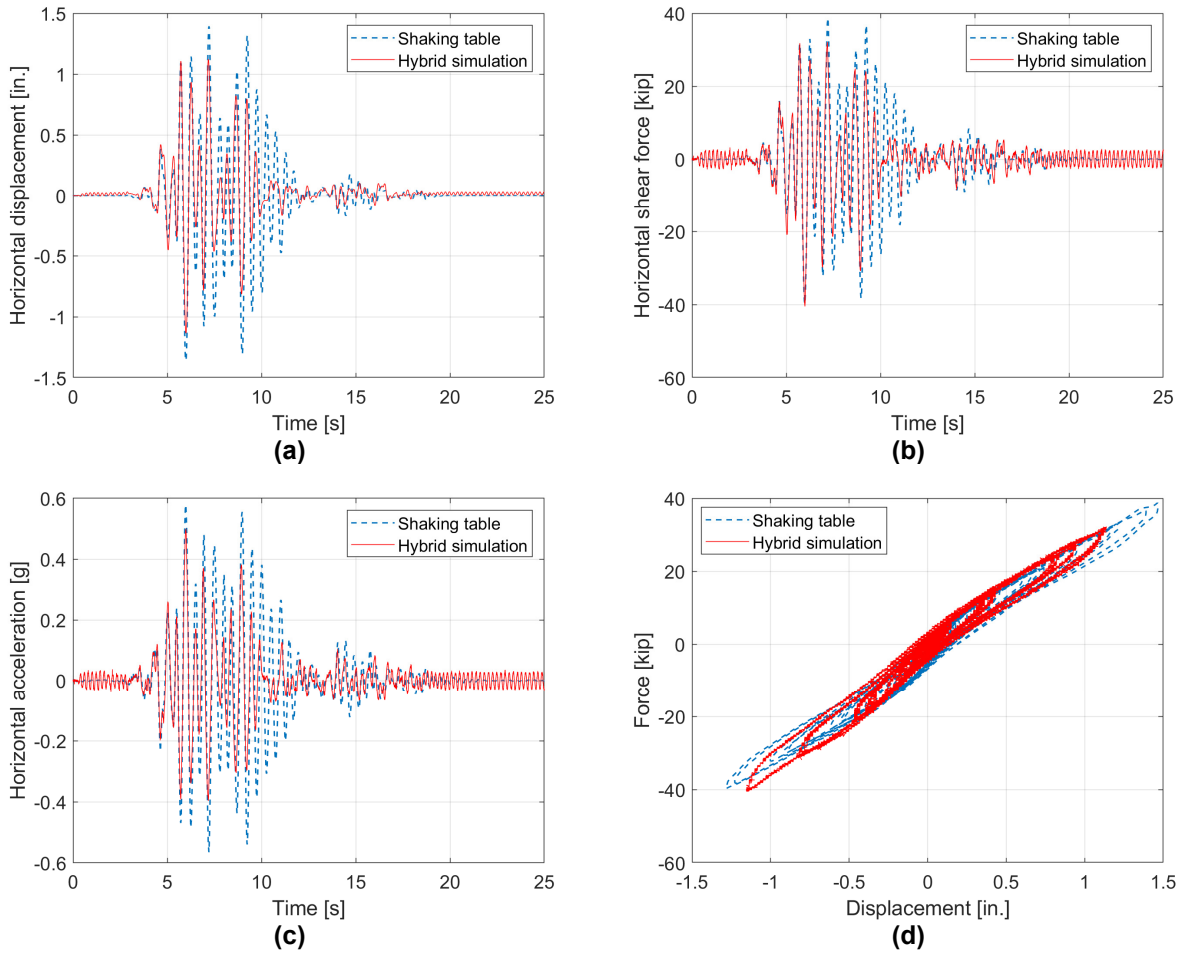

Figure 7.41 **(a) Displacement time history; (b) resisting force time history; (c) acceleration time history; and (d) force-displacement relationship comparisons of EQ4 in the horizontal direction.**

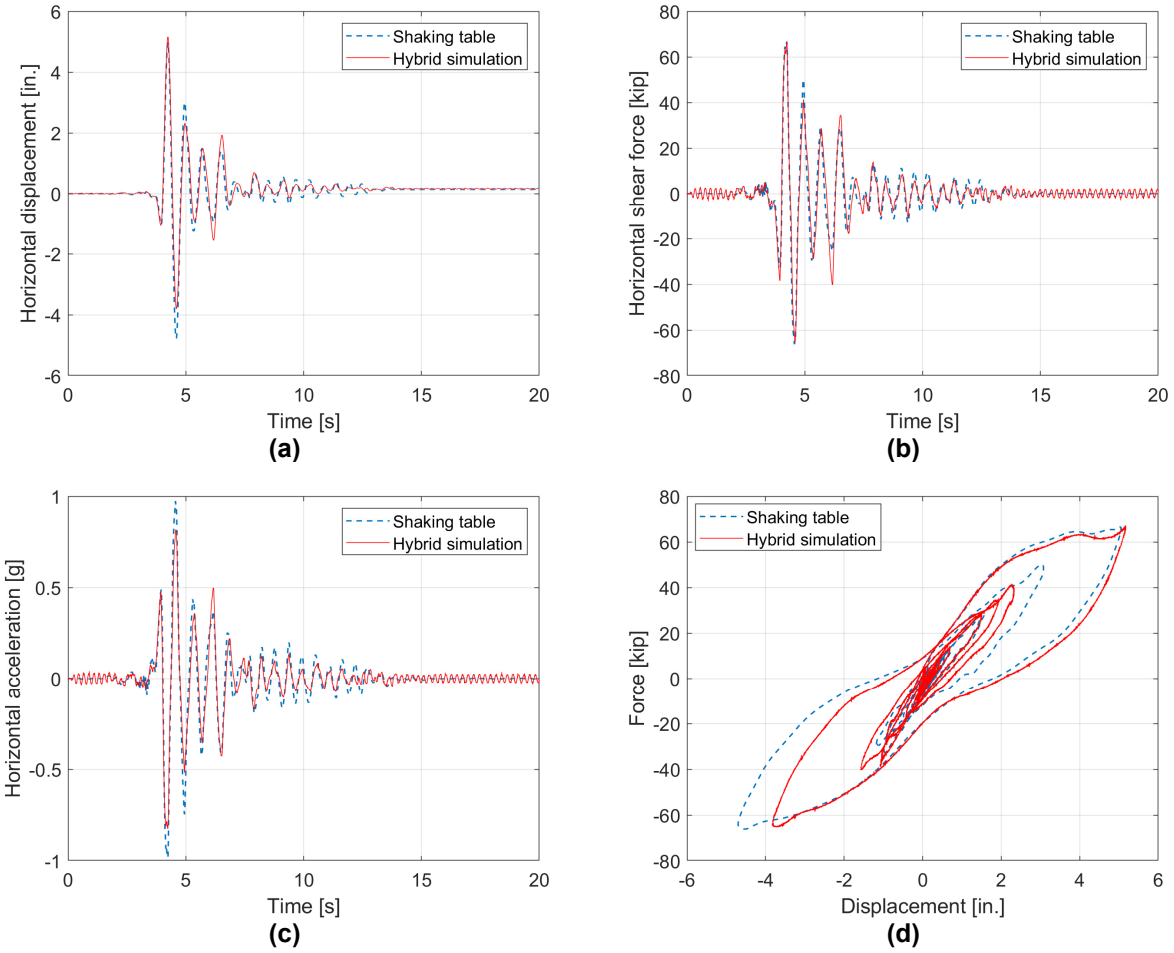

Figure 7.42 **(a) Displacement time history; (b) resisting force time history; (c) acceleration time history; and (d) force-displacement relationship comparisons of EQ5 in the horizontal direction.**

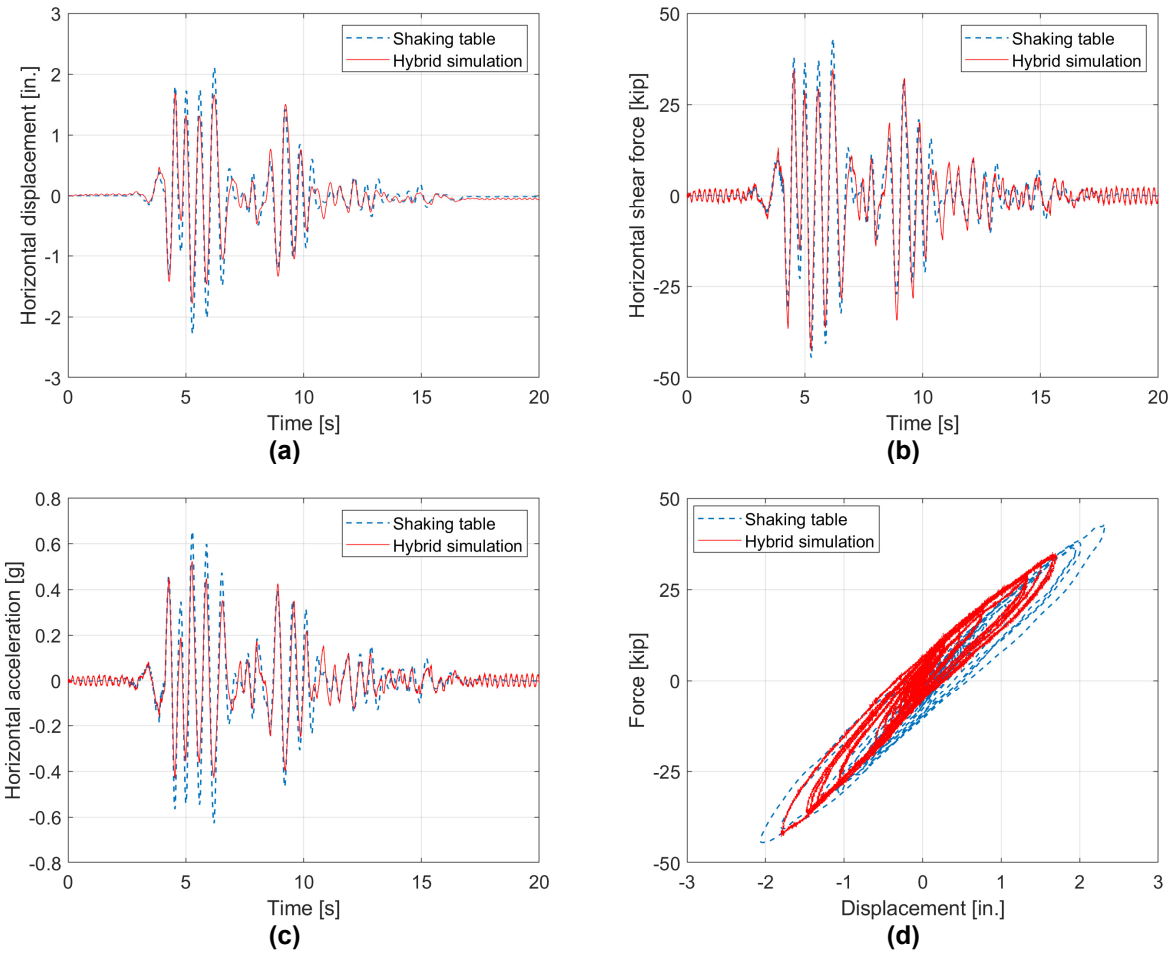

Figure 7.43 **(a) Displacement time history; (b) resisting force time history; (c) acceleration time history; and (d) force-displacement relationship comparisons of EQ6 in the horizontal direction.**

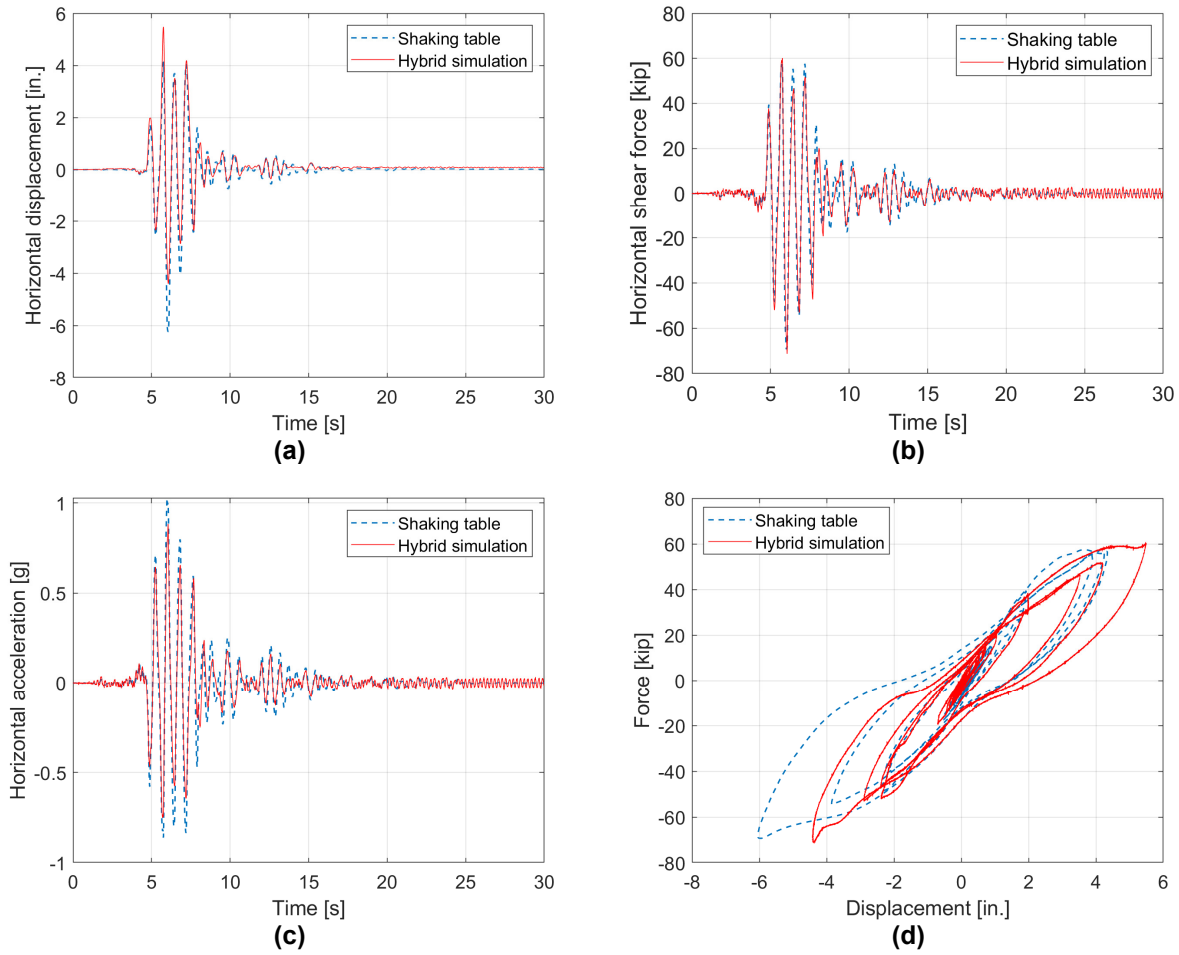

Figure 7.44 **(a) Displacement time history; (b) resisting force time history; (c) acceleration time history; and (d) force-displacement relationship comparisons of EQ7 in the horizontal direction.**

7.4.3.2 Deformations

The peak and residual drifts from each HS run are summarized in Table 7.3 together with the cumulative residual drift, which was calculated as the residual drift relative to the beginning of the first run (EQ2). Low levels of residual drift were observed in both the HS and shaking table tests, indicating the superior seismic response of the innovative design of the bridge bent with self-centering columns. The column end rotations (top and bottom) were measured by a total of 16 LVDTs mounted around the rocking interfaces, as shown in Figure 6.36. The rotation time histories for EQ6 and EQ7 during the HS test are shown in Figure 7.45. Similar to the observation from the shaking table test, the rotation response closely follows the drift response, indicating the obvious rocking behavior and that the column behaved nearly like a rigid body over the clear height.

Table 7.3 Summary of peak and residual drift ratios from the HS test.

EQ #	Peak Drift [%]	Residual Drift [%]	Residual/Peak	Cumulative Residual Drift [%]
02	0.879	0.009	0.011	0.009
03	1.845	0.173	0.094	0.164
04	0.856	0.014	0.016	0.178
05	3.898	0.125	0.032	0.303
06	1.344	0.040	0.030	0.263
07	4.135	0.067	0.016	0.330

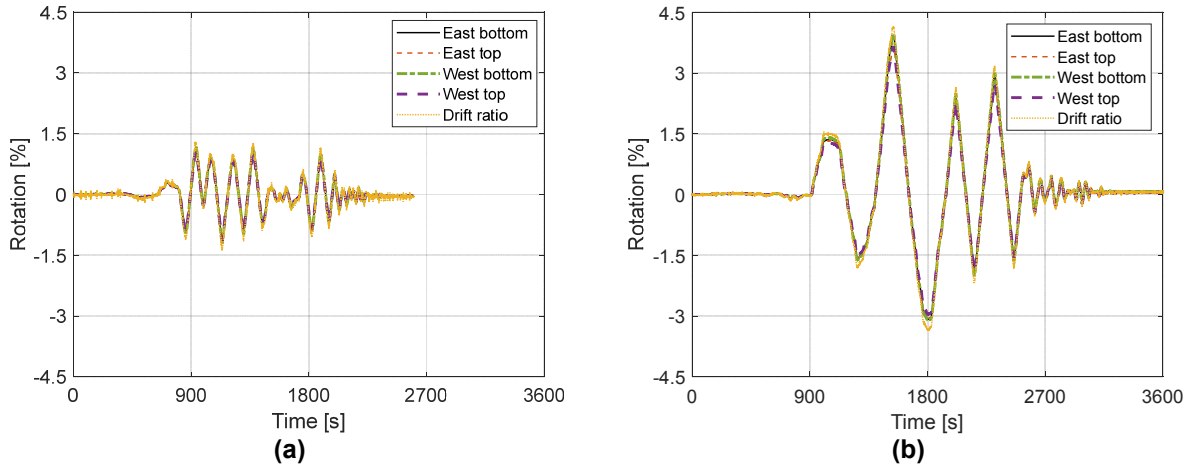

Figure 7.45 Column end rotations from (a) EQ6; and (b) EQ7.

The gap opening states at the instant of peak positive/negative drifts at the bottom interfaces of the east and west columns are shown in Figure 7.46 to Figure 7.48 for EQ3, EQ5, and EQ7. Also shown in these figures are the overall deformations of the specimen at the same instant of time, with the corresponding drift ratio listed in the sub-captions. Again, the rocking interface formed at the location where the steel strip of the column outer shell was removed. Minor concrete spalling took place around the interfaces during larger intensity test runs. Some cracks and crushing of the surface grout were also observed.

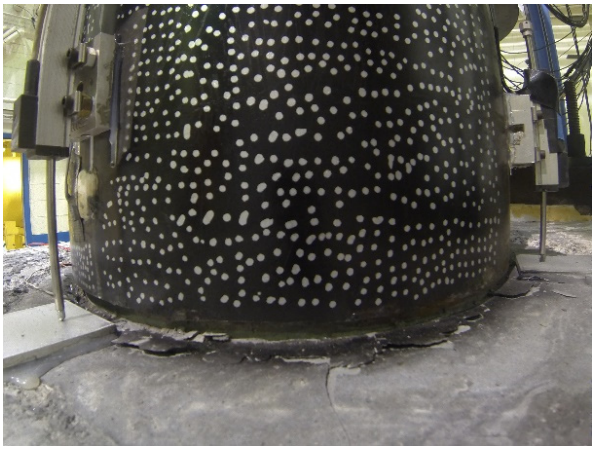

(a) West column interface, west side;
Δ = 1.85%

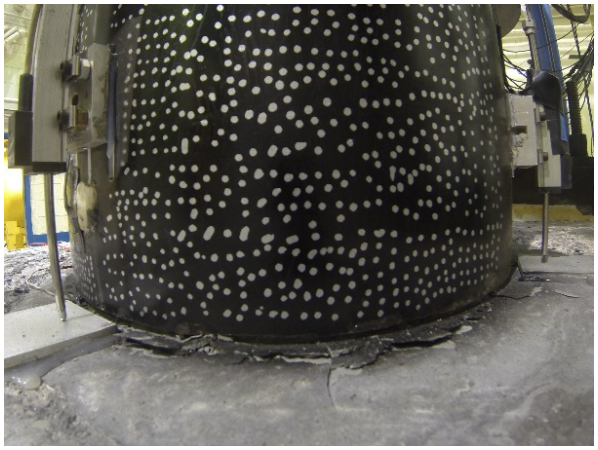

(b) West column interface, west side;
Δ = -1.34%

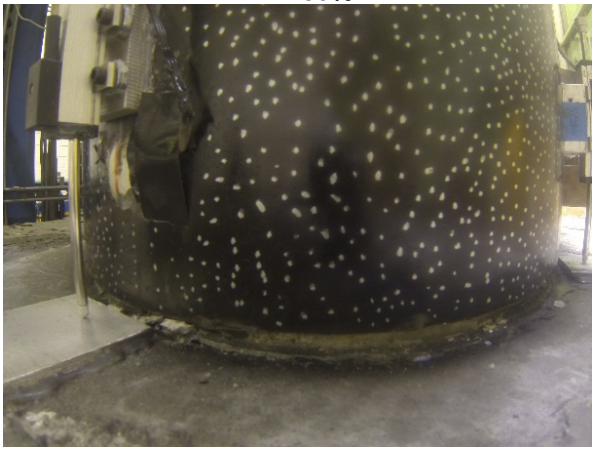

(c) East column interface, east side;
Δ = 1.85%

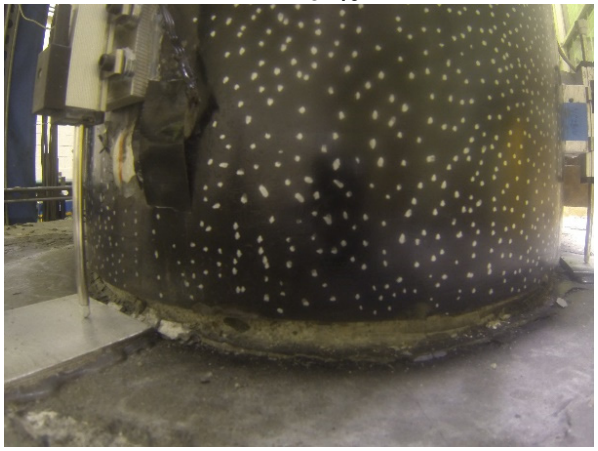

(d) East column interface, east side;
Δ = -1.34%

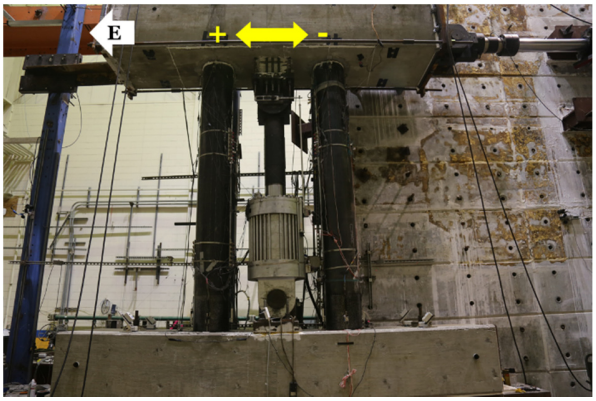

(e) Specimen deformation;
Δ = 1.85%

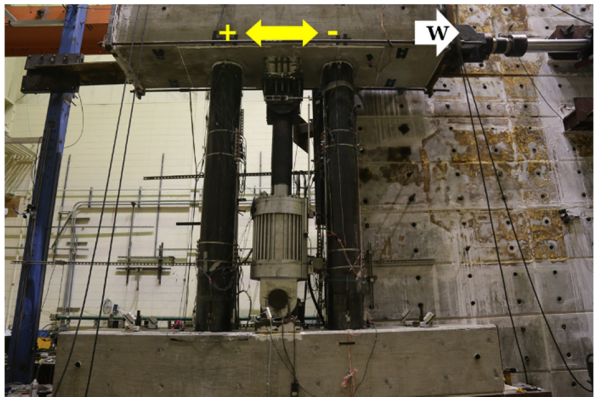

(f) Specimen deformation;
Δ = -1.34%

Figure 7.46 Specimen response at peak drifts (EQ3).

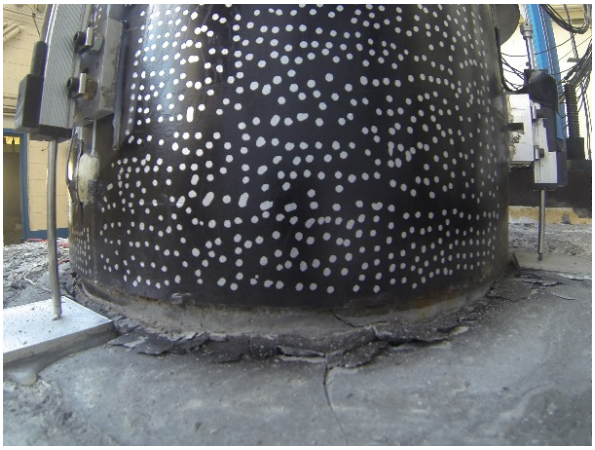

(a) West column interface, west side;
Δ = 3.9%

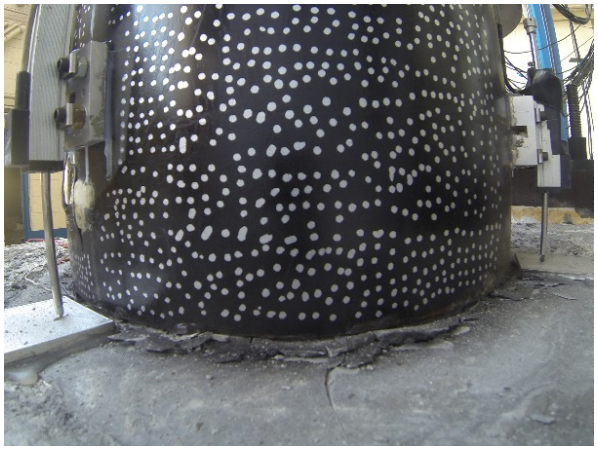

(b) West column interface, west side;
Δ = -2.87%

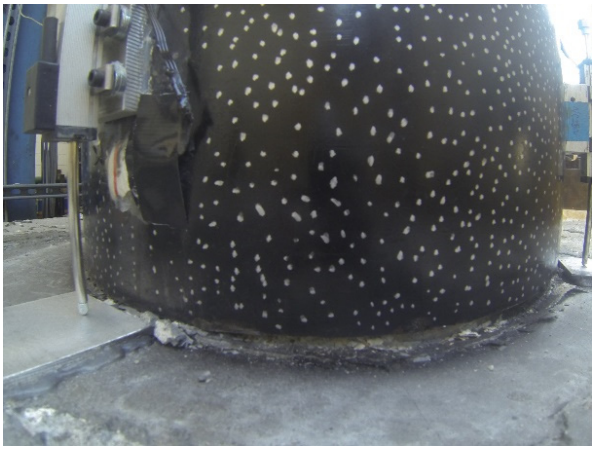

(c) East column interface, east side;
Δ = 3.9%

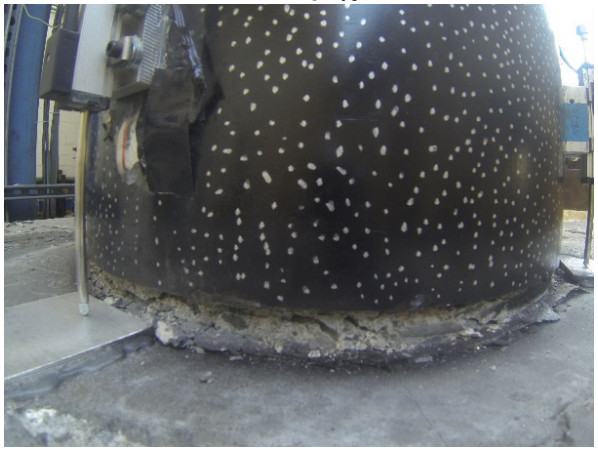

(d) East column interface, east side;
Δ = -2.87%

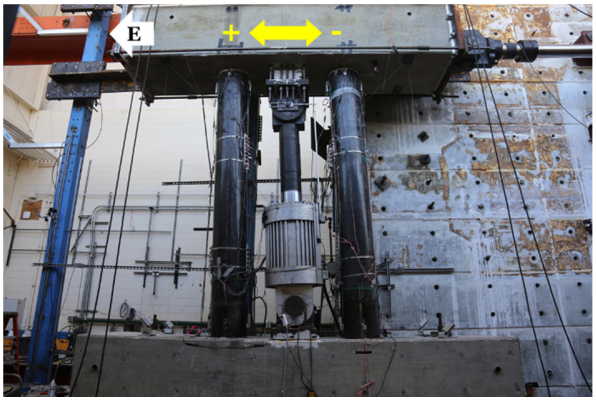

(e) Specimen deformation;
Δ = 3.9%

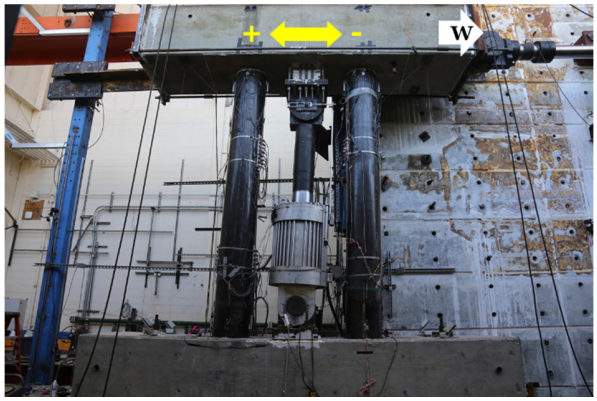

(f) Specimen deformation;
Δ = -2.87%

Figure 7.47 Specimen response at peak drifts (EQ5).

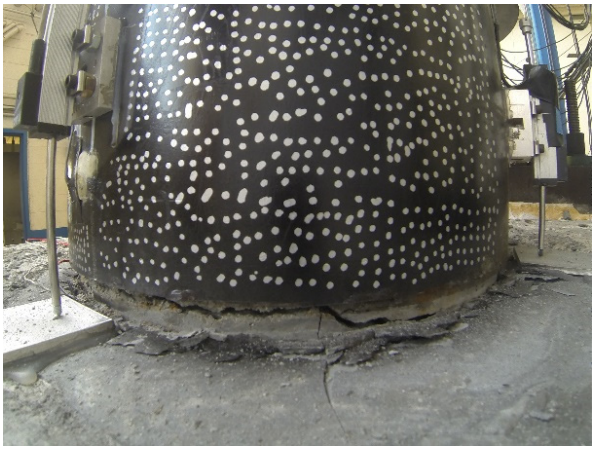

(a) West column interface, west side;
Δ = 4.14%

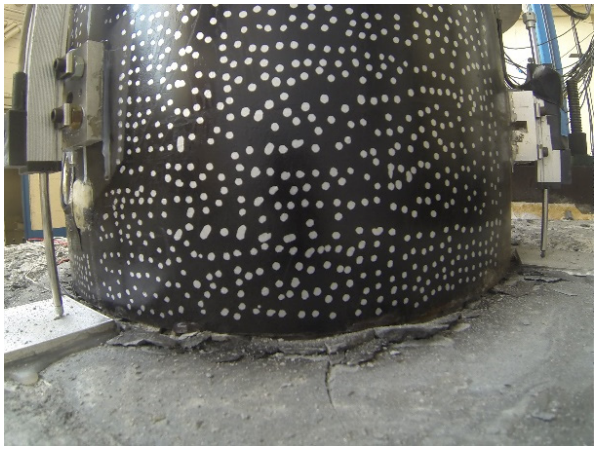

(b) West column interface, west side;
Δ = -3.3%

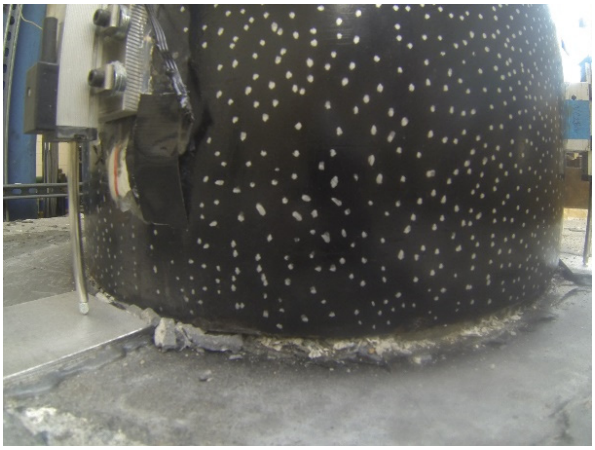

(c) East column interface, east side;
Δ = 4.14%

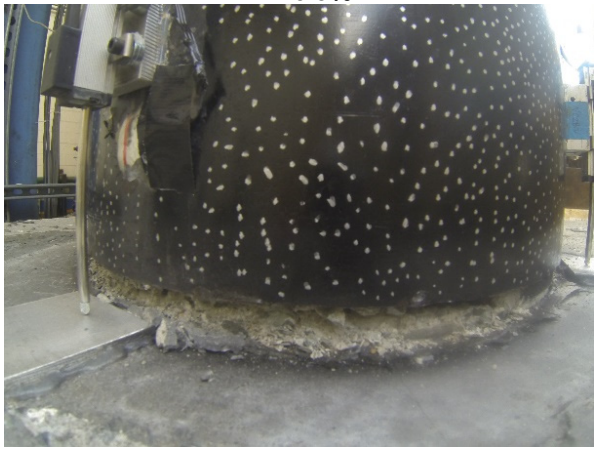

(d) East column interface, east side;
Δ = -3.3%

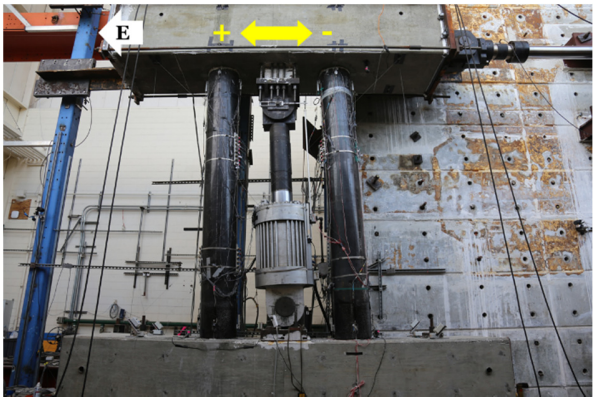

(e) Specimen deformation;
Δ = 4.14%

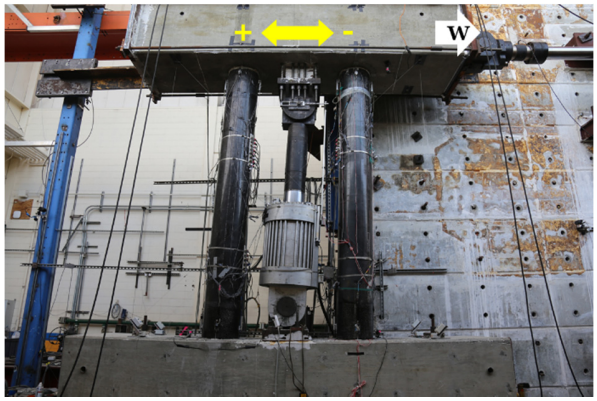

(f) Specimen deformation;
Δ = -3.3%

Figure 7.48 Specimen response at peak drifts (EQ7).

7.4.3.3 Strain histories

In this section, strain measurements are briefly presented. The locations of different strain gauges mentioned in the following can be found in section 6.8.3 and are repeated above each plot for easy reference.

Figure 7.49 plots the strains of the longitudinal reinforcing bars and the stirrups in the cap beam from EQ7. It can be concluded that the cap beam remained elastic during the entire phase I testing as the strain gauges did not capture any meaningful strain behaviors other than noises during the largest ground motion. Figure 7.50 shows the strains on the unbonded longitudinal reinforcing bars serving as energy dissipators inside the columns for all test runs. The average yield strain from the tests of the material properties is indicated on the plots. The yielding of the energy dissipators initiated starting from EQ3, with residual strains left over at the end of each run afterwards. Some strain gauges were broken after large intensity motions. The significant amount of the observed yielding justifies the used unbonded detailing in providing energy dissipation to the self-centering system.

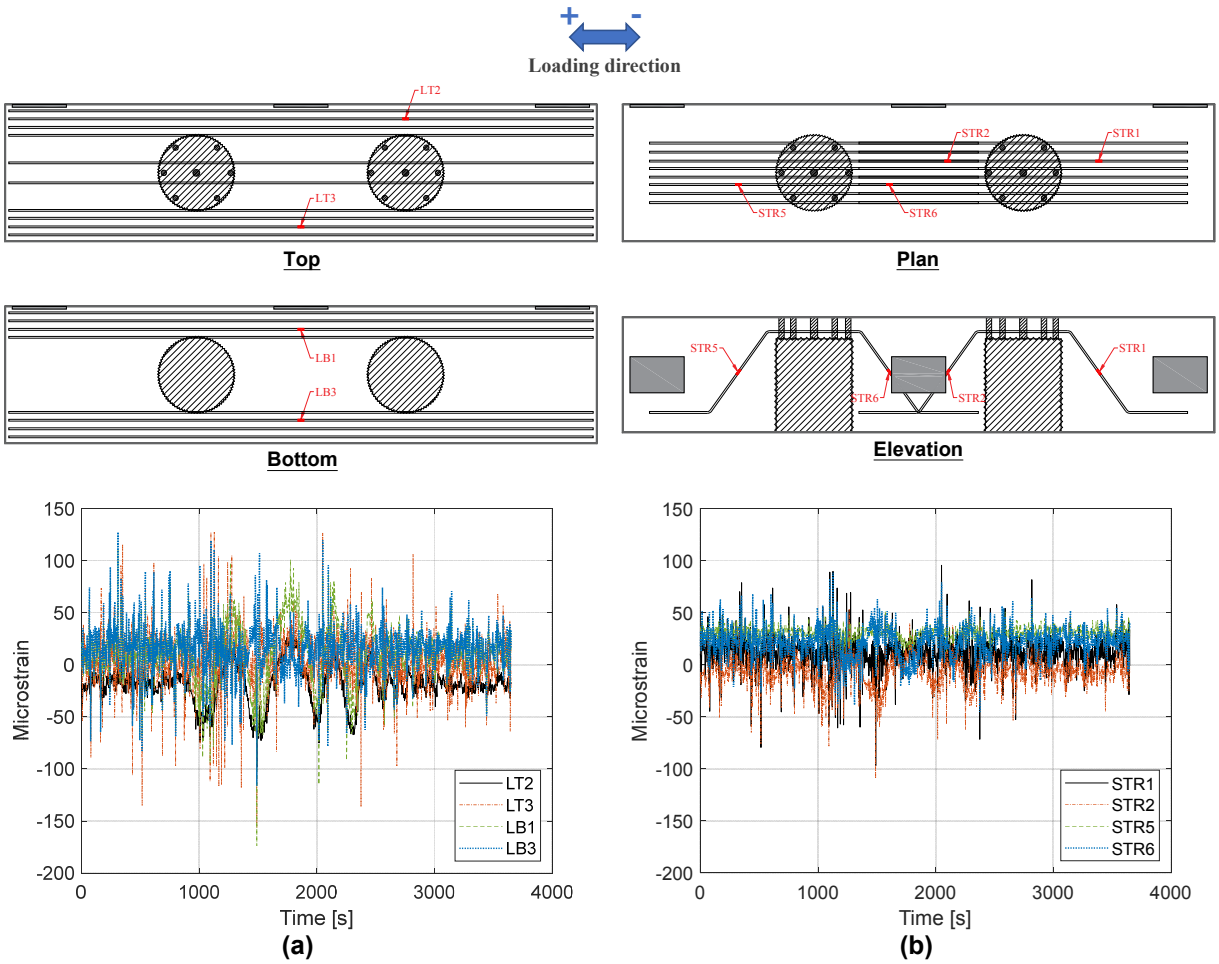

Figure 7.49 Strain histories of (a) longitudinal reinforcing bars; and (b) stirrups of the cap beam in EQ7.

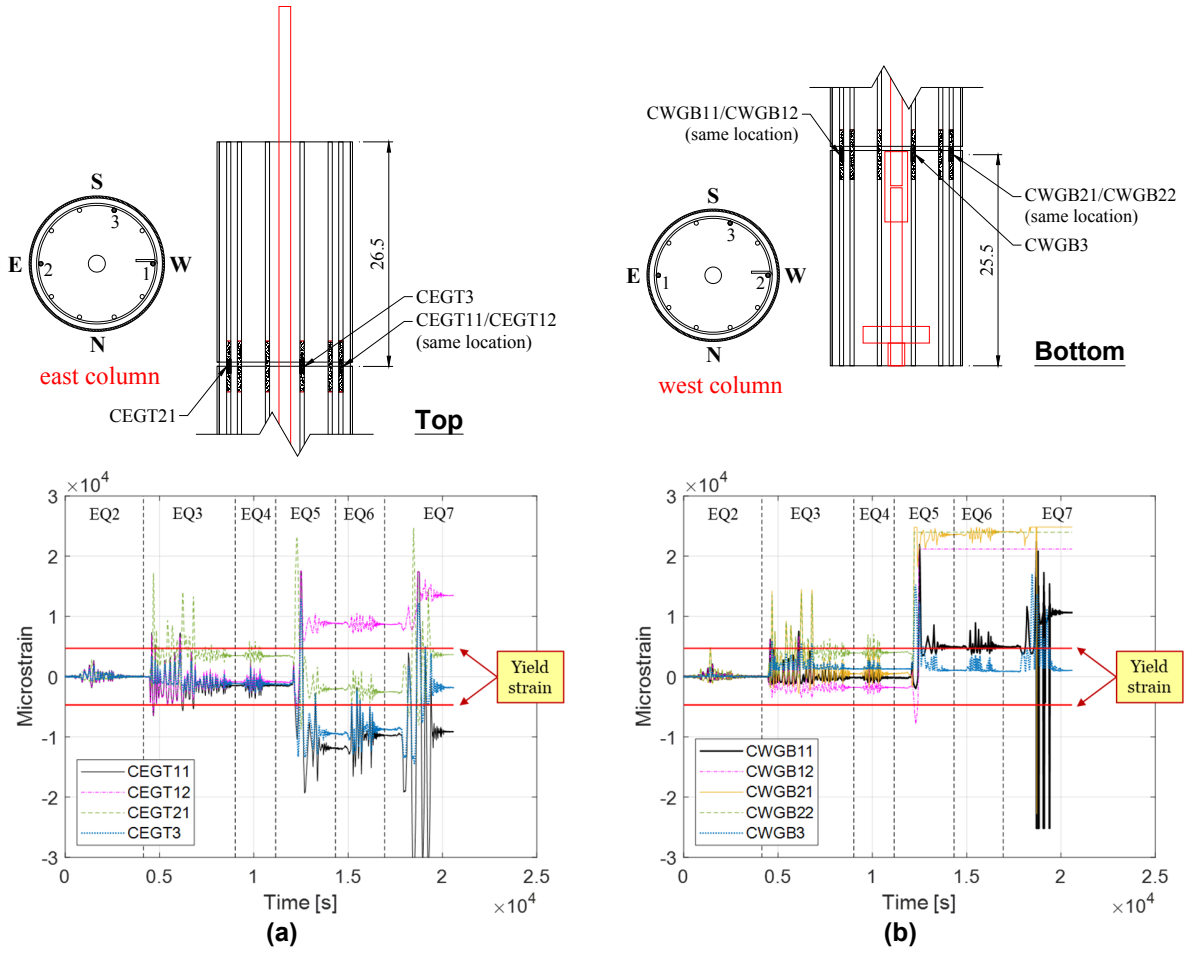

Figure 7.50 **Strain histories of the energy dissipators in (a) east column top; and (b) west column bottom.**

Figure 7.51 to Figure 7.53 give the strain behaviors of the steel shell for all test runs. The horizontal strain gauges mounted closer to the bottom interfaces (CESJH21 and CWSJH11 in Figure 7.51) showed some circumferential tensile strains. These strains were caused by the dilation of the steel shell or the volume increase because of the concrete disintegrating during the rocking, but were below the average yielding point according to the tests of the material properties. However, comparable strain level was not observed for the strain gauges closer to the top interfaces (CESJH24 and CWSJH14). This is probably attributed to the top interfaces being made much flatter than the bottom ones by the wood sealing panels when placing the grout (see Appendix C) and the steel shell was not axially compressed as much, leading to less dilation.

The vertical strain gauges installed on the top embedded steel shell did not experience any meaningful strain patterns (Figure 7.52). Therefore, it is concluded that the transfer of axial forces inside the socket connection occurred mainly along the lateral loading direction instead of the orthogonal direction. This conclusion is further supported by the plots shown in Figure 7.53. The rosette gauges on the embedded steel shell along the E-W loading direction gave larger strain readings compared to the vertical ones. The opposite sign shown in each rosette gauge couples (e.g., CWR121 and CWR122) was because of the Poisson's effect, i.e., when the steel shell was

stretched in the vertical direction, it tended to contract in the horizontal direction and vice versa. In addition, the closer to the rocking interfaces, the larger the measured strain on the steel shell. This observation can be explained by Figure 7.54, similar to the idea of bond-slip of the reinforcing bar anchorage. Assuming uniform bond stress along the interface between the infilled grout and the embedded steel shell for simplicity, the vertical stress distribution along the height of the steel shell is linear, with higher values closer to the rocking interfaces. The linear strain distribution follows that of the stress as the steel remains in the linear elastic range.

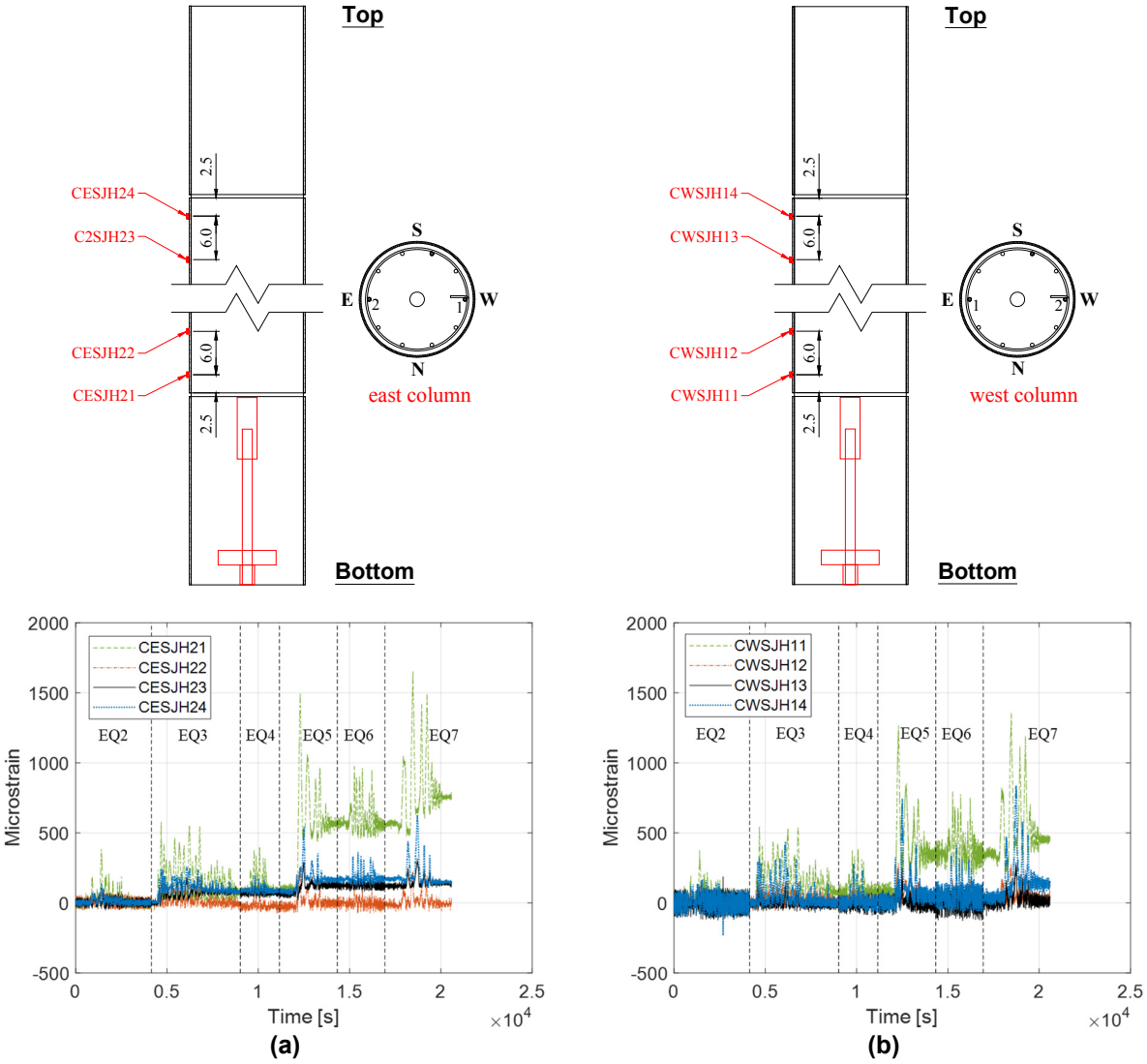

Figure 7.51 **Horizontal strains of the steel shell on (a) east column, east side; and (b) west column, east side.**

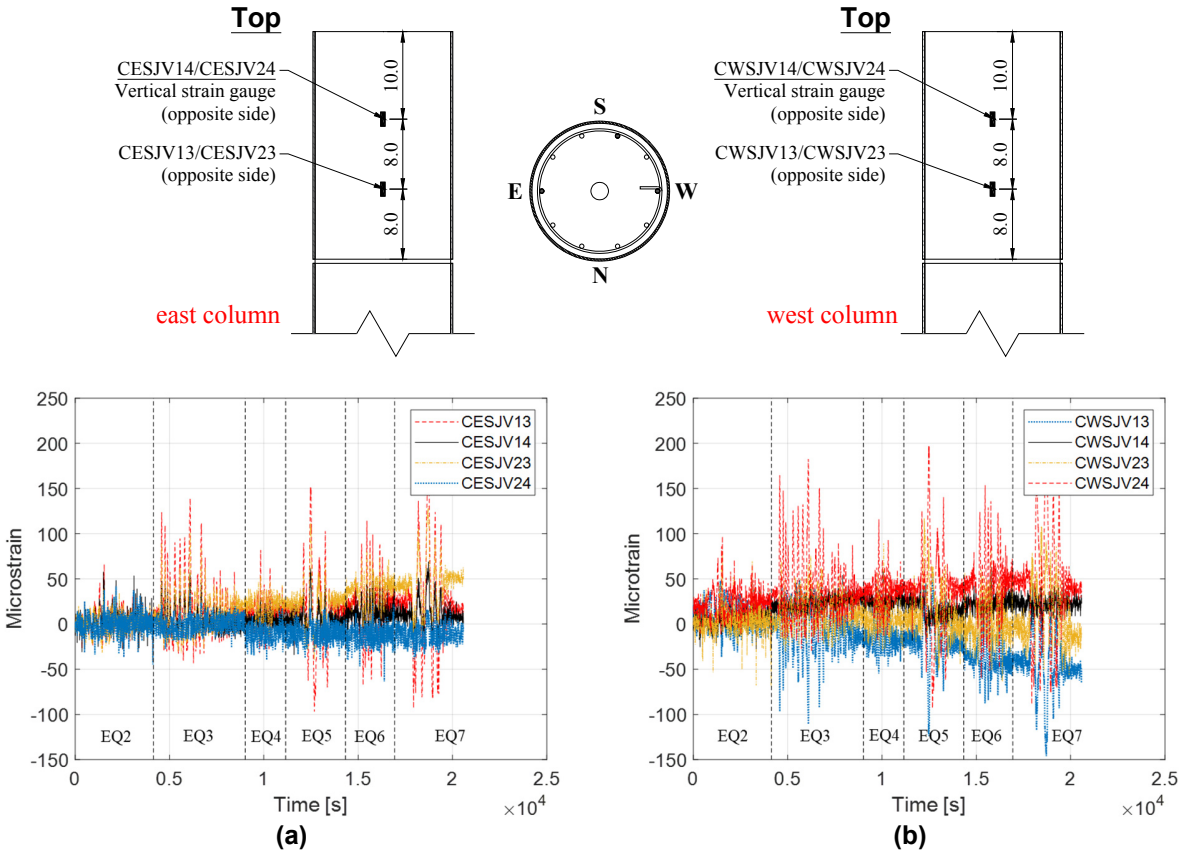

Figure 7.52 **Vertical strains of the top embedded steel shell on (a) east column; and (b) west column.**

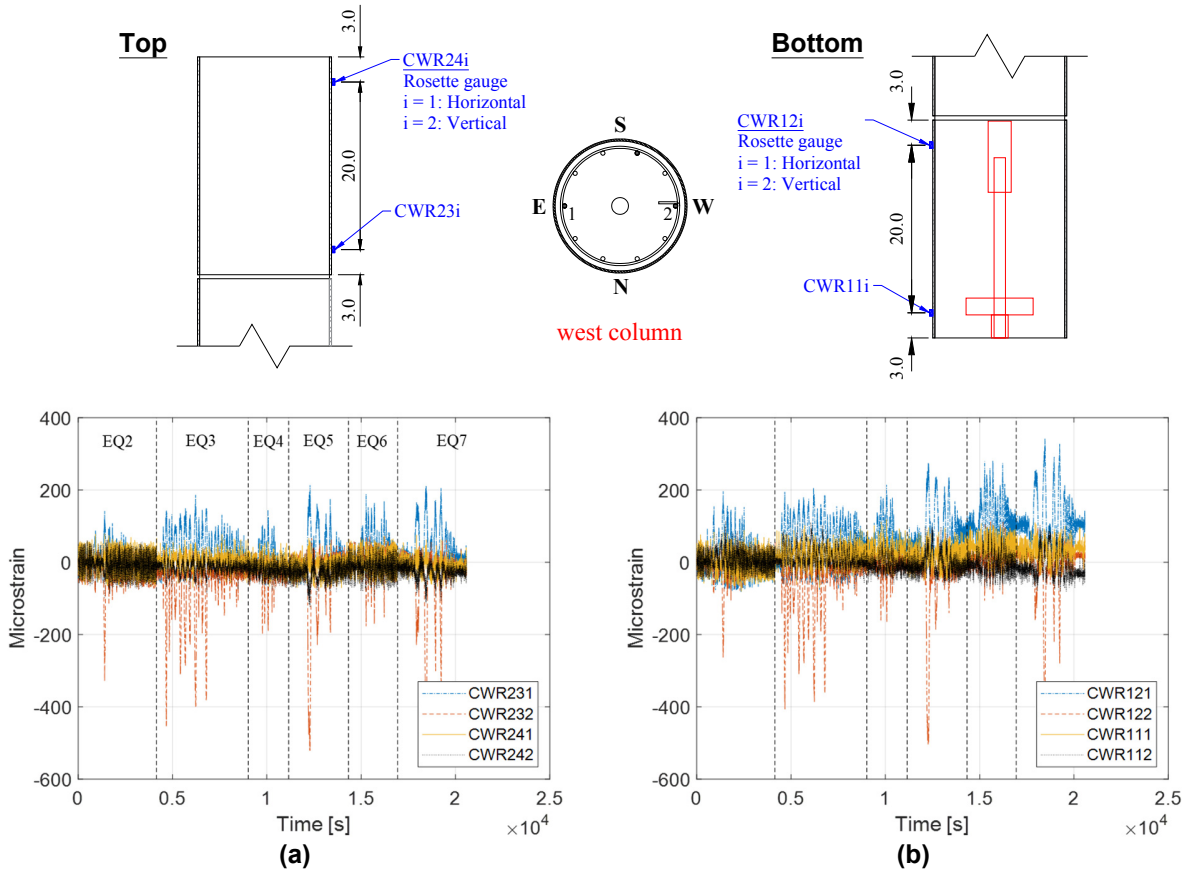

Figure 7.53 **Strains of the embedded steel shell on (a) west column top, west side; and (b) west column bottom, east side.**

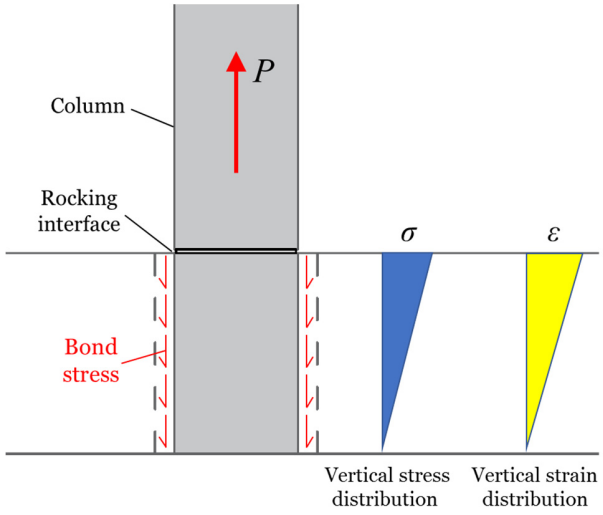

Figure 7.54 **Idealized stress/strain distribution along the embedded steel shell.**

7.4.3.4 Other Response Quantities

Figure 7.55 and Figure 7.56 show the PT bar force and strain time histories from EQ7. The forces were obtained by converting the pressure measurements according to the linear relationship in Figure 6.31(b). The maximum PT force of 167.8 kips occurred in the west column, which corresponded to a stress value of 106.2 ksi. For the rest of the ground motions, the PT bar stresses were smaller. This is to be expected, because the larger the drift ratio, the more deformation in the PT bars and the larger the stress. The strain plots came from two different measurements from the strain gauges mounted on the same location but opposite side of each PT bar. The difference in the strain measurements, especially for the east column, is an indication of slight PT bar bending during the test.

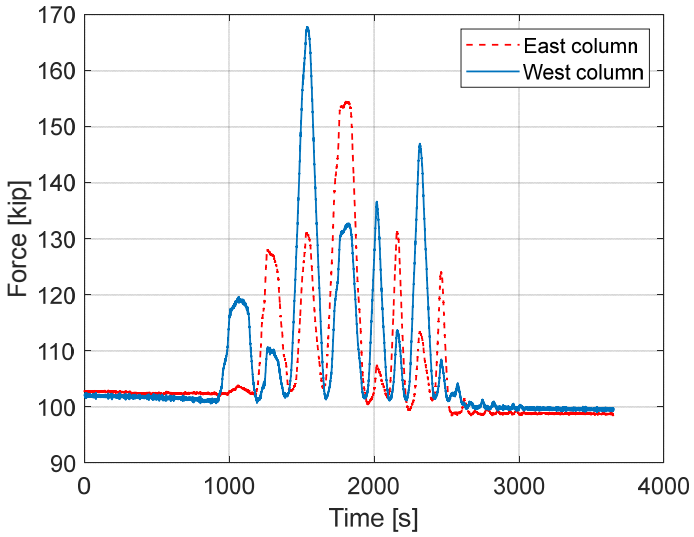

Figure 7.55 Time histories of PT bar forces in EQ7.

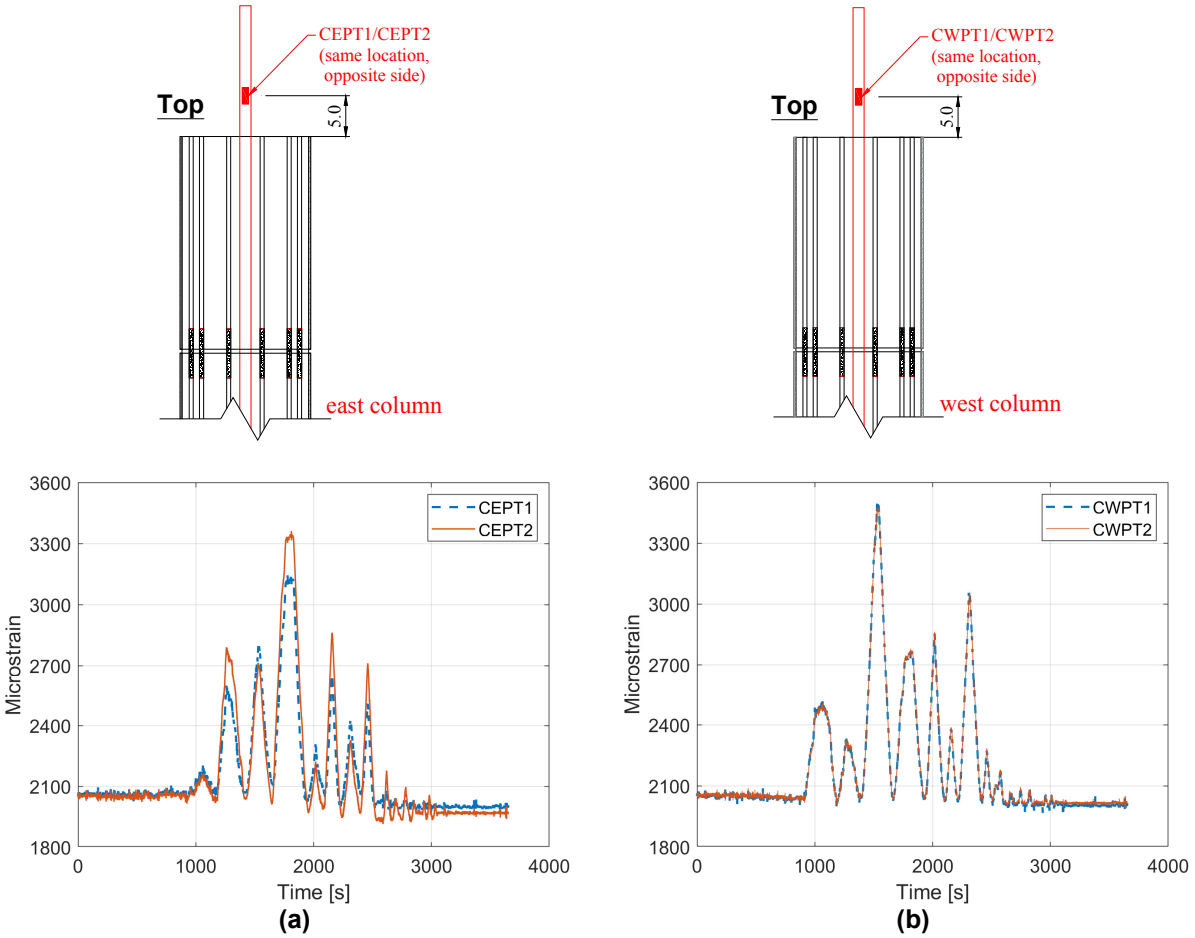

Figure 7.56 Time histories of the PT bar strains for (a) east column; and (b) west column in EQ7.

Figure 7.57 plots the stress against the average strain from each PT bar in EQ7. The stress was obtained by dividing the PT bar force with its cross-sectional area. The peak stress in the PT bar of the west column was higher than that of the east column. This is because the magnitude of peak positive displacement towards the east (5.48 in.) was bigger than the peak negative displacement towards the west (-4.40 in.) (see Figure 7.44(a)). Therefore, the PT bar in the west column was stretched more. In addition, the PT bars should remain essentially in the linear elastic range under this level of stress based on the tests of the material properties, which is not consistent with the plot. Due to the slight bending of the PT bars, the stress distribution on the cross section of each PT bar is not uniform. In this case, the stress-strain plot could possibly be nonlinear as the stress obtained this way is on an average sense. If somehow there is a way to obtain the stress of the specific point where the strain gauge was installed, the linear elastic relationship should be expected. Another observation is that there is some prestressing loss at the end of the test. Usually this is caused by the yielding of the PT bars. However, it was believed that the explanation does not apply here as the dropping of the PT bar forces before the large cycles was quite obvious. The two-stage pumps were not able to hold the pressures perfectly well, especially in the long-duration slow test situation. This was another limitation in terms of the test setup. Therefore, the pressure

was carefully adjusted so that the PT forces always started at 40% GUTS at the beginning of each test run.

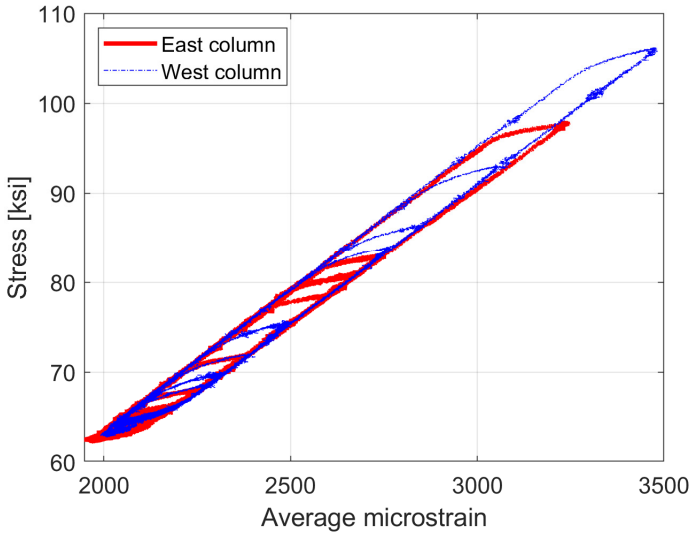

Figure 7.57 Stress vs. average strain for both PT bars in EQ7.

It should be noted that the yielding of the PT bar is usually considered unacceptable for the self-centering hybrid system. If the PT bar yields, it will display a permanent plastic elongation when the rocking behavior stops, causing a loss of PT force and compromising the system's self-centering capacity. For this reason, many different approaches have been investigated by researchers to prevent any early loss of the PT force. One straightforward approach is to limit the initial PT force. When this is not sufficient, additional deformability can be added to the PT bars by placing elastic devices in series with the bars. Guerrini et al (2015) proposed the usage of elastomeric bearing pads, inserted between the top anchor plate and the cap beam (see Figure 7.58). With this configuration, the tensile deformation demand on the bars is partially transformed into compressive deformation of the bearing pads.

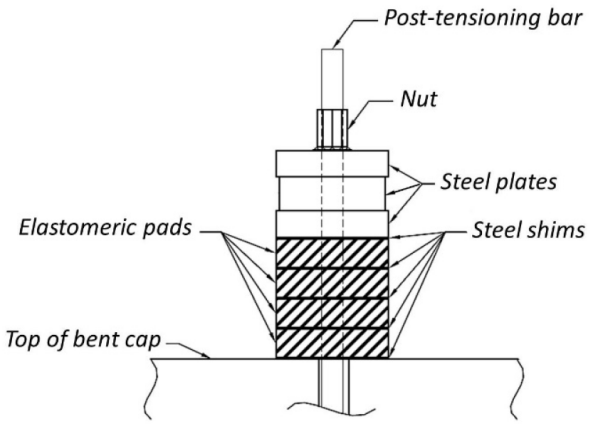

Figure 7.58 Elastomeric bearings in series with the PT bars (Guerrini et al., 2015).

8 Hybrid Simulation of a Resilient Bridge Bent Design: Phase II

The main accomplishment in phase I HS was the HSS development, validation and comparison of the test results with the shaking table test. In phase II, the main focus is the system level response evaluation by incorporating a full bridge model. The key change made was in the Matlab function block shown in Figure 7.22. Instead of a single mass, the analytical substructure was replaced by the remaining part of a representative bridge, including the bridge superstructure and the abutments. The same prototype bridge previously used in the V-connector study, the Jack Tone Road On-Ramp Overcrossing as described in section 4.1.1, was selected again for this purpose. Similar to the V-connector study, the reason of selecting this prototype is that it has only one single bent, making it an ideal candidate for simulating the two-column bridge bent as the experimental substructure and the rest of the bridge as the analytical substructure. This system level investigation would not have been practically feasible for a shaking table test and therefore it reflects a significant contribution of the HS.

This chapter starts with describing the prototype bridge modeling techniques and details. Some background information on the formulation of stiffness/mass/damping matrices and the resisting force vector is provided. The bridge was also modeled the same way in OpenSEES (McKenna et al., 2000) to check the new implementation. Three new ground motion records, one for each intensity level, were selected from the ground motion database based on the target spectrum of a specific location. The system level HS test is then presented, followed by the discussion of the test results through a parametric study that provides insights on the observed bridge system response.

8.1 BRIDGE MODELING

The simplified bridge model in this study consists of three parts: the bridge superstructure (the deck), the bridge abutments, and the two-column bridge bent (the test specimen). Considering the size of the full-scale bridge and the two-column bridge bent specimen, the scale of the test specimen was selected to be 30% (S_L = 3.333). A spine-line model of the bridge structure was used, with line elements located at the centroid of the cross sections following the alignment of the bridge. A schematic representation of the bridge model can be found in Figure 8.1. To capture the responses of the entire bridge system and the individual components under specific seismic demand characteristics, three-dimensional modeling was adopted. The developed model incorporated nonlinear behavior of individual components, including the abutment springs and the

nonlinearity from the tested bridge bent. Important assumptions and main aspects of the modeling process are described in the following subsections.

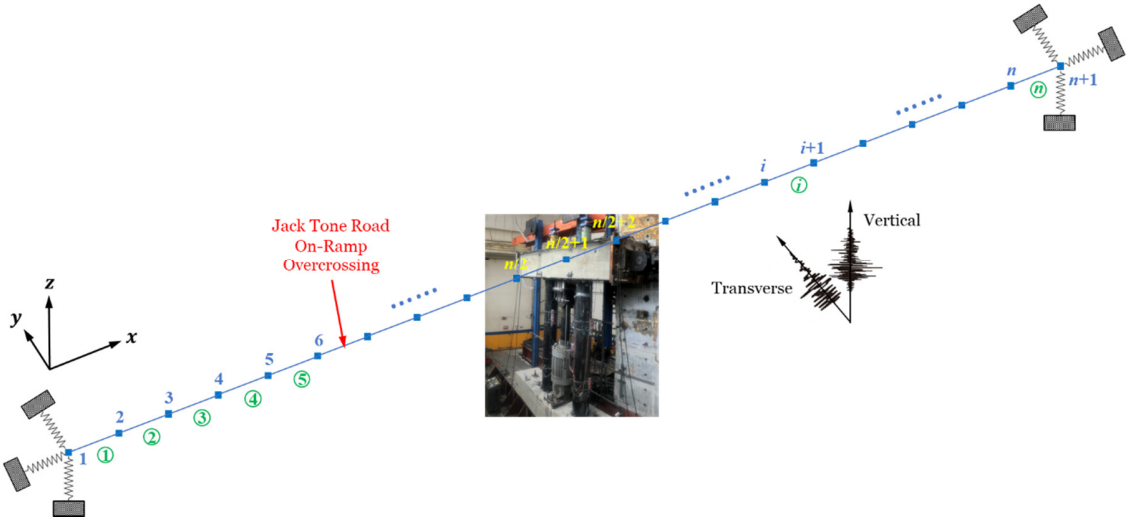

Figure 8.1 Schematic representation of the utilized bridge model.

8.1.1 Bridge Deck Modeling

The prestressed concrete box girder of the deck was modeled as a "spine-line" using 3D linear elastic frame elements, because flexural yielding of the deck during the seismic response is not expected according to Caltrans SDC (2013). The effective moment of inertia of the box girder, denoted as I_{eff}, depends on the extent of cracking: for conventional reinforced concrete box girder sections, $I_{eff} = 0.5I_g$ or $0.75I_g$. However, according to Caltrans SDC (2013), no stiffness reduction is recommended for prestressed concrete box girder sections (i.e., $I_{eff} = I_g$). Other modeling parameters for the bridge deck followed the cross section geometry of the deck as listed in Table 4.1.

8.1.2 Abutment Modeling

Numerous studies (Aviram et al., 2008; Bozorgzadeh et al., 2006, 2008; Goel and Chopra, 1997; Shamsabadi et al., 2007, 2010) have addressed the issues inherent in abutment modeling. Here, the focus was on seat-type abutment (see Figure 8.2) using simplified abutment modeling techniques. In this simplified model, the abutment was represented by three nonlinear springs — longitudinal, transverse, and vertical — connected to each end of the bridge deck as shown in Figure 8.1. The utilized modeling parameters were based on the prototype bridge and were all on the prototype scale. Note that for this specific study, it was unnecessary to model the longitudinal direction of the abutment response as the input ground motions were in the transverse and vertical directions only and no longitudinal responses were expected. However, for completeness of the modeling process and for possible future usage and reference, the longitudinal abutment response was included.

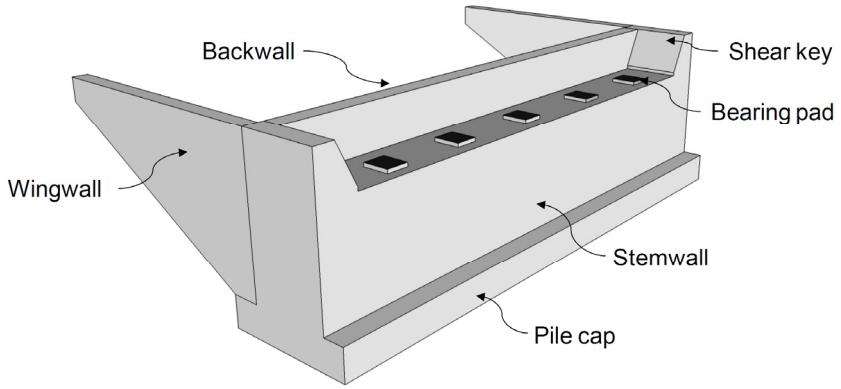

Figure 8.2 Configuration of typical seat-type abutment (Kavianijopari, 2011).

8.1.2.1 Longitudinal Direction

According to the guidelines described in Caltrans SDC (2013), a backbone curve representing the passive earth pressure based on results from a large-scale abutment testing at UC Davis (Maroney, 1995) and UCLA (Stewart et al., 2007) was used in the longitudinal direction. Equation (8.1) shows the initial stiffness of this backbone curve. The formula was proportionally adjusted to the backwall/diaphragm height which is equal to 1.7 m (5.5 ft).

$$K_{abut} = \begin{cases} K_i \times w \times \dfrac{h}{5.5\text{ ft}} & \left(K_i = 25\dfrac{\text{kip/in.}}{\text{ft}}\right) \quad \text{U.S. units} \\ K_i \times w \times \dfrac{h}{1.7\text{ m}} & \left(K_i = 14.35\dfrac{\text{kN/mm}}{\text{m}}\right) \quad \text{S.I. units} \end{cases} \tag{8.1}$$

Here, w and h are the width and height of the backwall or the diaphragm abutments, respectively. K_i is the initial embankment fill stiffness.

The force-displacement backbone curve of the seat-type abutment in the longitudinal direction is shown in Figure 8.3. Δ_{eff} is the mobilization of the passive soil resistance, which is expressed in Caltrans SDC (2013) as the effective longitudinal displacement at an idealized yield point. For the seat-type abutments, Δ_{gap} is the gap distance between seat-type abutment and superstructure which can be estimated from structural drawings (e.g., Δ_{gap} = 1 in.). The resistance force assigned to the seat-type abutment P_{bw} is calculated according to the following equation:

$$P_{bw} = A_e \times 5.0\text{ ksf} \times \frac{h_{bw}}{5.5} \qquad \text{(unit: ft, kip)} \tag{8.2}$$

The maximum passive pressure of 5.0 ksf presented in Equation (8.2) is based on the ultimate static force developed in the full-scale abutment testing. The height proportionality factor, h_{bw}/5.5 ft, is based on the height of the tested abutment walls. The effective abutment wall area A_e for calculating the ultimate longitudinal force capacity of an abutment is presented in Equation (8.3) where h_{bw} and w_{bw} are the effective height and width of the backwall in the seat-type abutment.

$$A_e = h_{bw} \times w_{bw} \tag{8.3}$$

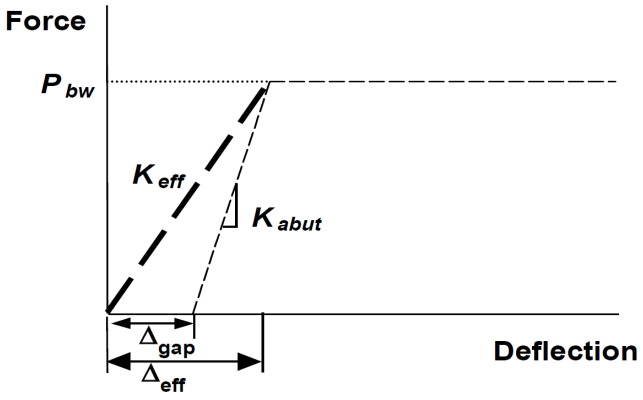

Figure 8.3 Effective abutment stiffness for seat-type abutment (Caltrans SDC, 2013).

Based on the above provisions, a compression-only spring was assigned with an EPP gap material for the backbone curve representing the abutment backwall, see Figure 8.4. It accounts for the gap between the seat-type abutment and the superstructure and embankment fill response, where passive pressure (the compression) is produced by the abutment backwall. In comparison to the embankment fill stiffness, the shear stiffness of the bearing pads was ignored. According to the prototype bridge geometry, the gap value Δ_{gap} was taken to be 1 in. while the effective height h_{bw} and width w_{bw} were taken to be 55.68 in. and 215.42 in., respectively, resulting in a longitudinal stiffness K_{abl} of 378.6 kips/in. and a corresponding strength P_{bwl} of 351.4 kips.

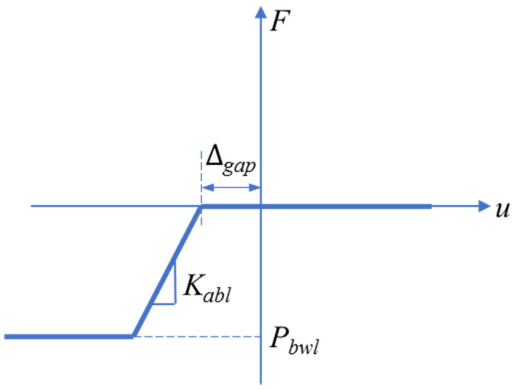

Figure 8.4 Force-displacement relationship of the longitudinal abutment response.

8.1.2.2 Transverse Direction

In the transverse direction, Caltrans SDC (2013) states that seat-type abutments are designed to behave elastically for service loads and moderate earthquake loads. In extreme events, the linear analysis cannot capture the nonlinear behavior of the shear keys and wingwalls. Therefore, the transverse stiffness of the seat-type abutment should be assumed to be negligible unless the designer can demonstrate the force-deflection and stiffness of each component that contributes to the transverse response. Caltrans SDC (2013) recommends a nominal transverse spring, K_{nom} equal to 50% of the adjacent bent for the elastic domain.

To account for the possibility of transverse nonlinearity, a spring that works in both tension and compression was defined with an assigned EPP backbone curve representing the backfill, wingwall, and pile system, see Figure 8.5. The abutment stiffness and strength for the longitudinal direction were modified using factors corresponding to the wall effectiveness (C_L = 2/3) and the participation coefficient (C_W = 4/3) according to Maroney and Chai (1994). The resistance of the brittle shear keys and distributed bearing pads were ignored in this model for simplicity. The resulting transverse stiffness K_{abt} was 112.2 kips/in. and the corresponding yielding strength P_{bwt} was 104.1 kips.

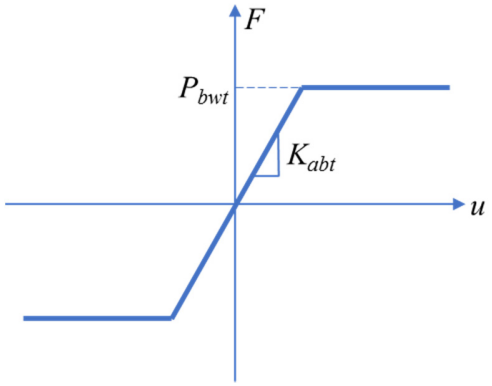

Figure 8.5 Force-displacement relationship of the transverse abutment response.

8.1.2.3 Vertical Direction

In the vertical direction, a compression-only linear elastic spring (see Figure 8.6) was defined at each end of the bridge deck with the stiffness K_v equals to 1200 kips/in., representing the vertical stiffness of the bearing pads in the prototype bridge.

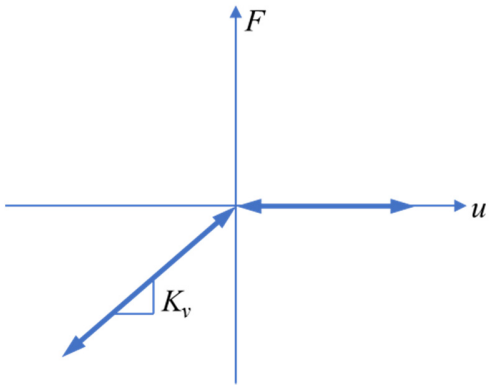

Figure 8.6 Force-displacement relationship of the vertical abutment response.

8.1.3 Stiffness Matrix

In the 1950's and 60's, significant research was directed towards developing efficient computer implementations of suitable structural analysis methods. One of the methods of structural analysis,

namely the stiffness method, is particularly suited for computer-automated analysis of complex structures including the statically indeterminate ones. It is a matrix method that makes use of the members' stiffness relationships for computing member forces and displacements. This method is the most common implementation of the FEM. In applying the method, the structural system must be modeled as a set of simpler, idealized elements interconnected at the nodes. The stiffness properties of these elements are then, through matrix mathematics, compiled into a system of algebraic equations which govern the behavior of the entire idealized structure. The unknown displacements and forces of the structure can then be determined by solving this system of equations. The stiffness method forms the basis for most available commercial and open-source finite element software programs, and was selected for the formulation at hand.

The response of the discrete structural model to external effects is completely described by variables associated with its nodes: the static variables and the kinematic variables. The static variables are the generalized forces at each node which consist of a force and a moment; each of these can be decomposed into three components in the x (longitudinal), y (transverse), and z (vertical) directions of the global coordinate system, refer to Figure 8.1. The kinematic variables are the generalized displacements at each node which consist of a translation and a rotation where they can be decomposed into three components in the x, y, and z directions of the global coordinate system, considering infinitesimal rotations.

For the 3D bridge model considered in this study, there are 6 independent DOFs at each node (three translational components and three rotational components) and 12 DOFs for each individual element because each element has two nodes. For the nodes and elements of the model and the node variables, the following numbering convention is adopted:

- Nodes are numbered in an increasing order from left to right and denoted with Arabic numerals;
- Elements are numbered in an increasing order from left to right and denoted with circled Arabic numerals;
- Global structural DOFs are numbered following the node order, starting with the translation in x, then in y, then in z, and continuing with rotation about x, about y, and about z; and
- Local DOFs for each individual element are numbered from the left node to the right node, starting with translation in local $\bar{x}$, then in local $\bar{y}$, then in local $\bar{z}$, and continuing with rotation about local $\bar{x}$, about local $\bar{y}$, and about local $\bar{z}$. The starting number for local DOFs is always 1.

Figure 8.7 shows the numbering of nodes and elements for the bridge model with a subdivision of n elements of the bridge superstructure. Each element is of length L. To avoid coordinate transformation between local and global coordinate systems, the local element coordinate system was specifically chosen such that these two coordinate systems coincide. Figure 8.8 shows the global and local DOFs numbering for a representative element i.

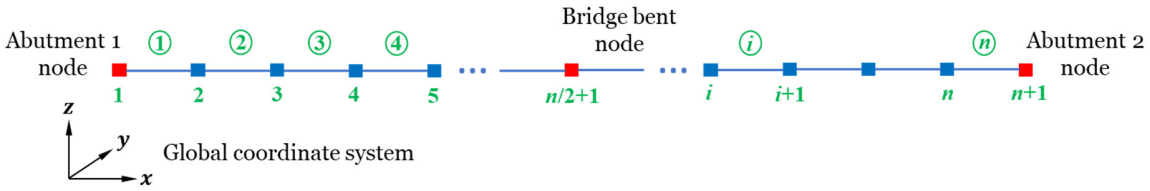

Figure 8.7 Nodes and elements numbering of the bridge model.

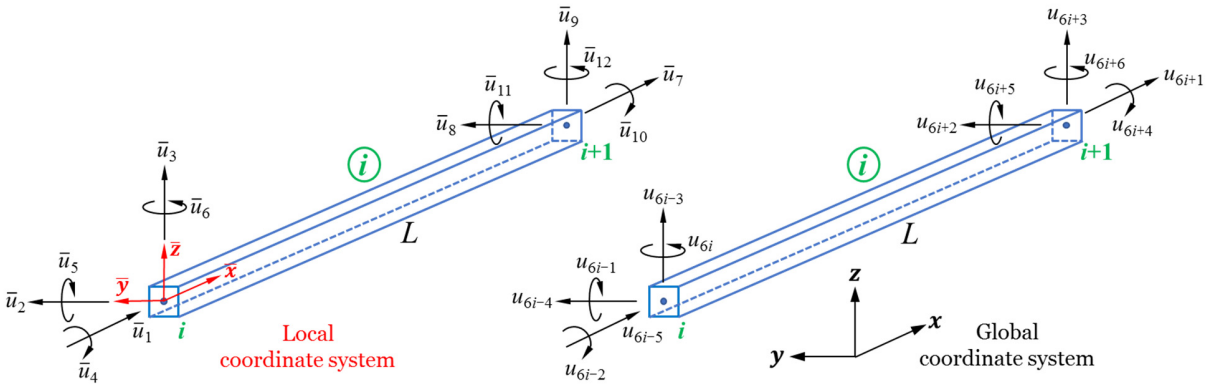

Figure 8.8 Local and global DOFs numbering for element *i*.

Since the element coordinate system coincides with the global coordinate system, the element kinematic matrix $\mathbf{a}_g$ that relates the element end deformations and element end displacements in the global coordinate system is given by:

$$\mathbf{a}_g = \begin{bmatrix} -1 & 0 & 0 & 0 & 0 & 0 & 1 & 0 & 0 & 0 & 0 & 0 \\ 0 & \frac{1}{L} & 0 & 0 & 0 & 1 & 0 & -\frac{1}{L} & 0 & 0 & 0 & 0 \\ 0 & \frac{1}{L} & 0 & 0 & 0 & 0 & 0 & -\frac{1}{L} & 0 & 0 & 0 & 1 \\ 0 & 0 & 0 & -1 & 0 & 0 & 0 & 0 & 0 & 1 & 0 & 0 \\ 0 & 0 & -\frac{1}{L} & 0 & 1 & 0 & 0 & 0 & \frac{1}{L} & 0 & 0 & 0 \\ 0 & 0 & -\frac{1}{L} & 0 & 0 & 0 & 0 & 0 & \frac{1}{L} & 0 & 1 & 0 \end{bmatrix} \tag{8.4}$$

The stiffness matrix **k** of a homogeneous, prismatic linear elastic 3D frame element is given by:

$$\mathbf{k} = \begin{bmatrix} \frac{EA}{L} & 0 & 0 & 0 & 0 & 0 \\ 0 & \frac{4EI_z}{L} & \frac{2EI_z}{L} & 0 & 0 & 0 \\ 0 & \frac{2EI_z}{L} & \frac{4EI_z}{L} & 0 & 0 & 0 \\ 0 & 0 & 0 & \frac{GJ}{L} & 0 & 0 \\ 0 & 0 & 0 & 0 & \frac{4EI_y}{L} & \frac{2EI_y}{L} \\ 0 & 0 & 0 & 0 & \frac{2EI_y}{L} & \frac{4EI_y}{L} \end{bmatrix} \tag{8.5}$$

The element stiffness matrix $\mathbf{k}_e$ in the global coordinate system can be obtained by:

$$\mathbf{k}_e = \mathbf{a}_g^T \mathbf{k} \mathbf{a}_g \tag{8.6}$$

Substituting into the above matrix multiplication yields the 12 by 12 element stiffness matrix:

$$\mathbf{k}_e = \begin{bmatrix} \frac{EA}{L} & 0 & 0 & 0 & 0 & 0 & -\frac{EA}{L} & 0 & 0 & 0 & 0 & 0 \\ 0 & \frac{12EI_z}{L^3} & 0 & 0 & 0 & \frac{6EI_z}{L^2} & 0 & -\frac{12EI_z}{L^3} & 0 & 0 & 0 & \frac{6EI_z}{L^2} \\ 0 & 0 & \frac{12EI_y}{L^3} & 0 & -\frac{6EI_y}{L^2} & 0 & 0 & 0 & -\frac{12EI_y}{L^3} & 0 & -\frac{6EI_y}{L^2} & 0 \\ 0 & 0 & 0 & \frac{GJ}{L} & 0 & 0 & 0 & 0 & 0 & -\frac{GJ}{L} & 0 & 0 \\ 0 & 0 & -\frac{6EI_y}{L^2} & 0 & \frac{4EI_y}{L} & 0 & 0 & 0 & \frac{6EI_y}{L^2} & 0 & \frac{2EI_y}{L} & 0 \\ 0 & \frac{6EI_z}{L^2} & 0 & 0 & 0 & \frac{4EI_z}{L} & 0 & -\frac{6EI_z}{L^2} & 0 & 0 & 0 & \frac{2EI_z}{L} \\ -\frac{EA}{L} & 0 & 0 & 0 & 0 & 0 & \frac{EA}{L} & 0 & 0 & 0 & 0 & 0 \\ 0 & -\frac{12EI_z}{L^3} & 0 & 0 & 0 & -\frac{6EI_z}{L^2} & 0 & \frac{12EI_z}{L^3} & 0 & 0 & 0 & -\frac{6EI_z}{L^2} \\ 0 & 0 & -\frac{12EI_y}{L^3} & 0 & \frac{6EI_y}{L^2} & 0 & 0 & 0 & \frac{12EI_y}{L^3} & 0 & \frac{6EI_y}{L^2} & 0 \\ 0 & 0 & 0 & -\frac{GJ}{L} & 0 & 0 & 0 & 0 & 0 & \frac{GJ}{L} & 0 & 0 \\ 0 & 0 & -\frac{6EI_y}{L^2} & 0 & \frac{2EI_y}{L} & 0 & 0 & 0 & \frac{6EI_y}{L^2} & 0 & \frac{4EI_y}{L} & 0 \\ 0 & \frac{6EI_z}{L^2} & 0 & 0 & 0 & \frac{2EI_z}{L} & 0 & -\frac{6EI_z}{L^2} & 0 & 0 & 0 & \frac{4EI_z}{L} \end{bmatrix} \tag{8.7}$$

The Boolean matrix $\mathbf{A}_b$ for a particular element of the structural model needed to form the global stiffness matrix **K** has as many rows as element end displacement components (in this case 12) and as many columns as structural DOFs (in this case $6n + 6$). It has only one non-zero term in each row at the column with number equal to the entry of the element ***id***-array for the corresponding row. The entry in row k of the incidence array ***id*** of a particular element matches the number of the global structural DOF to which the end displacement component $\bar{u}_k$ coincides with. The ***id***-array for a typical element i (refer to Figure 8.8) is:

$$\boldsymbol{id}^{(i)} = \begin{bmatrix} 6i-5 \\ 6i-4 \\ 6i-3 \\ 6i-2 \\ 6i-1 \\ 6i \\ 6i+1 \\ 6i+2 \\ 6i+3 \\ 6i+4 \\ 6i+5 \\ 6i+6 \end{bmatrix} \tag{8.8}$$

Therefore, the corresponding Boolean matrix for element i is:

$$\mathbf{A}_b^{(i)} = \begin{array}{c} \begin{matrix} 1 & 2 & \cdots & 6i-6 & 6i-5 & 6i-4 & 6i-3 & 6i-2 & 6i-1 & 6i & 6i+1 & 6i+2 & 6i+3 & 6i+4 & 6i+5 & 6i+6 & 6i+7 & \cdots & 6n+5 & 6n+6 \end{matrix} \\ \begin{bmatrix} 0 & 0 & \cdots & 0 & 1 & 0 & 0 & 0 & 0 & 0 & 0 & 0 & 0 & 0 & 0 & 0 & 0 & \cdots & 0 & 0 \\ 0 & 0 & \cdots & 0 & 0 & 1 & 0 & 0 & 0 & 0 & 0 & 0 & 0 & 0 & 0 & 0 & 0 & \cdots & 0 & 0 \\ 0 & 0 & \cdots & 0 & 0 & 0 & 1 & 0 & 0 & 0 & 0 & 0 & 0 & 0 & 0 & 0 & 0 & \cdots & 0 & 0 \\ 0 & 0 & \cdots & 0 & 0 & 0 & 0 & 1 & 0 & 0 & 0 & 0 & 0 & 0 & 0 & 0 & 0 & \cdots & 0 & 0 \\ 0 & 0 & \cdots & 0 & 0 & 0 & 0 & 0 & 1 & 0 & 0 & 0 & 0 & 0 & 0 & 0 & 0 & \cdots & 0 & 0 \\ 0 & 0 & \cdots & 0 & 0 & 0 & 0 & 0 & 0 & 1 & 0 & 0 & 0 & 0 & 0 & 0 & 0 & \cdots & 0 & 0 \\ 0 & 0 & \cdots & 0 & 0 & 0 & 0 & 0 & 0 & 0 & 1 & 0 & 0 & 0 & 0 & 0 & 0 & \cdots & 0 & 0 \\ 0 & 0 & \cdots & 0 & 0 & 0 & 0 & 0 & 0 & 0 & 0 & 1 & 0 & 0 & 0 & 0 & 0 & \cdots & 0 & 0 \\ 0 & 0 & \cdots & 0 & 0 & 0 & 0 & 0 & 0 & 0 & 0 & 0 & 1 & 0 & 0 & 0 & 0 & \cdots & 0 & 0 \\ 0 & 0 & \cdots & 0 & 0 & 0 & 0 & 0 & 0 & 0 & 0 & 0 & 0 & 1 & 0 & 0 & 0 & \cdots & 0 & 0 \\ 0 & 0 & \cdots & 0 & 0 & 0 & 0 & 0 & 0 & 0 & 0 & 0 & 0 & 0 & 1 & 0 & 0 & \cdots & 0 & 0 \\ 0 & 0 & \cdots & 0 & 0 & 0 & 0 & 0 & 0 & 0 & 0 & 0 & 0 & 0 & 0 & 1 & 0 & \cdots & 0 & 0 \end{bmatrix} \end{array} \begin{matrix} \bar{u}_1 \\ \bar{u}_2 \\ \bar{u}_3 \\ \bar{u}_4 \\ \bar{u}_5 \\ \bar{u}_6 \\ \bar{u}_7 \\ \bar{u}_8 \\ \bar{u}_9 \\ \bar{u}_{10} \\ \bar{u}_{11} \\ \bar{u}_{12} \end{matrix} \tag{8.9}$$

Finally, the assembled global stiffness matrix **K**, which is of size $6n + 6$ by $6n + 6$ is given by:

$$\mathbf{K} = \sum_{i=1}^{n} \mathbf{A}_b^{(i)^T} \mathbf{k}_e^{(i)} \mathbf{A}_b^{(i)} \tag{8.10}$$

One thing that needs to be clarified here is that the global stiffness matrix of the bridge formulated this way did not take into account the stiffness contribution from the abutment springs and the tested bridge bent. Instead, their contribution to the structural response was considered by adding their resisting forces to the resisting force vector. The resisting forces from the abutments were obtained by performing state determination at each time step. Similarly, the contribution from the two-column bridge bent serving as the experimental substructure was considered by adding the measured/calculated resisting forces. Details will be discussed in section 8.1.6.

8.1.4 Mass Matrix

Two types of mass matrix are commonly used in dynamic analysis: the lumped mass matrix and the consistent mass matrix. The lumped mass matrix is diagonal and formulated by assuming that the distributed mass of the element can be lumped as point masses along the translational DOFs at

the element ends, with these point masses being determined by static analysis of the beam under its own weight. The consistent mass matrix, however, assumes that the mass is distributed along the element length following the function $m(x)$. The mass matrix derived this way is known as the consistent mass matrix because the same interpolation functions used in the displacement interpolation are also used in deriving the mass matrix. The dynamic analysis of a consistent-mass system requires more computational effort than does a lumped-mass idealization. However, the consistent-mass formulation has two advantages. First, it leads to greater accuracy in the results and rapid convergence to the exact solution with an increasing number of elements. Second, with a consistent-mass approach, the potential energy and kinetic energy quantities are evaluated in a consistent manner.

The consistent mass matrix formulation was chosen for this study. For a 3D frame element with uniform mass (i.e., $m(x) = m = \rho A$ with mass density ρ and cross-sectional area A), length L, cross-sectional torsional constant J, the following integrals are computed:

$$m_{ij} = \int_0^L m(x)\psi_i(x)\psi_j(x)dx \tag{8.11}$$

where $\psi_i(x)$ and $\psi_j(x)$ are the element interpolation (shape) functions. Upon the analytical evaluation of these integrals using standard linear shape functions for the axial and torsional deformations and cubic shape functions for the flexural/shear deformations of a two-node 12 DOFs frame element, one obtains the following 12 by 12 element (consistent) mass matrix:

$$\mathbf{m}_e = \rho AL \times \begin{bmatrix} \frac{1}{3} & 0 & 0 & 0 & 0 & 0 & \frac{1}{6} & 0 & 0 & 0 & 0 & 0 \\ 0 & \frac{13}{35} & 0 & 0 & 0 & \frac{11L}{210} & 0 & \frac{9}{70} & 0 & 0 & 0 & -\frac{13L}{420} \\ 0 & 0 & \frac{13}{35} & 0 & -\frac{11L}{210} & 0 & 0 & 0 & \frac{9}{70} & 0 & \frac{13L}{420} & 0 \\ 0 & 0 & 0 & \frac{J}{3A} & 0 & 0 & 0 & 0 & 0 & \frac{J}{6A} & 0 & 0 \\ 0 & 0 & -\frac{11L}{210} & 0 & \frac{L^2}{105} & 0 & 0 & 0 & -\frac{13L}{420} & 0 & -\frac{L^2}{140} & 0 \\ 0 & \frac{11L}{210} & 0 & 0 & 0 & \frac{L^2}{105} & 0 & \frac{13L}{420} & 0 & 0 & 0 & -\frac{L^2}{140} \\ \frac{1}{6} & 0 & 0 & 0 & 0 & 0 & \frac{1}{3} & 0 & 0 & 0 & 0 & 0 \\ 0 & \frac{9}{70} & 0 & 0 & 0 & \frac{13L}{420} & 0 & \frac{13}{35} & 0 & 0 & 0 & -\frac{11L}{210} \\ 0 & 0 & \frac{9}{70} & 0 & -\frac{13L}{420} & 0 & 0 & 0 & \frac{13}{35} & 0 & \frac{11L}{210} & 0 \\ 0 & 0 & 0 & \frac{J}{6A} & 0 & 0 & 0 & 0 & 0 & \frac{J}{3A} & 0 & 0 \\ 0 & 0 & \frac{13L}{420} & 0 & -\frac{L^2}{140} & 0 & 0 & 0 & \frac{11L}{210} & 0 & \frac{L^2}{105} & 0 \\ 0 & -\frac{13L}{420} & 0 & 0 & 0 & -\frac{L^2}{140} & 0 & -\frac{11L}{210} & 0 & 0 & 0 & \frac{L^2}{105} \end{bmatrix} \tag{8.12}$$

The consistent mass matrix assembly follows the same procedure as described in the global stiffness matrix assembly. Finally, the assembled global consistent mass matrix **M**, which is of size $6n + 6$ by $6n + 6$ is given by:

$$\mathbf{M} = \sum_{i=1}^{n} \mathbf{A}_b^{(i)^T} \mathbf{m}_e^{(i)} \mathbf{A}_b^{(i)} \tag{8.13}$$

8.1.5 Damping Matrix

Classical damping is an appropriate idealization if similar damping mechanisms are distributed throughout the structure. One of the procedures in defining a classical damping, the Rayleigh damping model, was employed. Its expression is given by:

$$\mathbf{C} = a_0\mathbf{M} + a_1\mathbf{K} \tag{8.14}$$

The damping ratio for the n^{th} mode of such a system is:

$$\zeta_n = \frac{a_0}{2}\frac{1}{\omega_n} + \frac{a_1}{2}\omega_n \tag{8.15}$$

Considering 5% damping ratio ζ in the first two modes of vibration, the coefficients a_0 and a_1 can be calculated as follows:

$$a_0 = \zeta \frac{2\omega_1 \omega_2}{\omega_1 + \omega_2} \qquad a_1 = \zeta \frac{2}{\omega_1 + \omega_2} \tag{8.16}$$

where ω_1 and ω_2 are the natural circular frequencies associated with the 1st and the 2nd mode of vibration, respectively.

8.1.6 Resisting Force Vector

The dynamic analysis problem of a system is usually formulated with its static equilibrium position as the reference position, e.g., the equilibrium position under gravity loading. Therefore, the resisting force vector in the matrix equations of motion for a multi-degrees-of-freedom (MDOF), denoted with $\boldsymbol{P}_r$, is the one that corresponds to the dynamic displacement $\boldsymbol{u}$, representing the dynamic response of the system. Figure 8.9 shows a sample calculation of the resisting force P_r of a linear elastic system. To obtain the total resisting force $P_{r,total}$ in an element, the static displacement δ_{st} needs to be added to the dynamic displacement u to obtain the total displacement u_{total}. This is important because the effect of gravity on different bridge components needs to be explicitly considered during phase II HS test as the bridge was subjected to both the transverse and vertical ground motion inputs, same as in phase I.

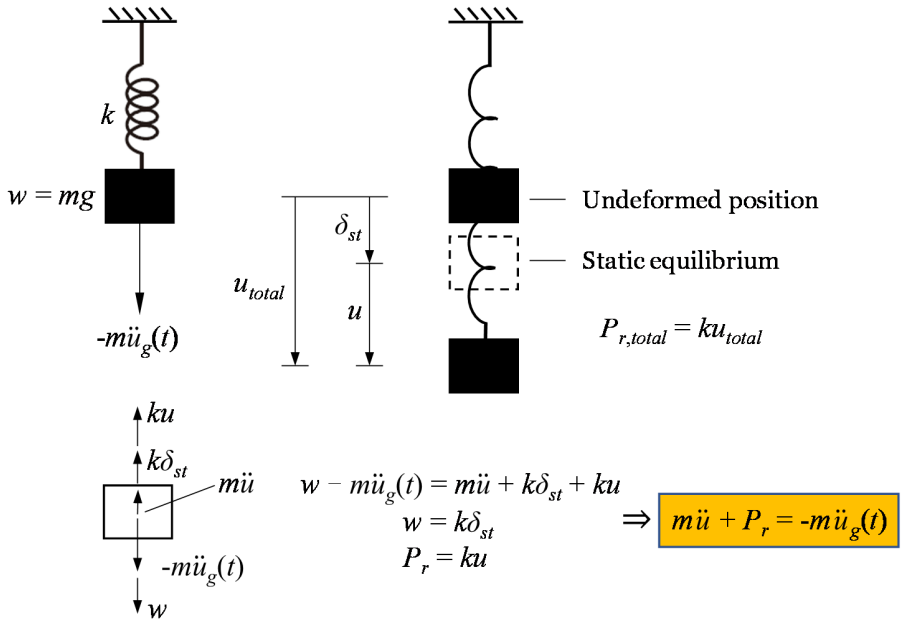

Figure 8.9 Demonstration of resisting force calculation.

The resisting force vector of the bridge in question is given by Equation (8.17). It has contributions from three parts: the deck, the end abutments, and the two-column bridge bent. Details of the resisting force calculations from each part are presented in the following subsections.

$$\boldsymbol{P}_r = \sum_{el} \boldsymbol{P}_r^{(el)} = \boldsymbol{P}_{r,deck} + \boldsymbol{P}_{r,abutments} + \boldsymbol{P}_{r,bent} \tag{8.17}$$

8.1.6.1 Bridge Deck

Since the bridge deck is modeled using 3D linear elastic frame elements, the $6n + 6$ resisting force vector from the deck is simply:

$$\boldsymbol{P}_{r,deck} = \mathbf{K}\boldsymbol{U} \tag{8.18}$$

where $\mathbf{K}$ is the global stiffness matrix given by Equation (8.10) and $\boldsymbol{U}$ is the displacement vector representing the dynamic response.

8.1.6.2 Abutments

The resisting forces from the nonlinear abutments given the corresponding displacement values at each time step were obtained through a procedure known as the state determination. This is discussed in the following paragraphs for the abutment response in different directions.

The longitudinal direction of the abutment does not experience any displacements during the gravity load or during the transverse/vertical ground excitations. However, the state determination was still implemented for completeness. The force-displacement (deformation) relationship shown in Figure 8.10(a) is path dependent, meaning that the resisting force depends on the prior history of motion of the system and whether the displacement is currently increasing or decreasing. More precisely, the resisting force at the current step i depends on not only the current step displacement, u_i, but also on the displacement and resisting force values from the previous step, $i - 1$. The flow chart for the state determination procedure is shown in Figure 8.10(b). One thing worth noticing for future use of the model is that the state determination results for the longitudinal responses of the abutments at the two ends of the bridge differ if the longitudinal ground motion is applied. This is because a positive global displacement in the longitudinal direction leads to a positive longitudinal deformation for the abutment connected to node 1, but a negative longitudinal deformation for the one connected to node $n + 1$. However, the underlying idea is exactly the same. The resisting forces in the longitudinal direction from the two abutments were added to the 1st and the $(6n + 1)^{th}$ entries of the resisting force vector, according to the global DOFs numbering as shown in Figure 8.8.

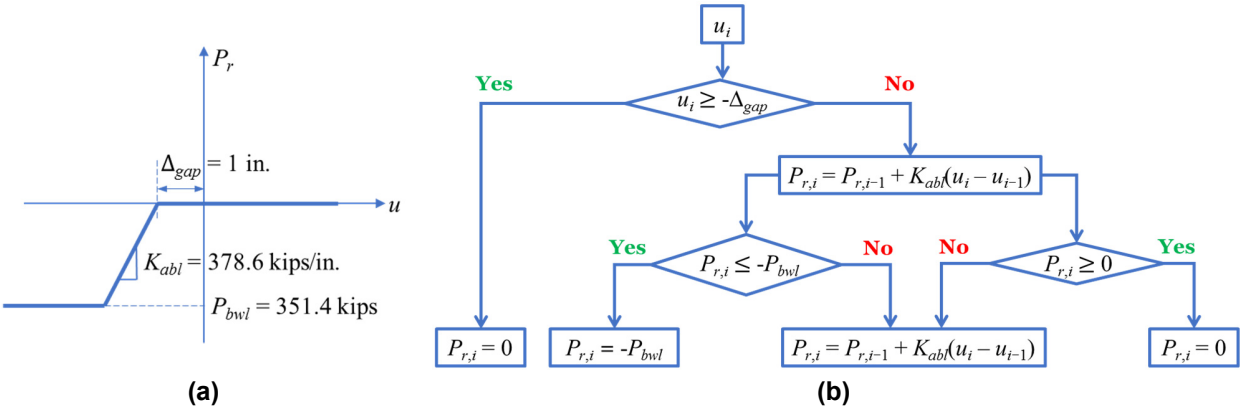

Figure 8.10 (a) Force-displacement relationship; and (b) state determination procedure of the longitudinal abutment response.

For the transverse direction of the abutment, the only source of displacements comes from the transverse ground motion. Therefore, the EPP backbone curve shown in Figure 8.11(a), which is the relationship between the total resisting force and the total displacement, directly applies to the ground motion scenario. Similar to the longitudinal direction of the abutment, the force-displacement relationship is also path dependent. The flow chart for the state determination procedure is shown in Figure 8.11(b), with the upper and lower bound of the resisting force set by the yield strength P_{bwt}. According to the global DOFs numbering from Figure 8.8, the resisting forces in the transverse direction of the two abutments were added to the 2nd and the $(6n + 2)^{th}$ entries of the resisting force vector.

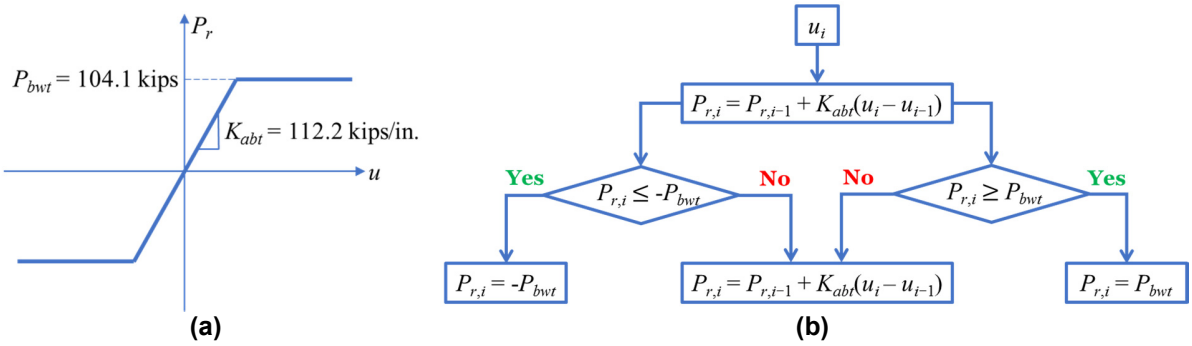

Figure 8.11 (a) Force-displacement relationship; and (b) state determination procedure of the transverse abutment response.

The displacements in the vertical direction of the abutments can be split into two parts: the static displacement u_{st} due to the gravity load and the dynamic displacement u_{EQ} caused by the vertical ground acceleration. Therefore, to determine the resisting forces $P_{r,EQ}$ during the earthquake, the original force-displacement relationship needs to be shifted, as shown Figure 8.12(a). The static displacement u_{st} = 0.487 in. and the resisting force F_{st} = 584 kips were obtained from the gravity analysis of the bridge. In the gravity analysis, the vertical response of the bridge bent is represented by a linear elastic spring, with the same vertical stiffness used in phase I HS multiplied by the length scale factor S_L = 3.333 according to the laws of similitude (Harris and Sabnis, 1999). The gravity load comes from the self-weight of the superstructure. With all needed information, the state determination procedure is shown in Figure 8.12(b). The resisting forces from the two abutments in the vertical direction were added to the 3rd and the $(6n + 3)^{th}$ entries of the resisting force vector based on the global DOFs numbering, refer to Figure 8.8.

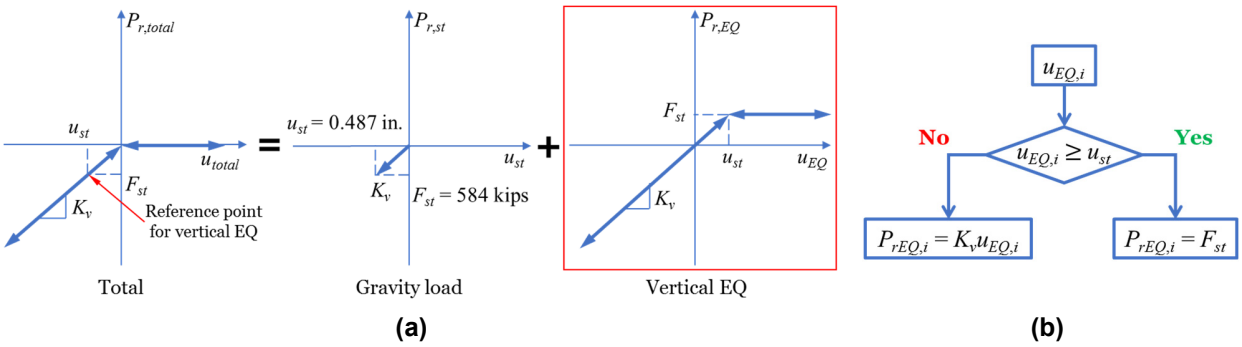

Figure 8.12 (a) Force-displacement relationship break-down; and (b) state determination procedure of the vertical abutment response.

8.1.6.3 Test Specimen

One of the interactions between the test specimen and the analytical part of the bridge was through the horizontal and vertical resisting forces of the test specimen. The horizontal resisting force was measured by the actuator's load cell, while the vertical resisting force was obtained by multiplying the dynamic vertical displacement as an output from the numerical integration with the assumed vertical stiffness. Before adding to the resisting force vector, the laws of similitude (Harris and Sabnis, 1999) were taken into consideration, i.e., scaling up the measured horizontal resisting force by a factor of $S_L{}^2$. The entry numbers for the horizontal and vertical resisting forces in the global resisting force vector are $3n + 2$ and $3n + 3$, respectively, according to the adopted global DOFs numbering rule described before, refer to Figure 8.8.

The effect of gravity was considered by applying the gravity load to the test specimen before starting the HS. From the gravity analysis results, the force on top of the bridge bent was 1,907 kips. Therefore, a gravity load of 172 kips was applied to the test specimen through the vertical actuator after proper scaling.

8.2 SIMULINK IMPLEMENTATION

To accommodate the change in the analytical substructure in phase II, the Simulink model described in Chapter 7 needs to be modified. Comparing with the model shown in Figure 7.19, the implementation outside the "if" statement followed the exact same approach in fulfilling the tasks of interpolation, communication, and selected quantities output. The main change was the numerical integration inside the "if" action box, as shown in Figure 8.13. Considering the stability limit of the Explicit Newmark integration algorithm in Equation (7.1) and that the higher mode periods of the bridge can be unexpectedly small, the Alpha-OS integration algorithm (Combescure and Pegon, 1997; Elkhoraibi and Mosalam, 2007; Nakashima et al., 1990; Schellenberg et al., 2009), previously used in the V-connector HS, was chosen for phase II of the HS study of the tested bridge bent together with the simulated bridge deck and abutment models. Since this algorithm has a prediction step and a correction step, the implementation was more involved. In addition, the resisting force vector calculations required summing up contributions from different

parts of the bridge, including the nonlinear end abutments. All these issues added complexity to the Simulink implementation. Details are discussed in the following subsections.

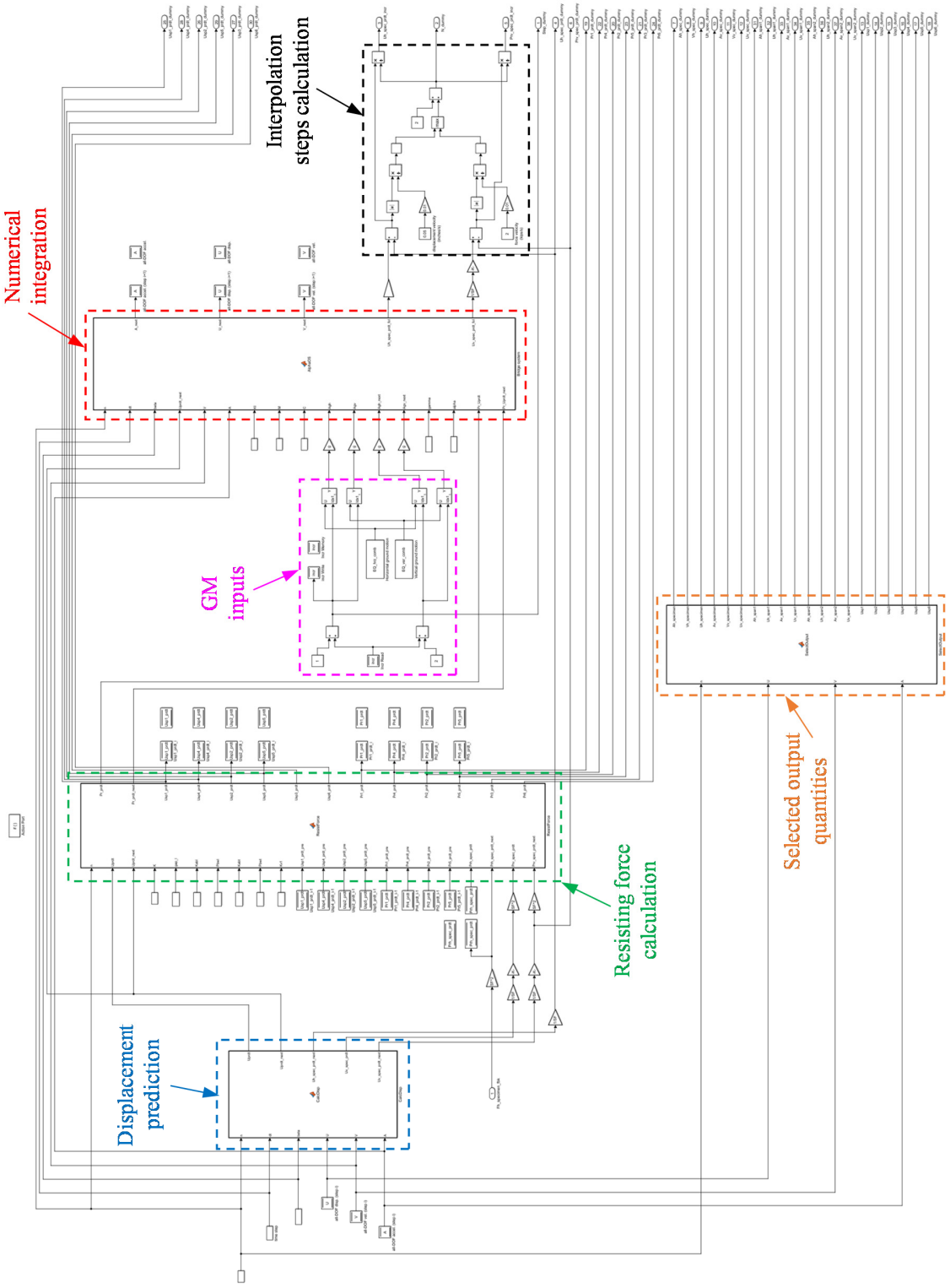

Figure 8.13 Detailed implementation inside the "If" action box.

8.2.1 Ground Motion Manipulation

The matrix equations of motion for a MDOF system subjecting to ground excitation(s) can be written as:

$$\mathbf{M}\ddot{\boldsymbol{U}} + \mathbf{C}\dot{\boldsymbol{U}} + \boldsymbol{P}_r = -\mathbf{M}\mathbf{L}\ddot{\boldsymbol{U}}_g \tag{8.19}$$

For the case at hand, Equation (8.19) can be further expanded as:

$$\mathbf{M}\ddot{\boldsymbol{U}} + \mathbf{C}\dot{\boldsymbol{U}} + \boldsymbol{P}_r = -\mathbf{M}\mathbf{L}\ddot{\boldsymbol{U}}_g = -(\mathbf{M}\boldsymbol{l}_h\ddot{u}_{gh} + \mathbf{M}\boldsymbol{l}_v\ddot{u}_{gv}) \tag{8.20}$$

where $\ddot{u}_{gh}$ and $\ddot{u}_{gv}$ are the horizontal and vertical ground accelerations at a certain instant of time, $\mathbf{L}$ is the influence matrix (Chopra, 2011), with its columns $\boldsymbol{l}_h$ and $\boldsymbol{l}_v$, each of size $6n + 6$ by 1, representing the displacements of all DOFs resulting from the static application of a unit horizontal and vertical ground displacement, respectively. Therefore, $\boldsymbol{l}_h$ and $\boldsymbol{l}_v$ can be expressed as follows:

$$\boldsymbol{l}_h = \begin{bmatrix} \boldsymbol{l}_h^{(1)} \\ \boldsymbol{l}_h^{(2)} \\ \vdots \\ \boldsymbol{l}_h^{(n+1)} \end{bmatrix} \qquad \boldsymbol{l}_v = \begin{bmatrix} \boldsymbol{l}_v^{(1)} \\ \boldsymbol{l}_v^{(2)} \\ \vdots \\ \boldsymbol{l}_v^{(n+1)} \end{bmatrix} \tag{8.21}$$

where

$$\boldsymbol{l}_h^{(1)} = \boldsymbol{l}_h^{(2)} = \cdots = \boldsymbol{l}_h^{(n+1)} = \begin{bmatrix} 0 \\ 1 \\ 0 \\ 0 \\ 0 \\ 0 \end{bmatrix}; \quad \boldsymbol{l}_v^{(1)} = \boldsymbol{l}_v^{(2)} = \cdots = \boldsymbol{l}_v^{(n+1)} = \begin{bmatrix} 0 \\ 0 \\ 1 \\ 0 \\ 0 \\ 0 \end{bmatrix} \tag{8.22}$$

Written more compactly, Equation (8.20) is equivalent to the following:

$$\mathbf{M}\ddot{\boldsymbol{U}} + \mathbf{C}\dot{\boldsymbol{U}} + \boldsymbol{P}_r = -\mathbf{M}\boldsymbol{l}\ddot{u}_{gh} \tag{8.23}$$

where

$$\boldsymbol{l} = \begin{bmatrix} \boldsymbol{l}^{(1)} \\ \boldsymbol{l}^{(2)} \\ \vdots \\ \boldsymbol{l}^{(n+1)} \end{bmatrix} \qquad \boldsymbol{l}^{(1)} = \boldsymbol{l}^{(2)} = \cdots = \boldsymbol{l}^{(n+1)} = \begin{bmatrix} 0 \\ 1 \\ \ddot{u}_{gv}/\ddot{u}_{gh} \\ 0 \\ 0 \\ 0 \end{bmatrix} \tag{8.24}$$

8.2.2 Numerical Integration

The detailed execution steps for the Alpha-OS integration algorithm can be found in Figure 5.3. The numerical integration was performed through the Matlab function block in Simulink (MathWorks, 2015). Before embarking on the solution algorithm, several tasks need to be completed.

The first task was the calculation of the predicted displacement vectors $\tilde{\boldsymbol{u}}_i$ and $\tilde{\boldsymbol{u}}_{i+1}$ at the current and the next step, as these quantities were necessary for determining the resisting force

vectors $\boldsymbol{p}_r(\tilde{\boldsymbol{u}}_i)$ and $\boldsymbol{p}_r(\tilde{\boldsymbol{u}}_{i+1})$. The Matlab function block and its implementation are shown in Figure 8.14. It takes as inputs the bridge deck's subdivision number n, the discrete time step dt, the Newmark acceleration coefficient β, the displacement vector $\boldsymbol{u}_i$, the velocity vector $\dot{\boldsymbol{u}}_i$, and the acceleration vector $\ddot{\boldsymbol{u}}_i$ at current step i, and its output consists of the predicted displacement vectors $\tilde{\boldsymbol{u}}_i$ and $\tilde{\boldsymbol{u}}_{i+1}$, together with some displacement quantities associated with the test specimen for the subsequent calculations. The calculation starts from $i = 1$.

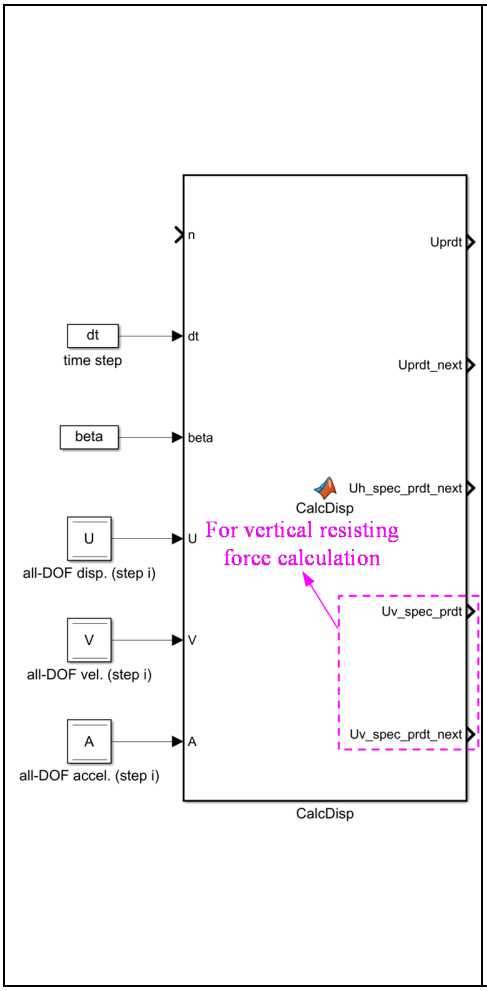


```
function
[Uprdt,Uprdt_next,Uh_spec_prdt_next,Uv_spec_prdt,Uv_sp
ec_prdt_next] = CalcDisp(n,dt,beta,U,V,A)
% calculated the predicted displacement vector at
current step i and next step i+1
% Inputs: n - number of bridge deck subdivision
%         dt - time step
%         beta - Newmark acceleration coefficient
%         U - displacement vector at current step i
          (size: 6(n+1) x 1)
%         V - velocity vector at current step i (size:
          6(n+1) x 1)
%         A - acceleration vector at current step i
          (size: 6(n+1) x 1)
% Outputs: Uprdt - predicted displacement vector at
           current step i (size: 6(n+1) x 1)
%          Uprdt_next - predicted displacement vector
           at next step i+1 (size: 6(n+1) x 1)
%          Uh_spec_prdt_next - predicted test specimen
           horizontal displacement at next step i+1
           (scalar)
%          Uv_spec_prdt - predicted test specimen
           vertical displacement at current step i
           (scalar)
%          Uv_spec_prdt_next - predicted test specimen
           vertical displacement at next step i+1
           (scalar)
%% Overall quantities
Uprdt = U - dt^2*beta*A;
Uprdt_next = U + dt*V + dt^2*(1 - 2*beta)*A/2;
%% Current step quantities
Uv_spec_prdt = Uprdt(3*n+3,:);
%% Next step quantities
Uh_spec_prdt_next = Uprdt_next(3*n+2,:);
Uv_spec_prdt_next = Uprdt_next(3*n+3,:);
```

Figure 8.14 Matlab function block for the predicted displacement calculation.

After determining the predicted displacement, the second task was to obtain the resisting force vectors $\boldsymbol{p}_r(\tilde{\boldsymbol{u}}_i)$ and $\boldsymbol{p}_r(\tilde{\boldsymbol{u}}_{i+1})$. The procedures for determining these resisting forces from different parts of the bridge described in section 8.1.6 were implemented as shown in Figure 8.15. The associated Matlab code can be found in Appendix D.

The state determination in the longitudinal (denoted with springs 1 and 4) and the transverse (denoted with springs 2 and 5) directions of the abutments requires the predicted displacement and associated resisting force values from the previous step (i.e., $\tilde{u}_{i-1}$ and $p_r(\tilde{u}_{i-1})$ to determine $p_r(\tilde{u}_i)$), as can be seen from Figure 8.10 and Figure 8.11. This was accounted for by the Simulink blocks "DataStoreWrite", "DataStoreRead", and "DataStoreMemory". The calculation

reads the predicted displacements $\tilde{u}_{sp1,2,4,5\_i-1}$ and resisting forces $\tilde{p}_{r1,2,4,5\_i-1}$ of the abutments at the previous time step $i-1$ through the "DataStoreRead" blocks, while it writes and stores $\tilde{u}_{sp1,2,4,5\_i}$ and $\tilde{p}_{r1,2,4,5\_i}$ at the current time step i to the respective "DataStoreWrite" and "DataStoreMemory" blocks. When the execution progresses, the new values being read then become the stored ones from the previous execution with the subscript i. The starting values $\tilde{u}_{sp1,2,4,5\_0}$ and $\tilde{p}_{r1,2,4,5\_0}$ are obviously set to zero as $\tilde{\boldsymbol{u}}_0 = 0$.

For the horizontal resisting force of the test specimen, the resisting force $p_{rh}(\tilde{u}_i)$ at the current step i is read from the "DataStoreRead" block and the next step value $p_{rh}(\tilde{u}_{i+1})$ is the one measured from the actuator load cell and scaled up by $S_L{}^2$. Notice that by the time when the very first horizontal resisting force $p_{rh}(\tilde{u}_2)$ is measured, the horizontal actuator remains still as the specimen displacement $\tilde{u}_2$ (denoted with "*Uh_spec_prdt_next*" in Figure 8.14) is equal to zero, see Equation (8.25). The measured value should be very close to zero, if the load cell noise is inevitable. The horizontal actuator starts moving until the predicted displacement $\tilde{u}_3$ (denoted with "*Uh_spec_prdt_fol*" in Figure 8.16) at the following step is calculated. Similarly, the vertical actuator under force control starts applying the earthquake-induced forces from $p_{rv}(\tilde{u}_2)$ to $p_{rv}(\tilde{u}_3)$ (denoted with "*Prv_spec_prdt_next*" and "*Prv_spec_prdt_fol*", respectively in Figure 8.16) to the test specimen. Therefore, the displacement/force interpolation for the actuators, in fact, starts from $i = 2$ instead of $i = 1$.

$$\boldsymbol{u}_1 = 0,\ \dot{\boldsymbol{u}}_1 = 0,\ \ddot{\boldsymbol{u}}_1 = 0 \Rightarrow \tilde{\boldsymbol{u}}_2 = \boldsymbol{u}_1 + \Delta t\dot{\boldsymbol{u}}_1 + \frac{(\Delta t)^2}{2}[(1-2\beta)\ddot{\boldsymbol{u}}_1] = 0 \tag{8.25}$$

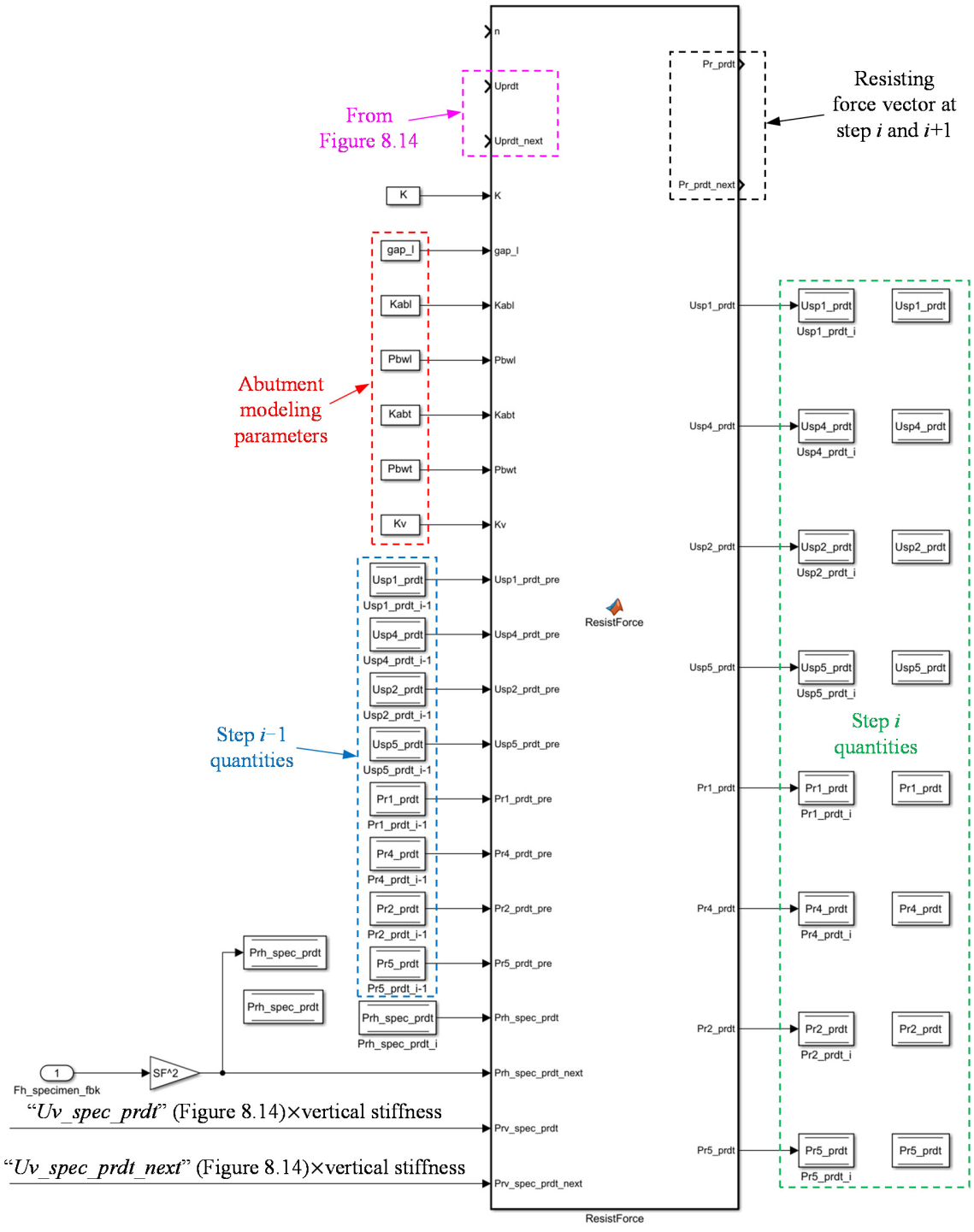

Figure 8.15 Matlab function block for the resisting force vector calculation.

Finally, with the above tasks readily completed, the numerical integration was performed using another Matlab function block shown in Figure 8.16. Per steps 4(b) to 4(f) in Figure 5.3, the function block takes as inputs the bridge deck's subdivision number n, the discrete time step dt, the Newmark coefficients α and β, the Alpha-OS parameter γ, the mass/damping/initial stiffness

matrices, the ground motion inputs from current step i and next step $i + 1$, the velocity vector $\dot{\boldsymbol{u}}_i$ and the acceleration vector $\ddot{\boldsymbol{u}}_i$ at current step i, the next step predicted displacement vector $\tilde{\boldsymbol{u}}_{i+1}$, and the resisting force vectors $\boldsymbol{p}_r(\tilde{\boldsymbol{u}}_i)$ and $\boldsymbol{p}_r(\tilde{\boldsymbol{u}}_{i+1})$. The output consists of the displacement vector $\boldsymbol{u}_{i+1}$, the velocity vector $\dot{\boldsymbol{u}}_{i+1}$, and the acceleration vector $\ddot{\boldsymbol{u}}_{i+1}$ at the next step i. In addition, the test specimen's predicted displacements in both directions at the following step $i + 2$ were obtained for the displacement/force interpolations. The associated Matlab code for the numerical integration is included in Appendix D.

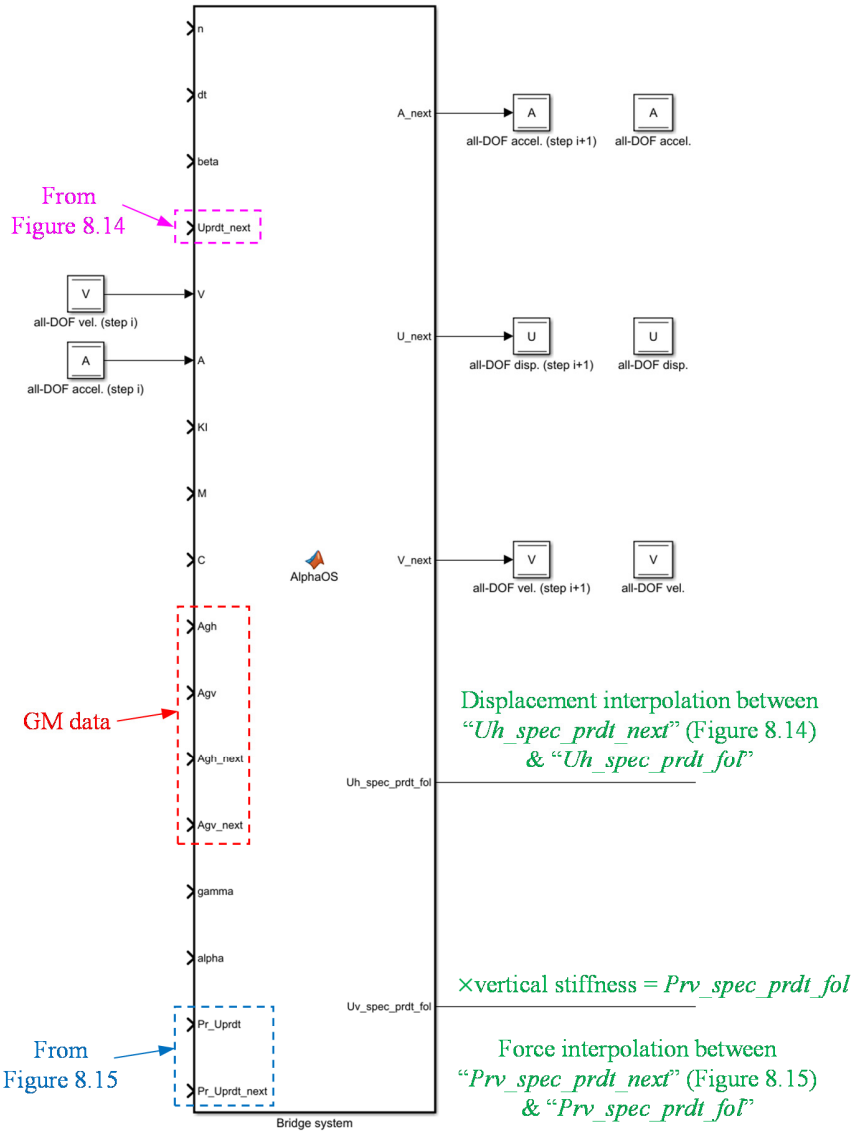

Figure 8.16 Matlab function block for performing the Alpha-OS numerical integration.

8.2.3 Simulink Model Verification

The newly developed HSS was shown to be robust and well-functioning during the verification and phase I HS test. Therefore, no more checks were necessary in terms of the displacement/force

interpolation, the D/A and A/D conversions, the communication between different hardware components, and the control quality of the actuators. However, the Simulink model was changed in phase II with the addition of the bridge model, including the formulation of the stiffness/mass/damping matrices, the change in the integration algorithm, and the assembly of the resisting force vector.

To ensure correctness of the new implementation, the bridge model was developed in OpenSEES (McKenna et al., 2000) as a side check, utilizing the exact same geometry, modeling parameters, solution algorithm, and other modeling options as the Simulink model. For simplicity, the behavior of the bridge bent in the transverse and vertical directions was represented by linear elastic springs. The transverse stiffness was estimated by taking the secant value of the hysteretic curve from phase I EQ7, refer to Figure 8.17, and scaled up by S_L. Moreover, the same vertical stiffness for the gravity analysis (see section 8.1.6.2) was applied. Both models were subjected to the same two-directional ground motion inputs and the results were compared.

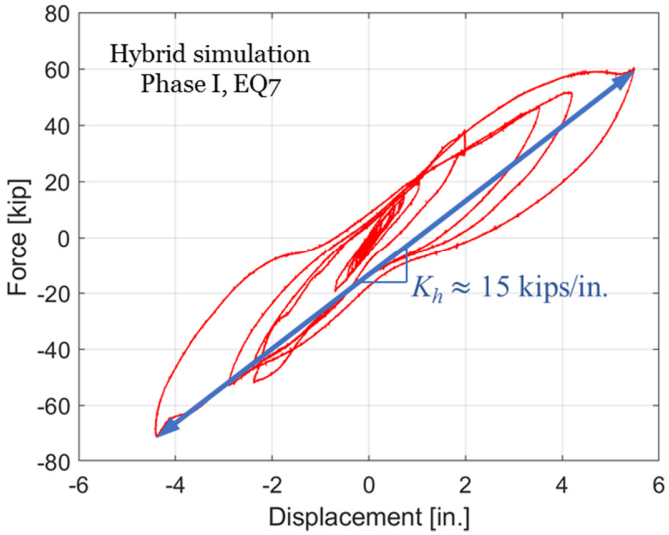

Figure 8.17 Transverse stiffness estimation of the bridge bent from phase I, EQ7.

Figure 8.18 to Figure 8.21 compare different response quantities of the bridge. The Simulink results completely agree with OpenSEES, thus proving the reliability of the developed Simulink model. In addition, the behaviors of different bridge components were observed. Figure 8.19 shows the linear elastic behavior in both directions of the bridge bent, which agrees with the model setting. Figure 8.21(a) shows the EPP response of the transverse abutment, with the correct initial stiffness and the yield strength. Figure 8.21(b) does not reflect the "no-tension" property of the vertical abutment because the maximum earthquake-induced uplift was smaller than the gravity-induced settlement. Therefore, the vertical abutment remained in the linear elastic compression state during the selected ground motion as expected in any good design.

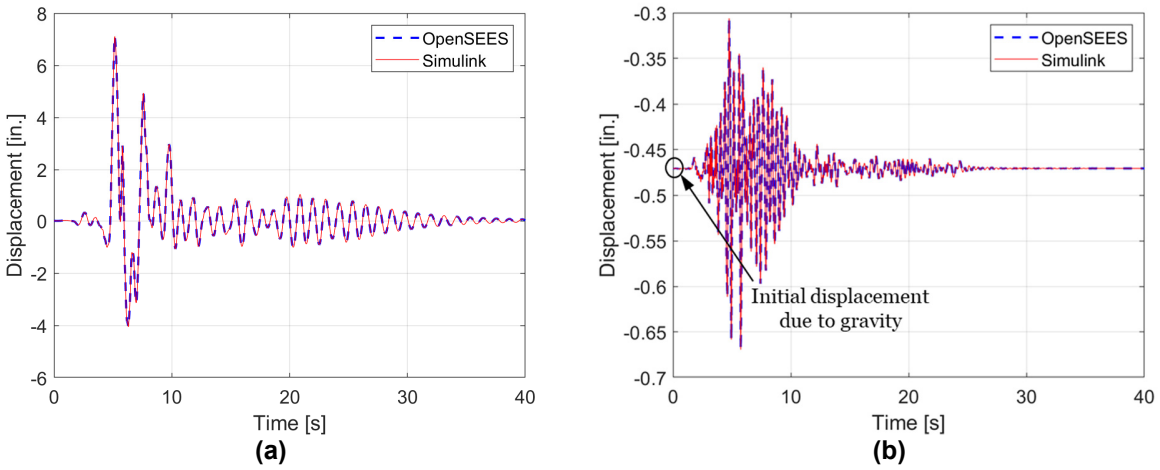

Figure 8.18 **Displacement time history comparisons of the bridge bent (prototype scale) in (a) horizontal; and (b) vertical directions.**

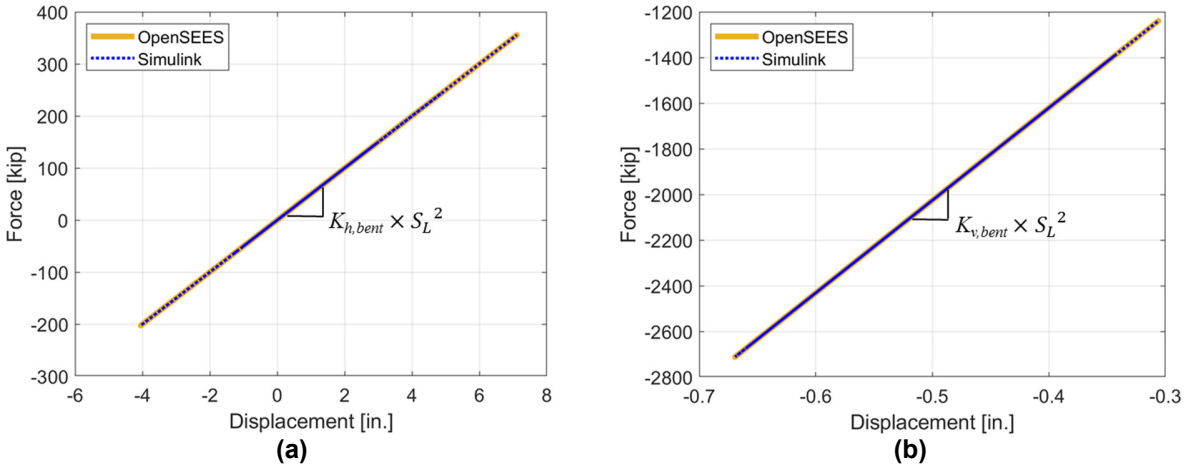

Figure 8.19 **Force-displacement relationship comparisons of the bridge bent (prototype scale) in (a) transverse; and (b) vertical directions.**

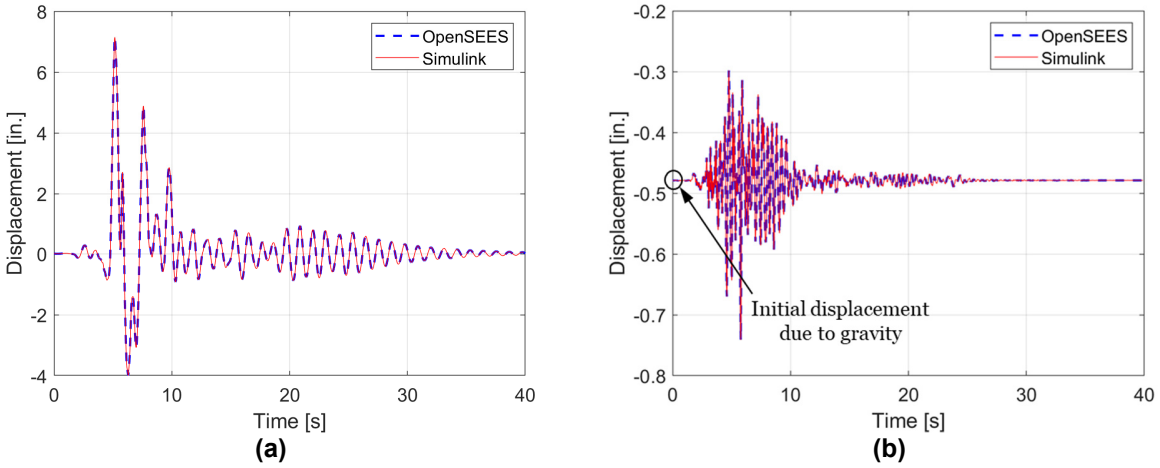

Figure 8.20 **Displacement time history comparisons of the abutment (prototype scale) in (a) transverse; and (b) vertical directions.**

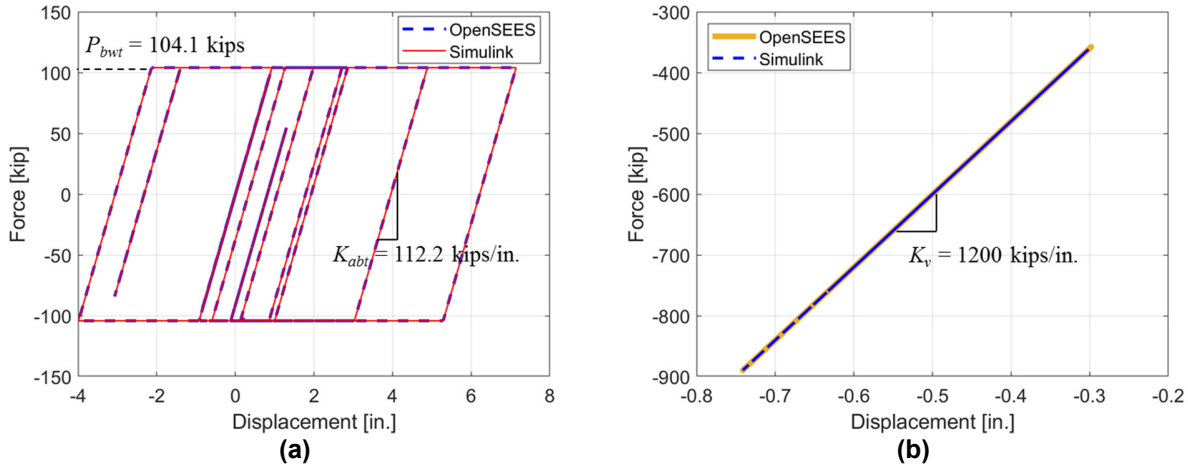

Figure 8.21 **Force-displacement relationship comparisons of the abutment (prototype scale) in (a) transverse; and (b) vertical directions.**

8.3 HYBRID SIMULATION TEST AND DISCUSSION OF RESULTS

8.3.1 Test Plan

Two runs were originally planned for this phase. The first run was the repetition of EQ7 on the full bridge system to investigate the effect of different analytical substructures on the response of the bridge bent. The second run was to have three combined motions with increasing intensity, similar to the idea of the run conducted during the V-connector testing. As the test progressed, a third run, which is the repetition of EQ6 but on the hybrid structure from phase I using all parameters of phase I HS, was added between the two originally planned runs to have a better

understanding on some of the unexpected phenomena that appeared during the first run. The final testing program of phase II HS is listed in Table 8.1.

Table 8.1 Test matrix for phase II HS experiment.

Test #	EQ Information	Physical Substructure	Analytical Substructure
1	EQ7 from phase I	Bridge bent	Bridge superstructure & abutments
2	EQ6 from phase I	Bridge bent	Analytical mass of phase I
3	Three motions combined	Bridge bent	Bridge superstructure & abutments

8.3.2 Loading

The loading sequence for phase II was the same as in phase I: gravity loading first, followed by selected two-directional ground motion records (one transverse and the vertical component). The gravity load was 172 kips as explained before. In addition to the ground motion records at hand, a new set of ground motions was selected based on the target spectrum of a high seismicity region in the San Francisco Bay Area, with increasing intensity. The hazard spectrum calculation tool from the Open-source Seismic Hazard Analysis (OpenSHA) (Field et al., 2013) framework was used for this purpose. The average seismic shear-wave velocity from the surface to a depth of 30 m, denoted with VS_{30}, was chosen to be 560 m/s, representing soil type C. By inputting the longitude and latitude of the site and varying the probability of exceedance in 50 years from 0.5 to 0.1 to 0.02, the spectrum calculator tool gives the target spectrum of SLE, DBE and MCE for that specific site.

The original geographical location of the prototype bridge is 37.753° N, 121.142° W, with the target spectra shown in Figure 8.22. The maximum spectral acceleration for the MCE is only about 0.75g, which is quite small for the purpose of this study. To ensure reasonable displacement amplitude during the phase II HS test, a higher seismicity site located at the intersection of I-80 and I-580 in the Bay Area (37.83° N, 122.294° W) was selected (see Figure 8.23). The resulting target spectra were entered into the NGA West2 ground motion database (Bozorgnia et al., 2014) for the ground motion selection. For each intensity level, several ground motion records were selected and scaled to minimize the mean squared error (MSE) with respect to the target spectrum (see Figure 8.24). The matching period range of interest was limited to 0.1 s to 3.0 s as the fundamental period of the bridge was estimated to be around 1.1 s. To avoid repetition of the same loading pattern, the ground motions with the same name but only different scale factors were eliminated. The final selected ground motion records, one for each intensity level, are summarized in Table 8.2.

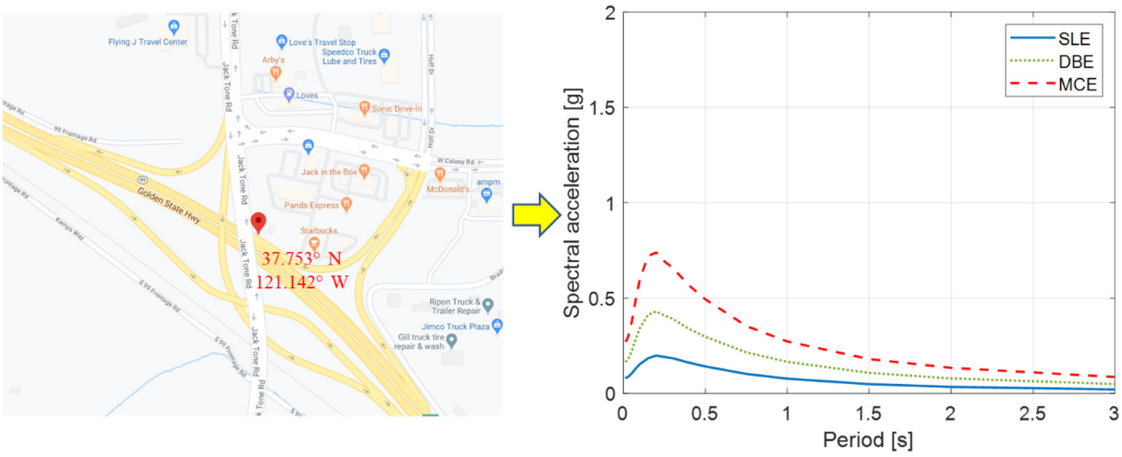

Figure 8.22 **Original site location (source: Google Maps) and the corresponding target spectra.**

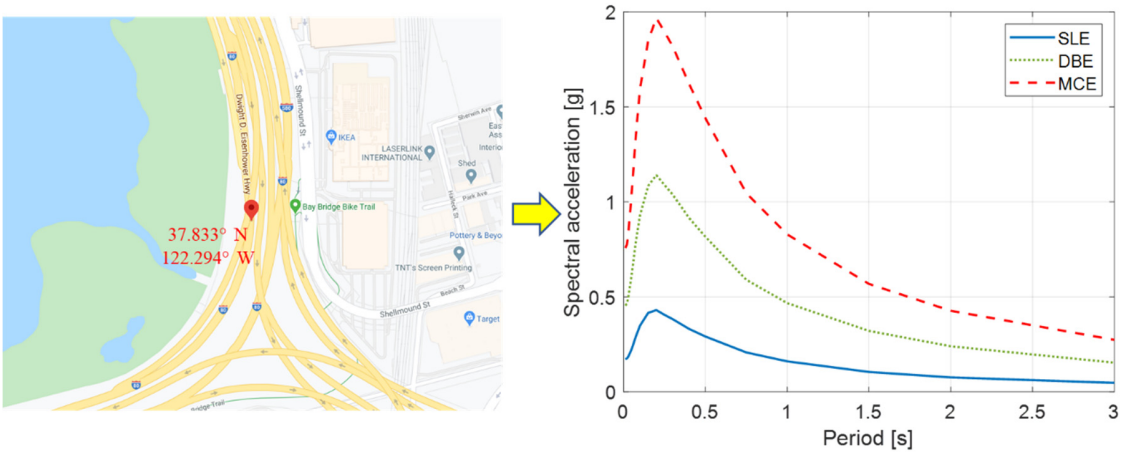

Figure 8.23 **Selected site location (source: Google Maps) and the corresponding target spectra.**

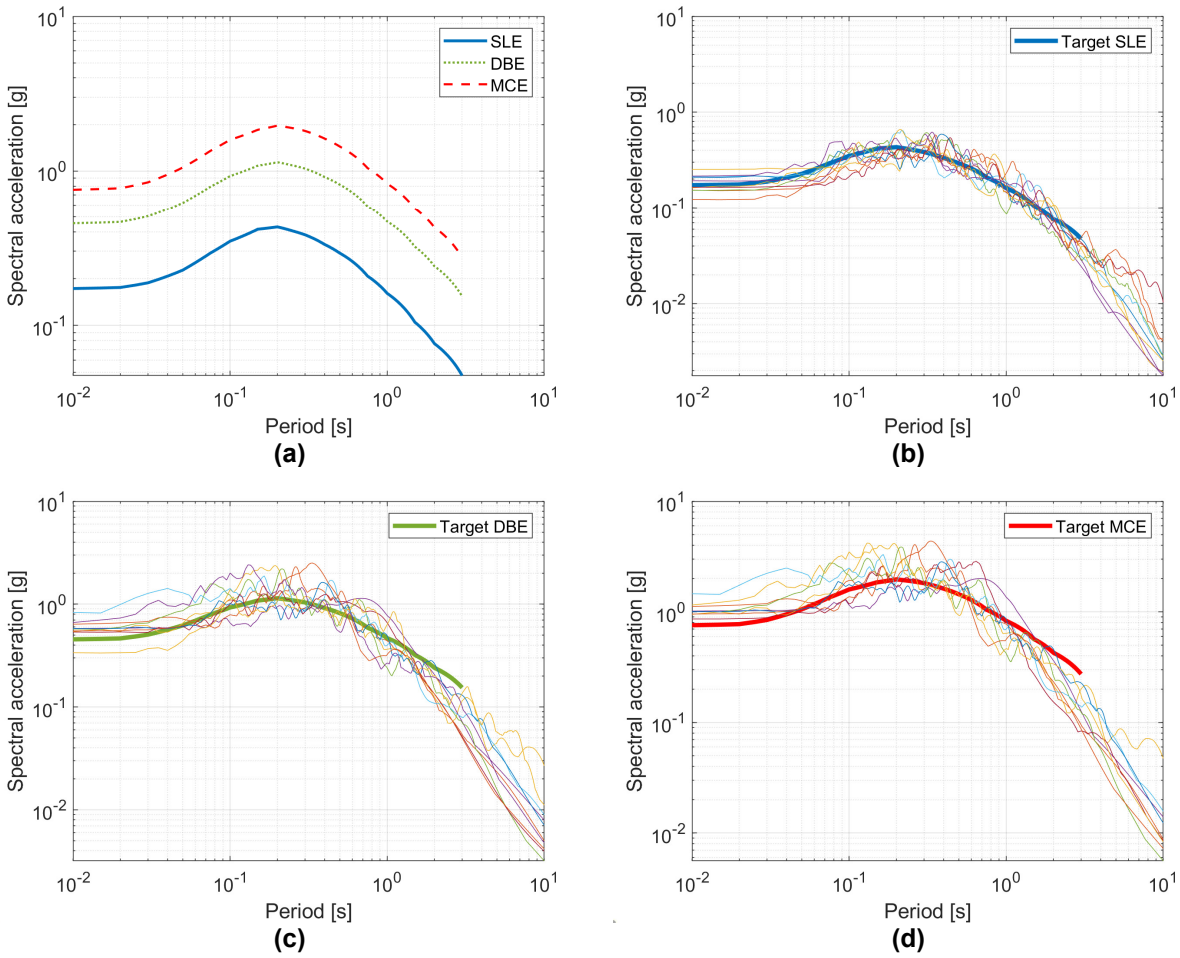

Figure 8.24 **(a) Target response spectra in log-log plot; selected ground motions for (b) SLE; (c) DBE; and (d) MCE.**

Table 8.2 **Selected ground motions for each intensity level.**

EQ Level	Event Name	Station Name	Unscaled PGA [g]	Scale Factor
SLE	Livermore, 1980	Del Valle Dam	0.256	0.983
DBE	Tabas, 1978	Dayhook	0.41	1.402
MCE	Coyote Lake, 1979	Gilroy	0.42	2.411

In order to have a reliable prediction of the 30% scale bridge bent in terms of the horizontal displacement amplitude and the vertical actuator force during the HS, the selected ground motions above were applied to the OpenSEES (McKenna et al., 2000) bridge model in a concatenate manner with increasing intensity and nonlinear time history analysis was conducted before the phase II HS experiment. A series of zero values were added in between the ground motions to allow for enough time for the damping-out phase. The bridge bent was modeled in the same simplified manner as mentioned in section 8.2.3 (linear elastic spring in each direction). Figure

8.25 shows the response quantities of interest in the prototype scale. The horizontal displacement range was between -12 in. and 5 in. while the vertical force range was between -2,600 kips and -940 kips. Therefore, the maximum horizontal displacement and vertical force to be applied to the test specimen were 3.6 in. and 235 kips, respectively. These values were considered to be acceptable.

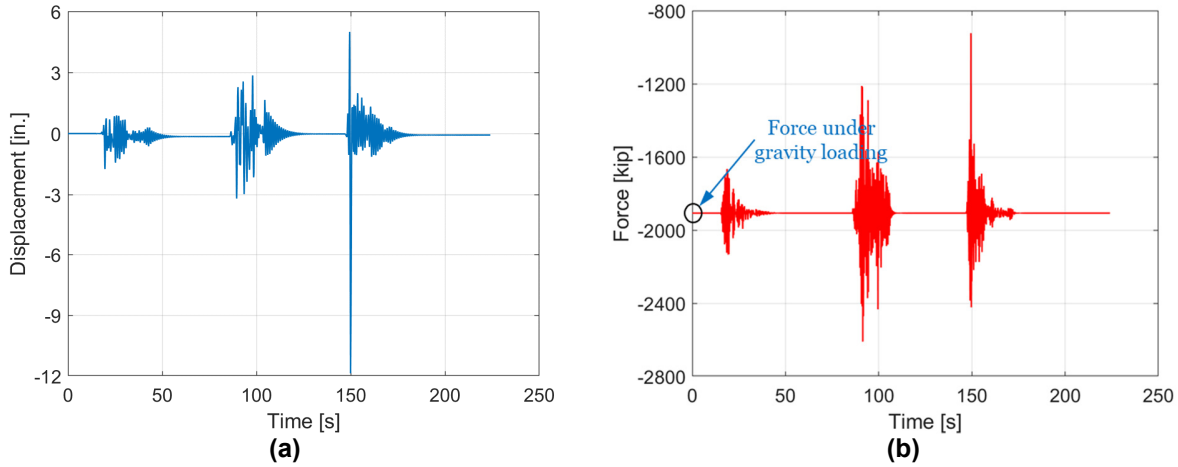

Figure 8.25 **(a) Horizontal displacement time history; and (b) vertical force time history of the bridge bent (prototype scale).**

8.3.3 Test Results

The test results and key observations are presented in this section. For the first and third test runs, the subdivision number *n* of the bridge deck was chosen to be 10 (Figure 8.26). Response quantities from different locations of the bridge, including the bridge bent, the end abutments, and the nodes at mid-span, were recorded during the test. At the beginning of each run, enough time was given for the test specimen to slowly adjust itself to its new self-equilibrium position (not necessarily the position with no residual deformations). In other words, the horizontal actuator load cell should have zero initial readings.

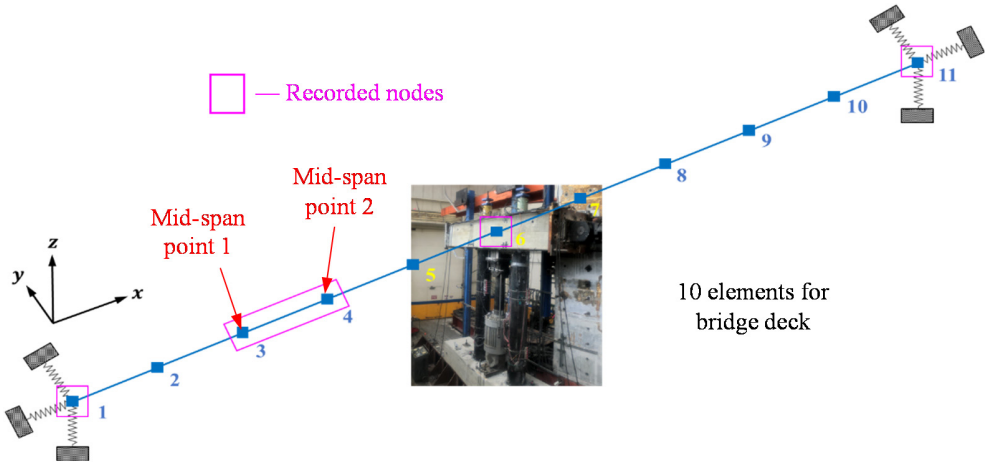

Figure 8.26 **Bridge model with 10 deck subdivisions including recorded nodes during phase II HS experiment.**

8.3.3.1 Test 1: Bridge System, Repeat EQ7

In the first run, the ground motion record of EQ7 previously used in phase I HS test was repeated and the behavior of the bridge bent is compared. Figure 8.27 and Figure 8.28 show the comparison of the displacement time history, the resisting force time history and the acceleration time history of the bridge bent in the transverse direction. Here, phase I (single bent) represents the HS conducted using only mass and damping as the analytical substructure and phase II (full bridge) represents the HS conducted to explore the system level response with the remainder of the prototype bridge modeled as the analytical substructure. The target of this comparison is not the displacement amplitudes as they represent two completely different dynamic systems. Rather, the goal is to compare the general characteristics of the two responses to observe if there are fundamental differences between the two cases when the resilient bridge bent is simulated by itself and the full bridge including the resilient bridge bent. As can be seen from the plots, the period elongation due to the change of the analytical substructure is quite obvious from both plots, which was expected as the bridge system was more flexible than the SDOF system. One important finding is that while the displacement amplitude from phase II was smaller, a much larger residual displacement of 0.7 in., about 35% of the peak value, was observed towards the end. This was not expected as the bridge bent failed to demonstrate its excellent re-centering capacity in phase II HS compared with phase I HS.

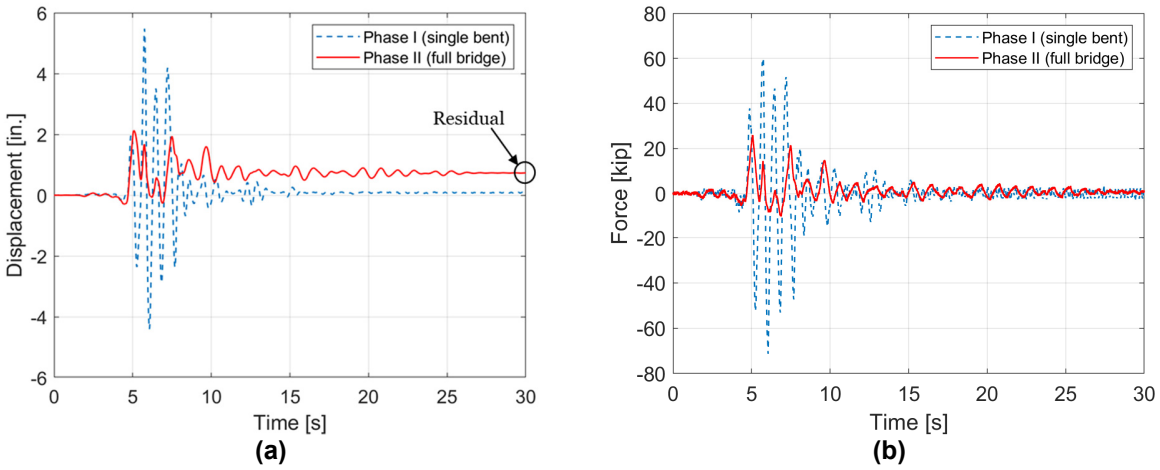

Figure 8.27 **(a) Displacement time history; and (b) resisting force time history comparisons of the bridge bent (specimen scale) in the transverse direction.**

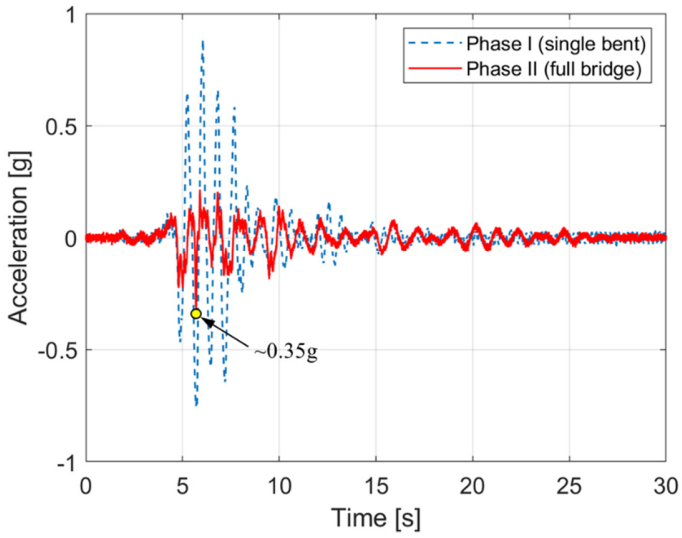

Figure 8.28 **Acceleration time history comparison of the bridge bent in the transverse direction.**

Figure 8.29 illustrates the horizontal force-displacement relationship comparison. There was a clear stiffness degradation after EQ7 in phase I, as indicated from the lower initial stiffness in phase II. This shows that even if the bridge bent was designed for self-centering and more resilient behavior, the damage in the form of energy dissipator yielding, concrete spalling, and grout crushing at the interfaces was inevitable.

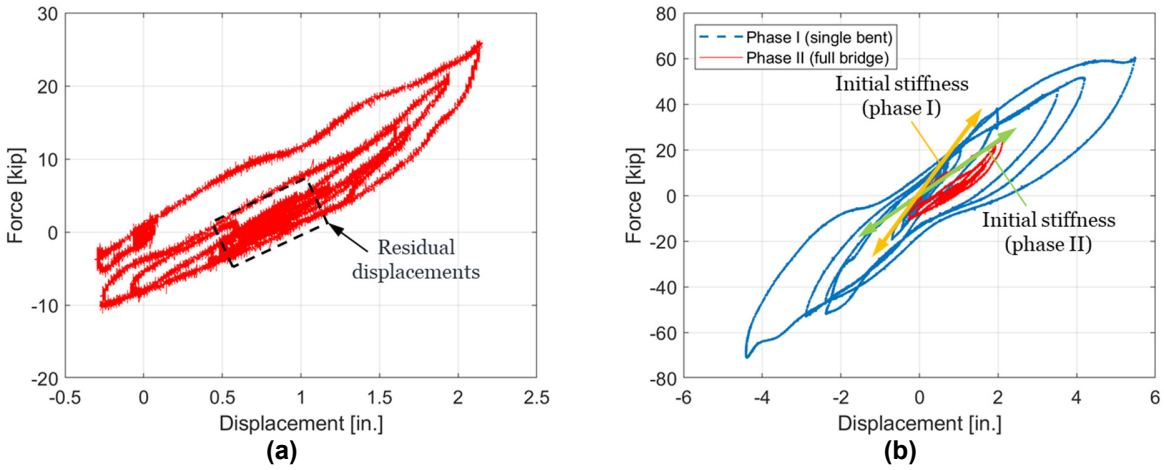

Figure 8.29 **(a) Horizontal force-displacement relationship of the bridge bent (specimen scale) from phase II HS; and (b) comparison with phase I HS.**

Another observation is that the transverse displacement time histories from different bridge locations (nodes) are almost identical, as shown in Figure 8.30(a). This means that the bridge deck behaved like a rigid body in the transverse direction with negligible bending deformation. A very simple calculation was conducted to verify this behavior. In that regard, one span of the bridge was treated as a simply supported beam, while the lateral inertia forces acting on the bridge were assumed to be represented by a uniformly distributed load w, see Figure 8.30(b). The geometric and section properties of this simplified model can be found in Table 4.1. The uniform load w was obtained by the following:

$$w = \frac{F}{L} = \frac{ma_{\max}}{L} \tag{8.26}$$

where

m = the total mass of one span;

$a_{\max}$ = maximum transverse acceleration over the span; and

L = length of a single span, which is half the length of the bridge.

The maximum transverse acceleration from phase II HS was around 0.35g (Figure 8.28). To be on the conservative side, taking $a_{\max} = 0.5$g yields:

$$w = \frac{ma_{\max}}{L} = \frac{\rho A L a_{\max}}{L} = 2.156 \times 10^{-7} \times 13946.46 \times 0.5 \times 386.4 = 0.58 \text{ kips/in.}$$

The maximum deflection of the simply supported beam under uniform load can be obtained by:

$$\delta = \frac{5wL^4}{384EI} \tag{8.27}$$

The value I was taken to be the second moment of area about the strong axis I_y. Plugging in other relevant values gives:

$$\delta = \frac{5wL^4}{384EI} = \frac{5 \times 0.58 \times 1323^4}{384 \times 4030 \times 76911540} = 0.075 \text{ in.}$$

$$\Rightarrow \frac{\delta}{L} = 0.006\%$$

The small deflection value (0.006% of a single span length L) justifies the observation that the bridge deck behaved like a rigid body with negligible deflection in the transverse direction during the ground shaking.

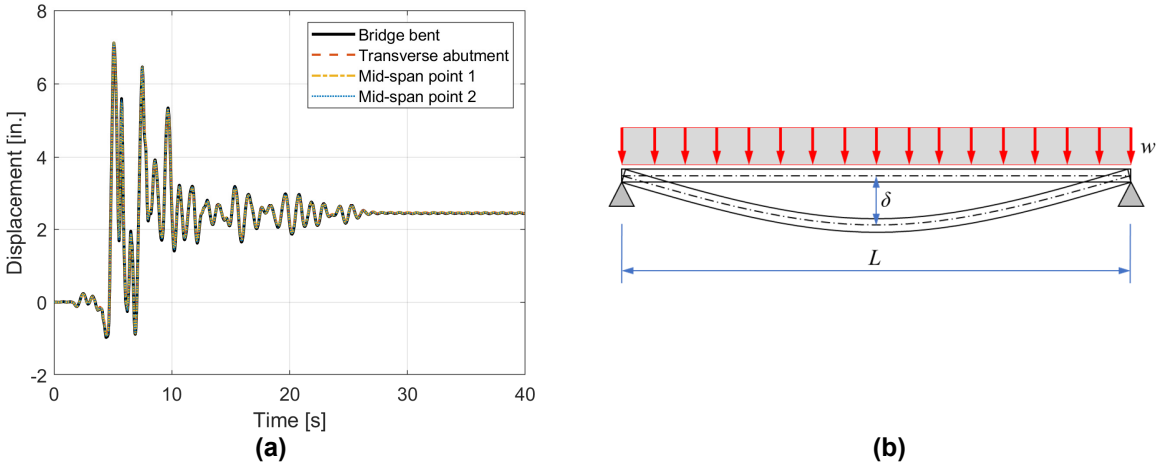

Figure 8.30 **(a) Displacement time histories from different bridge locations (nodes) in the transverse direction (prototype scale); (b) deformed shape of a simply supported beam under uniformly distributed load.**

Finally, the displacement time histories and the force-displacement relationships of the end abutments are given in Figure 8.31 and Figure 8.32. Yielding was observed in the transverse direction of the abutment response. This fact, combined with the flexural rigidity of the bridge deck as shown above, is most likely the cause of the large residual displacement of the bridge bent, and has been verified in later runs. The abutment response in the vertical direction remained in compression without uplifting.

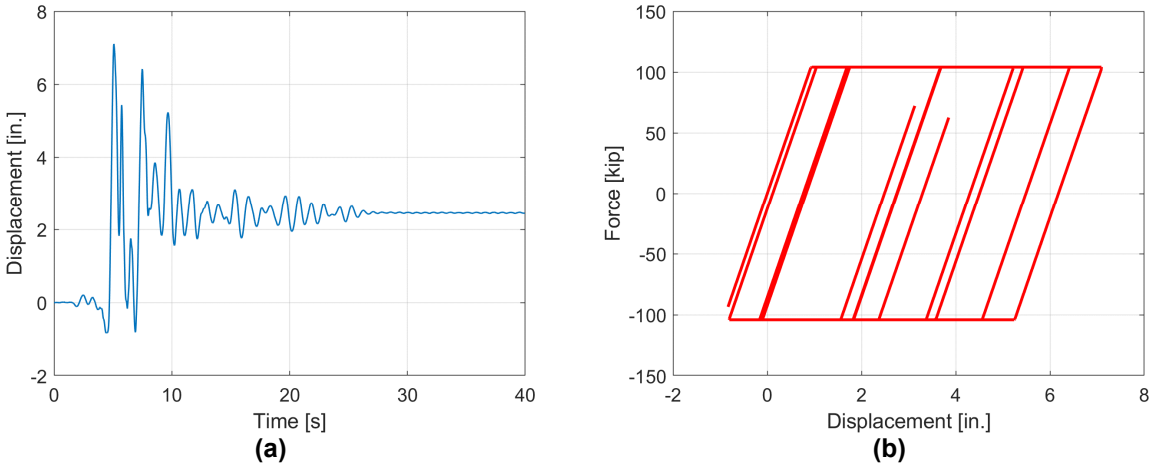

Figure 8.31 **Displacement time history; and (b) force-displacement relationship of the abutment (prototype scale) in the transverse direction.**

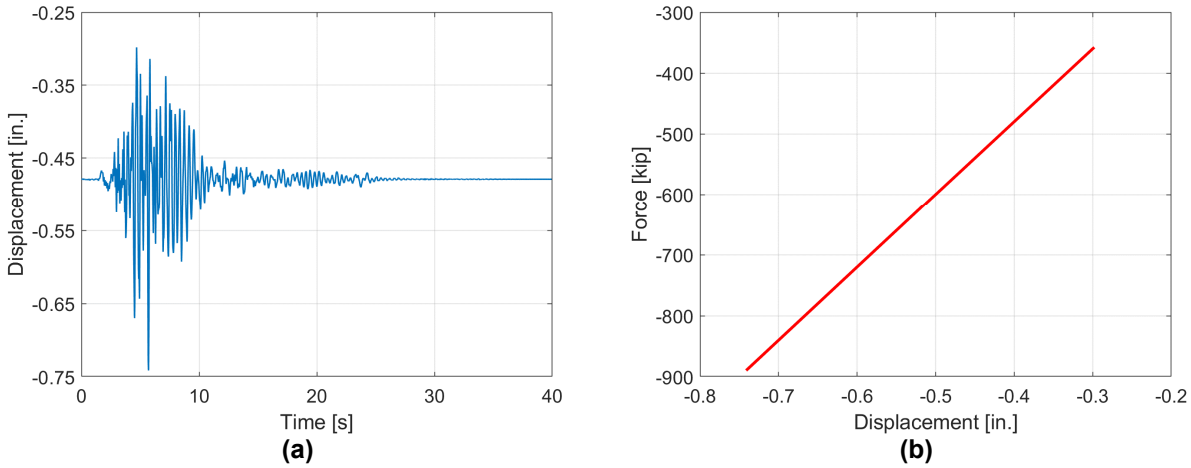

Figure 8.32 **Displacement time history; and (b) force-displacement relationship of the abutment (prototype scale) in the vertical direction.**

8.3.3.2 Test 2: Single Bent, Repeat EQ6

The most important finding from test 1 of phase II HS was the large residual displacement at the end of the time history. Several factors might have contributed to this, including the inherent properties of the bridge system like the yielding of the abutment in the transverse direction, or possible unknown test-limitation induced errors like the friction force from the lateral supporting system. In order to further investigate this phenomenon, EQ6 was repeated, with the hybrid substructure changed back to a single bridge bent with modeled analytical mass/damping as is the case in phase I HS. This specific ground motion was chosen because of its comparable displacement amplitude (see Figure 7.43(a)) with the conducted test 1 of phase II HS. If the test specimen can demonstrate a much better re-centering behavior compared with the first test, then

it can be more confidently concluded that the residual displacement indeed came from the bridge system rather than other external factors.

Figure 8.33 shows the displacement time history comparison between the 1st and the 2nd test of phase II HS. Similar to the observation from Figure 8.27(a), the single bent test yielded larger peak displacement, but smaller residual displacement (13% of the peak for the 2nd test compared to 35% of the peak for the 1st test) than the system level test, indicating an improved re-centering capacity. However, it is noted that this residual displacement was still higher than those from phase I HS because of possible initial displacement offset inherited from all previous runs or because of the corresponding accumulated specimen damage.

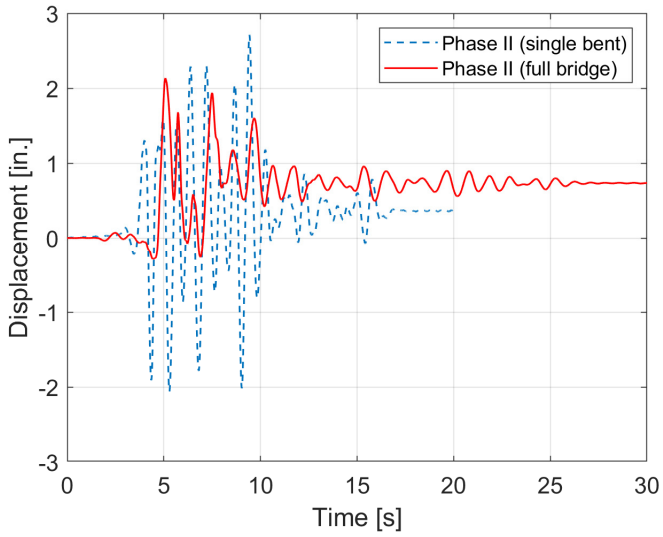

Figure 8.33 Displacement time history comparison of the bridge bent (specimen scale) between test 1 and test 2 of phase II HS.

8.3.3.3 Test 3: Bridge System, Ground Motions with Increasing Intensity

The earthquake excitation for test 3 of phase II HS was a combination of three selected motions with increasing intensity (Table 8.2). Figure 8.34 shows the displacement time history and the hysteretic behavior of the test specimen in the transverse direction. The responses of the end abutments can be found in Figure 8.35 and Figure 8.36. For the SLE and DBE levels, the bridge bent maintained its good self-centering capabilities with negligible residual displacement (< 0.05 in., i.e., 0.04% drift), while the transverse response of the abutment remained mostly in the linear elastic range. When the MCE level was applied, the test specimen first went through a positive peak of 1.45 in. (1.09% drift), then suddenly reached a negative peak of 3.47 in. (-2.62% drift) due to the near-fault pulse-like nature of the ground motion (Figure 8.37). After the peaks, it stayed and oscillated in the negative displacement region, with the final residual displacement being -1.59 in. (-1.2% drift), whose implications are discussed in detail in the next paragraph. The end abutments in the transverse direction experienced significant amount of yielding during the MCE level and ended up with similar residual displacement (-5.38 in.) to the bridge bent on the prototype scale because of the rigid body behavior of the bridge deck. The vertical response of the abutment

again stayed in its linear elastic compression-only state without going into positive (tension or uplift) displacement.

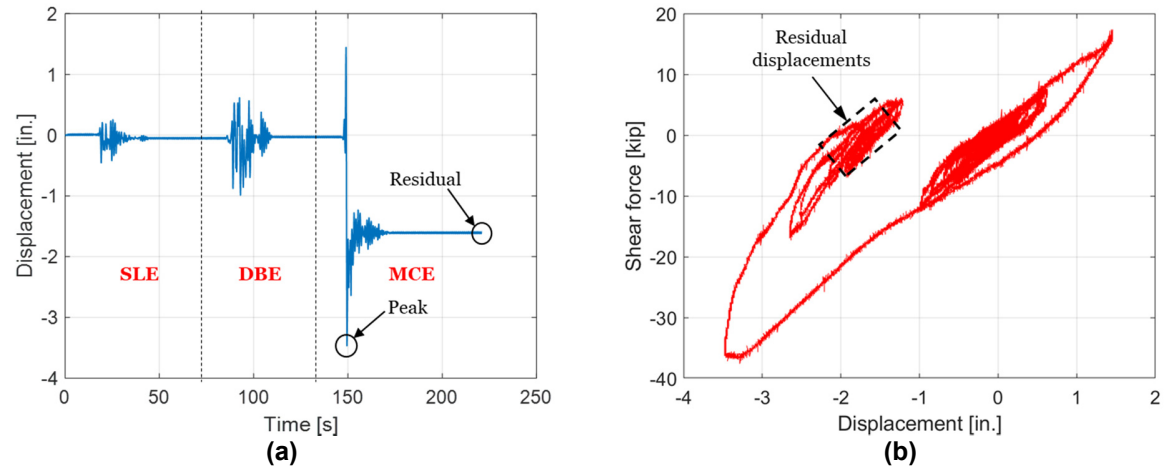

Figure 8.34 **(a) Displacement time history; and (b) force-displacement relationship of the bridge bent (specimen scale) in the transverse direction for the three combined motions.**

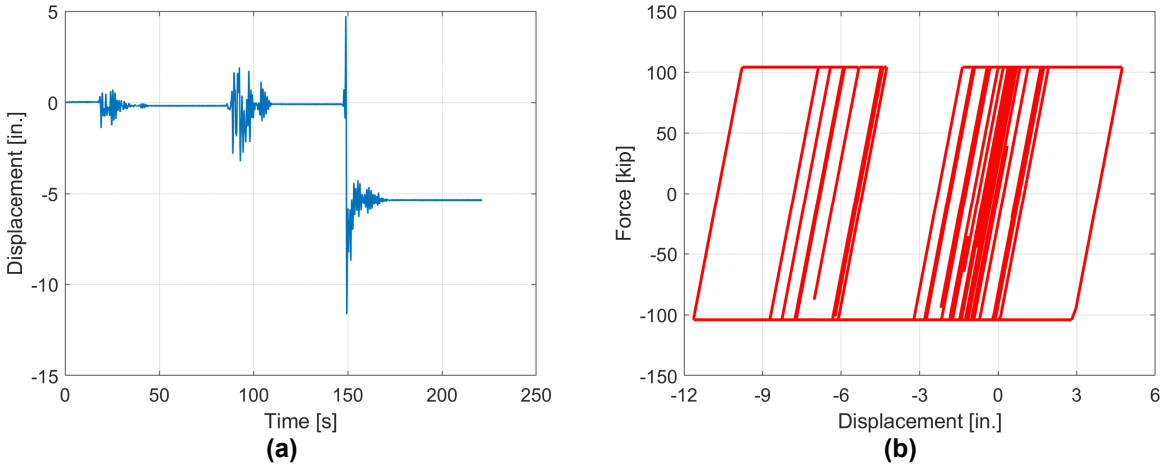

Figure 8.35 **Displacement time history; and (b) force-displacement relationship of the abutment (prototype scale) in the transverse direction for the three combined motions.**

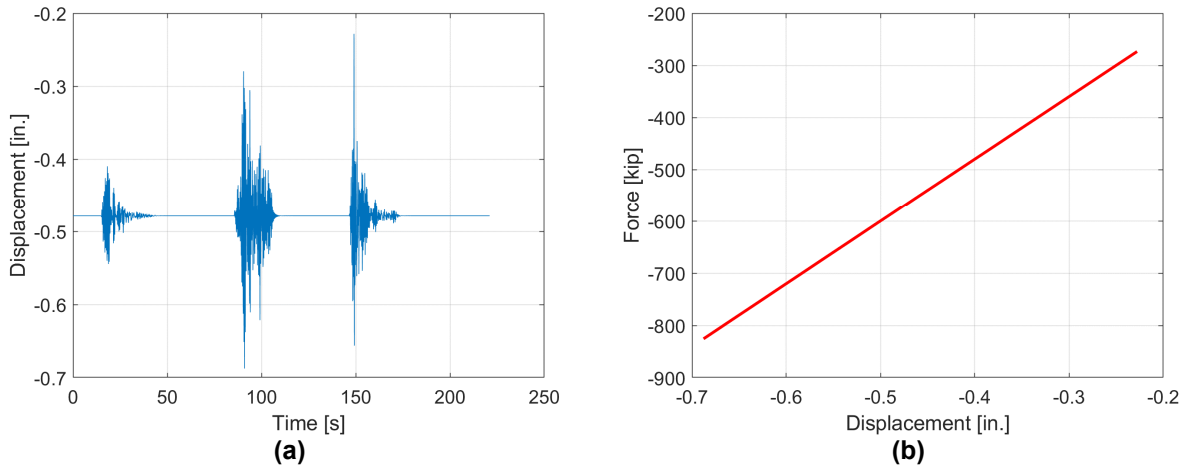

Figure 8.36 **Displacement time history; and (b) force-displacement relationship of the abutment (prototype scale) in the vertical direction for the three combined motions.**

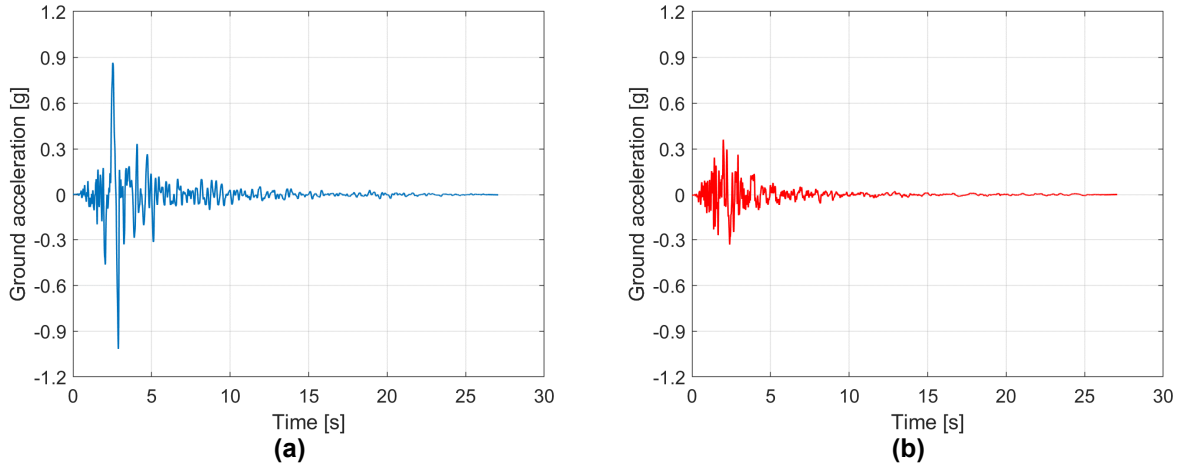

Figure 8.37 **(a) Horizontal; and (b) vertical ground motion records for the MCE level.**

The residual displacement of 1.59 in., which corresponds to a residual drift of 1.2%, is discussed in the context of some current design code provisions for residual displacement. This discussion is summarized in the following points:

- In Japan, over 100 reinforced concrete bridge columns with residual drift ratios of more than 1.75% were demolished and rebuilt after the 1995 Kobe earthquake (Kawashima et al., 1998). Following this earthquake, Japanese seismic design specifications for highway bridges were revised to specify an allowable residual displacement for bridge columns. Under these provisions, no more than 1% drift ratio is allowed;

- Caltrans SDC (2013) includes provisions pertaining to near-fault ground motions by amplification of the design spectra. However, no limits on residual displacements are specified;
- AASHTO (2012) requires site-specific analysis when the site is close to an active fault, but there are no guidelines for the design of reinforced concrete bridge columns with respect to the control of residual displacement; and
- The PEER tall buildings initiative (Hamburger et al., 2017) states that for MCE, the mean of the absolute values of residual drift ratios from the suite of analyses shall not exceed 1% in each story. In addition, in each story, the maximum residual story drift ratio in any analysis shall not exceed 1.5%. Based on this guideline, the residual story drift ratio of 1% is intended to protect against excessive post-earthquake deformations that will likely cause condemnation or excessive downtime for a building. The limits on residual drifts are also based on the concern that tall buildings with large residual drifts may pose substantial hazards to surrounding construction in the event of strong aftershocks. Repair or demolition of tall buildings with large residual drifts also may pose risks to the community.

Although the PEER tall building initiative is not a bridge provision, it is still listed as a guidance herein. With all the information above, it can be concluded that the obtained 1.2% residual drift exceeded the strictest limit of 1%, but still below the 1.5% limit of maximum residual story drift for buildings or the 1.75% limit for bridge demolishing. Considering that the bridge bent has already had some damages before the final test and that the large residual displacement was strongly related to the yielding in the transverse response of the abutment but not the loss of re-centering capacity, this residual drift was still considered to be acceptable.

8.4 PARAMETRIC STUDY

Based on the test results, a conjecture was proposed that the observed large residual displacement towards the end of the motion was caused by the yielding of the abutment in the transverse direction. In order to prove this in a rigorous way and to investigate the effect of the transverse abutment's properties on the behavior of the bridge bent, a parametric study was analytically conducted in OpenSEES (McKenna et al., 2000), since it was impractical to test the specimen in the laboratory repeatedly with different cases. Moreover, the accumulated degrading behavior of the test specimen could not lead to an acceptable comparison. The bridge bent was represented by a zero-length spring in the transverse direction whose hysteretic response was calibrated against a representative test run. This simplified model, although impossible to replicate the force-displacement relationship of the bridge bent from all the runs, was sufficiently accurate for the intended comparative parametric study.

8.4.1 Simplified Bridge Bent Modeling

For the simplified model calibration, the horizontal hysteretic behavior of the test specimen from phase I EQ7 HS was selected as a reference (see Figure 8.38(a)). This is because the "flag-shaped" force-displacement curve for this run is an ideal reflection of the self-centering and energy

dissipation properties. Similar to the method used in the V-connector model calibration, the simplified bridge bent model was subjected to the displacement time history measured from EQ7, with the resisting forces calculated based on the pre-assigned material model. Different materials in OpenSEES were exploited and it turned out that the hysteretic material (a brief description of the material can be found in section 4.3.1) could yield the closest match between the test and the model by adjusting the parameters. Figure 8.38(b) gives the force-displacement comparison on the specimen scale (or reduced-scale).

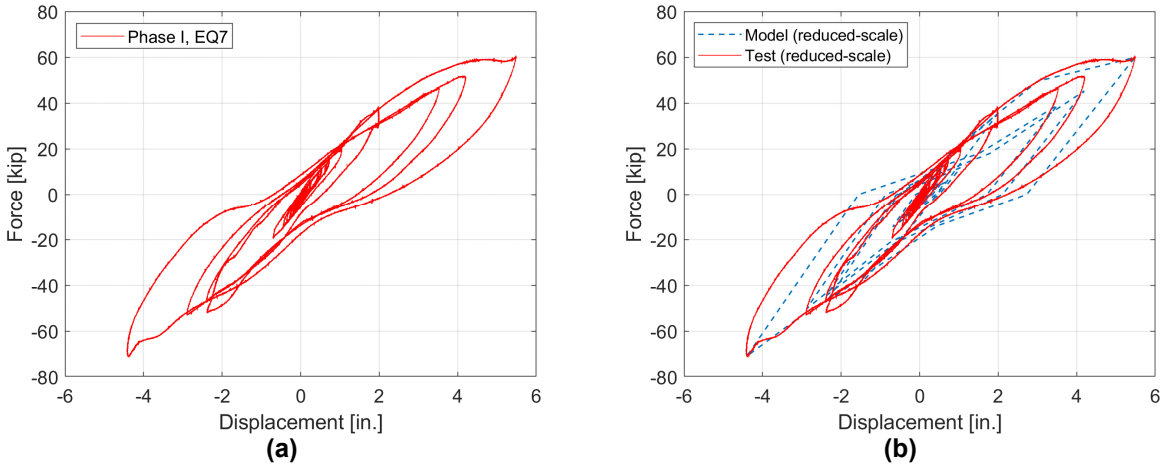

Figure 8.38 (a) Hysteretic curve of the bridge bent from phase I, EQ7; (b) model calibration of the bridge bent (specimen scale).

To combine the calibrated transverse bridge bent model with the bridge, the modeling parameters were scaled up by S_L = 3.333. The modeling of the bridge bent's vertical response remained unchanged, i.e., a linear elastic spring with the same stiffness used before (Figure 8.39).

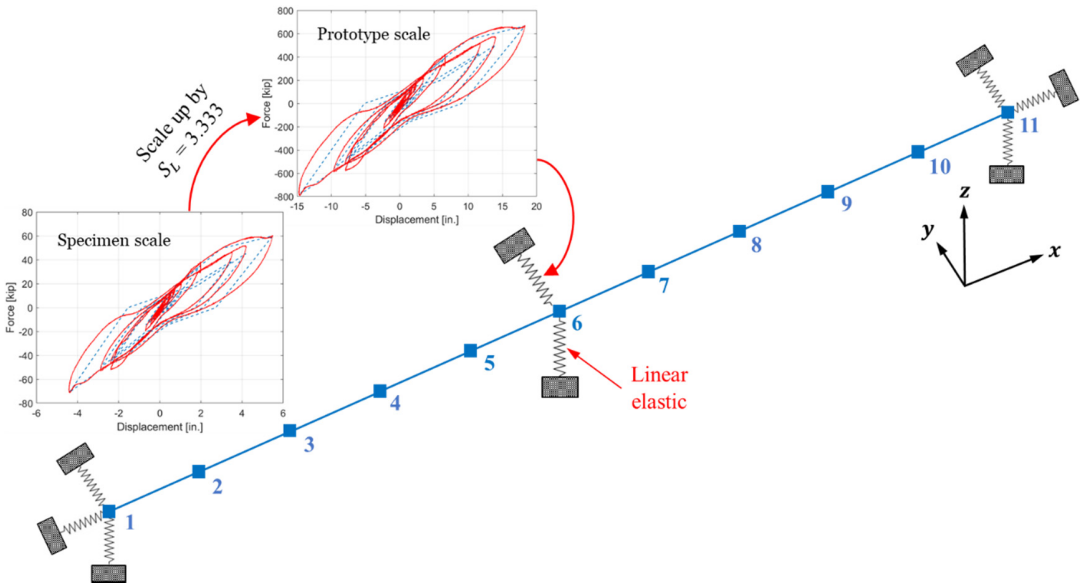

Figure 8.39 Schematic representation of the bridge with updated bridge bent modeling.

8.4.2 Effect of the Abutment Initial Stiffness in the Transverse Direction

Two parameters controlling the behavior of the abutment in the transverse direction, the initial stiffness K_{abt} and the yield strength P_{abt}, were investigated in the parametric study. The effect of the first parameter K_{abt} was investigated by keeping the yield strength constant and varying the stiffness value. EQ7 and the three combined motions for phase II HS testing were again used as the ground motion input. Table 8.3 provides different stiffness values used in the parametric study.

As can be seen from Figure 8.40, the transverse stiffness of the bridge was provided by the transverse response of the abutment and the bridge bent in parallel, assuming the bridge deck is sufficiently rigid. If the large residual displacement was indeed caused by the abutment yielding, a positive correlation between the residual displacement and the abutment stiffness should be expected. This is because as the abutment's transverse stiffness increases, the transverse bridge response is dominated by the abutments rather than the bridge bent. Moreover, under the same yield strength, P_{abt}, the abutment with higher stiffness is more likely to yield.

Table 8.3 Different stiffness values for the parametric study.

Case	1	2	3	4	5	6	7	8	9	10
Stiffness [kip/in.]	50	100	**112.2 (original)**	200	300	400	500	600	700	800

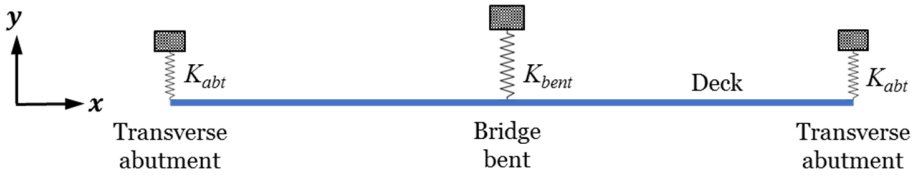

x—longitudinal direction; y—transverse direction.

Figure 8.40 Composition of transverse bridge stiffness.

Figure 8.41 and Figure 8.42 give the transverse displacement time history of the bridge bent and the force-displacement relationship of the abutment for different stiffness values. The absolute values of the residual displacements for each case were extracted and plotted against the abutment stiffness in Figure 8.43. It can be concluded that the residual displacement increases "on average" as the abutment stiffness becomes larger, although there exist some exceptions for certain cases. These exceptions can be explained as follows: the residual displacement not only depends on whether the abutment yields or not, but also on the prior history of yielding and the details of the input motions. If the abutment stopped vibrating at a small displacement value even if it yielded before, then the residual displacement of the bridge bent would also be small. However, the general trend (in an average sense) agrees with the previous inferences, which proves the relationship between the abutment yielding and the residual displacement from one aspect.

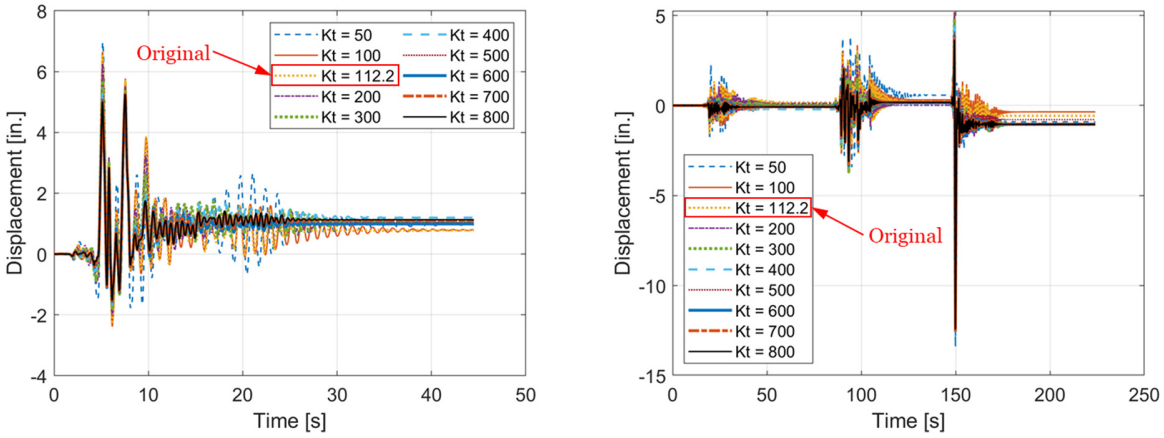

Figure 8.41 **Transverse displacement time histories of the bridge bent (prototype scale) for different stiffness values in (a) EQ7; and (b) the three combined motions.**

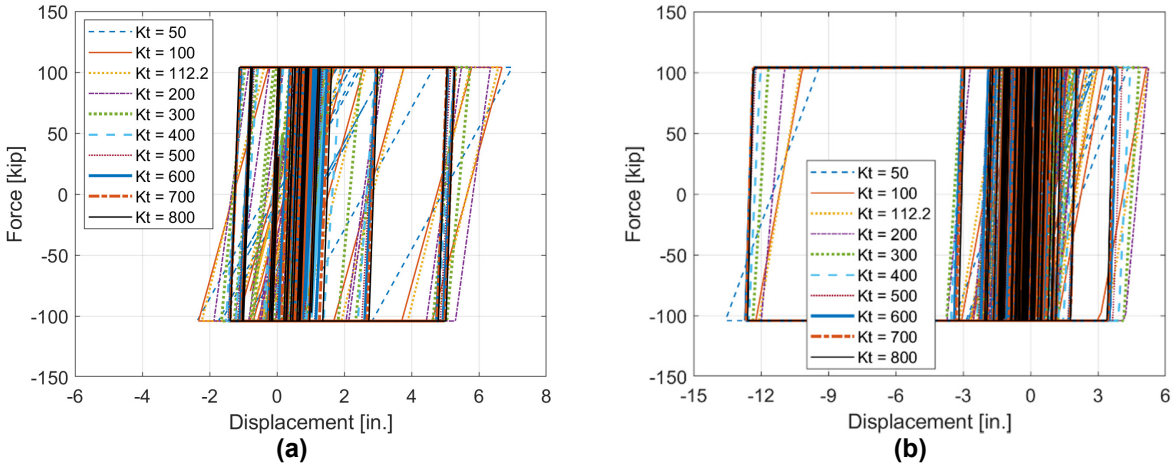

Figure 8.42 **Hysteretic responses in the transverse direction of the abutment (prototype scale) for different stiffness values in (a) EQ7; and (b) the three combined motions.**

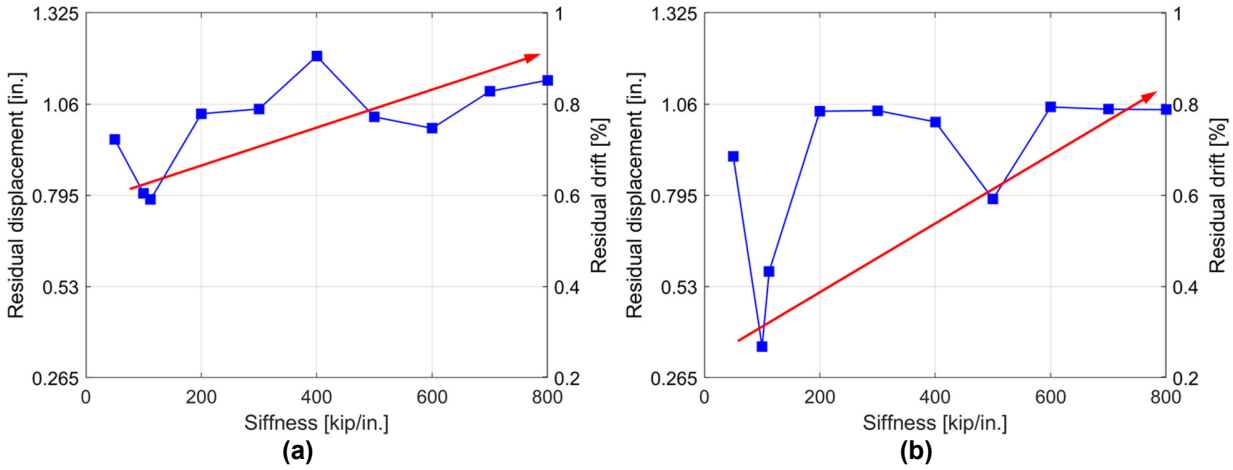

Figure 8.43 **Transverse residual displacement of the bridge bent vs. the abutment stiffness (prototype scale) for (a) EQ7; and (b) the three combined motions.**

8.4.3 Effect of the Abutment Yield Strength in the Transverse Direction

The effect of the other parameter, P_{abt}, was investigated by keeping the initial stiffness constant and varying the value of yield strength. A common prediction would be that if the yield strength was high enough so that the abutment behaved elastically, then the residual displacement of the bridge bent would be very close to zero because of its self-centering nature. Table 8.4 summarizes the different yield strength values used in this parametric study. Two different sets of parameters were used for different ground motions such that the largest value in each set could lead to linear elastic response of the abutment in the transverse direction.

Table 8.4 **Different yield strength values for the parametric study.**

Case		1	2	3	4	5	6
Yield Strength [kip]	EQ7	100	**104.1 (original)**	200	400	600	800
	Combined motion	**104.1 (original)**	200	400	800	1200	1500

Figure 8.44 and Figure 8.45 give the transverse displacement time history of the bridge bent and the force-displacement relationship of the abutment for different yield strength values. The absolute values of the residual displacements for each case were extracted and plotted against the yield strength of the abutment in Figure 8.46. No clear relationship was observed between the residual displacement and the yield strength. However, the most important finding was that the linear elastic transverse response of the abutment resulted in the re-centering behavior of the bridge bent. This evidence, together with that from the previous subsection, strongly support the original conjecture that the large residual displacement at the end of phase II HS was caused by the yielding of the abutment model in the transverse direction.

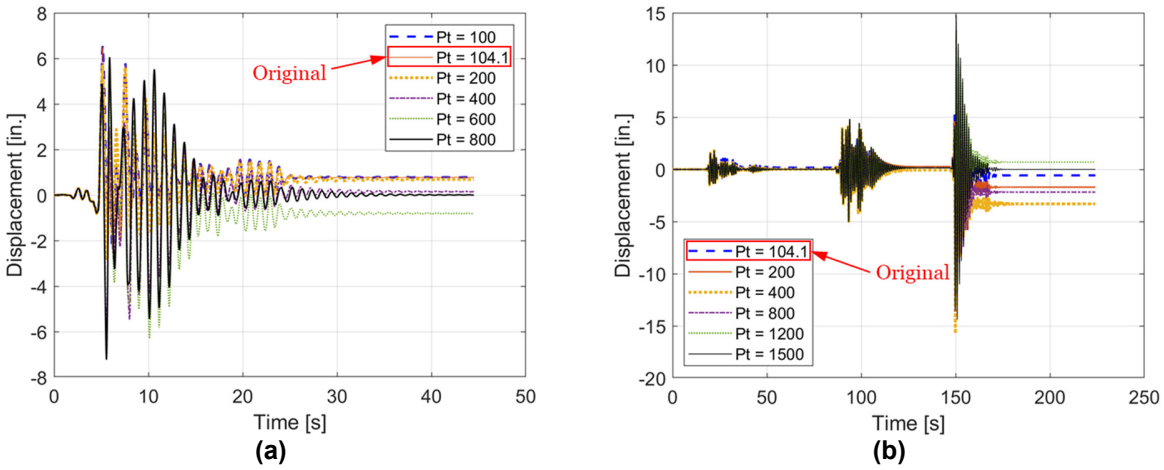

Figure 8.44 **Transverse displacement time histories of the bridge bent (prototype scale) for different yield strength values in (a) EQ7; and (b) the three combined motions.**

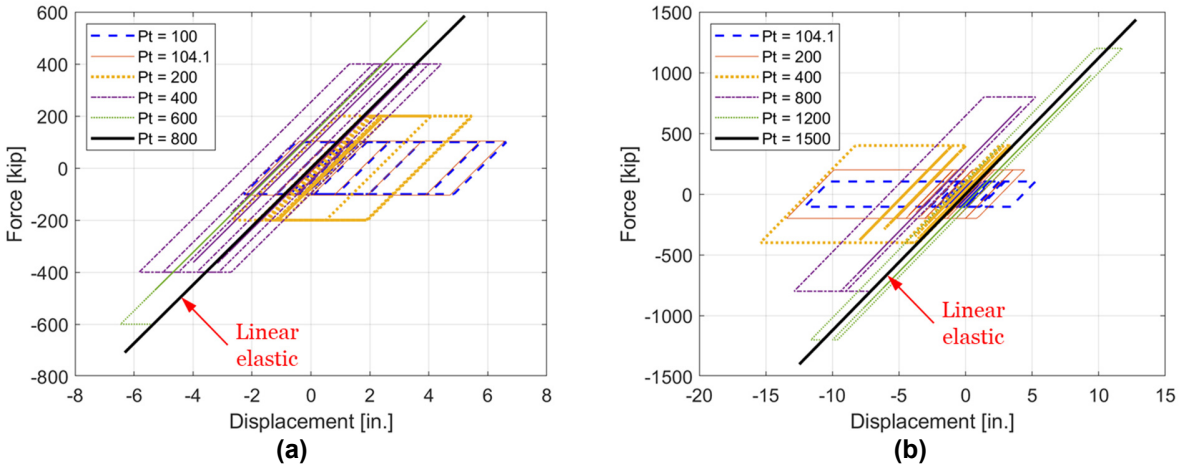

Figure 8.45 **Hysteretic responses in the transverse direction of the abutment (prototype scale) for different yield strength values in (a) EQ7; and (b) the three combined motions.**

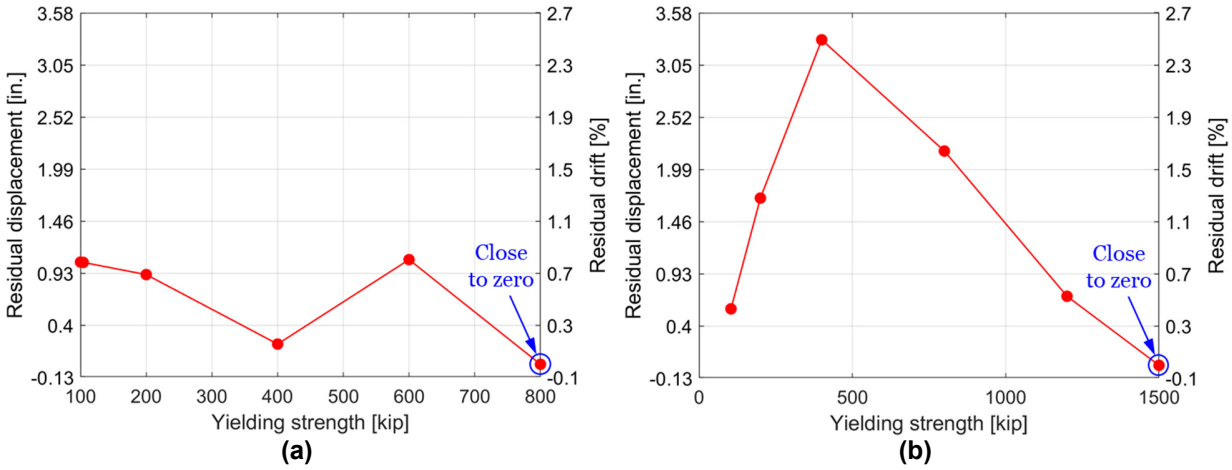

Figure 8.46 **Transverse residual displacement of the bridge bent vs. the abutment yield strength (prototype scale) for (a) EQ7; and (b) the three combined motions.**

9 Conclusions and Future Extensions

A summary of the developed computational and experimental studies is first presented in this chapter. This is followed by the main conclusions, and recommendations for future work based on the entire study.

9.1 SUMMARY

This dissertation reported a combined numerical and experimental research. The scope was to investigate the structural behavior and system level response of two bridge subsystems, aiming at bringing seismic resiliency and accelerated bridge construction (ABC) to the bridge engineering practice.

The first study focused on the system response of reinforced concrete highway bridges incorporating a class of innovative connecting devices called the "V-connector". This device is used to connect two components in a structural system, e.g., the column and the bridge deck, or the column and its foundation. By providing an isolation surface and limiting the amount of transferred forces and relative displacements between the two connection parts through a flexible connection rod, the V-connector elongates the fundamental period of the bridge and protects the bridge columns from being damaged, leading to a resilient bridge system design. The intrinsic energy dissipation mechanism is provided by the interface friction forces generated along the sliding contact surfaces. Furthermore, the device facilitates the ABC by allowing on-site assembly of precast structural elements.

A single-column two-span highway bridge located in California (the Jack Tone Road On-Ramp Overcrossing) was used as a prototype bridge for a proof-of-concept of this system. Before embarking on the experimental program, a pre-test nonlinear time history analysis of the bridge model was carried out, with an idealized hysteretic behavior of the V-connector. This resulted in a set of design parameters for the V-connector that can lead to an elastic bridge response. A 1/3-scale V-connector was fabricated accordingly. A quasi-static cyclic test was first conducted on the V-connector to obtain its hysteretic response, with two 1D OpenSEES (McKenna et al., 2000) models calibrated based on the test results. These models were then used to select the ground motion scale factors for the hybrid simulation (HS) test. In the HS test, all bridge components were analytically modeled except for the V-connector, which was simulated as the experimental substructure in a specially designed and constructed test setup. The proper communication among the HS components, the validity of the geometric transformation and the verification of the hybrid simulation system (HSS) were performed using a low intensity HS trial run with actuators attached

to the test specimen. This was important because the geometric transformation depends on the actuator layout during the real test. Finally, one single HS test run with three combined ground motions of increasing intensity was conducted. Linear elastic bridge response was confirmed by the HS results. The comparison of the bridge response with and without the V-connector justifies the usage of these connectors in ABC.

The study of the second bridge subsystem has two main objectives: (1) Conduct HS on a single two-column bridge bent with innovative design features and compare the test results against a previously conducted shaking table test; and (2) Conduct HS on a full bridge system and evaluate the system level performance of the bridge involving the same bridge bent. The design of the re-centering columns was rationally derived from that of an existing monolithic bridge, the Massachusetts Avenue Over Crossing (MAOC), and the final configuration was selected on the basis of a parametric analysis performed on the 3D OpenSEES model of the MAOC bridge. The specimen construction was performed following the principles of ABC and utilizing readily available technologies. The use of a socket connection provides the possibility for the simultaneous fabrication of all the subcomponents that can result in higher quality of the construction, which is further simplified by the proposed use of an external steel shell, specially engineered around rocking behavior to serve as both the formwork and the transverse reinforcement of the bridge column. As an added benefit, this technology eliminates the need for a mortar bed at the column base, commonly used to accommodate construction tolerances in systems with precast columns over the clear height, which can limit the optimal performance of the system under earthquake loading.

To fulfill the experimental program, a new HSS was designed, utilizing the computational platform Matlab/Simulink (MathWorks, 2015), the interface hardware/software platform dSPACE (2017), the MTS controllers and data acquisition (DAQ) system for the utilized actuators and sensors. The operation of the HSS was verified by a HS trial run without utilizing the test specimen. In phase I HS, the inertia mass blocks attached to the top of the specimen in the shaking table test were removed and modeled in the computer (analytical substructure), with the modeling parameters estimated based on the shaking table test results. The two-column bridge bent with the same design was treated as the experimental substructure. Six out of the twelve ground motions from the shaking table test were repeated and the results were compared. Good matching was achieved in terms of the different measured response quantities. In phase II HS, the analytical substructure was expanded to include the remaining part of a two-span bridge, including the entire bridge deck and its abutments. 3D linear elastic frame element was used for the bridge deck, while the abutments were modeled using spring elements with different force-displacement relationships in different directions. The formulation of the stiffness/mass/damping matrices and the resisting force vector followed the standard finite element method (FEM) and has been checked against OpenSEES results. A set of additional ground motion records were selected based on the target response spectrum of different earthquake intensities for a specific high-seismicity region in the San Francisco Bay Area. The test results were further interpreted through a parametric study, which shed more light on the system level performance of the entire bridge system with an innovative bridge bent and provided a good reminder to the engineering communities in achieving resilient structural system (involving sound modeling of the bridge bents, deck, as well as abutments) designs.

9.2 CONCLUSIONS

Several conclusions were drawn from this study and are summarized as follows:

- Both bridge subsystems proved to be effective in mitigating the earthquake-induced damage, protecting the key components of the bridge system and providing ABC.
- The hysteretic behavior and the energy dissipation mechanism of the V-connector remained stable and consistent after large deformation amplitudes, indicating its reliability as a seismic protective system. The resiliency of the bridge with a V-connector was achieved in terms of the linear elastic behavior of the bridge column, which would otherwise be severely damaged following conventional design approaches.
- A hardening behavior and an increase of the friction force were observed in the V-connector's hysteresis loop. The change of the V-pin's free length, possible strain hardening due to yielding of the V-pin, and the abrasion between the Teflon washer and the stainless steel surface were believed to be the reasons. The developed 1D OpenSEES (McKenna et al., 2000) models were capable of capturing these observations.
- A new HSS was developed using Matlab/Simulink (MathWorks, 2015) as a computational platform for single- and multi-degree-of-freedom analytical substructures, and has been verified through a HS trial run;
- Phase I HS of the bridge bent utilizing self-centering columns was successfully conducted. The small residual drifts and the observed re-centering behavior demonstrate the resilient nature (reducing any down time for repairs or bridge closure) of the subsystem.
- The results from phase I HS were compared against the shaking table test. Good matching of the test results indicates:
    - Correctness of the utilized equations of motion;
    - Minimum level of simulation errors;
    - The reliability of the newly developed HSS; and
    - Correctness of the employed damping model.

  This proves that HS is a good alternative of the costly shaking table test and will increase the confidence of HS in the testing of new and innovative structural/geotechnical systems.
- The bridge bent showed larger residual displacement during the phase II system level HS test compared to phase I, due to the yielding of the transverse abutments modeled in the computer as part of the analytical substructure. An important conclusion drawn from this is that the resiliency of the bridge cannot be guaranteed by just making the bridge bent resilient, as different parts of the bridge system are interacting in a complicated manner in the system response. Therefore, attention should be given to the bridge system response including not only the main parts like the bridge bents and the deck, but also other parts of the bridge like the abutments for achieving the optimal bridge performance.

- Findings from standalone bridge bent and system level HS tests increase our understanding for damage-free bridges towards resilient transportation networks.

9.3 RECOMMENDATIONS FOR FUTURE STUDIES

Several research topics that are appropriate for future investigations can be extended from this study. The following are relevant possible topics:

- **Improve the V-connector design**: the damage state of the V-connector shown in section 5.3.1.4 indicates that the V-connector was damaged to some extent. Because of the plastic deformation of the V-pin, its response cannot be treated as elastic during the test, especially when subjected to large displacement amplitudes. Some unexpected scratch damage occurred on the surface of the ball hinge, which was originally designed to rotate freely. Improvement can be made for redesigning the geometry of the V-tube to make sure the V-pin always stays in the linear elastic range and for reducing the friction between the ball hinge and the hinge holder, maybe through lubrication or smoother contact surface. Moreover, a residual displacement, even if not large, was observed at the end of the HS. Therefore, introducing a re-centering mechanism for the V-connector to mitigate the post-earthquake residual displacement will be useful.
- **Develop a more detailed 3D finite element model of the V-connector**: the 1D V-connector models described in section 4.3 are good enough in representing the hysteretic behavior and predicting the response of the V-connector during the HS, but they failed to provide valuable information in terms of stress/strain distribution, deformed shape and contact surface interactions. In this case, a more detailed 3D finite element model will be necessary. This, of course, requires the support from the V-connector manufacturer as the material properties and more accurate surface friction coefficients need to be provided and characterized.
- **Explore the effect of the computational model size on the HS**: the number of subdivisions for the bridge deck in the bridge bent study was chosen to be 10. However, the implemented Simulink model was generalized to any even number of subdivisions (this way a node exists at the center of the deck where the bridge bent is connected to the bridge deck). More future HS experiments can be conducted using the analytical substructure with varying degrees of freedom in an effort to determine the largest analytical substructure that the HS can handle. The preliminary investigation of this task can be conducted with dry runs (i.e., using the HSS without hydraulics, similar to the HS trial run described in section 7.3). After drawing conclusions, a few critical limiting cases can be validated by completing HS experiments involving the use of the hydraulics and actual specimens.
- **Explore different modeling techniques**: the abutment modeling in the system level testing of the bridge bent is highly simplified. It delivers the essential behavioral aspects and gives a good example of the computational formulation involved in a full bridge system using self-developed code, but it might not be able to accurately capture the complex behavior of the abutments in real-world situation (e.g., the torsional stiffness or the skew angles). The future research can be extended to explore different abutment modeling techniques, in terms of

different hysteretic behavior, different element types, etc., and their effect on the bridge response. This can be conducted in a pure analytical manner without involving the test specimen. In addition, the modeling of the test specimen can be revised. Instead of using a zero-length spring element, a more detailed model that can better match the test results and take into account the effect of gravity/earthquake forces can be used. Nema (2018) proposed an OpenSEES model (see Figure 9.1) and there is still room to improve it even further.

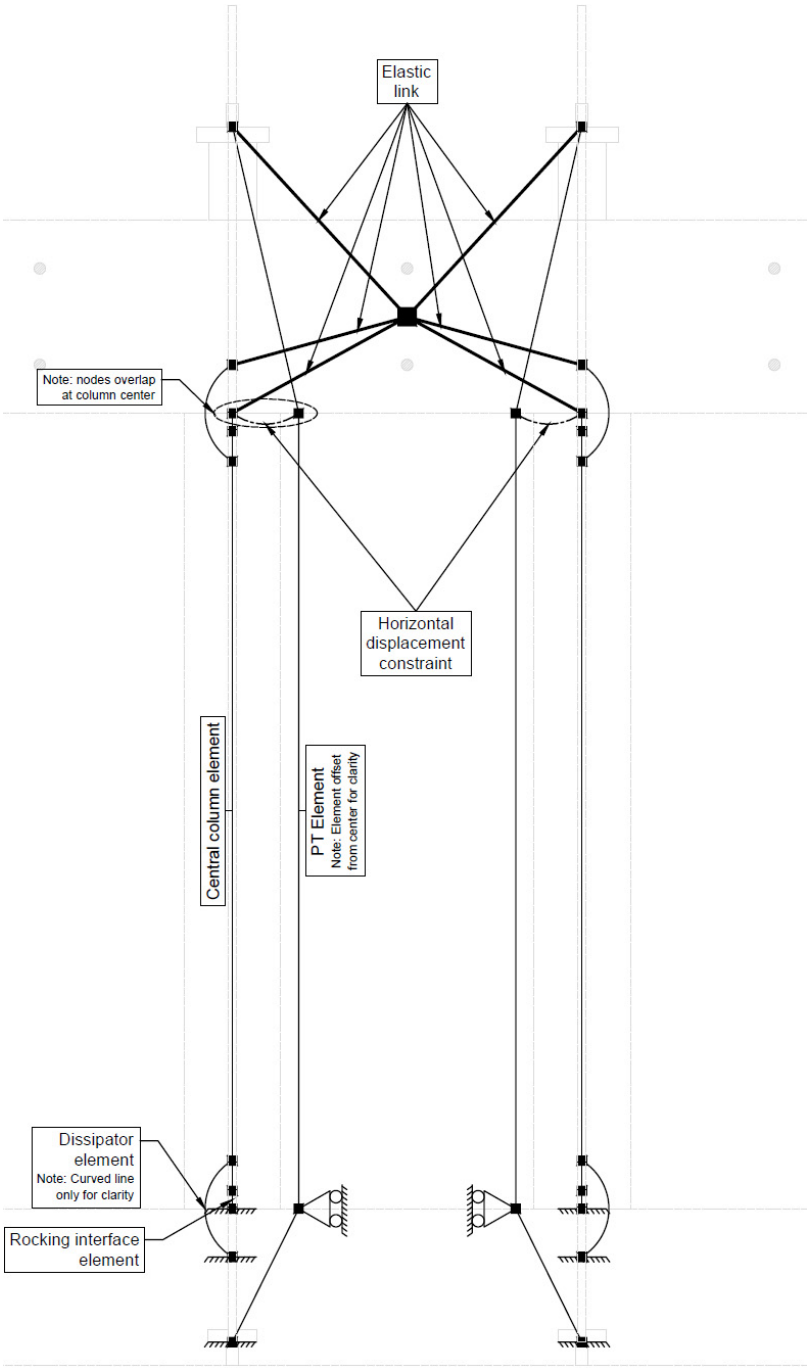

Figure 9.1 OpenSEES model of the bridge bent (Nema, 2018).

- **Retrofit using external energy dissipators**: both internal and external energy dissipators in the self-centering hybrid columns (Figure 9.2) have been extensively studied by researchers. In this study, the internal energy dissipators have been employed for the convenience in the construction process, because they also serve as part of the longitudinal reinforcement. However, the internal energy dissipators went through significant amount of yielding during the test and they are hard (and disruptive) to be replaced. On the other hand, the external energy dissipators, which are easy to be installed and replaced, can be used to retrofit the test specimen for more promising responses towards even more resilient bridge systems in future studies.

(a) (b)

Figure 9.2 (a) Internal; and (b) external energy dissipators (Guerrini et al., 2015).

REFERENCES

AASHTO (2012). *AASHTO Guide Specifications for LRFD Seismic Bridge Design*, 6th edition, American Association of State Highway and Transportation Officials. Washington, D.C.

ACI Committee 318 (2011). *Building Code Requirements for Structural Concrete and Commentary*, ACI 318-11, American Concrete Institute, Farmington Hills, MI.

ASTM (2005). *Standard Test Method for Compressive Strength of Cylindrical Concrete Specimens: Designation ASTM C39/C39M-05*, American Society for Testing Materials, west Conshohocken, PA.

ASTM (2012). *Standard Specification for Pipe, Steel, Black and Hot-dipped, Zinc-coated Welded and Seamless: Designation ASTM A53/A53M-12*, American Society for Testing Materials, west Conshohocken, PA.

ASTM (2012). *Standard Specification for Uncoated High-Strength Steel Bars for Prestressing Concrete: Designation A722/A722M-12*, American Society for Testing Materials, west Conshohocken, PA.

ASTM (2016). *Standard Specification for Deformed and Plain Low-Alloy Steel Bars for Concrete: Designation A706/A706M-16*, American Society of Testing Materials, west Conshohocken, PA.

ATC-24 (1992). Guidelines for cyclic seismic testing of components of steel structures for buildings, Report No. ATC-24, Applied Technology Council, Redwood City, CA.

Aviram, A., Mackie, K.R., Stojadinovic, B. (2008). Guidelines for nonlinear analysis of bridge structures in California, *PEER Report No. 2008/03*, Pacific Earthquake Engineering Research Center, University of California, Berkeley, CA.

Beckwith, F. (2015). *Nonlinear Time History Earthquake Analysis of Bridges with Varying Skew Angle to Determine the Design Parameters for Shear Keys*, Caltrans.

Bonelli, A., Bursi, O.S. (2004). Generalized-α methods for seismic structural testing, *Earthquake Engineering & Structural Dynamics*, 33(10): 1067-1102.

Bonnet, B.A., Williams, M.S., Blackeborough, A. (2008). Evaluation of numerical time integration schemes for real-time hybrid testing, *Earthquake Engineering & Structural Dynamics*, 37(13):1467–1490.

Bozorgnia, Y., Abrahamson, N.A., Al Atik, L., Ancheta, T.D., Atkinson, G.M., Baker, J.W., Baltay, A., Boore, D.M., Campbell, K.W., Chiou, B.S.-J., Darragh, R., Day, S., Donahue, J., Graves, R.W., Gregor, N., Hanks, T., Idriss, I.M., Kamai, R., Kishida, T., Kottke, A., Mahin, S.A., Rezaeian, S., Rowshandel, B., Seyhan, E., Shahi, S., Shantz, T., Silva, W., Spudich, P., Stewart, J.P., Watson-Lamprey, J., Wooddell, K., Youngs, R. (2014). NGA-West2 research project, *Earthquake Spectra*, 30(3): 973-987.

Bozorgzadeh, A., Ashford, S.A., Restrepo, J.I. (2008). Effect of backfill soil type on stiffness and ultimate capacity of bridge abutments, ASCE, *Geotechnical Earthquake Engineering and Soil Dynamics IV*.

Bozorgzadeh, A., Megally, S., Restrepo, J.I., Ashford, S.A. (2006). Capacity evaluation of exterior sacrificial shear keys of bridge abutments, ASCE, *Journal of Bridge Engineering*, 11(5): 555-565.

Bruneau, M., Chang, S., Eguchi, R., Lee, G., O'Rourke, T., Reinhorn, A., Shinozuka, M., Tierney, K., Wallace, W., von Winterfeldt, D. (2003). A framework to quantitatively assess and enhance the seismic resilience of communities, Earthquake Spectra, 19(4): 733-752.

Bursi, O.S., Gonzalez-Buelga, A., Vulcan, L., Neild, S.A., Wagg, D.J. (2008). Novel coupling Rosenbrock-based algorithms for real-time dynamic substructure testing, *Earthquake Engineering & Structural Dynamics*, 37(3): 339-360.

Caltrans (2013). *Seismic Design Criteria version 1.7*, California Department of Transportation, Sacramento, CA.

Cha, Y.J., Zhang, J., Agrawal, A.K., Dong, B., Friedman, A., Dyke, S.J., Ricles, J. (2013). Comparative studies of semiactive control strategies for MR dampers: pure simulation and real-time hybrid tests, ASCE, *Journal of Structural Engineering*, 139(7): 1237-1248.

Chae, Y., Kazemibidokhti, K., Ricles, J.M. (2013). Adaptive time series compensator for delay compensation of servo-hydraulic actuator systems for real-time hybrid simulation, *Earthquake Engineering & Structural Dynamics*, 42(11): 1697-1715.

Chang, S.Y. (1997). Improved numerical dissipation for explicit methods in pseudodynamic tests, *Earthquake Engineering & Structural Dynamics*, 26(9): 917-929.

Chen, C., Ricles, J.M. (2009). Improving the inverse compensation method for real-time hybrid simulation through a dual compensation scheme, *Earthquake Engineering & Structural Dynamics*, 38(10): 1237-1255.

Chen, C., Ricles, J.M. (2010). Tracking error-based servohydraulic actuator adaptive compensation for real-time hybrid simulation, ASCE, *Journal of Structural Engineering*, 136(4): 432-440.

Chen, C., Ricles, J.M., Marullo, T.M., Mercan, O. (2009). Real-time hybrid testing using the unconditionally stable explicit CR integration algorithm, *Earthquake Engineering & Structural Dynamics*, 38(1): 23-44.

Chopra, A.K. (2011). *Dynamics of Structures*, 4th edition, Prentice Hall, Upper Saddle River, NJ.

Christopoulos, C., Filiatrault, A., Uang, C.-M., Folz, B. (2002). Post-tensioned energy dissipating connections for moment resisting steel frames, ASCE, *Journal of Structural Engineering*, 128(9): 1111-1120.

Clark, P.W., Frank, K., Krawinkler H., Shaw R., (1997). Protocol for fabrication, inspection, testing, and documentation of beam-column connection tests and other experimental specimens, *Report No. SAC/BD-97/02*, SAC Steel Project Background Document, October.

Combescure, D., Pegon, P. (1997). α-Operator splitting time integration technique for pseudodynamic testing error propagation analysis, *Soil Dynamics and Earthquake Engineering*, 16: 427-443.

Cormack, L.G. (1988). The design and construction of the major bridges on the Mangaweka rail deviation, *Transactions of the Institution of Professional Engineers New Zealand: Civil Engineering Section*, 15(1): 6-23.

Dermitzakis, S.N., Mahin, S.A. (1985). Development of substructuring techniques for on-line computer controlled seismic performance testing, *Report No. UCB/EERC-85/04*, Earthquake Engineering Research Center, University of California, Berkeley, CA.

dSACE, Inc. (2017). dSPACE, http://www.dspaceinc.com/ww/en/inc/home.cfm.

Eatherton, M.R., Hajjar, J.F. (2014). Hybrid simulation testing of a self-centering rocking steel braced frame system, *Earthquake Engineering & Structural Dynamics*, 43(11): 1725-1742.

Elkhoraibi T., Mosalam K.M. (2007). Generalized hybrid simulation framework for structural systems subjected to seismic loading, *PEER Report No. 2007/101*, Pacific Earthquake Engineering Research Center, University of California, Berkeley, CA.

Elkhoraibi, T., Mosalam, K.M. (2007). Towards error-free hybrid simulation using mixed variables, *Earthquake Engineering & Structural Dynamics*, 36(11): 1497-1522.

El-Sheikh, M.T., Sause, R., Pessiki, S., Lu, L.-W. (1999). Seismic behavior and design of unbonded post-tensioned precast concrete frames, Precast/Prestressed Concrete Institute, *PCI Journal*, 44(3): 54-71.

FEMA 461 (2007). *Interim Testing Protocols for Determining the Seismic Performance Characteristics of Structural and Nonstructural Components*, Federal Emergency Management Agency, Washington, D.C.

Field E.H., Jordan T.H., Cornell C.A. (2003). OpenSHA: a developing community-modeling environment for seismic hazard analysis, *Seismological Research Letters*, 74(4): 406-419.

Friedman, A., Dyke, S.J., Phillips, B., Ahn, R., Dong, B., Chae, Y., Castaneda, N., Jiang, Z., Zhang, J., Cha, Y., Ozdagli, A.I. (2014). Large-scale real-time hybrid simulation for evaluation of advanced damping system performance, ASCE, *Journal of Structural Engineering*, 141(6), 04014150.

Goel, R.K., Chopra A.K. (1997). Evaluation of bridge abutment capacity and stiffness during earthquakes, *Earthquake Spectra*, 13(1): 1-24.

Guerrini, G. (2014). *Seismic Performance of Precast Concrete Dual-shell Steel Columns for Accelerated Bridge Construction*, PhD Dissertation, University of California, San Diego, CA.

Guerrini, G., Massari, M., Vervelidis, A., Restrepo, J.I. (2012). Self-centering precast concrete dual-shell steel columns, *Proceedings, 15th World Conference on Earthquake Engineering*, Lisbon, Portugal.

Guerrini, G., Restrepo, J.I. (2013). Seismic response of composite concrete-dual steel shell columns for accelerated bridge construction, *Proceedings, 7th National Seismic Conference on Bridges and Highways*, Oakland, CA.

Günay, S., Hu, F., Mosalam, K.M., Nema, A., Restrepo, J.I., Zsarnoczay, A., Baker, J. (2020). Blind prediction of shaking table tests of a new bridge bent design, *PEER Report*, Pacific Earthquake Engineering Research Center, University of California, Berkeley, Under Review.

Günay, S., Mosalam, K.M. (2014). Seismic performance evaluation of high voltage disconnect switches using real-time hybrid simulation: Part II: parametric study, *Earthquake Engineering & Structural Dynamics*, 43(8): 1223-1237.

Günay, S., Mosalam, K.M. (2015). Enhancement of real-time hybrid simulation on a shaking table configuration with an advanced control method, *Earthquake Engineering & Structural Dynamics*, 44(5): 657-675.

Hamburger, R., Moehle, J., Baker, J., Bray, J., Crouse, C.B., Deierlein, G., Hooper, J., Lew, M., Maffei, J., Mahin, S.A., Malley, J., Naeim, F., Stewart, J., Wallace, J. (2017). Guidelines for performance-based seismic design of tall buildings, version 2.03, *PEER Report No. 2017/06*, Pacific Earthquake Engineering Research Center, University of California, Berkeley, CA.

Hao, S. (2018). A class of V-connectors for bridge deck-pier and pier-footing joints with combined advantage of integrated design and seismic isolation while enabling accelerated bridge construction, *Project No. IDEA 20-30/IDEA 188*, National Cooperative Highway Research Program.

Haraldsson, O.S., Finnsson, G., Davis, P.M., Stanton, J.F., Eberhard, M.O., Schoettler, M.J. (2013). Seismic resistance of precast concrete bridge columns made with unbonded pre-tensioning and hybrid fiber reinforced concrete, *Proceedings, 7th National Seismic Conference on Bridges and Highways*, Oakland, CA.

Harris, H.G., Sabnis, G.M. (1999). *Structural Modeling and Experimental Techniques*, 2nd edition, CRC Press, Boca Raton, FL.

Hashemi, M.J., Mosqueda, G. (2014). Innovative substructuring technique for hybrid simulation of multistory buildings through collapse, *Earthquake Engineering & Structural Dynamics*, 43(14): 2059-2074.

Heiber, D.G., Wacker, J.M., Eberhard, M.O., Stanton, J.F. (2005). Precast concrete pier systems for rapid construction of bridges in seismic regions, *Report No. WA-RD 611.1*, Washington Department of Transportation, Olympia, WA.

Hessabi, R.M., Mercan, O. (2012). Phase and amplitude error indices for error quantification in pseudodynamic testing, *Earthquake Engineering & Structural Dynamics*, 41(10): 1347-1364.

Hewes, J.T., Priestley, M.J.N. (2002). Seismic design and performance of precast concrete segmental bridge columns, *Report No. SSRO-2001/25*, Department of Structural Engineering, University of California at San Diego, La Jolla, CA.

Holden, T., Restrepo, J.I., Mander, J.B (2003). Seismic performance of precast reinforced and prestressed concrete walls, ASCE, *Journal of Structural Engineering*, 129(3): 286-296.

Horiuchi, T., Inoue, M., Konno, T., Namita, Y. (1999). Real-time hybrid experimental system with actuator delay compensation and its application to a piping system with energy absorber, *Earthquake Engineering & Structural Dynamics*, 28(10): 1121-1141.

Horiuchi, T., Konno, T. (2001). A new method for compensating actuator delay in real-time hybrid experiments, *Philosophical Transaction: Mathematical, Physical and Engineering Sciences*, 359(1786): 1893-1909.

ISO (1998). Timber Structures – joints made with mechanical fasteners – quasi-static reversed-cyclic test method, *ISO/TC 165 WD 16670*, International Organization for Standardization, Geneva, Switzerland.

Ji, X., Kouichi, K., Takuya, N., Ryuta, E., Masayoshi, N. (2009). A substructure shaking table test for reproduction of earthquake responses of high-rise buildings, *Earthquake Engineering & Structural Dynamics*, 38(12): 1381-1399.

Karavasilis, T.L., Ricles, J.M., Sause, R., Chen, C. (2011). Experimental evaluation of the seismic performance of steel MRFs with compressed elastomer dampers using large-scale real-time hybrid simulation, *Engineering Structures*, 33(6): 1859-1869.

Kavianijopari, P. (2011). *Performance-based Seismic Assessment of Skewed Bridges*, PhD Dissertation, University of California, Irvine, CA.

Kawashima, K., MacRae, G. A., Hoshikuma, J., Nagaya, K. (1998). Residual displacement response spectrum, ASCE, *Journal of Structural Engineering*, 124(5): 523-530.

Kim, S.J., Christenson, R., Phillips, B., Spencer, B. (2012). Geographically distributed real-time hybrid simulation of MR dampers for seismic hazard mitigation, *Proceedings, 20th Analysis and Computation Specialty Conference*, Chicago, USA.

Kim, S.J., Holub, C.J., Elnashai, A.S. (2011). Experimental investigation of the behavior of RC bridge piers subjected to horizontal and vertical earthquake motion, *Engineering Structures*, 33(7): 2221-2235.

Krawinkler, H. (1996). Cyclic loading histories for seismic experimentation on structural components, *Earthquake Spectra*, 12(1): 1-12.

Krawinkler, H. (2009). Loading histories for cyclic tests in support of performance assessment of structural components, *Proceedings, 3rd International Conference on Advances in Experimental Structural Engineering*, San Francisco, CA.

Krawinkler, H., Parisi, F., Ibarra, L., Ayoub, A., Medina, R. (2000). Development of a testing protocol for woodframe structures, CUREE Publication No. W-02, Consortium of Universities for Research in Earthquake Engineering, Richmond, CA.

Kwan, W.P., Billington, S. (2003a). Unbonded posttensioned concrete bridge piers, I: monotonic and cyclic analyses, ASCE, *Journal of Bridge Engineering*, 8(2): 92-101.

Kwan W.P., Billington S. (2003b). Unbonded posttensioned concrete bridge piers, II: seismic analyses, ASCE, *Journal of Bridge Engineering*, 8(2): 102-111.

Kwon, O., Elnashai, A.S., Spencer, B.F. (2008). A framework for distributed analytical and hybrid simulations, *Structural Engineering and Mechanics*, 30(3): 331-350.

Kumar, P., Jen, G., Trono, W., Panagiotou, M., Ostertag, C.P. (2011). Self compacting hybrid fiber reinforced concrete composites for bridge columns, *PEER Report No. 2011/106*, Pacific Earthquake Engineering Research Center, University of California, Berkeley, CA.

Kurama, Y., Sause, R., Pessiki, S., Lu, L.-W. (1999). Lateral load behavior and seismic design of unbonded posttensioned precast concrete walls, American Concrete Institute, *ACI Structural Journal*, 96(4): 622-632.

Lai, J.-W., Mahin, S.A. (2013). Experimental and analytical studies on the seismic behavior of conventional and hybrid braced frames, *PEER Report No. 2013/20*, Pacific Earthquake Engineering Research Center, University of California, Berkeley, CA.

Lee, S., Parka, E., Mina, K., Park, J. (2007). Real-time substructuring technique for the shaking table test of upper substructures, *Engineering Structures*, 29(9): 2219–2232.

Leon, R.T., Deierlein, G.G. (1996). Considerations for the use of quasi-static testing, *Earthquake Spectra*, 12(1): 87-109.

Lin, Y.C., Sause, R., Ricles, J.M. (2013). Seismic performance of steel self-centering, moment-resisting frame: hybrid simulations under design basis earthquake, ASCE, *Journal of Structural Engineering*, 139(11): 1823-1832.

MacRae, G.A., Priestley, M.J.N. (1994). Precast post-tensioned ungrouted concrete beam-column subassemblage tests, *Report No. SSRP-94/10*, Department of Applied Mechanics and Engineering Sciences, University of California at San Diego, La Jolla, CA.

Mahin, S.A., Williams, M.E. (1980). Computer controlled seismic performance testing, *Dynamic Response of Structures: Experimentation, Observation, Prediction and Control*, American Society of Civil Engineers, New York, NY.

Makris, N., Roussos, Y. (1998). Rocking response and overturning of equipment under horizontal-type pulses, *PEER Report No. 1998/05*, Pacific Earthquake Engineering Research Center, University of California, Berkeley, CA.

Mander, J.B., Cheng, C.-T. (1997). Seismic resistance of bridge piers based on damage avoidance design, *Technical Report NCEER-97-0014*, NCEER, Department of Civil and Environmental Engineering, State University of New York at Buffalo, Buffalo, NY.

Maroney, B.H. (1995). *Large Scale Abutment Tests to Determine Stiffness and Ultimate Strength Under Seismic Loading*, PhD Dissertation, University of California, Davis, CA.

Maroney, B.H., Chai, Y.H. (1994). Seismic design and retrofitting of reinforced concrete bridges, *2nd International Workshop*, Earthquake Commission of New Zealand, Queenstown.

Marriott, D., Pampanin, S., Palermo, A. (2009). Quasi-static and pseudo-dynamic testing of unbonded post-tensioned rocking bridge piers with external replaceable dissipaters, *Earthquake Engineering & Structural Dynamics*, 38(3): 331-354.

Marriott, D., Pampanin, S., Palermo, A. (2011). Biaxial testing of unbonded post-tensioned rocking bridge piers with external replaceable dissipaters, *Earthquake Engineering & Structural Dynamics*, 40(15): 1723-1741.

MathWorks, Inc. (2015). *MATLAB Release 2015b*, The MathWorks, Inc., Natick, MA.

MathWorks, Inc. (2018). *MATLAB Release 2018b*, The MathWorks, Inc., Natick, MA.

McKenna, F., Fenves, G.L., Scott, M.H., Jeremic, B. (2000). *Open System for Earthquake Engineering Simulation (OpenSees)*, University of California, Berkeley, CA.

Mercan, O., Ricles, J.M. (2007). Stability and accuracy analysis of outer loop dynamics in real-time pseudodynamic testing of SDOF systems, *Earthquake Engineering & Structural Dynamics*, 36(11): 1523-1543.

Moehle, J. (2014). *Seismic Design of Reinforced Concrete Buildings*, McGraw-Hill Education, New York, NY.

Mosalam, K.M,, Günay, S. (2013). Hybrid simulations: theory, applications, and future directions, *Advanced Materials Research*, Vols. 639-640: 67-95.

Mosalam, K.M., Günay, S. (2014). Seismic performance evaluation of high voltage disconnect switches using real-time hybrid simulation: Part I: system development and validation, *Earthquake Engineering & Structural Dynamics*, 43(8): 1205-1222.

Mosalam, K., Kumar, P., Günay, S. (2013). Experimental investigation to assess the effectiveness of CFRP jacket repair of RC column with construction flaw, *Proceedings, 7th National Seismic Conference on Bridges and Highways*, Oakland, CA.

Mosqueda, G., Cortes-Delgado, M.D., Wang, T., Nakashima, M. (2010). Substructuring techniques for hybrid simulation of complex structural systems, *Proceedings, 9th U.S. National and 10th Canadian Conference on Earthquake Engineering*, Toronto.

Moustafa, M.A. (2015). Structural behavior of column-bent cap beam-box girder systems in reinforced concrete bridges subjected to gravity and seismic loads: Part II: hybrid simulation and post-test analysis, *PEER Report No. 2015/10*, Pacific Earthquake Engineering Research Center, University of California, Berkeley, CA.

Nakaki, S.D., Stanton, J.F., Sritharan, S. (1999). An overview of the PRESSS five-story precast test building, Precast/Prestressed Concrete Institute, *PCI Journal*, 44(2): 26-39.

Nakashima, M., Kaminosono, T., Ishida, I., Ando, K. (1990). Integration techniques for substructure pseudo dynamic test, *Proceedings, 4th U.S. National Conference on Earthquake Engineering*, Earthquake Engineering Research Institute, Palm Springs, CA.

Nakashima, M., Kato, M., Takaoka, E. (1992). Development of real-time pseudo-dynamic testing, *Earthquake Engineering & Structural Dynamics*, 21(1): 79-92.

Nakashima, M., Masaoka, N. (1999). Real-time on-line test for MDOF systems, *Earthquake Engineering & Structural Dynamics*, 28: 393-420.

Nema, A. (2018). *Development of Low Seismic Damage Structural Systems*, PhD Dissertation, University of California, San Diego, CA.

Nema, A., Restrepo, J.I. (2020). Resilient columns for accelerated bridge construction, *PEER Report*, Pacific Earthquake Engineering Research Center, University of California, Berkeley, In Preparation.

Ou, Y.-C., Chiewanichakorn, M., Ahn, I.-S., Aref, A.J., Chen, S.S., Filiatrault, A., Lee, G.C. (2006). Cyclic performance of precast concrete segmental bridge columns: simplified analytical and finite element studies, *Transportation Research Record: Journal of the Transportation Research Board*, 1976: 66-74.

Palermo, A., Pampanin, S., Calvi, G.M. (2005). Concept and development of hybrid solutions for seismic resistant bridge systems, *Journal of Earthquake Engineering*, 9(6): 899-921.

Palermo, A., Pampanin, S. (2008). Enhanced seismic performance of hybrid bridge systems: comparison with traditional monolithic solutions, *Journal of Earthquake Engineering*, 12(8): 1267-1295.

Pérez, F.J., Pessiki, S., Sause, R., Lu, L.-W. (2003). Lateral load tests of unbonded post-tensioned precast concrete walls, *Special Publication of Large-Scale Structural Testing, Paper No. SP 211-8*, American Concrete Institute, pp. 161-182, Detroit, MI.

Porter, D.M., Cherif, Z.E. (1987). *Ultimate Shear Strength of Thin Webbed Steel and Concrete Composite Girders*, Elsevier Applied Science Publishers, pp. 55-64.

Priestley, M.J.N., Sritharan, S., Conley, J.R., Pampanin, S. (1999). Preliminary results and conclusions from the PRESSS five-story precast concrete test building, Precast/Prestressed Concrete Institute, *PCI Journal*, 44(6): 42-67.

Priestley, M.J.N., Tao, J.R.T. (1993). Seismic response of precast prestressed concrete frames with partially debonded tendons, Precast/Prestressed Concrete Institute, *PCI Journal*, 38(1): 58-69.

Restrepo, J.I., Rahman, A. (2007). Seismic performance of self-centering structural walls incorporating energy dissipators, ASCE, *Journal of Structural Engineering*, 133(11): 1560-1570.

Sakai, J., Mahin, S.A. (2004). Analytical investigations of new methods for reducing residual displacements of reinforced concrete bridge column, *PEER Report No. 2004/02*, Pacific Earthquake Engineering Research Center, University of California, Berkeley, CA.

Schellenberg, A.H., Mahin S.A., Fenves G.L. (2009). Advanced implementation of hybrid simulation, *PEER Report No. 2009/104*, Pacific Earthquake Engineering Research Center, University of California, Berkeley, CA.

Schellenberg, A.H., Becker, T.C., Mahin, S.A. (2017). Hybrid shake table testing method: theory, implementation and application to midlevel isolation, *Structural Control and Health Monitoring*, 24(5): e1915.

Schoettler, M.J., Eberhard, M.O., Mahin, S.A., Mosalam, K.M., Ostertag, C.P., Panagiotou, M., Restrepo, J.I., Stanton, J.F., Terzic, V. (2013). Advancing the performance of bridge columns: Overview of a shake table test program, *Proceedings, 7th National Seismic Conference on Bridges and Highways*, Oakland, CA.

Seyed Ardakani, S.M. (2013). *Design of Reinforced Concrete Bridge Columns for Near-Fault Earthquakes*, PhD Dissertation, University of Nevada, Reno, NV.

Shamsabadi, A., Khalili-Tehrani, P., Stewart, J.P., Taciroglu, E. (2010). Validated simulation models for lateral response of bridge abutments with typical backfills, ASCE, *Journal of Bridge Engineering*, 15(3): 302-311.

Shamsabadi, A., Rollins, K.M., Kapuskar, M. (2007). Nonlinear soil-abutment-bridge structure interaction for seismic performance-based design, ASCE, *Journal of Geotechnical and Geoenvironmental Engineering*, 133(6): 707-720.

Sharpe, R.D., Skinner, R.I. (1983). The seismic design of an industrial chimney with rocking base, *Bulletin of the New Zealand National Society for Earthquake Engineering*, 16(2): 98-106.

Shing, P.B., Vannan, M.T., Cater, E. (1991). Implicit time integration for pseudodynamic tests, *Earthquake Engineering & Structural Dynamics*, 20(6): 551-576.

Shing, P.B., Mahin, S.A. (1983). Experimental error propagation in pseudodynamic testing, *Report No. UCB/EERC-83/12*, Earthquake Engineering Research Center, University of California, Berkeley.

Spacone, E., Filippou, F.C., Taucer, F.F. (1996). Fiber beam-column model for non-linear analysis of R/C frames: Part I: formulation, *Earthquake Engineering & Structural Dynamics*, 25(7): 711-725.

Stewart, J.P., Wallace, J.W., Taciroglu, E., Ahlberg, E.R., Lemnitzer, A., Rha, C., Tehrani, P.K., Keowen, S., Nigbor, R.L., Salamanca, A. (2007). Full scale cyclic testing of foundation support systems for highway bridges: Part II: abutment backwalls, *Report No. UCLA SGEL 2007/02*, Department of Civil and Environmental Engineering, University of California, Los Angeles, CA.

Stojadinovic, B., Mosqueda, G., Mahin, S.A. (2006). Event-driven control system for geographically distributed hybrid simulation, ASCE, *Journal of Structural Engineering*, 132(1): 68-77.

Stone, W.C., Cheok, G.S., Stanton, J.F. (1995). Performance of hybrid moment-resisting precast beam-column concrete connections subjected to cyclic loading, American Concrete Institute, *ACI Structural Journal*, 91(2): 229-249.

Takanashi, K., Udagawa, K., Seki, M., Okada, T., Tanaka, H. (1975). Nonlinear earthquake response analysis of structures by computer-actuator on-line system, *Bulletin of Earthquake Resistant Structure Research Center*, Institute of Industrial Science, University of Tokyo, Japan.

Takhirov, S.M. (2010). Laser scanners in structural assessment and finite element modeling, *Proceedings, Structures Congress 2010*, Orlando, Florida.

Terzic, V., Stojadinovic, B. (2013). Hybrid simulation of bridge response to three-dimensional earthquake excitation followed by truck load, ASCE, *Journal of Structural Engineering*, 140(8), A4014010.

Thewalt, C.R., Mahin, S.A. (1987). Hybrid solution technique for generalized pseudodynamic testing, *Report No. UCB/EERC-87/09*, Earthquake Engineering Research Center, University of California, Berkeley, CA.

Toranzo, L.A., Restrepo, J.I., Mander, J.B., Carr, A.J. (2009). Shake-table tests of confined-masonry rocking walls with supplementary hysteretic damping, *Journal of Earthquake Engineering*, 13(6): 882-898.

Trono, W., Jen, G., Ostertag, C.P., Panagiotou, M. (2013). Tested and modeled seismic response of a rocking, post-tensioned HyFRC bridge column, *Proceedings, 7th National Seismic Conference on Bridges and Highways*, Oakland, CA.

Whyte, C.A. and Stojadinovic, B. (2013). Effect of ground motion sequence on response of squat reinforced concrete shear walls, ASCE, *Journal of Structural Engineering*, 140(8), A4014004.

Wilson, J.C., Tan, B.S. (1990). Bridge abutments: formulation of simple model for earthquake response analysis, ASCE, *Journal of Engineering Mechanics*, 116(8): 1828-1837.

Zayas, V.A., Low, S.S., Mahin, S.A. (1987). The FPS earthquake resisting system: experimental report, *Report No. UCB/EERC-87/01*, Earthquake Engineering Research Center, University of California, Berkeley, CA.

APPENDIX A: V-connector's Rigid Blocks Design

A.1 DESIGN FORCES

From the results of the pre-test analysis (section 4.1.3.3) with K_v = 30 kips/in. and F_0 = 200 kips, the force demand on the V-connector (before and after proper scaling with length scale factor S_L = 3.0) is summarized in Table A.1. Therefore, the top and bottom block should be designed to be able to resist axial force P = 220.7 kips and shear force V = 80.4 kips. More importantly, to make sure that the rigid assumption of the top and bottom block is valid, elastic design approach for the blocks should be adopted without utilizing their ultimate capacities.

Table A.1 Design shear and axial forces.

Condition	Axial force P [kip]	Shear force V [kip]
Before scaling	1986.4	723.7
After scaling	220.7	80.4

A.2 MATERIAL PROPERTIES

A.2.1 Concrete

Concrete compressive strength: $f_c^{'}$ = 5 ksi

Concrete elastic modulus: $E_c = 57000\sqrt{f_c^{'}}$ = 4030 ksi

A.2.2 Reinforcing Steel

Reinforcing steel yield strength: f_y = 60 ksi

Reinforcing steel elastic modulus: E_s = 29000 ksi

A.3 SHEAR DESIGN AND CHECK

A.3.1 Design Dimensions

According to ACI 318 (2011) section 11.1.1, design of cross sections subjected to shear shall be based on:

$$\phi V_n \geq V_u \tag{A.1}$$

where V_u is the factored shear force at the section considered and V_n is the nominal shear force capacity computed by:

$$V_n = V_c + V_s \tag{A.2}$$

Based on ACI 318 (2011) section 11.2.1.2, for members subject to axial compression:

$$\begin{aligned} V_c &= 2\left(1 + \frac{N_u}{2000A_g}\right)\lambda\sqrt{f_c'}b_w d \\ V_s &= \frac{A_v f_{yt} d}{s} \end{aligned} \tag{A.3}$$

Here, to be on the conservative side, V_u was taken to be $1.25 \times V = 100$ kips. The contribution from the transverse reinforcement was neglected and N_u was set to zero. Assuming the cross section for the shear resistance to be square leading to:

$$\begin{aligned} \phi V_n = \phi V_c = \phi \times 2\lambda \times \sqrt{f_c'}b_w d \approx 0.75 \times 2 \times \sqrt{5000} \times {b_w}^2 \geq V_u = 100 \text{ kips} \\ \Rightarrow b_w \geq 30.7 \text{ in.} \end{aligned} \tag{A.4}$$

Based on the laboratory setup, the cross section of the top block was chosen to be 45 in. by 45 in. and the bottom block to be 81 in. by 46 in. Obviously, these dimensions are far more than sufficient. The reinforcement design and check were based on these dimensions.

A.3.2 Shear Reinforcement

Shear Reinforcement Requirement

According to ACI 318 (2011) section 7.10.5.1, all nonprestressed bars shall be enclosed by transverse ties, at least No. 3 in size for longitudinal bars No. 10 or smaller, and at least No. 4 in size for No. 11, No. 14, No. 18, and bundled longitudinal bars. According to ACI 318 (2011) section 7.10.5.2, vertical spacing of ties shall not exceed 16 longitudinal bar diameters, 48 tie bar or wire diameters, or least dimension of the compression member. According to ACI 318 (2011) section 7.10.5.3, rectilinear ties shall be arranged such that every corner and alternate longitudinal bar shall have lateral support provided by the corner of a tie with an included angle of not more than 135° and no bar shall be farther than 6 in. clear on each side along the tie from such a laterally supported bar. According to ACI 318 (2011) section 11.4.5.1, spacing of shear reinforcement placed perpendicular to the axis of the member shall not exceed $d/2$ in nonprestressed members or $0.75h$ in prestressed members, nor 24 in. The shear reinforcement design satisfying all the abovementioned requirements is given below in Figure A.1 and Figure A.2.

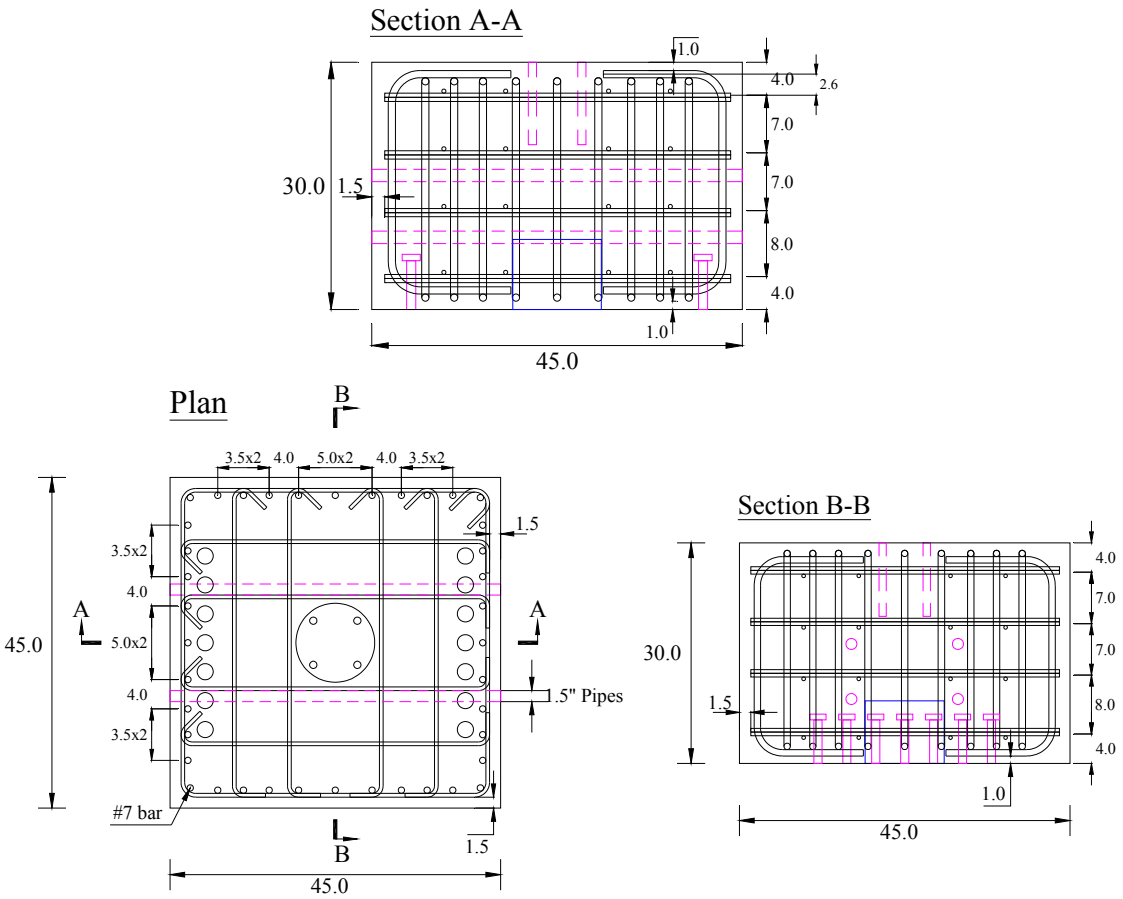

Figure A.1 Top block shear reinforcement design.

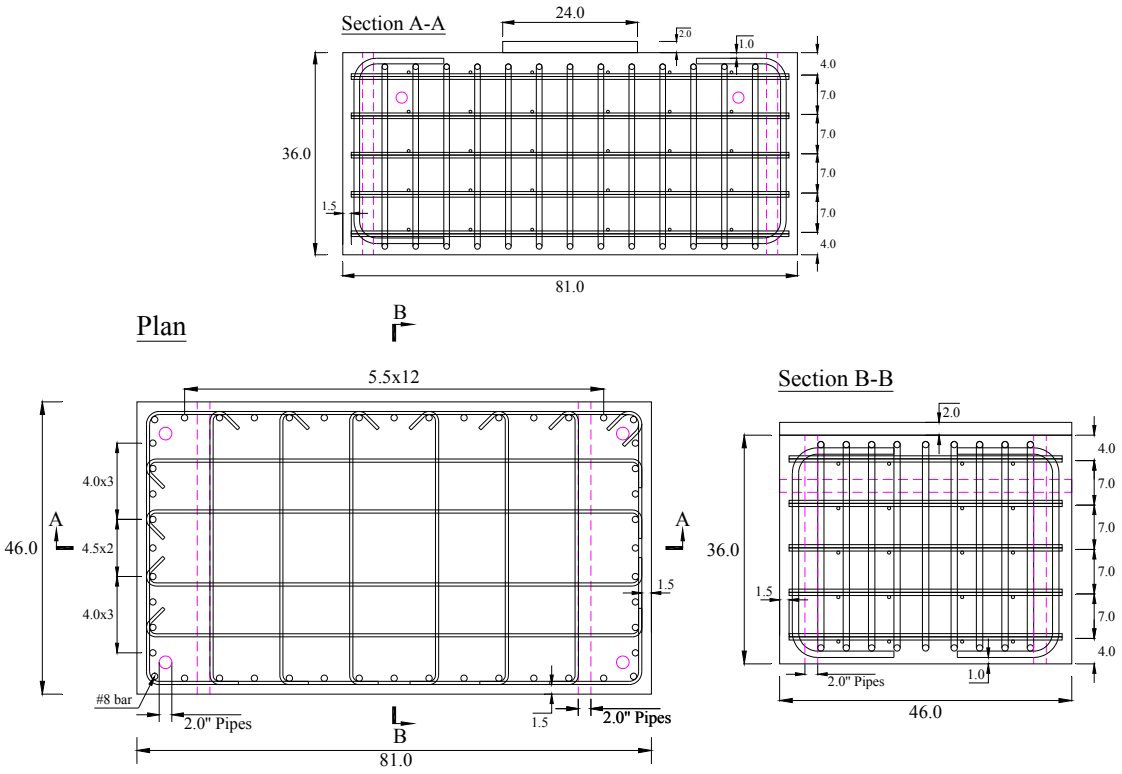

Figure A.2 Bottom block shear reinforcement design.

Shear Reinforcement Amount

Based on previous calculations, only minimum amount of shear reinforcement needs to be provided. According to ACI 318 (2011) section 11.4.6, $A_{v,\min}$ for prestressed and nonprestressed members shall be computed by Equation (A.5), but shall not be less than $(50b_w s)/f_{yt}$.

$$A_{v,\min} = 0.75\sqrt{f'_c}\frac{b_w s}{f_{yt}} \qquad \text{(A.5)}$$

For the case at hand, the top block:

$$A_v = 6 \times A_{\#4} = 6 \times 0.2 = 1.2 \text{ in}^2 > A_{v,\min}$$

$$= 0.75\sqrt{f'_c}\frac{b_w s}{f_{yt}} = \frac{0.75 \times \sqrt{5000} \times 45 \times 8}{1000 \times 60} = 0.318 \text{ in}^2 \Rightarrow OK.$$

$$A_v = 6 \times A_{\#4} = 6 \times 0.2 = 1.2 \text{ in}^2 > (50b_w s)/f_{yt} = \frac{50 \times 45 \times 8}{60000} = 0.3 \text{ in}^2 \Rightarrow OK.$$

The bottom block:

$$A_{v1} = 8 \times A_{\#4} = 8 \times 0.2 = 1.6 \text{ in}^2 > A_{v1,\min}$$

$$= 0.75\sqrt{f'_c}\frac{b_{w1} s}{f_{yt}} = \frac{0.75 \times \sqrt{5000} \times 81 \times 7}{1000 \times 60} = 0.5 \text{ in}^2 \Rightarrow OK.$$

$$A_{v1} = 8 \times A_{\#4} = 8 \times 0.2 = 1.6 \text{ in}^2 > (50 b_{w1} s)/f_{yt} = \frac{50 \times 81 \times 7}{60000} = 0.4725 \text{ in}^2 \Rightarrow OK.$$

$$A_{v2} = 6 \times A_{\#4} = 6 \times 0.2 = 1.2 \text{ in}^2 > A_{v2,\min}$$
$$= 0.75\sqrt{f_c'}\frac{b_{w2}s}{f_{yt}} = \frac{0.75 \times \sqrt{5000} \times 46 \times 7}{1000 \times 60} = 0.285 \text{ in}^2 \Rightarrow OK.$$

$$A_{v2} = 6 \times A_{\#4} = 6 \times 0.2 = 1.2 \text{ in}^2 > (50 b_{w2} s)/f_{yt} = \frac{50 \times 46 \times 7}{60000} = 0.268 \text{ in}^2 \Rightarrow OK.$$

To achieve ductile response of an axially loaded column, the rectilinear hoop-confined compression member should also satisfy:

$$\min\left(\frac{A_{sh2}f_{yt}}{b_{c3}s}, \frac{A_{sh3}f_{yt}}{b_{c2}s}\right) \geq 0.3\left(\frac{A_g}{A_{ch}} - 1\right)f_c' \tag{A.6}$$

Assume concrete clear cover to be 1.5 in. For the top block:

$$\min\left(\frac{A_{sh2}f_{yt}}{b_{c3}s}, \frac{A_{sh3}f_{yt}}{b_{c2}s}\right) = \frac{1.2 \times 60}{42 \times 8} = 0.214$$
$$< 0.3\left(\frac{A_g}{A_{ch}} - 1\right)f_c' = 0.3 \times \left(\frac{45^2}{41.5^2} - 1\right) \times 5 = 0.264 \Rightarrow \textit{not OK}.$$

For the bottom block:

$$\min\left(\frac{A_{sh2}f_{yt}}{b_{c3}s}, \frac{A_{sh3}f_{yt}}{b_{c2}s}\right) = \min\left(\frac{1.2 \times 60}{43 \times 7}, \frac{1.6 \times 60}{78 \times 7}\right) = 0.176$$
$$< 0.3\left(\frac{A_g}{A_{ch}} - 1\right)f_c' = 0.3 \times \left(\frac{81 \times 46}{77.5 \times 42.5} - 1\right) \times 5 = 0.197 \Rightarrow \textit{not OK}.$$

Although the proposed design does not meet the ductility requirement for axially loaded members, here the situation is different because the design goal is to keep the blocks elastic without utilizing any of the ductility capacities. Therefore, it is *OK* to accept the above design and move on to the next design step.

A.4 AXIAL DESIGN

A.4.1 Dimension Check

To proceed with the axial design, the cross-sectional dimension 45 in. by 45 in. for the top block and 81 in. by 46 in. for the bottom block obtained from the shear design were used. As stated before, the behavior of the blocks is expected to be in the linear elastic range.

The axial design should satisfy:

$$\phi P_n \geq P_u \tag{A.7}$$

where P_u is the factored axial force at the section considered and P_n is the axial capacity. For linear elastic response, the relationship between axial load and internal stresses can be written as:

$$
\begin{aligned}
P_n &= (A_g - A_{st})f_c' + A_{st}f_s \\
&= (A_g - A_{st})\varepsilon E_c + A_{st}\varepsilon E_s \\
&= \varepsilon E_c\left[(A_g - A_{st}) + nA_{st}\right] \\
&= f_c'\left[A_g + (n-1)A_{st}\right] \\
n &= \frac{E_s}{E_c} = \frac{29000}{4030} = 7.2
\end{aligned}
$$

To be on the conservative side, take $P_u = 1.25P = 1.25 \times 220.7 = 276$ kips and ignore the contribution from the longitudinal reinforcement. In addition, set $f_c' = 3$ ksi in calculating the axial capacity and the strength reduction factor ϕ to be 0.5 instead of 0.9. Based on all these assumptions, for the top block:

$$\phi P_n = \phi A_g f_c' = 0.5 \times 45^2 \times 3 = 3037.5 \text{ kips} \gg P_u = 276 \text{ kips}, \textit{OK}.$$

The bottom block is also *OK*, which is obvious because of its larger dimensions.

A.4.2 Longitudinal Reinforcement

It was proposed to use 40 #7 longitudinal bars with proper bending, resulting in the total area of longitudinal reinforcement to be $A_{st} = 40 \times 0.6 = 24$ in^2 for the top block, and 48 #8 ($A_{st} = 37.92$ in^2) for the bottom block. The cross sections are shown below in Figure A.3.

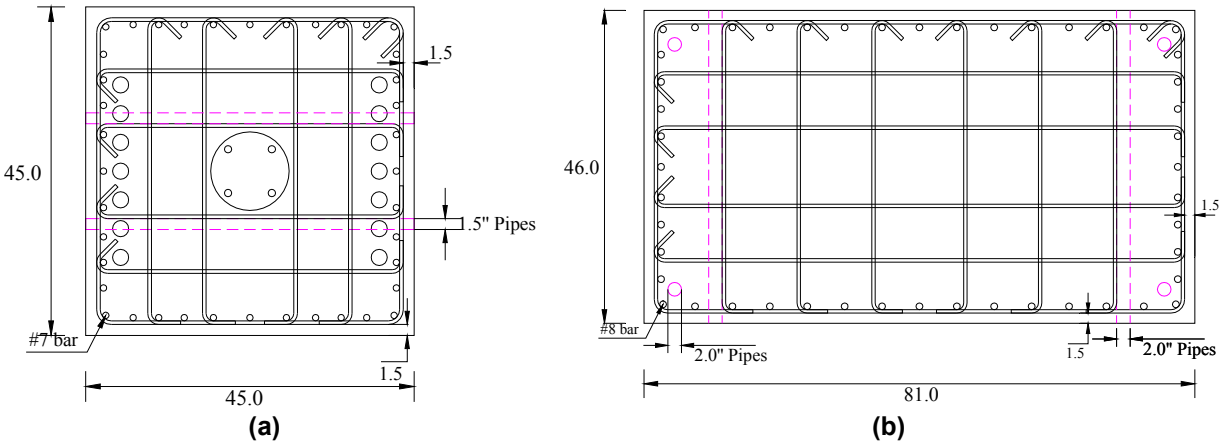

Figure A.3 Longitudinal reinforcement design for (a) top block; and (b) bottom block.

Longitudinal Reinforcement Amount

According to ACI 318 (2011) section 10.9.1, area of longitudinal reinforcement A_{st} for non-composite compression members shall be not less than $0.01A_g$ or more than $0.08A_g$.

For the case at hand, the top block:

$$0.01A_g = 20.25 \text{ in}^2 < 24 \text{ in}^2 < 0.08A_g = 162 \text{ in}^2 \Rightarrow \textit{OK}.$$

The bottom block:

$$0.01A_g = 37.26 \text{ in}^2 < 37.92 \text{ in}^2 < 0.08A_g = 298.1 \text{ in}^2 \Rightarrow OK.$$

According to ACI 318 (2011) section 10.9.2, the minimum number of longitudinal bars in compression members shall be 4 for bars within rectangular or circular ties. This requirement is clearly satisfied for the proposed design.

Longitudinal Reinforcement Requirement

According to ACI 318 (2011) section 7.6.1, the minimum clear spacing between parallel bars in a layer shall be d_b, but not less than 1 in. According to ACI 318 (2011) section 7.6.3, in spirally reinforced or tied reinforced compression members, clear distance between longitudinal bars shall be not less than $1.5d_b$ nor less than 1-1/2 in. It is clear that the proposed design satisfies these two requirements.

A.5 REINFORCEMENT DETAILING CHECK

A.5.1 Standard Hooks

According to ACI 318 (2011) section 7.1.2, standard hooks should satisfy 90° bend plus $12d_b$ extension at the free end of the bar. According to ACI 318 (2011) section 7.1.3 (a), stirrup and tie hooks using No. 5 bar and smaller should satisfy 90° bend plus $6d_b$ extension at the free end of the bar. According to ACI 318 (2011) section 7.1.3 (c), stirrup and tie hooks using No. 8 bar and smaller should satisfy 135° bend plus $6d_b$ extension at the free end of the bar. From the detailed drawing of the longitudinal and transverse reinforcement shown in Figure A.4 and Figure A.5, these requirements are clearly satisfied.

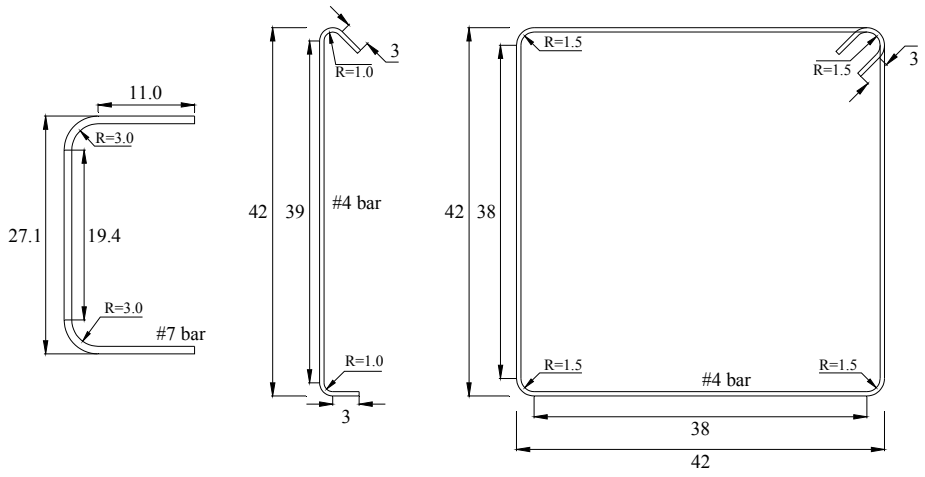

Figure A.4 Top block reinforcement detailing.

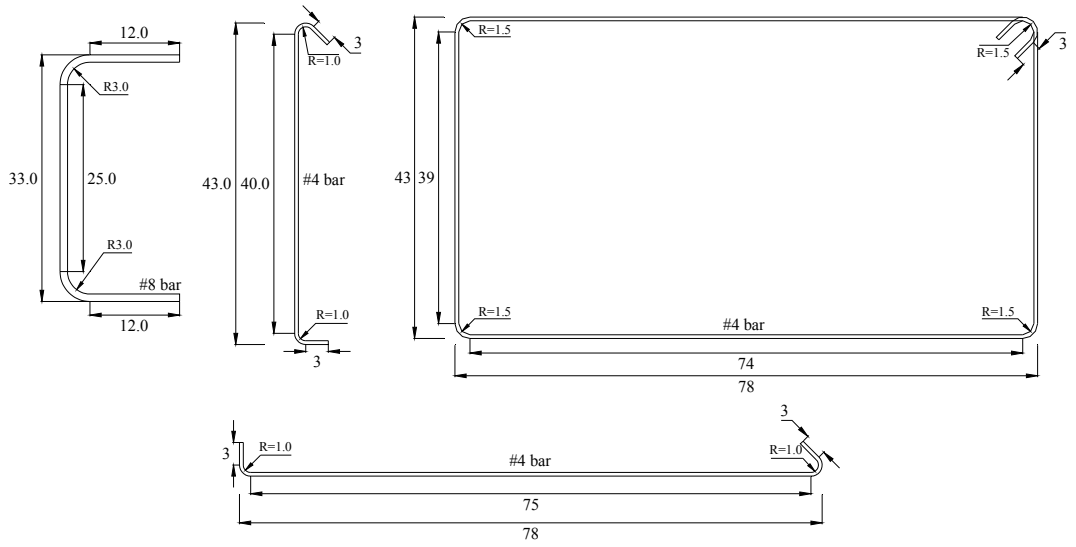

Figure A.5 Bottom block reinforcement detailing.

A.5.2 Minimum Bending Diameters

According to ACI 318 (2011) section 7.2.1, for No. 3 through No. 8 bars, the diameter of bending measured on the inside of the bar shall not be less than $6d_b$. According to ACI 318 (2011) section 7.2.2, inside diameter of bending for stirrups and ties shall not be less than $4d_b$ for No. 5 bars and smaller. From Figure A.4 and Figure A.5 above, these requirements are clearly satisfied.

A.6 DEMAND TO CAPACITY RATIO (DCR)

A.6.1 Axial DCR

Based on section A.1, the axial force demand P is 220.7 kips. To calculate the ultimate axial capacity of the proposed design, the hollow portion in the top block used to place the top hinge of the V-connector was not considered and the concrete net section was used. The net section area was given by:

$$A_n \approx 45^2 - 11^2 = 1904 \text{ in}^2$$

The axial strength at the onset of spalling can be calculated as:

$$\begin{aligned} P_0 &= 0.85f_c'(A_n - A_{st}) + A_{st}f_y \\ &= 0.85 \times 5 \times (1904 - 24) + 24 \times 60 = 9430 \text{ kips} \end{aligned}$$

The post-spalling strength can be calculated as:

$$\begin{aligned} P_{00} &= f_{cc}'(A_{ch} - A_{st}) + \eta A_{st}f_y \\ &= 4.9 \times (41.5^2 - 11^2 - 24) + 0.5 \times 24 \times 60 = 8448.5 \text{ kips} \end{aligned}$$

where

$$f'_{cc} = 0.85f'_c + 4.1f_{e\min} = 0.85 \times 5 + 4.1 \times 0.158 = 4.9 \text{ ksi}$$

$$f_{e\min} = k_e f_{\min 2,3} = \frac{n_l - 2}{n_l}\left(1 - \frac{s}{b_c}\right) \times \frac{f_y A_{sh}}{b_c s} = \frac{20 - 2}{20} \times \left(1 - \frac{8}{41.5}\right) \times \frac{60 \times 6 \times 0.2}{41.5 \times 8} = 0.158 \text{ ksi}$$

$$\eta = 0.5$$

Take the ultimate capacity $P_n = \min\{P_0, P_{00}\} = 8448.5$ kips. The axial DCR is given as:

$$DCR_{axial} = P/P_n = 220.7/8448.5 = 0.026 \Rightarrow OK.$$

A.6.2 Shear DCR

Similar to section A.6.1, only the concrete net section was considered to calculate the ultimate shear capacity. From section A.1, the shear force demand V is 80.4 kips. The ultimate shear capacity is given by:

$$V_n = V_c + V_s = 275.3 + 389.25 = 664.55 \text{ kips}$$

where

$$V_c = 2\left(1 + \frac{N_u}{2000A_n}\right)\lambda\sqrt{f'_c}\,b_w d$$

$$= 2 \times \left(1 + \frac{220.7}{2000 \times (45^2 - 11^2)}\right) \times \frac{\sqrt{5000}}{1000} \times 45 \times 43.25 = 275.3 \text{ kips}$$

$$V_s = \frac{A_v f_{yt} d}{s} = \frac{6 \times 0.2 \times 60 \times 43.25}{8} = 389.25 \text{ kips}$$

Therefore, the shear DCR is given as:

$$DCR_{shear} = V/V_n = 80.4/664.55 = 0.121 \Rightarrow OK.$$

APPENDIX B: Bridge Bent Construction

This appendix illustrates the two stages for constructing the bridge bent, including the construction of the bridge columns and the cap beam/foundation. The two bridge columns used in this study were constructed together with those used in the shaking table test by a professional construction company located in the city of Richmond and then delivered to the laboratory, while the construction of the cap beam and the foundation was all conducted making use of the help of some intern students and the laboratory technicians.

B.1 COLUMN CONSTRUCTION

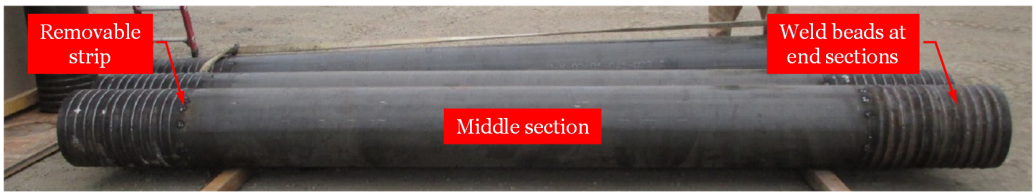

(a)

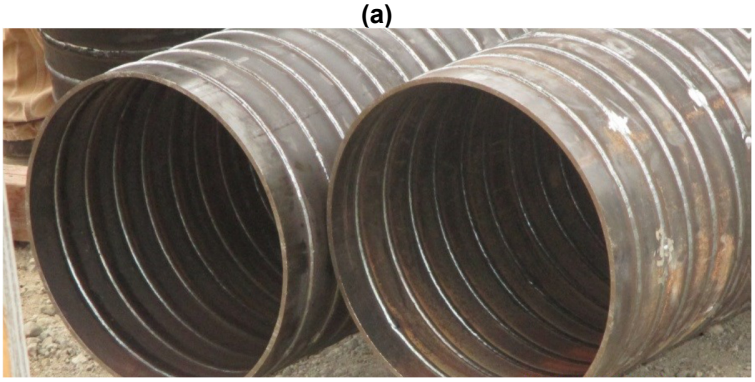

(b)

Figure B.1 (a) Column steel shells; (b) details of weld beads at column ends.

(a)

(b)

Figure B.2 (a) Column reinforcing bar cages; (b) mild steel debonding details.

(a)

(b)

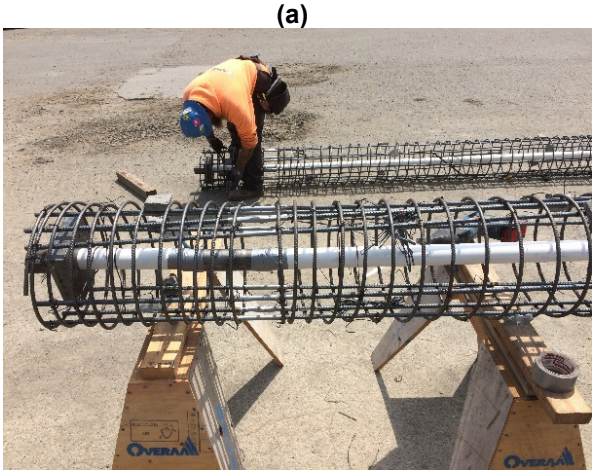

(c)

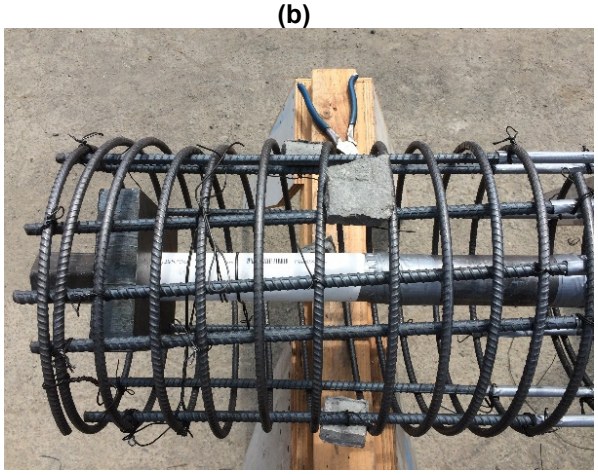

(d)

Figure B.3 (a) Insert the PVC pipe used to debond the PT bar; (b) slide the tape-wrapped PT bar into the PVC pipe; (c) install the PT bar anchorage system at the column end; and (d) PT bar anchorage details.

(a) (b)

Figure B.4 Concrete placing setup: (a) erect the column steel shells as the permanent formwork; (b) column reinforcing bar cages installation.

(a) (b)

Figure B.5 (a) Cast the concrete; (b) final completed columns.

B.2 FOUNDATION/CAP BEAM CONSTRUCTION

Figure B.6 Different stages of foundation reinforcing bar cage construction.

Figure B.7 Cap beam reinforcing bar cage detailing.

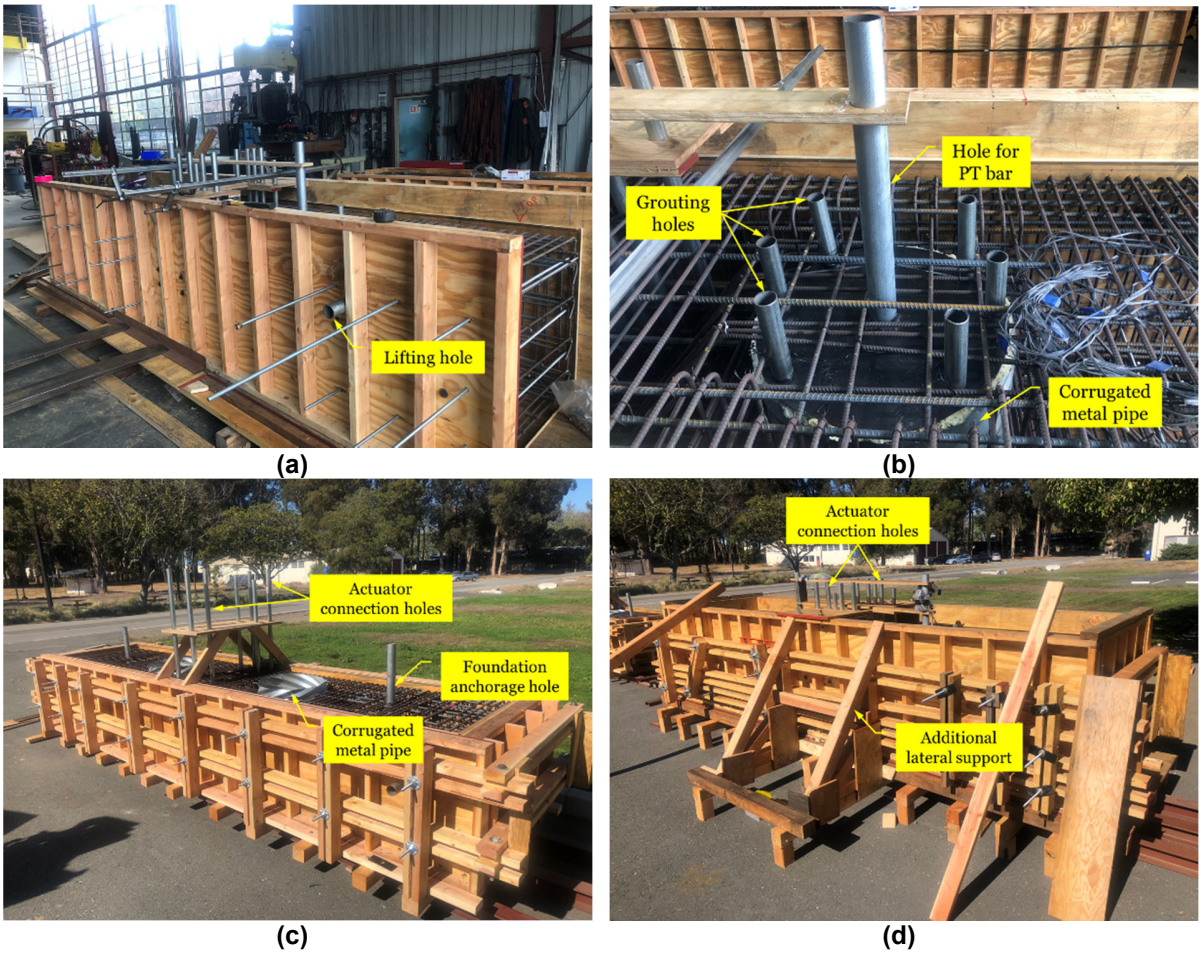

Figure B.8 (a) Reinforcing bar cage in the formwork; (b) holes preparation for cap beam grouting and PT bars; (c) finished foundation reinforcing bar cage and formwork before concrete placing; and (d) finished cap beam reinforcing bar cage and formwork before concrete placing.

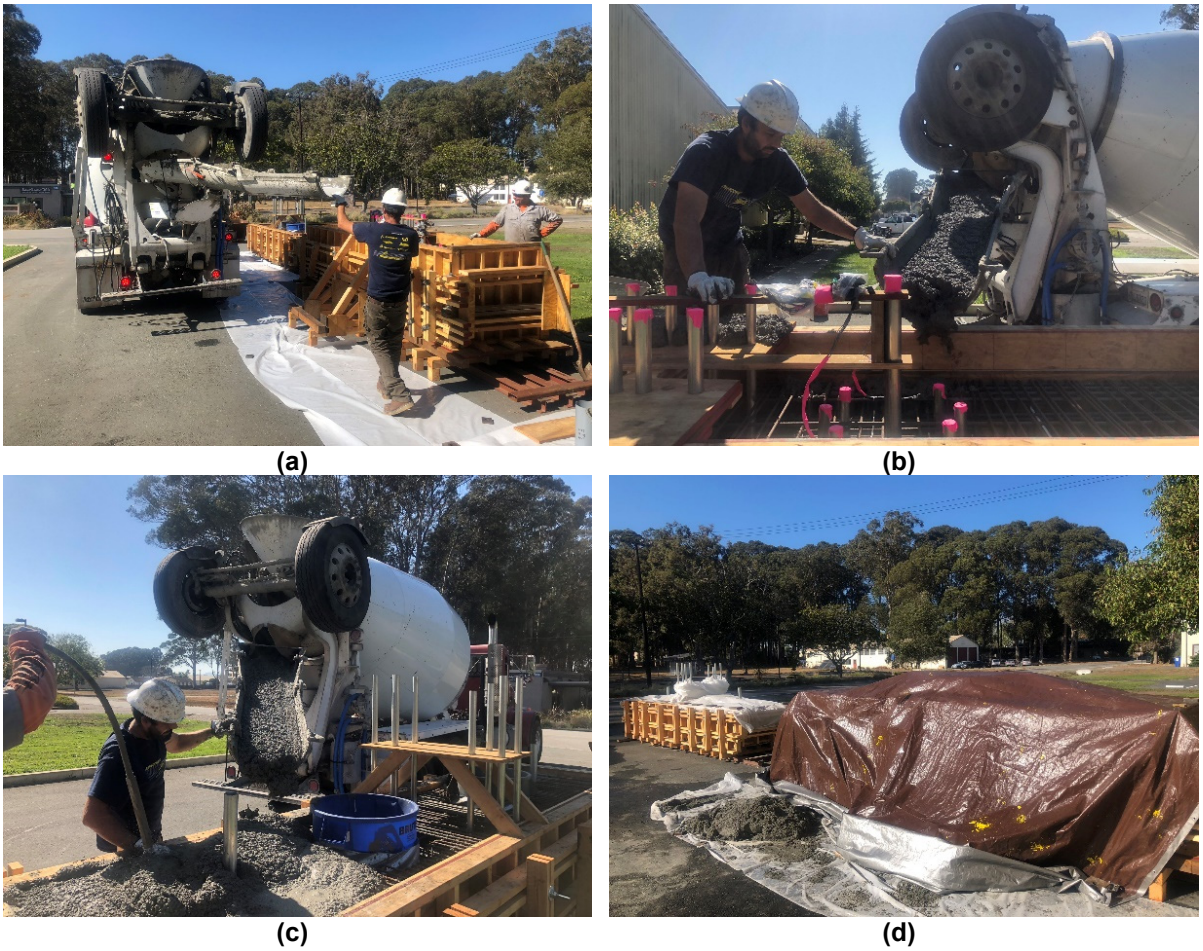

Figure B.9 (a) Preparation prior to concrete placing; (b) cap beam concrete casting; (c) foundation concrete casting; and (d) curing blankets in addition to the E-CURE to avoid shrinkage cracks.

Figure B.10 Remove the formwork.

(a) (b)

Figure B.11 Finished (a) cap beam; and (b) foundation after all formwork removal.

APPENDIX C: Bridge Bent Assembly and Test Setup

Figure C.1 to Figure C.14 illustrate different stages and phases for setting up the two-column bridge bent subassembly at the PEER Earthquake Simulation Laboratory located in Richmond Field Station.

(a) (b)

Figure C.1 **(a) Prepare the surface and seal the holes in the supporting anchor beam; (b) lift up and install the foundation in place using the overhead crane.**

(a) (b) (c)

Figure C.2 (a) Mix the hydro-stone; (b) place the hydro-stone through corrugated metal pipes; and (c) prestress the foundation to the supporting beam.

Figure C.3 Remove the 0.25 in. steel strips at the column rocking interfaces.

(a) (b) (c)

Figure C.4 (a) Pick up the column; (b) install and level the column; and (c) install the vertical actuator between the two columns.

Figure C.5 Foundation sockets grouting.

(a)

(b)

Figure C.6 (a) Prepare the end connection plates for the cap beam; (b) install, grout and prestress the end connection plates to the cap beam.

(a)

(b)

Figure C.7 (a) Install the cap beam and set up temporary wood frame support; (b) seal the cap beam sockets from the bottom.

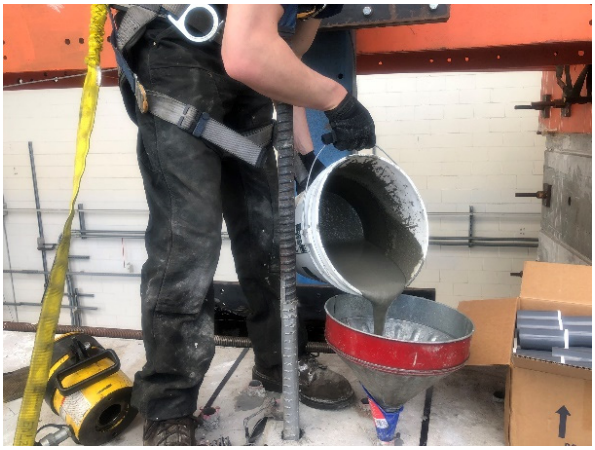

(a)

(b)

Figure C.8 (a) Place the grout from the top grouting holes; (b) wait for the grout to dry and remove the wood sealing panel.

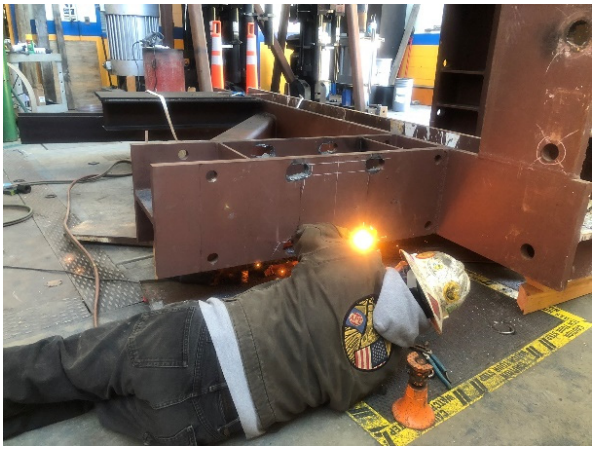

(a)

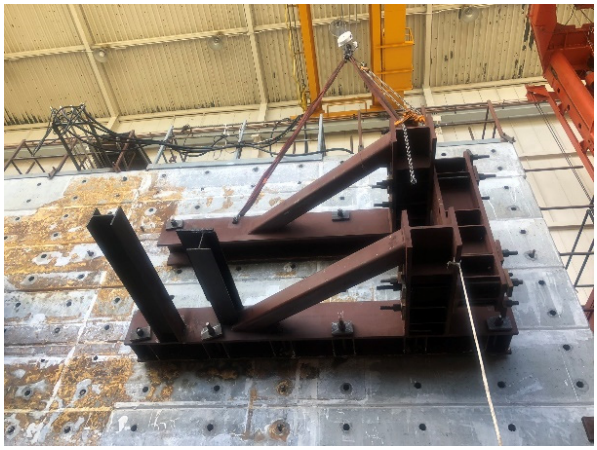

(b)

(c)

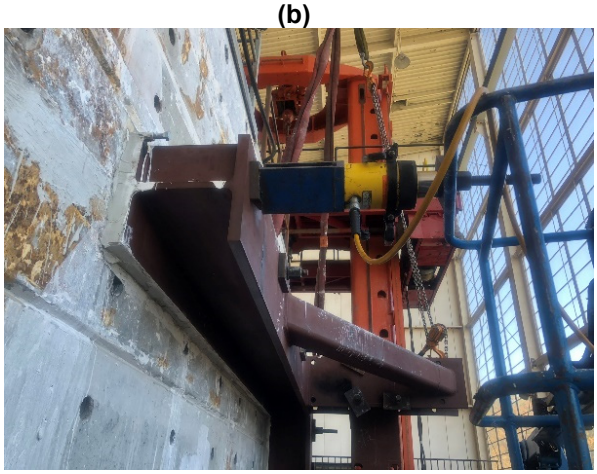

(d)

Figure C.9 (a) Prepare the horizontal actuator reaction bracket; (b) set the actuator bracket in place; (c) grout between the actuator bracket and the reaction wall; and (d) prestress the actuator bracket to the reaction wall.

(a)

(b)

Figure C.10 (a) T-beam to be welded to the embedded steel plates inside the cap beam for lateral support; (b) clamps for the T-beam to slide on.

(a)

(b)

Figure C.11 (a) Lift up and install the horizontal actuator; (b) extend the horizontal actuator and weld the connection plate to the cap beam end plate.

(a)

(b)

Figure C.12 **(a) Install additional spacer plates to fill the gap between the vertical actuator and the cap beam; (b) extend the vertical actuator, grout the vertical actuator to the cap beam and install the vertical actuator connection rods.**

(a)

(b)

Figure C.13 **(a) Top view of the vertical actuator connection rods; (b) set up the prestressing jacks and prestress the PT bars to 40% GUTS.**

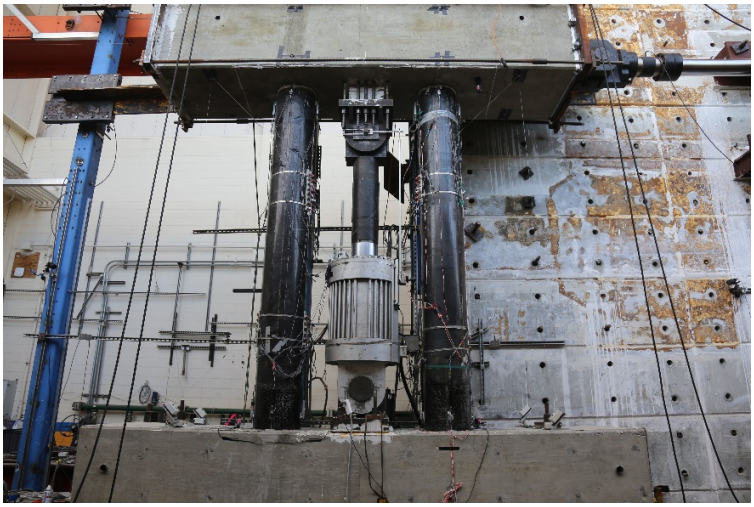

Figure C.14 Completed specimen and test setup.

APPENDIX D: Matlab Function Blocks Implementation

The Matlab (MathWorks, 2015) codes associated with the Matlab function blocks shown in Figure 8.15 and Figure 8.16 from section 8.2.2, is presented in the following.

Matlab code for the resisting force vector calculations

```
function [Pr_prdt, Pr_prdt_next, Usp1_prdt, Usp4_prdt, Usp2_prdt, Usp5_prdt,
Pr1_prdt, Pr4_prdt, Pr2_prdt, Pr5_prdt]
= ResistForce(n, Uprdt, Uprdt_next, K, gap_l, Kabl, Pbwl, Kabt, Pbwt, Kv,
Usp1_prdt_pre, Usp4_prdt_pre, Usp2_prdt_pre, Usp5_prdt_pre, Pr1_prdt_pre,
Pr4_prdt_pre, Pr2_prdt_pre, Pr5_prdt_pre, Prh_spec_prdt, Prh_spec_prdt_next,
Prv_spec_prdt, Prv_spec_prdt_next)
% calculate and assemble the resisting force vector
%
% Inputs: n - bridge deck subdivision number
%         Uprdt - predicted displacement vector at current step i (size: 6(n+1) x
          1)
%         Uprdt_next - predicted displacement vector for all DOFs at next step i+1
          (size: 6(n+1) x 1)
%         K - stiffness matrix of the bridge deck (size: 6(n+1) x 6(n+1))
%         gap_l - longitudinal abutment expansion hinge gap (unit: in)
%         Kabl - longitudinal abutment stiffness (unit: kip/in)
%         Pbwl - longitudinal abutment strength (unit: kip)
%         Kabt - transverse abutment stiffness (unit: kip/in)
%         Pbwt - transverse abutment strength (unit: kip)
%         Kv - stiffness of the flexible bearing pad (unit: kip/in)
%         Usp1_prdt_pre - longitudinal abutment (spring 1) predicted displacement
          at previous step i-1 (scalar)
%         Usp4_prdt_pre - longitudinal abutment (spring 4) predicted displacement
          at previous step i-1 (scalar)
%         Usp2_prdt_pre - transverse abutment (spring 2) predicted displacement at
          previous step i-1 (scalar)
%         Usp5_prdt_pre - transverse abutment (spring 5) predicted displacement at
          previous step i-1 (scalar)
%         Pr1_prdt_pre - spring 1 resisting force corresponding to predicted
          displacement at previous step i-1 (scalar)
%         Pr4_prdt_pre - spring 4 resisting force corresponding to predicted
          displacement at previous step i-1 (scalar)
```

```
%          Pr2_prdt_pre - spring 2 resisting force corresponding to predicted
           displacement at previous step i-1 (scalar)
%          Pr5_prdt_pre - spring 5 resisting force corresponding to predicted
           displacement at previous step i-1 (scalar)
%          Prh_spec_prdt - test specimen horizontal resisting force corresponding
           to predicted displacement at current step i (scalar)
%          Prh_spec_prdt_next - test specimen horizontal resisting force
           corresponding to predicted displacement at next step i+1 (scalar)
%          Prv_spec_prdt - test specimen vertical resisting force corresponding to
           predicted displacement at current step i (scalar)
%          Prv_spec_prdt_next - test specimen vertical resisting force
           corresponding to predicted displacement at next step i+1 (scalar)
%
% Outputs: Pr_prdt - resisting force vector corresponding to predicted
           displacement at current step i (size: 6(n+1) x 1)
%          Pr_prdt_next - resisting force vector corresponding to predicted
           displacement at next step i+1 (size: 6(n+1) x 1)
%          Usp1_prdt - longitudinal abutment (spring 1) predicted displacement at
           current step i (scalar)
%          Usp4_prdt - longitudinal abutment (spring 4) predicted displacement at
           current step i (scalar)
%          Usp2_prdt - transverse abutment (spring 2) predicted displacement at
           current step i (scalar)
%          Usp5_prdt - transverse abutment (spring 5) predicted displacement at
           current step i (scalar)
%          Pr1_prdt - spring 1 resisting force corresponding to predicted
           displacement at current step i (scalar)
%          Pr4_prdt - spring 4 resisting force corresponding to predicted
           displacement at current step i (scalar)
%          Pr2_prdt - spring 2 resisting force corresponding to predicted
           displacement at current step i (scalar)
%          Pr5_prdt - spring 5 resisting force corresponding to predicted
           displacement at current step i (scalar)
%
% written: WYJ 08/2019

%% Current step quantities
Usp1_prdt = Uprdt(1,:);
Usp2_prdt = Uprdt(2,:);
Usp3_prdt = Uprdt(3,:);
Usp4_prdt = Uprdt(6*n+1,:);
Usp5_prdt = Uprdt(6*n+2,:);
Usp6_prdt = Uprdt(6*n+3,:);

%% Next step quantities
Usp1_prdt_next = Uprdt_next(1,:);
Usp2_prdt_next = Uprdt_next(2,:);
Usp3_prdt_next = Uprdt_next(3,:);
Usp4_prdt_next = Uprdt_next(6*n+1,:);
Usp5_prdt_next = Uprdt_next(6*n+2,:);
Usp6_prdt_next = Uprdt_next(6*n+3,:);

%% Resisting forces from end abutments
% end spring 1 resisting force corresponding to predicted displacement at current
step i
if Usp1_prdt >= -gap_l
```

```
    Pr1_prdt = 0;
else
    Pr1_prdt = Pr1_prdt_pre + Kabl*(Usp1_prdt - Usp1_prdt_pre);
    if Pr1_prdt <= -Pbwl
        Pr1_prdt = -Pbwl;
    elseif Pr1_prdt >= 0
        Pr1_prdt = 0;
    end
end

% end spring 1 resisting force corresponding to predicted displacement at next
step i+1
if Usp1_prdt_next >= -gap_l
    Pr1_prdt_next = 0;
else
    Pr1_prdt_next = Pr1_prdt + Kabl*(Usp1_prdt_next - Usp1_prdt);
    if Pr1_prdt_next <= -Pbwl
        Pr1_prdt_next = -Pbwl;
    elseif Pr1_prdt_next >= 0
        Pr1_prdt_next = 0;
    end
end

% end spring 4 resisting force corresponding to predicted displacement at current
step i
if Usp4_prdt <= gap_l
    Pr4_prdt = 0;
else
    Pr4_prdt = Pr4_prdt_pre + Kabl*(Usp4_prdt - Usp4_prdt_pre);
    if Pr4_prdt >= Pbwl
        Pr4_prdt = Pbwl;
    elseif Pr4_prdt <= 0
        Pr4_prdt = 0;
    end
end

% end spring 4 resisting force corresponding to predicted displacement at next
step i+1
if Usp4_prdt_next <= gap_l
    Pr4_prdt_next = 0;
else
    Pr4_prdt_next = Pr4_prdt + Kabl*(Usp4_prdt_next - Usp4_prdt);
    if Pr4_prdt_next >= Pbwl
        Pr4_prdt_next = Pbwl;
    elseif Pr4_prdt_next <= 0
        Pr4_prdt_next = 0;
    end
end

% end spring 2 resisting force corresponding to predicted displacement at current
step i
Pr2_prdt = Pr2_prdt_pre + Kabt*(Usp2_prdt - Usp2_prdt_pre);
if Pr2_prdt >= Pbwt
    Pr2_prdt = Pbwt;
elseif Pr2_prdt <= -Pbwt
    Pr2_prdt = -Pbwt;
end

% end spring 2 resisting force corresponding to predicted displacement at next
step i+1
```

```
Pr2_prdt_next = Pr2_prdt + Kabt*(Usp2_prdt_next - Usp2_prdt);
if Pr2_prdt_next >= Pbwt
    Pr2_prdt_next = Pbwt;
elseif Pr2_prdt_next <= -Pbwt
    Pr2_prdt_next = -Pbwt;
end

% end spring 5 resisting force corresponding to predicted displacement at current
step i
Pr5_prdt = Pr5_prdt_pre + Kabt*(Usp5_prdt - Usp5_prdt_pre);
if Pr5_prdt >= Pbwt
    Pr5_prdt = Pbwt;
elseif Pr5_prdt <= -Pbwt
    Pr5_prdt = -Pbwt;
end

% end spring 5 resisting force corresponding to predicted displacement at next
step i+1
Pr5_prdt_next = Pr5_prdt + Kabt*(Usp5_prdt_next - Usp5_prdt);
if Pr5_prdt_next >= Pbwt
    Pr5_prdt_next = Pbwt;
elseif Pr5_prdt_next <= -Pbwt
    Pr5_prdt_next = -Pbwt;
end

% end spring 3 resisting force corresponding to predicted displacement at current
step i
if Usp3_prdt >= F_st/Kv
    Pr3_prdt = F_st;
else
    Pr3_prdt = Kv*Usp3_prdt;
end

% end spring 3 resisting force corresponding to predicted displacement at next
step i+1
if Usp3_prdt_next >= F_st/Kv
    Pr3_prdt_next = F_st;
else
    Pr3_prdt_next = Kv*Usp3_prdt_next;
end

% end spring 6 resisting force corresponding to predicted displacement at current
step i
if Usp6_prdt >= F_st/Kv
    Pr6_prdt = F_st;
else
    Pr6_prdt = Kv*Usp6_prdt;
end

% end spring 6 resisting force corresponding to predicted displacement at next
step i+1
if Usp6_prdt_next >= F_st/Kv
    Pr6_prdt_next = F_st;
else
    Pr6_prdt_next = Kv*Usp6_prdt_next;
end

%% Resisting forces from bridge deck
Pr_prdt = K*Uprdt;
Pr_prdt_next = K*Uprdt_next;
```

```
%% Resisting force vector assembly
% resisting force vector at current step i (size: 6(n+1) x 1)
Pr_prdt(1,:) = Pr_prdt(1,:) + Pr1_prdt;
Pr_prdt(2,:) = Pr_prdt(2,:) + Pr2_prdt;
Pr_prdt(3,:) = Pr_prdt(3,:) + Pr3_prdt;
Pr_prdt(6*n+1,:) = Pr_prdt(6*n+1,:) + Pr4_prdt;
Pr_prdt(6*n+2,:) = Pr_prdt(6*n+2,:) + Pr5_prdt;
Pr_prdt(6*n+3,:) = Pr_prdt(6*n+3,:) + Pr6_prdt;
Pr_prdt(3*n+2,:) = Pr_prdt(3*n+2,:) + Prh_spec_prdt;
Pr_prdt(3*n+3,:) = Pr_prdt(3*n+3,:) + Prv_spec_prdt;

% resisting force vector at next step i+1 (size: 6(n+1) x 1)
Pr_prdt_next(1,:) = Pr_prdt_next(1,:) + Pr1_prdt_next;
Pr_prdt_next(2,:) = Pr_prdt_next(2,:) + Pr2_prdt_next;
Pr_prdt_next(3,:) = Pr_prdt_next(3,:) + Pr3_prdt_next;
Pr_prdt_next(6*n+1,:) = Pr_prdt_next(6*n+1,:) + Pr4_prdt_next;
Pr_prdt_next(6*n+2,:) = Pr_prdt_next(6*n+2,:) + Pr5_prdt_next;
Pr_prdt_next(6*n+3,:) = Pr_prdt_next(6*n+3,:) + Pr6_prdt_next;
Pr_prdt_next(3*n+2,:) = Pr_prdt_next(3*n+2,:) + Prh_spec_prdt_next;
Pr_prdt_next(3*n+3,:) = Pr_prdt_next(3*n+3,:) + Prv_spec_prdt_next;
```

Matlab code for performing the Alpha-OS numerical integration

```
function [A_next, U_next, V_next, Uh_spec_prdt_fol, Uv_spec_prdt_fol]
= AlphaOS(n, dt, beta, Uprdt_next, V, A, KI, M, C, Agh, Agv, Agh_next, Agv_next,
gamma, alpha, Pr_Uprdt, Pr_Uprdt_next)
% computation function of the HS system using Alpha-OS integration algorithm
%
% Inputs: n - bridge deck subdivision number
%         dt - time step
%         beta - Newmark acceleration coefficient
%         Uprdt_next - predicted displacement vector for all DOFs at next step i+1
          (size: 6(n+1) x 1)
%         V - velocity vector for all DOFs at current step i (size: 6(n+1) x 1)
%         A - acceleration vector for all DOFs at current step i (size: 6(n+1) x
          1)
%         KI - initial stiffness matrix of the whole bridge system, including end
          springs and test specimen (size: 6(n+1) x 6(n+1))
%         M - consistent mass matrix of the whole bridge system (size: 6(n+1) x
          6(n+1))
%         C - damping matrix of the whole bridge system (size: 6(n+1) x 6(n+1))
%         Agh - horizontal ground acceleration at current step i (scalar)
%         Agv - vertical ground acceleration at current step i (scalar)
%         Agh_next - horizontal ground acceleration at next step i+1 (scalar)
%         Agv_next - vertical ground acceleration at next step i+1 (scalar)
%         gamma - Newmark velocity coefficient
%         alpha – Alpha-OS parameter
%         Pr_Uprdt - resisting force vector corresponding to the predicted
          displacement at current step i (size: 6(n+1) x 1)
%         Pr_Uprdt_next - resisting force vector corresponding to the predicted
          displacement at next step i+1 (size: 6(n+1) x 1)
%
```

```
% Outputs: A_next - acceleration vector for all DOFs at next step i+1 (size:
          6(n+1) x 1)
%          U_next - displacement vector for all DOFs at next step i+1 (size:
          6(n+1) x 1)
%          V_next - velocity vector for all DOFs at next step i+1 (size: 6(n+1) x
          1)
%          Uh_spec_prdt_fol - predicted test specimen horizontal displacement at
          following step i+2 (scalar)
%          Uv_spec_prdt_fol - predicted test specimen vertical displacement at
          following step i+2 (scalar)
%
% written: WYJ 08/2019

%% compute the acceleration vector for all DOFs at next step i+1 (size 6(n+1) x 1)
% effective earthquake force (see section 8.2.1)
iota_node = [0; 1; Agv/Agh; 0; 0; 0];
iota_node_next = [0; 1; Agv_next/Agh_next; 0; 0; 0];
iota = repmat(iota_node, n+1 ,1);
iota_next = repmat(iota_node_next, n+1, 1);

% effective earthquake force vector at current step i (size: 6(n+1) x 1)
P = -M*iota*Agh;

% effective earthquake force vector at next step i+1 (size: 6(n+1) x 1)
P_next = -M*iota_next*Agh_next;

M_eff = M + (1 - alpha)*dt*gamma*C + dt^2*beta*(1 - alpha)*KI;
P_eff = (1 - alpha)*P_next + alpha*P - (1 - alpha)*Pr_Uprdt_next - alpha*Pr_Uprdt
        - ((1 - alpha)*C*dt*(1- gamma) + alpha*dt^2*beta*KI)*A - C*V;
A_next = M_eff\P_eff;

%% compute the displacement vector for all DOFs at next step i+1 (size: 6(n+1) x
1)
U_next = Uprdt_next + dt^2*beta*A_next;

%% compute the velocity vector for all DOFs at next step i+1 (size: 6(n+1) x 1)
V_next = V + dt*((1 - gamma)*A + gamma*A_next);

%% compute the predicted displacement vector for all DOFs at following step i+2
(size: 6(n+1) x 1)
Uprdt_fol = U_next + dt*V_next + dt^2*(1 - 2*beta)*A_next/2;

Uh_spec_prdt_fol = Uprdt_fol(3*n+2,:);
Uv_spec_prdt_fol = Uprdt_fol(3*n+3,:);
```